Waste to Resources – Elemental Sulfur for Functional Materials

Zur Erlangung des akademischen Grades eines

DOKTORS DER NATURWISSENSCHAFTEN (Dr. rer. nat.)

von der KIT-Fakultät für Chemie und Biowissenschaften
des Karlsruher Instituts für Technologie (KIT)

genehmigte

Dissertation

von

M. Sc. Johannes Martin Scheiger

1. Referent: Prof. Dr. Patrick Théato
2. Referent: Prof. Dr. Pavel A. Levkin
Tag der mündlichen Prüfung: 14.12.2021

Dedicated to Charlotte Sautter on the occasion of her 90th birthday.

Kurzfassung

Schwefel wird als Nebenprodukt der Erdöl- und Erdgasraffination jedes Jahr im Megatonnenmaßstab produziert. Die Deponierung großer Mengen überschüssigen Schwefels verursacht eine ökologische und wirtschaftliche Notwendigkeit, geeignete Verwendungsmöglichkeiten für diese günstige Ressource zu finden. Ein 2013 erfundenes Verfahren, die so genannte inverse Vulkanisation, zeigte eine Möglichkeit auf große Mengen Schwefels (90 Gew.-%) in polymere Materialien einzubringen. Die inverse Vulkanisation bietet jedoch nur eine unzureichende Reaktionskontrolle und ermöglicht es Chemikern daher nicht, Polymere mit definierten molekularen oder mechanischen Eigenschaften zu entwickeln. Daher wird nach chemischen Strategien gesucht, die eine Kontrolle über invers vulkanisierte Polymere bieten, um ein zielgerichtetes Materialdesign und die Entwicklung von Produkten zu ermöglichen.

Die synthetische Strategie in dieser Arbeit beschreibt die Verbindung von siliziumorganischer Chemie mit der inversen Vulkanisation. In dieser Symbiose ermöglicht die inverse Vulkanisations die Nutzung signifikanter Mengen an Schwefel, während die Organosiliziumchemie als chemische Schraube zur Einstellung der Eigenschaften des invers vulkanisierten Polymers dient. Zu diesem Zweck wurden geeignete ungesättigte Silane und Vinylsiloxane mit Schwefel bei erhöhten Temperaturen von 130 - 160°C umgesetzt, um Polymere mit hohem Schwefelgehalt zu erhalten. Diese Polymere können Folgereaktionen wie der Hydrolyse und Polykondensation oder der Ringöffnenden Polymerisation unterzogen werden.

Ausgehend von der inversen Vulkanisation von Styrylethyltrimethoxysilan (StyTMS) wurde elementarer Schwefel in eine in Lösung prozessierbare Beschichtung mit einem Schwefelgehalt von 35 Gew.-% überführt. Dazu wurde StyTMS mit elementarem Schwefel umgesetzt, um Präpolymere zu erhalten, die hydrolysierbare funktionelle Methoxysilangruppen tragen, welche in Lösung durch die Zugabe einer verdünnten Säure bei Raumtemperatur hydrolysiert wurden. Die hydrolysierten Präpolymerlösungen wurden durch Sprüh-, Tauch- oder Schleuderbeschichtung auf eine Vielzahl von Oberflächen wie Glas, Silizium, Gold oder Substrate wie Zellulosefilter, Glasfaserfilter oder Siliziumdioxidpartikel aufgebracht. Nach dem Verdampfen des Lösungsmittels bildet das hydrolysierte Präpolymer durch Polykondensation Siloxanvernetzungen. Durch die Bildung von Siloxanbindungen wurde die hochschwefelhaltige Beschichtung kovalent an Oberflächen gebunden und unlöslich. Beschichteten Siliziumdioxidpartikel besaßen die Fähigkeit, giftige Quecksilber(II)-Ionen aus dem Wasser zu extrahieren. Mit dieser Strategie konnte die Löslichkeit eines invers vulkanisierten Polymers kontrolliert werden, was seine Verwendung als lösungsmittelbeständige Beschichtung ermöglichte. Die entwickelten Beschichtungen und Präpolymere wurden mit AFM, ATR FT-IR, Ellipsometrie, EDX, SEM, ToF-SIMS, UV-vis, XPS und ^{29}Si NMR untersucht.

Die inverse Vulkanisation von hydrolysierbaren Norbornenylsilanen wurde genutzt, um lösliche Polymere mit einem Schwefelgehalt von 50 Gew.-% und einstellbaren molekularen und makroskopischen Eigenschaften zu synthetisieren. Dazu wurde elementarer Schwefel mit Mischungen aus einem hydrolysierbaren Chlor- oder Ethoxynorbornenylsilan und dem nicht hydrolysierbaren Trimethylnorbornenylsilan umgesetzt, um invers vulkanisierte Präpolymere zu erhalten. Je nach Wahl und Anteil des hydrolysierbaren Norbornenylsilans, welches zwischen einer und drei hydrolysierbare Gruppen enthält, können unterschiedliche Mengen an M-, D- oder T-Siloxanbindungen in das invers vulkanisierte Polymer eingebaut werden. Trimethylnorbornenylsilan wurde durch Methylierung eines Monoethoxynorbornenylsilans synthetisiert und ermöglichte die Bildung löslicher Polymere, indem es die Anzahl der Siloxanbindungen unterhalb der Vernetzungsschwelle hält. Die Polykondensation der invers vulkanisierten Präpolymere erfolgte in der Schmelze und die Produkte wurden durch Fällung gereinigt. Durch feines Variieren der Anzahl der Siloxanbindungen in den invers vulkanisierten Polymeren wurden grundlegende Eigenschaften wie die molare Masse oder die Glasübergangstemperatur gezielt verändert. Die elementare Zusammensetzung der Polymere blieb konstant, während ihre makroskopischen Eigenschaften von hart bis weich, von starr bis dehnbar und von spröde bis verformbar eingestellt wurden. Die synthetisierten Polymere wurden mittels ATR-FTIR, Elementaranalyse, DSC, PXRD, GPC und ^{29}Si NMR eingehend charakterisiert.

Es konnte gezeigt werden, dass die inverse Vulkanisation von Vinyl(cyclo)siloxanen flexible Polymere mit einem Schwefelgehalt bis zu 40 Gew.-% durch eine einfache und skalierbare Synthese ermöglicht. Dies wird auf die einzigartigen Eigenschaften der Siloxanbindung zurückgeführt, wie z. B. eine niedrige Rotationsenergie um die Bindungsachse oder eine niedrige Energie für die Linearisierung der Bindung. Die Ringstrukturen der Cyclosiloxane blieben erhalten und konnten mit starken Säuren geöffnet werden. Die mechanischen Eigenschaften der invers vulkanisierten Polymere wurden anhand von Zug- und Drucktests untersucht.

Zusammenfassend konnte gezeigt werden, dass die inverse Vulkanisation mit der industriell relevanten Organosiliziumchemie kompatibel ist. Die Kombination eines hohen Schwefelgehalts mit siliziumorganischer Folgechemie ermöglichte die Kontrolle über die Löslichkeit sowie die thermischen, molekularen, mechanischen und rheologischen Eigenschaften von invers vulkanisierten Polymeren, was zur Entwicklung von Beschichtungen und weichen Materialien mit hohem Schwefelgehalt führte.

Abstract

Sulfur is produced on the megaton scale every year due to being a side product of natural oil and gas refining. The landfilling of large amounts of excess sulfur creates an ecological and economical imperative to find suitable uses for this cheap resource. A process invented in 2013, termed the inverse vulcanization, revealed a way to incorporate large quantities of sulfur (90 wt%) into polymeric materials. However, the inverse vulcanization offers only poor reaction control and does not allow chemists to predict and design polymers with targeted molecular or mechanical properties. Therefore, chemical strategies offering control over inverse vulcanized polymers are sought to enable a purposeful material design and product development.

The synthetic strategy in this thesis describes the marriage of organosilicon chemistry with the inverse vulcanization. In this symbiosis, the inverse vulcanization enables the utilization of significant quantities of sulfur whereas the organosilicon chemistry serves as a chemical screw to tune the properties of the inverse vulcanized polymer. For this, suitable unsaturated silanes and vinylsiloxanes were reacted with sulfur at elevated temperatures around 130 – 160°C to obtain high sulfur content polymers. These polymers could undergo follow-up reactions such as hydrolysis and polycondensation, or ring opening polymerization.

Based on the inverse vulcanization of styrylethyltrimethoxysilane (StyTMS), elemental sulfur was converted into a solution processable coating with a sulfur content of 35 wt%. For this, StyTMS was reacted with elemental sulfur to obtain prepolymers carrying hydrolysable methoxysilane functional groups, which were hydrolyzed in solution by addition of a dilute acid at room temperature. Hydrolyzed prepolymer solutions were applied to a variety of surfaces such as glass, silicon, gold, or substrates such as cellulose filters, glass fiber filters, or silica particles via spray-, dip-, or spin-coating. Upon evaporation of the solvent, the hydrolyzed prepolymer formed siloxane crosslinks via polycondensation. As a result of siloxane bond formation, the high sulfur content coating bound to surfaces covalently and was rendered insoluble. Silica particles coated with the high sulfur content coating possessed the ability to extract toxic mercury(II) ions out of water. By this strategy, control over the solubility of an inverse vulcanized polymer was demonstrated which enabled its use as a solvent resistant coating. The developed coatings and prepolymers were examined with AFM, ATR FT-IR, ellipsometry, EDX, SEM, ToF-SIMS, UV-vis, XPS, and ^{29}Si NMR.

The inverse vulcanization of hydrolysable norbornenylsilanes was used to allow for the synthesis of soluble polymers with a sulfur content of 50 wt% and tunable molecular and macroscopic properties. To achieve this, elemental sulfur was reacted with mixtures consisting of a hydrolysable chloro- or ethoxynorbornenylsilane and the non-hydrolysable trimethylnorbornenylsilane to obtain inverse vulcanized prepolymers. Different amounts of M, D, or T siloxane bonds could be installed into the inverse vulcanized polymer depending on the choice and the share of the hydrolysable norbornenylsilane, which contained between one and three hydrolysable groups, respectively. Trimethylnorbornenylsilane was synthesized via methylation of a monoethoxynorbornenylsilane and enabled the formation of soluble polymers by keeping the number of siloxane bonds below the threshold of crosslinking. The polycondensation of the inverse vulcanized prepolymers was conducted in the melt and the products were purified by precipitation. By finely varying the number of siloxane bonds in the inverse vulcanized polymers, fundamental properties such as the molar mass or the glass transition temperature were altered in a targeted way. The elemental composition of the polymers remained constant, whereas their macroscopic properties were tuned from hard to soft, rigid to stretchable, and brittle to malleable. Synthesized polymers were characterized thoroughly using ATR-FTIR, elemental analysis, DSC, PXRD, GPC, and ^{29}Si NMR.

It could be shown that the inverse vulcanization of vinyl(cyclo)siloxanes affords flexible polymers with a sulfur content of up 40 wt% via a straightforward and scalable synthesis. This is attributed to the unique properties of the siloxane bond, such as a low energy of rotation and low energy of bond linearization. The ring structures of the cyclosiloxanes were retained and could be opened with strong acids. The mechanical properties of the inverse vulcanized polymers were investigated using tensile and compression tests.

In conclusion, it could be demonstrated that the inverse vulcanization is compatible with the industrially relevant organosilicon chemistry. Merging a high sulfur content with the organosilicon follow-up chemistry gave control over the solubility, as well as the thermal, molecular, mechanical, and rheological properties of inverse vulcanized polymers, which lead to the development of high sulfur content coatings and soft materials.

CV

NAME	Johannes Martin Scheiger (27)

CONTACT

Musterstr. 1
12345 Musterstadt
☎ -----------
✉ johannes.scheiger@kit.edu

EDUCATION

8/2018 – 12/2021	**Doctoral Researcher (Summa Cum Laude)** *Karlsruhe Institute of Technology (Karlsruhe)* ▪ Thesis: "Waste as a Resource – Sulfur for Functional Materials" with Prof. Théato and Prof. Levkin ▪ Member of the Biointerfaces International Graduate School
4/2018 – 7/2018	**Researcher** *Chulalongkorn University (Bangkok)* ▪ Project: "Efficient Lithium-Ion Transfer in Polymer Electrolytes" with Prof. Suwabun Chirachanchai
10/2015 – 3/2018	**Chemistry M. Sc.** *Karlsruhe Institute of Technology (Karlsruhe)* ▪ Thesis: "Preprogrammed UV induced Formation and Degradation of Hydrogels" with Prof. Levkin
10/2012 – 10/2015	**Chemistry B. Sc.** *Karlsruhe Institute of Technology (Karlsruhe)* ▪ Thesis: „Reactions of Samarocene" with Prof. Roesky
09/2004 – 06/2012	**Abitur** *Johann-Vanotti Gymnasium (Ehingen)*

WORK

Research Assistant KIT
06/2018 – 07/2018
Institute of Biolog. and Chem. Systems (Karlsruhe)

Intern VCI e.V
09/2016 – 01/2017
German Chemical Industry Association (Brussels)

- Monitoring and reporting about EU legislation relevant for the German chemical industry

Intern UBC
04/2017 – 05/2017
University of British Columbia (Vancouver)

- Project: „Redox Properties of Bimetallic Cobalt Complexes" with Prof. Fryzuk

Teaching Assistant KIT
04/2016 – 06/2016
Institute of Organic Chemistry (Karlsruhe)

- Tutorial for students about basic organic chemistry

Student Service ZLMT
04/2013 – 07/2016
Hospital Karlsruhe, Central Laboratory (Karlsruhe)

- Blood analysis, quality assurance, and validation of blood tests in late-, weekend-, and nightshifts.

LANGUAGES

German	native
English	fluent
French	basics
Chinese	basics

STIPENDS AND GRANTS

DBU PhD full scholarship (2018 - 2021)
KHYS Research Travel Grant (2021)
KHYS Networking Grant (2020)
BIF-IGS Conference Grant (2019)
PROMOS DAAD Travel Grant (2017)

22nd of January 2022, Karlsruhe

Table of Contents

Kurzfassung ..... **i**

Abstract ..... **iii**

CV ..... **v**

Table of Contents ..... **vii**

List of Figures ..... **xi**

List of Tables ..... **xxi**

List of Abbreviations ..... **xxiii**

Acknowledgements ..... **xxv**

Preface **1**

1 Introduction **3**

- 1.1 The element sulfur 3
  - 1.1.1 Abundance, production, and general reactivity 3
  - 1.1.2 Allotropes 5
  - 1.1.3 Applications 6
- 1.2 The sulfur-sulfur bond 7
  - 1.2.1 S-S in disulfides 7
  - 1.2.2 S-S in polysulfides 8
- 1.3 Sulfur containing polymers 9
  - 1.3.1 Polysulfides 9
  - 1.3.2 Poly(thioether)s, poly(sulfoxide)s, and poly(sulfone)s 11
  - 1.3.3 Poly(thiophene)s 12
  - 1.3.4 Poly(thioester)s and poly(thiocarbonate)s 12
- 1.4 Inverse vulcanization 14
- 1.5 Organosilicon chemistry 16
  - 1.5.1 Alkoxy- and chlorosilanes 16
  - 1.5.2 Polycondensation of alkoxy- and chlorosilanes 17
  - 1.5.3 Cyclosiloxanes 19
  - 1.5.4 Ring opening polymerization of cyclosiloxanes 20
  - 1.5.5 The silicon-oxygen bond 21

2 Motivation **23**

3 Results and Discussion **25**

- 3.1 Inverse Vulcanization of Styrylethyltrimethoxysilane 25
  - 3.1.1 Disclaimer 25
  - 3.1.2 Nomenclature 26
  - 3.1.3 Introduction 26

3.1.4 Synthesis of poly(S_n-*r*-StyTMS) and *net*-poly(S_n-*r*-StyTMS) 26
3.1.5 Stability of *net*-poly(S_{35}-*r*-StyTMS) against degradation 32
3.1.6 Coatings of *net*-poly(S_{35}-*r*-StyTMS) 34
3.1.7 Summary 48
3.2 Inverse Vulcanization of Norbornenylsilanes 49
3.2.1 Disclaimer 49
3.2.2 Nomenclature 49
3.2.3 Introduction 50
3.2.4 Synthesis of TMNBS 51
3.2.5 Inverse vulcanization of NBS_x 52
3.2.6 Melt polycondensation of poly(S-*r*-NBS_x) 57
3.2.7 Solution polycondensation of poly(S-*r*-NBS_x) 59
3.2.8 Chemical analysis of *branch*-poly(S-*r*-NBS_x) 62
3.2.9 Molar mass analysis of *branch*-poly(S-*r*-$MENBS_x$) 67
3.2.10 Theoretical considerations of *branch*-poly(S-*r*-$MENBS_x$) formation 69
3.2.11 Molar mass analysis of *branch*-poly(S-*r*-NBS_x) 72
3.2.12 Molar mass analysis of poly(S_x-*r*-$DENBS_{20}$) 76
3.2.13 Stability of *branch*-poly(S-*r*-NBS_{20}) against degradation 78
3.2.14 Partial polycondensation of poly(S-*r*-$MENBS_x$) 80
3.2.15 Thermomechanical properties of *branch*-poly(S-*r*-NBS_x) 83
3.2.16 Mechanical properties of *branch*-poly(S-*r*-$MENBS_x$) 87
3.2.17 Summary 88
3.3 Inverse Vulcanization of Vinyl(cyclo)siloxanes 89
3.3.1 Introduction 89
3.3.2 Nomenclature 90
3.3.3 Inverse vulcanization of TVS-D_4 90
3.3.4 Inverse vulcanization of DVS-MM, TVS-D_3, and PVS-D_5 96
3.3.5 DSC, tensile-, and compression tests 99
3.3.6 Summary 101

4 Experimental 103

4.1 Analysis 103
4.1.1 AFM 103
4.1.2 ATR FT-IR 103
4.1.3 Digital microscopy and light microscopy 103
4.1.4 DLS 103
4.1.5 DSC 104
4.1.6 EDX and SEM 104
4.1.7 Elemental analysis 104
4.1.8 Ellipsometry 104
4.1.9 GPC 104
4.1.10 Raman spectroscopy 105
4.1.11 Rheometry 105
4.1.12 PXRD 105
4.1.13 Universal Tester 105

4.1.14 TGA coupled MS 105
4.1.15 ToF-SIMS 106
4.1.16 UV-vis 106
4.1.17 WCA 106
4.1.18 XPS 106
4.1.19 ^{1}H and ^{13}C NMR 106
4.1.20 ^{29}Si NMR 106
4.1.21 ^{29}Si CP/MAS and HPDEC NMR 107
4.2 Methods 107
4.2.1 AFM scratch analysis 107
4.2.2 Spin-coating 107
4.2.3 Dip-coating 108
4.2.4 Preparation of *net*-poly(S_{35}-*r*-StyTMS) coated silica particles 108
4.2.5 Mercury(II) ion removal 108
4.2.6 Solution casting of *net*-poly(S_{35}-*r*-StyTMS) 108
4.2.7 Molding of *branch*-poly(S-*r*-NBS_x) 109
4.2.8 Thin film interference color calculation 109
4.3 Synthesis 110
4.3.1 General procedures 110
4.3.2 Synthesis of monomers, polymers, and polymer networks 110

5 Conclusion and Outlook 123

Literature 125

Appendix 133

List of Figures

Figure 1. True color image of Jupiter's moon Io taken from the spacecraft Galileo of the National Aeronautics and Space Administration (NASA) on the 3rd of July in 1999. Image from NASA (public image database). 3

Figure 2. Reaction equations of the part reactions (yellow) and the overall reaction equation (green) of the Claus process. 4

Figure 3. Thermal transitions of sulfur allotropes in the solid, liquid, and gas state.....................5

Figure 4. Reaction equation for (I) the synthesis of S_{5n} (n = 1, 2, or 3) from [Cp_2TiS_5] and SO_2Cl_2, and (II) the synthesis of S_{5+n} (x =1, 2, 4, 6, 7, and 8) from [Cp_2TiS_5] and S_nCl_2. 6

Figure 5. Structure of the *gauche*, *cis*, and *trans*-conformation for R_2S_2. 7

Figure 6. Structure of H_2S_2, Me_2S_2, and *t*-Bu_2S_2 with a S-S bond length d, a H-S-S bond angle α and a dihedral angle φ. 8

Figure 7. Structure of S_2F_2, S_2Cl_2, and S_2Br_2 with a S-S bond length d, a X-S-S bond angle α and a dihedral angle φ. 8

Figure 8. Schematic visualization of a vicinal π-electron interaction stabilizing the S-S bonds next to a stretched or homolytically dissociated S-S bond, i.e., thiyl radicals. 9

Figure 9. Sulfur containing functional groups with relevance for sulfur containing polymers. EDOT = 3,4-ethylenedioxythiophene. R is an organic rest. 9

Figure 10. Reaction equations for the formation of polysulfides R-S_n-R (R = alkyl and aryl, $n \leq 2$). 10

Figure 11. Reaction equation for (I) the formation of Thiokol type copolymers and (II) their selective reduction and oxidation. 10

Figure 12. Reaction equation for the synthesis of poly(thioether)s via (I) ring opening polymerization (ROP) of ethylene sulfide derivatives, (II) polycondensation of alkylbromides, and (III) thiol-ene polyaddition. Selective oxidation yields the respective poly(sulfoxide)s or poly(sulfone)s.. 11

Figure 13. Reaction equation for the oxidation of a (I) 3,4-disubstituted thiophen and (II) 3,4-ethylendioxythiophen. 12

Figure 14. Synthesis of poly(thioester)s via (I) microbial polycondensation, (II) ring opening polymerization of ε-thiolactone, and (III) the reaction of a thioanhydride with substituted ethylene sulfide. 13

Figure 15. Synthesis strategies for poly(thiocarbonate)s. In (IV) there can be 1-3 sulfur or oxygen atoms in a repeating unit due to the oxygen-sulfur exchange reaction. In (III) the oxygen-sulfur exchange reaction is inhibited by using low temperatures. Y indicates either a sulfur or oxygen atom while R_1 and R_2 denote organic rests. PPNCL (bis(triphenylphosphoranylidene) ammonium chloride) is a co-catalyst........... 13

Figure 16. General reaction equation of the inverse vulcanization of a divinyl compound. 14

Figure 17. Synthetic route from trichlorosilane to functional alkoxysilanes. (I) Hydrosilylation, (II) alcoholysis, and (III) substitution with metal organyls (RLi, RMgX). R_1 can be aryl or alkyl, R_2 is mostly methyl- or ethyl-, R_3 can be alkyl or aryl.. 17

Figure 18. Reaction equation of the (I) hydrolysis and polycondensation of a silane containing four hydrolysable groups (simplified) and (II) the formation of M, D, T, and Q siloxanes.. 18

Figure 19. Reaction equations of some of the possible equilibria occurring during the polycondensation of a diorganodimethoxysilane. 19

Figure 20. Hydrolysis and polycondensation of dichlorodimethylsilane to form a mixture of ring molecules and linear chains.. 20

Figure 21. Reaction equations of the kinetically (green) or thermodynamically (blue) controlled anionic ROP of 2,2,4,4,6,6-hexamethylcyclotrisiloxane using potassium trimethylsilanolate as an initiatior and 1,1,1,3,3,3-hexamethyldisiloxane as an end capping agent. 20

Figure 22. (A) Schematic reaction of sulfur with styrylethyltrimethoxysilane (StyTMS) to form a soluble prepolymer which can be hydrolyzed and polycondensated to yield high sulfur content coatings on surfaces and particles as well as crosslinked bulk *net*-poly(S_n-*r*-StyTMS). (B) Reaction equation of the inverse vulcanization of sulfur with styrylethyltrimethoxysilane (StyTMS) and the subsequent hydrolysis and polycondensation of the formed poly(S_n-*r*-StyTMS) to yield *net*-poly(S_n-*r*-StyTMS). 27

Figure 23. Molecular structures of the four constitutional isomers of (A) StyTMS and (B) EPTMS. The respective *meta* and *para* isomers are grouped. In each group of *meta* and *para* isomers, the left structure is the product of an anti-Markovnikov addition, whereas the right structure is the product of a Markovnikov addition. 28

Figure 24. ^{1}H NMR spectrum of (A) StyTMS and (B) poly(S_n-*r*-StyTMS) in $CDCl_3$. The $CDCl_3$ in (A) contained 0.03 vol% TMS as a reference. 29

Figure 25. Molecular structures of the constitutional isomers of poly(S_n-*r*-StyTMS) for a (A) linear and a (B) terminal micrstructure. The respective *meta* and *para* isomers are grouped. In each group of *meta* and *para* isomers, the left structure is the product of an anti-Markovnikov addition, whereas the right structure is the product of a Markovnikov addition. 30

Figure 26. GPC traces of poly(S_x-r-StyTMS) for varying ratios of sulfur (A) and different reaction times (B). The index *x* instead of *n* refers to the feed ratio and not to the factual content of sulfur... 31

Figure 27. GPC traces of partially polycondensated poly(S_n-*r*-StyTMS). $M_N = 1600$ g mol^{-1}, $M_W = 5500$ g mol^{-1}, Đ = 3.4. 31

Figure 28. (A) PXRD patterns of *net*-poly(S_{35}-*r*-StyTMS) powder aged for two months. Elemental sulfur was used as a reference. (B) DSC thermograms of *net*-poly(S_{35}-*r*-StyTMS) powder aged for two months....................33

Figure 29. (A) TGA thermogram of *net*-poly(S_{35}-*r*-StyTMS) from 50 to 500 °C. (B) Formation of SO_2, H_2O, and CO_2 in dependence of the temperature as determined with a mass spectrometer coupled to the TGA....................34

Figure 30. Microscopy images of glass surfaces coated with *net*-poly(S_{35}-*r*-StyTMS) with different coating techniques. The spin-coated surface was scratched with a needle to visualize the presence of a coating. An "Emboss (strong)" filter was used for the dip coated sample, to enhance the visibility of the micropores on the surface. Scalebars are 200 µm....................34

Figure 31. (A) Microscopy images of glass slides dip-coated via slow (40 mm min^{-1}) and fast (760 mm min^{-1}) removal of the glass slide from a hydrolyzed poly(S_{35}-*r*-StyTMS) solution. The slow-removal surface appeared to contain many micropores, whereas the fast-removal surface appeared to be smooth. (B) AFM images of glass slides being removed from a poly(S_{35}-*r*-StyTMS) solution with a speed of (i) 40, (ii) 45, (iii) 125, and (iv) 760 mm min^{-1}, respectively. The heights of the *net*-poly(S_{35}-*r*-StyTMS) features were 26, 24, 45, and 70 nm for (i)-(iv), respectively. Scalebars are 3 µm. 35

Figure 32. Digital microscope images of surfaces spin-coated with three different concentrations of poly(S_n-*r*-StyTMS), i.e., 40, 20, and 13.3 mg mL^{-1}. The AFM cantilever and tip can be seen on the right side of the pictures. Scalebars are 100 µm....................36

Figure 33. AFM (A) height images and (B) amplitude error images of *net*-poly(S_{35}-*r*-StyTMS) coatings on glass prepared with a concentration of (i) 40 mg mL^{-1} and (ii) 13.3 mg mL^{-1} of hydrolyzed poly(S_n-*r*-StyTMS) for one spin-coating cycle, and (iii) 13.3 mg mL^{-1} of hydrolyzed poly(S_n-*r*-StyTMS) for three spin-coating cycles. Scalebars are 8 µm. 37

Figure 34. Top row: Examples for AFM scratch analysis for surfaces prepared via spin-coating of 13.3 mg mL-1 hydrolyzed poly(S-*r*-StyTMS) solution on (A) glass, (B) gold, and (C) silicon. Bottom row: Graphs showing the average height along the cross-section. The respective step heights were analyzed with the software NanoScope Analysis. Scalebars are 4 µm. 38

Figure 35. (A) Influence of the number of spin-coating cycles on the film thickness on glass. (B) Influence of the poly(S-*r*-StyTMS) concentration on the film thickness on different substrates via spin-coating (glass, silicon, gold). Error bars are standard deviations (N=3). 39

Figure 36. Digital images of (A) a poly(S-*r*-StyTMS) solution in THF in a Teflon mold and (B) a solution casted film of *net*-poly(S-*r*-StyTMS). (C) UV-vis spectrum of poly(S-*r*-StyTMS) in THF. The concentration of poly(S-*r*-StyTMS) was 0.16 µg mL^{-1}. 40

Figure 37. (A) Digital images of silicon wafers (0 – 13) spin-coated with *net*-poly(S_{35}-*r*-StyTMS) taken at a viewing angle of ca. 30 ° relative to the surface normal. (B) Calculated thin film interference colors in dependence of the film thickness and the viewing angle. Parameters required for the calculation were based on the Cauchy model with absorbance corrections. The thicknesses of the *net*-poly(S_{35}-*r*-StyTMS) coatings are indicated by the sample numbers (0 – 13) and are marked as white stripes. 41

Figure 38. (A) Thickness of *net*-poly(S_{35}-*r*-StyTMS) coatings in dependence of the relative concentration of poly(S_n-*r*-StyTMS), with 40 mg mL^{-1} in THF corresponding to 100 %. Error bars represent the 90% confidence value. Linear fit: $y = 2.57x \pm 0.07$, $R^2 = 0.992$. (B) Refractive index n and the extinction coefficient k in dependence of the wavelength. Cauchy fit: $n = 1.591 + 0.01935\ nm^{-2}$ and $k = 0.02425 + 0.1552\ nm^{-2}$. 42

Figure 39. (A) EDX spectra of glass and glass coated with *net*-poly(S_{35}-*r*-StyTMS). (B) XPS spectra of elemental sulfur and glass coated with *net*-poly(S_{35}-*r*-StyTMS). 43

Figure 40. (A) FTIR IR spectrum of *net*-poly(S_{35}-*r*-StyTMS) coated on a gold surface. (B) Relative distribution of polysulfide fragments (S_n^-) for *net*-poly(S_{35}-*r*-StyTMS) coating as determined with ToF-SIMS. Elemental sulfur was used as a reference. (C) Map of S_3^- ion counts as detected with ToF-SIMS. A surface area of 500 × 500 µm (0.025 mm^2) was examined. Scalebar is 100 µm. 44

Figure 41. (A) ^{29}Si NMR spectra of StyTMS (bottom) and poly(S-*r*-StyTMS) (top) in $CDCl_3$. Ar denotes a styryl or ethylphenyl substituent, respectively. (B) ^{29}Si NMR CP-MAS spectrum of powdered *net*-poly(S_{35}-*r*-StyTMS) showing Si in T_1, T_2, and T_3 siloxane binding states. (C) ^{29}Si HPDEC-MAS NMR spectrum of powdered *net*-poly(S_{35}-*r*-StyTMS) showing Si in T_1, T_2, and T_3 siloxane binding states after the polycondensation and a background spectrum (rotor). 45

Figure 42. Digital images of a (A) glass fiber filter, a (B) cellulose filter, and (C) silica gel before (left) and after (right) coating with *net*-poly(S_{35}-*r*-StyTMS). The hydrophobicity of the filter surfaces were increased after coating with *net*-poly(S_{35}-*r*-StyTMS) as seen from the formation of a water droplet (dyed blue) blue dye) instead of spreading of the droplet. Scalebars are 1, 3, and 1 cm, respectively. 46

Figure 43. (A) EDX spectrum of a pristine and a cellulose filter coated with *net*-poly(S_{35}-*r*-StyTMS). (B) SEM images of a cellulose filter before and after coating with *net*-poly(S_{35}-*r*-StyTMS). Scalebars are 100 µm. (C) DLS measurements of SiO_2 nanoparticles before (270 nm) and after functionalization (300 nm) with *net*-poly(S_{35}-*r*-StyTMS). Each curve represents the average of three measurements. 47

Figure 44. Mercury remediation experiments evaluated with hydride-AAS for different initial concentrations of Hg^{2+}. Stock refers to the Hg^{2+} stock solution, pristine refers to silica microparticles, and coated refers to silica microparticles coated with *net*-poly(S_{35}-*r*-StyTMS). (A) Mercury remediation experiments using different initial Hg^{2+} concentrations. (B) Mercury remediation experiments for an initial Hg^{2+} concentration of ca. 10 ppmw. Values are given as the average of three measurements with the error bars being the standard deviation....................48

Figure 45. (A) Reaction equation for the synthesis of TMNBS....................51

Figure 46. Insets in the (A) ^{1}H NMR, (B) ^{13}C NMR, and (C) ^{29}Si NMR spectra of MENBS and TMNBS in $CDCl_3$ as well as an inset in the (D) ATR FT-IR spectra of TMNBS and MENBS. The insets highlight areas or peaks relevant for the substitution of the ethoxy group in MENBS with a methyl group in TMNBS....................52

Figure 47. (A) Schematic of the inverse vulcanization and polycondensation (PC) of mixtures of norbornenylsilanes (NBS_x). NBS_x containing of a M, D, or T siloxane precursor and TMNBS react with sulfur to form poly(S-*r*-NBS_x), which polycondensates to yield *branch*-poly(S-*r*-NBS_x). (B) Generalized reaction equation of the inverse vulcanization and polycondensation of sulfur with NBS_x. The *branch*-poly(S-*r*-NBS_x) can contain either M, D, or T siloxane bonds. (C) Chemical structures, acronyms, and designated color of NBS serving as comonomer (TMNBS) or termonomers (MENBS, DENBS, DCNBS, TENBS, and TCNBS. 53

Figure 48. (A) ATR FT-IR spectra of poly(S-*r*-$DENBS_{100}$) formed by reacting equal masses of sulfur and DENBS at 150°C for 1, 2, 3, 4, and 8 h, respectively. (B) Inset of the normalized ethoxy bands between 1200 – 1000 cm^{-1}. 54

Figure 49. Digital image showing the products of the inverse vulcanization of sulfur with equal amounts of (A) TMNBS, (B) MENBS, (C) DENBS, and (D) TENBS for different reaction times. The total mass of each sample 1 g. 55

Figure 50. Inset of ^{1}H NMR spectra showing the consumption of norbornene C=C double bonds for the inverse vulcanization of sulfur with equal amounts of either (A) TMNBS, (B) MENBS, (C) DENBS, or (D) TENBS after different reaction times....................56

Figure 51. DSC thermograms (75 – 130°C) of the products of the inverse vulcanization of (A) TMNBS, (B) MENBS, (C) DENBS, and (D) TENBS after different reaction times. The masses of sulfur and the respective NBS was 500 mg....................57

Figure 52. Digital images of the purification of *branch*-poly(S-*r*-NBS_x) after precipitation. (i) Sedimentation, (ii) vacuum filtration, (iii) vacuum oven drying and (iv) molding. The shown *branch*-poly(S-*r*-MENBS$_{20}$) were ductile but not sticky. Scalebar is 5 mm. 58

Figure 53. (A) GPC elugram of *branch*-poly(S-*r*-MENBS$_{20}$) before and after precipitation from THF into MeOH. (B) GPC elugrams of *branch*-poly(S-*r*-MENBS$_{25}$) for different reaction times. 58

Figure 54. (A) GPC traces and (B) analysis of the molar mass of poly(S-*r*-DENBS$_{100}$) prepared in THF solution using different volume ratios of HCl (pH 4). Molar mass: 1 vol% (M_N = 1200 g mol^{-1}, M_W = 5400 g mol^{-1}), 10 vol% (M_N = 900 g mol^{-1}, M_W = 2000 g mol^{-1}), 15 vol% (M_N = 800 g mol^{-1}, M_W = 1500 g mol^{-1}), and 20 vol% (M_N = 700 g mol^{-1}, M_W = 1200 g mol^{-1}).. 59

Figure 55. (A) GPC traces and (B) analysis of the molar mass of poly(S-*r*-DENBS$_{100}$) after different reaction or work-up steps. Molar mass: (1) Inverse vulcanization (M_N = 600 g mol^{-1}, M_W = 1300 g mol^{-1}), (2) hydrolysis (M_N = 600 g mol^{-1}, M_W = 1400 g mol^{-1}), (3) removal of volatiles (M_N = 800 g mol^{-1}, M_W = 1800 g mol^{-1}), and (4) vacuum drying (M_N = 1200 g mol^{-1}, M_W = 5400 g mol^{-1}). 60

Figure 56. (A) GPC traces and (B) analysis of the molar mass of poly(S-*r*-DENBS$_{100}$) polycondensated in different solvents. Molar mass: toluene (M_N = 300 g mol^{-1}, M_W = 400 g mol^{-1}), 1-butanol (M_N = 700 g mol^{-1}, M_W = 1600 g mol^{-1}), THF (M_N = 1200 g mol^{-1}, M_W = 5400 g mol^{-1}), 2-propanol (M_N = 900 g mol^{-1}, M_W = 9000 g mol^{-1}). Poly(S-*r*-DENBS$_{100}$), the alcohols 1-butanol and 1-propanol suffered from a limited solubility of poly(S-*r*-DENBS$_{100}$). 61

Figure 57. (A) Digital image of a nano-dispersion of hydrolyzed poly(S-*r*-DENBS$_{100}$) in water. (B) Differential light scattering of the poly(S-*r*-DENBS$_{100}$) dispersion. The size of the particles was 132.2 ± 0.1 nm (N=3). 62

Figure 58. (A) Melting behavior of *branch*-poly(S-*r*-NBS$_{20}$) containing different siloxane bonds. Granules of b*ranch*-poly(S-*r*-MENBS$_{20}$) before (i) and after 2 h (i') at 80°C. Granules of (ii) *branch*-poly(S-*r*-DCNBS$_{20}$) and (iii) *branch*-poly(S-*r*-TCNBS$_{20}$) after 2 h at 80°C. (B) Molded objects made from 2 g of *branch*-poly(S-*r*-NBS$_{20}$) at 80°C overnight. 63

Figure 59. (A) Digital images showing the melting of *branch*-poly(S-*r*-MENBS$_{20}$) granulates into a transparent film). (i) granulated *branch*-poly(S-*r*-MENBS$_{20}$) on a glass slide after (ii) 2 min, (iii) and 10 min at 80°C. (iv) Molten *branch*-poly(S-*r*-MENBS$_{20}$) in between two glass slides. Scalebar is 5 mm. (A) UV-vis spectrum from 250 – 800 nm of a thin film of *branch*-poly(S-*r*-MENBS$_{20}$). 63

Figure 60. ^{29}Si CP/MAS NMR spectra of (A) *branch*-poly(S-*r*-MENBS$_{20}$), (B) *branch*-poly(S-*r*-DENBS$_{20}$), and (C) *branch*-poly(S-*r*-TENBS$_{20}$). The peak appearing in each spectrum at 1.4 ppm corresponds to the -SiMe$_3$ group from TMNBS... 60

Figure 61. ATR FT-IR spectra of the (A) M, D, and T siloxane forming termonomers and (B) of *branch*-poly(S-*r*-NBS$_{20}$) for different termonomers. Dashed lines highlight peaks corresponding to hydrolysable ethoxy- (MENBS, DENBS, TENBS) or chlorosilane (DCNBS, TCNBS) vibrations (left) and characteristic siloxane vibrations (right). 65

Figure 62. Insets of the ATR FT-IR spectra of (A) DCNBS and DENBS termonomers. Diagnostic chloro- (DCNBS) and ethoxysilane (DENBS) vibrations are highlighted in green. Insets highlighting the siloxane vibration peaks in the ATR FT-IR spectra of (B) *branch*-poly(S-*r*-DENBS$_{30}$), (C) *branch*-poly(S-*r*-DCNBS$_{30}$), and (D) PDMS (10 cSt) as reference...............................66

Figure 63. (A) GPC traces and (B) ATR FT-IR spectra of *branch*-poly(S-*r*-MENBS$_x$) with *x* being 0, 10, 20, 30, and 50 wt%. 68

Figure 64. GPC traces of poly(S-*r*-Sty) and poly(S-*r*-DIB) prepared with 50 wt% of sulfur according to reported procedures. $M_N = 100$ g mol^{-1}, $M_W = 200$ g mol^{-1}. for poly(S-*r*-Sty) and $M_N = 100$ g mol^{-1}, $M_W = 200$ g mol^{-1} for poly(S-*r*-DIB). Sty is an abbreviation for styrene. DIB is an acronym for diisopropenylbenzene. 68

Figure 65. Schematic explanation of the model used to simulate the chain length distributions of *branch*-poly(S-*r*-MENBS$_x$) polymers. The steps are (1) random assembly of red and grey blocks into chains, (2) fusing chains containing at least one red block, (3) fusing of chains containing at least one unpaired block, (4) blending of chains to obtain a final distribution of chains. Percentages are relative to the total amount of chains after each respective step (1-4). 70

Figure 66. Simulated chain length distributions (DP$_n$) for different primary chain length distributions (grey) and for different ratios of red blocks. The primary distribution (grey) was approximated as a Poisson distribution with an expected value of (A) $\mu = 1$, (B) $\mu = 2$, (C) $\mu = 4$, and (D) $\mu = 8$.......................71

Figure 67. (A) GPC traces of *branch*-poly(S-*r*-NBS$_{20}$) with NBS being either MENBS, DENBS, DCNBS, TENBS, or TCNBS. (B) Comparison of M_W for different *branch*-poly(S-*r*-NBS$_x$). 73

Figure 68. GPC traces for three independently prepared samples of *branch*-poly(S-*r*-DENBS$_{20}$) to investigate the reproducibility of the obtained molar mass. $M_N = 1100 \pm 100$ g mol^{-1}, $M_W = 7600 \pm 700$ g mol^{-1}. 74

Figure 69. Insets of ATR FT-IR spectra (1500 – 500 cm^{-1}) of (A) *branch*-poly(S-*r*-DENBS$_x$), (B) *branch*-poly(S-*r*-DCNBS$_x$), (C) *branch*-poly(S-*r*-TENBS$_x$), and (D) *branch*-poly(S-*r*-TCNBS$_x$) for *x* being 10, 20, and 30 wt%. Green areas highlight D siloxane vibrations, blue areas highlight T siloxane vibrations...76

Figure 70. GPC traces of *branch*-poly(S$_x$-*r*-DENBS$_{20}$) with sulfur feed ratios of (A) 30 wt% ($M_N = 2400$ g mol^{-1}, $M_W = 6000$ g mol^{-1}, Đ = 2.5) and (B) 40 wt% ($M_N = 2700$ g mol^{-1}, $M_W = 13900$ g mol^{-1}, Đ = 5.2)...77

Figure 71. GPC traces of *branch*-poly(S_x-*r*-$DENBS_{20}$) with sulfur feed ratios of (A) 60 wt% (M_N = 700 g mol^{-1}, M_W = 5800 g mol^{-1}, Đ = 4.8) and (B) 70 wt% (M_N = 600 g mol^{-1}, M_W = 2900 g mol^{-1}, Đ = 4.8). 77

Figure 72. Molar mass M_N, M_W, and polydispersity Đ of *branch*-poly(S_x-*r*-$DENBS_{20}$) in dependence of the sulfur feed ratio for *x* being 30, 40, 50, 60, or 70 wt%. 78

Figure 73. (A) DSC thermograms of the first heat ramp of *branch*-poly(S-*r*-NBS_{20}) from 40 – 130°C and (B) pXRD patterns of *branch*-poly(S-*r*-NBS_{20}) from 2 – 90 ° (2θ) for NBS being MENBS, DENBS, DCNBS, TENBS, and TCNBS 79

Figure 74. (A) SEM image of the surface of *branch*-poly(S-*r*-NBS_x) powder. (B) EDX spectra of the background and the grain highlighted in the SEM image. Scalebar is 20 µm. 80

Figure 75. Reaction equation of the inverse vulcanization and partial polycondensation of poly(S-*r*-$MENBS_{100}$) to yield soluble *branch*-poly(S-*r*-$MENBS_{100}$). 80

Figure 76. Digital images of a *branch*-poly(S-*r*-$MENBS_{100}$) film prepared using (A) 0.10 eq., (B) 0.20 eq., and 3.00 eq. of HCl (pH 3) for the polycondensation of poly(S-*r*-$MENBS_{100}$). Both (A) and (B) became brittle after several weeks. 81

Figure 77. Reaction equation of the polycondensation of soluble *branch*-(S-*r*-$MENBS_{100}$) to form insoluble *net*-poly(S-*r*-$MENBS_{100}$). 81

Figure 78. (A) ^{13}C NMR spectra and (B) ^{29} Si NMR spectra of (i) MENBS, (ii) poly(S-*r*-$MENBS_{100}$), and (iii) *branch*-poly(S-*r*-$MENBS_{100}$) in $CDCl_3$. The soluble *branch*-poly(S-*r*-$MENBS_{100}$) was prepared by partial polycondensation of poly(S-*r*-$MENBS_{100}$) with 0.20 eq. of HCl solution (pH 3) relative to the number of ethoxy groups 82

Figure 79. ATR FT-IR spectra of *net*-poly(S-*r*-$MENBS_{100}$) and *branch*-poly(S-*r*-$MENBS_{100}$) prepared using 3.00 eq. and 0.20 eq. of HCl solution (pH 3), respectively. Poly(S-*r*-$MENBS_{100}$) served as a reference. Red areas highlight characteristic vibrations of ethoxy silanes and siloxanes. 83

Figure 80. Insets of DSC thermograms of *branch*-poly(S-*r*-$MENBS_x$) with *x* being 10, 20, 30, and 50 wt%. 84

Figure 81. Small amplitude oscillatory shear rheology measurements of the storage (G′) and loss (G′′) modulus of (A) *branch*-poly(S-*r*-$MENBS_{20}$), (B) *branch*-poly(S-*r*-$DCCBS_{20}$), and (C) *branch*-poly(S-*r*-$TENBS_{20}$) at different temperatures. (D) Comparison of G′ and G′′ *branch*-poly(S-*r*-NBS_{20}) at 60°C for NBS being MENBS, DCNBS, and TCNBS, respectively. In (C), vicinal data points including cross over points are marked red. 86

Figure 82. Small amplitude oscillatory shear rheology measurements of the complex viscosity of (A) *branch*-poly(S-*r*-NBS_{15}), *branch*-poly(S-*r*-NBS_{20}), and *branch*-poly(S-*r*-NBS_{25}) at 40 and 60°C (B) Comparison of the zero shear viscosity η_0 of *branch*-poly(S-*r*-NBS_{15}), *branch*-poly(S-*r*-NBS_{20}), and *branch*-poly(S-*r*-NBS_{25}) at 40 and 60°C. Complex viscosity of (C) *branch*-poly(S-*r*-$DCNBS_{20}$) at 40, 60, and 80°C, and (D) *branch*-poly(S-*r*-$TCNBS_{20}$) at 60, 80, 100, and 120°C....87

Figure 83. (A) Tensile strength measurements and (B) comparison of the toughness of *branch*-poly(S-*r*-$MENBS_{15}$), *branch*-poly(S-*r*-$MENBS_{20}$), and *branch*-poly(S-*r*-$MENBS_{25}$). Curves and bars are the average of three experiments and error bars are the standard error (N = 3)....88

Figure 84. Reaction equation of the inverse vulcanization of TVS-D_4 and sulfur to form poly(S_n-*r*-TVS-D_4). 91

Figure 85. ATR FT-IR spectra of (A) TVS-D_4, poly(S_{20}-*r*-TVS-D_4), and poly(S_{30}-*r*-TVS-D_4). Inset into (B) the C-H stretching region and (C) the Si-O-Si absorbance. The index x in S_x refers to the feed ratio of sulfur and not to the factual weight percentage of sulfur. 92

Figure 86. (A) GPC traces and (B) ATR FT-IR spectrum of poly(methylvinylsiloxane). Right: Inset (1300 – 800 cm^{-1}) highlighting the siloxane vibration of poly(methylvinylsiloxane). PDMS (10 cSt) and TVS-D_4 were used as references....93

Figure 87. Digital images of (A) a sheet and (B) stamped out specimens of poly(S_{30}-*r*-TVS-D_4). The dimensions of the sheet are 40 × 80 × 1 mm. 93

Figure 88. Small amplitude oscillatory shear rheology measurements of poly(S_{30}-*r*-TVS-D_4)....94

Figure 89. Digital image of a water droplet with a volume of 5 µL on the surface of poly(S_{30}-*r*-TVS-D_4). 94

Figure 90. GPC traces of (A) precipitated poly(S_{30}-*r*-TVS-D_n) for different reaction times and (B-D) GPC traces after the reaction steps (1) inverse vulcanization, (2) ROP, and (3) precipitation. 95

Figure 91. Reaction equation of the inverse vulcanization of poly(S_{30}-*r*-DVS-MM), poly(S_{30}-*r*-TVS-D_3), and poly(S_{30}-*r*-PVS-D_5). 97

Figure 92. ATR FT-IR spectra of (A) DVS-MM and poly(S_{30}-*r*-DVS-MM),(B) TVS-D_3 and poly(S_{30}-*r*-TVS-D_3), and (C) PVS-D_5 and poly(S_{30}-*r*-PVS-D_5)....98

Figure 93. DSC thermograms of poly(S_{30}-*r*-DVS-MM), poly(S_{30}-*r*-TVS-D_3), poly(S_{30}-*r*-TVS-D_4) and poly(S_{30}-*r*-PVS-D_5) from -40 – 160°C with 10 K s^{-1}....99

Figure 94. Stress-strain diagrams for poly(S_{30}-*r*-TVS-D_4) and poly(S_{30}-*r*-PVS-D_5). Three specimens were measured for each polymer....100

Figure 95. Stress-strain diagrams of compression tests for (A) poly(S_{30}-*r*-TVS-D_3), (B) poly(S_{30}-*r*-TVS-D_4), (C) poly(S_{30}-*r*-PVS-D_5), and (D) poly(S_{30}-*r*-DVS-MM). Three specimens were measured for each polymer. 101

Appendix 1. Raman spectra of powdered *net*-poly(S_{35}-*r*-StyTMS). No peaks could be identified due to fluorescence or black body irradiation. A reduction of the laser intensity from 4 to 1 mW decreased the background noise, however, no spectrum could be obtained. A further reduction of the laser intensity by moving the sample out of the focus of the laser failed to improve the spectrums quality 133

Appendix 2. Color-coded ion count obtained from ToF-SIMS examination of (A) *net*-poly(S-*r*-StyTMS) and (B) elemental sulfur. Unlike *net*-poly(S-*r*-StyTMS), elemental sulfur was not distributed homogeneously on the surface. The examined surface area was 500 × 500 µm (0.025 mm²). 134

Appendix 3. (A) ^{1}H NMR and (B) ^{13}C spectra of TMNBS in $CDCl_3$ referenced to the solvent peak at 7.26 and 77.0 ppm, respectively. 135

Appendix 4. GPC traces of PDMS with a viscosity of 100 cSt. Aliphatic poly(siloxane)s do not absorb UV light rendering the polymer invisible for the UV detector. 135

Appendix 5. GPC traces of (A) *branch*-poly(S-*r*-$DENBS_x$), (B) *branch*-poly(S-*r*-$DCNBS_x$), (C) *branch*-poly(S-*r*-$TENBS_x$), and (D) *branch*-poly(S-*r*-$TCNBS_x$). 136

Appendix 6. ATR FTIR spectra of (A) TMNBS and (B) poly(S-*r*-TMNBS). 137

Appendix 7. ATR FTIR spectra of (A) MENBS and (B) *branch*-poly(S-*r*-$MENBS_x$). 137

Appendix 8. ATR FTIR spectra of (A) DENBS and (B) *branch*-poly(S-*r*-$DENBS_x$). 138

Appendix 9. ATR FTIR spectra of (A) DCNBS and (B) *branch*-poly(S-*r*-$DCNBS_x$). 138

Appendix 10. ATR FTIR spectra of (A) TENBS and (B) *branch*-poly(S-*r*-$TENBS_x$). 139

Appendix 11. ATR FTIR spectra of (A) TCNBS and (B) *branch*-poly(S-*r*-$TCNBS_x$). 139

Appendix 12. DSC thermograms showing the first heat ramp from 85 – 130°C of (A) poly(S-*r*-TMNBS), (B) *branch*-poly(S-*r*-$MENBS_x$), (C) *branch*-poly(S-*r*-$DENBS_x$), (D) *branch*-poly(S-*r*-$DCNBS_x$), (E) *branch*-poly(S-*r*-$TENBS_x$), and (F) *branch*-poly(S-*r*-$TCNBS_x$). 140

Appendix 13. (A) SEM images and (B) EDX spectra of granulated (i) poly(S-*r*-$MENBS_{20}$), (ii) *branch*-poly(S-*r*-$DCNBS_{20}$), (iii) *branch*-poly(S-*r*-$TENBS_{20}$), and (iv) *branch*-poly(S-*r*-$TCNBS_{20}$). 141

Appendix 14. DSC thermograms showing the second heat ramp from -40 – 130°C of (A) poly(S-*r*-TMNBS), (B) *branch*-poly(S-*r*-$DENBS_x$), (C) *branch*-poly(S-*r*-$DCNBS_x$), (D) *branch*-poly(S-*r*-$TENBS_x$), and (E) *branch*-poly(S-*r*-$TCNBS_x$). 142

List of Tables

Table 1. Comparison of the properties of the chalcogenides.[4] 4

Table 2. Oxidation states of sulfur.[4] 4

Table 3. Industrial chemicals produced from elemental sulfur and their applications. 6

Table 4. Nomenclature of ethoxy- and chlorosilanes used in this thesis.....................................49

Table 5. Nomenclature and composition of *branch*-poly(S_y-*r*-NBS_x) polymers discussed in this chapter...50

Table 6. Elemental analysis of poly(S-*r*-TMNBS) and *branch*-poly(S-*r*-NBS_x) with varying contents of M, D, and T building blocks..67

Table 7. Molar masses (M_N, M_W) and dispersity (Đ) of *branch*-poly(S-*r*-NBS_x) with varying contents of M, D, and T siloxane bonds...74

Table 8. Glass transition temperatures (T_G) of *branch*-poly(S-*r*-NBS_x) with varying contents of M, D, and T siloxane bonds...84

Table 9. Nomenclature of vinyl(cyclo)siloxanes used in this thesis. 90

Table 10. Molar masses (M_N, M_W) and dispersity (Đ) of poly(S_{30}-*r*-TVS-D_4) and poly(S_{30}-*r*-TVS-D_n) 96

Table 11. Elemental composition of poly(S-*r*-XVS-XX). 97

List of Abbreviations

Methods

AAS	atom absorption spectroscopy
AFM	atomic force microscopy
ATR FT-IR	attenuated total reflexion Fourier transform infrared spectroscopy
DLS	dynamic light scattering
DSC	differential scanning calorimetry
EDX	electron dispersive x-ray spectroscopy
GPC	gel permeation chromatography
NMR	nuclear magnetic resonance
PXRD	powder x-ray diffractometry
SEM	secondary electron microscopy
TGA	thermogravimetric analysis
ToF SIMS	time-of-flight secondary ion mass spectrometry
UV-vis	ultra-violet-visible
XPS	x-ray photoelectron spectroscopy
WCA	water contact angle goniometer

Monomers

StyTMS	styrylethyltrimethoxysilane
EPTMS	ethylphenethyltrimethoxysilane
TMNBS	trimethylnorbornenylsilane
MENBS	monoethoxynorbornenylsilane
DENBS	diethoxynorbornenylsilane
TENBS	triethoxynorbornenylsilane
DCNBS	dichloronorbornenylsilane
TCNBS	trichloronorbornenylsilane
DVS-MM	divinylsiloxane
TVS-D$_3$	trivinylcyclotrisiloxane
TVS-D$_4$	tetravinylcyclotetrasiloxane
PVS-D$_5$	pentavinylcyclopentasiloxane

Greek symbols

δ	chemical shift
η_0	zero shear viscosity
θ	angle of incidence
λ	wavelength
μ	expected value

Solvents

1-BuOH	1-butanol
DCM	dichloromethane
DET	diethyl ether
EtOH	ethanol
MeOH	methanol
THF	tetrahydrofuran

Time, length, mass, and volume

h	hour
min	minute
s	second
m	meter
cm	centimeter
mm	millimeter
µm	micrometer
nm	nanometer
kg	kilogram
g	gram
mg	milligram
L	litre
mL	millilitre
µL	microlitre

Amounts

eq.	equivalents
mol	mole, 6.022×10^{23}
ppm	parts per million
ppmw	parts per million by weight
vol%	volume percent
wt%	weight percent

Optics and spectroscopy

n	refractive index
k	extinction coefficient
(k)eV	(kilo) electron volt

Polymers

Đ	dispersity
DP_n	degree of polymerization
M_N	number average molar mass
M_W	weight average molar mass

Temperature

T	temperature
°C	degree Celsius
K	Kelvin

Mechanics

cSt	centistokes
G'	storage modulus
G''	loss modulus
N	Newton
Pas	Pascal second
W	Watt

Acknowledgements

Supervision

Prof. Pavel A. Levkin is thanked for the supervision. The mentoring and trust in my abilities was invaluable for my personal development and shaped my research activities.

Prof. Patrick Theato is thanked for the supervision and for granting me the scientific freedom necessary to pursue innovative and creative ideas.

Prof. Christof Wöll is thanked for the supervision in my thesis advisory committee (TAC).

Dr. Hedda Schlegel-Starmann is thanked for her helpfulness and critical evaluation of my yearly reports as my DBU supervisor.

Prof. Dr. Tom Hasell is thanked for welcoming me in his group at the University of Liverpool.

Funding bodies

The Deutsche Bundesstiftung Umwelt (DBU) is thanked for awarding me with a stipend. The financial independence, support, events, and feedback greatly improved my PhD experience. The BioInterfaces International Graduate School (BIF IGS) is thanked for providing a platform for interdisciplinary collaboration and exchange and for awarding me with a Conference Grant. The Karlsruhe House of Young Scientists (KHYS) is thanked for awarding me the “Networking Grant” and the “Research Travel Grant”.

Collaborators

Prof. Wilhelm is thanked for his help with rheometry investigations. Prof. Matysik is thanked for his help with NMR investigations. Dr. Michael Hirtz is thanked for his help with AFM. Chatrawee Direksilp is thanked for her help with XPS. Maxi Hoffmann is thanked for her help with rheometry. Yunji Nie is thanked for his help with NMR. Patricia Falkenstein is thanked for her help with ss NMR measurements. Stefan Heissler is thanked for his help with vibrational spectroscopy. Valentin Scheiger is thanked for his help with model calculations. Marc Rutschmann is thanked for his help with powder XRD. Dr. Alexander Welle is thanked for his help with ToF-SIMS. Dr. Meike König is thanked for her help with ellipsometry. Nicole Klaasen is thanked for her help with elemental analysis. Birgit Huber is thanked for her help with GPC, DSC, and NMR. Laura Scheiger is thanked for her help with the revision of this thesis. Fabian Scheiger is thanked for the legal advice for my students and colleagues. Linus Edelkott is thanked for his contribution.

Students and Trainees

Maria Kuzina, Klara Urbschat, Alexander Grimm, Tobias Sengpiel, and James Vincent are thanked for their ambitious and motivated contributions.

Miscellaneous

Emanuel Haberstumpf is thanked for the excellent accounting of my DBU fund.

Thanks to the wonderful people and friends in the Levkin group and the Theato group.

Preface

This thesis is based on the results gathered during my doctoral studies in the groups of Prof. Dr. Patrick Theato and Prof. Dr. Pavel A. Levkin and was conducted between August 2018 and December 2021 at the Institute of Technical Chemistry and Polymer Chemistry (ITCP) as well as the Institute of Biological and Chemical Systems – Functional Material Interfaces (IBCS-FMS). The contributions of collaborators are specified at the beginning of each chapter.

The last three years were scientifically fruitful and thus rewarding on a personal level. Much of the achievements can be boiled down to a few guidelines, which I gladly share with prospective doctoral candidates.

Invest 30 min to read “Writing a Paper” from George Whitesides.[1] Despite what the title suggests, the most important message is to internalize the methodology of drafting and using outlines. Moreover, it elaborates on the simple truth that no research project is ever truly finished, which implies to start writing outlines and drafts for articles early in a project to be able to close them out in a timely manner. During a PhD, problems (mostly labelled as challenges) will arise. For the communication with supervisors, it is mandatory to bring your own thoughts and solutions into the discussions and to voice your opinion confidently. There is no need to be afraid of challenging the opinions of superiors: After a research goal has been achieved, no tear is shed about whether the path deviated from anyone’s original plan. In the beginning of a PhD, the aims and interests of a doctoral student are congruent to those of their supervisors. Towards the end of a PhD there is an inherent divergence, since a doctoral journey must come to an end, whereas a research project can always move on. Thus, the first half of a PhD is the time to say yes too often. I found myself in many situations facing challenges for the first time, such as writing a review, a book chapter, or starting yet another side project. These are great opportunities to broaden your horizon and to become aware of your strengths at the price of occasional work overloads. The second half of a PhD is the time to decline some ideas and proposals if they are not leading directly to the goal of obtaining a PhD or another major benefit. I encourage doctoral researchers to engage into collaborations and to supervise students for their projects. Collaborations are a great way of getting to know interesting methods and exciting techniques beyond your core expertise. Supervision forces doctoral students to plan in advance but allows sharing the workload. The motivation and workforce of a student should be acknowledged by enabling them to learn as many things as possible during the supervision, which is rewarding for all parties involved. Overall, the doctoral studies are a great time to develop as a person. This does not happen intrinsically though, but rather requires the efforts of being proactive, ambitious, creative, and at times, demanding.

I wish all doctoral students the best for their endeavors.

Karlsruhe, November 2021

Johannes M. Scheiger

1 Introduction

1.1 The element sulfur

1.1.1 Abundance, production, and general reactivity

Sulfur is the chemical element with the ordinal number 16. It has four stable isotopes (^{32}S, ^{33}S, ^{34}S, and ^{36}S) with a terrestrial abundance of ~ 95, ~ 0.77, ~ 4.2, and ~ 0.017 %, respectively.[2,3] The molecular weight of sulfur is 32.065 g mol^{-1} according to the National Institute of Standards and Technology (NIST) database. In the periodic table sulfur is located in between oxygen and selenium in the chalcogenide main group. The abundance of sulfur in Earth's crust is 0.07 wt%. It is found in elemental form and as minerals such as sulfides (e.g., FeS_2, PbS, ZnS, HgS, or Cu_2S) and sulfates ($CaSO_4 \cdot n\,H_2O$, $BaSO_4$). Sulfur is essential for life and thus an important element in fertilizers.[4] In the human body sulfur is mainly present in amino acids such as cysteine, methionine, homocysteine, and taurine, amongst which only the first two are protein forming amino acids. As such, they play a vital role for the structure of proteins.[5] Chefs frequently encounter sulfur in their kitchens, as many flavor enhancing ingredients in *Allium sativum* L. (garlic) and *Allium cepa* L. (onion) are based on sulfur chemistry.[6] In the solar system, large amounts of sulfur are found on Jupiter's moon Io whose yellow, orange, and red color is attributed to different sulfur species (**Figure 1**). Spectroscopical measurements obtained by Voyager 1 detected emissions of SO_2 from Io's atmosphere.[7]

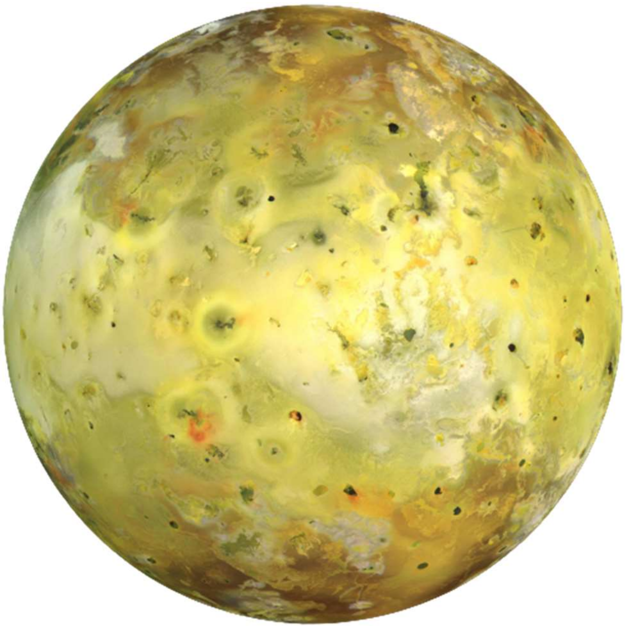

Figure 1. True color image of Jupiter's moon Io taken from the spacecraft Galileo of the National Aeronautics and Space Administration (NASA) on the 3rd of July in 1999. Image from NASA (public image database).

The chemical reactivity of sulfur is closer to that of selenium and tellurium than to the reactivity of oxygen. This is due to the similar covalence radii and electronegativity of sulfur, selenium, and tellurium (**Table 1**).

Table 1. Comparison of the properties of the chalcogenides.[4]

Element symbol	O	S	Se	Te
Covalence radius	66	105	120	138
χ (Allred-Rochow)	3.5	2.4	2.5	2.0
Valence electron configuration	$2s^2p^2p^1p^1$	$3s^2p^2p^1p^1$	$4s^2p^2p^1p^1$	$5s^2p^2p^1p^1$

From the electron configuration of sulfur $3s^2p^2p^1p^1$ it is apparent that an oxidation state of -II or a charge of -2 are required to obtain the noble gas configuration of argon $3s^2p^2p^2p^2$. This is the case in the molecule H_2S or the salt Li_2S. However, sulfur can adopt each of the nine possible oxidation states from -II to +VI. For substituents with low steric demand, the coordination number of sulfur can be up to six as found for the gas SF_6 (**Table 2**).[4]

Table 2. Oxidation states of sulfur.[4]

Oxidation state	-II	-I	0	I	II	III	IV	V	VI
Molecule	H_2S	H_2S_2	S_8	S_2Cl_2	CS_2	$[S_2O_4]^{2-}$	SO_2	S_2F_{10}	SO_3
Coordination number	2	2	2	2	1	3	2	6	3

Elemental sulfur can be mined from underground deposits using the FRASCH process, in which overheated water at high pressures is used to melt sulfur from the surrounding sand, which is then transported to the surface using pressurized air. However, most of the annual sulfur production does not stem from underground deposits of elemental sulfur. Instead, most sulfur is produced from H_2S, which is a component of natural gas and a product of the hydrodesulfurization (HDS) process of natural oil. In the HDS process, sulfur containing organic molecules are converted into H_2S using H_2 and a Mo-Ni or Mo-Co catalyst at a temperature of 300 – 400 °C and a pressure of 2 – 6 MPa. Isolated H_2S is then oxidized to elemental sulfur using a modified CLAUS process, in which S and H_2O form through a comproportionation of H_2S and SO_2 (**Figure 2**). The SO_2 is generated by oxidation of H_2S at 950 – 1200 °C in an oxygen enriched atmosphere to H_2O and SO_2.[4]

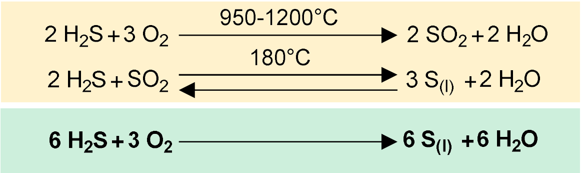

$$2\,H_2S + 3\,O_2 \xrightarrow{950\text{-}1200°C} 2\,SO_2 + 2\,H_2O$$

$$2\,H_2S + SO_2 \xrightleftharpoons{180°C} 3\,S_{(l)} + 2\,H_2O$$

$$\mathbf{6\,H_2S + 3\,O_2 \longrightarrow 6\,S_{(l)} + 6\,H_2O}$$

Figure 2. Reaction equations of the part reactions (yellow) and the overall reaction equation (green) of the CLAUS process.

Since the standard enthalpy of the oxidation is strongly negative ($\Delta H = -660$ kJ mol^{-1}), the comproportionation step is successively conducted at temperatures down to 180 °C to shift the equilibrium towards the formation of sulfur.[4]

1.1.2 Allotropes

The most stable allotrope of sulfur at 25 °C and 0.1 MPa is *cyclo*-octasulfur (S_8). At room temperature the crown-shaped S_8 crystalizes in an orthorhombic ($a \neq b \neq c$, $\alpha = \beta = \gamma = 90°$) crystal structure containing 16 S atoms in its elemental cell (α-S_8). Above 96 °C, α-S_8 is converted to β-S_8, which crystalizes in a monoclinic ($a \neq b \neq c$, $\alpha = \beta = 90° \neq \gamma$) crystal structure which melts at 120 °C. However, if a melt of β-S_8 is kept at 120 °C for ca. 12 h, the melting point reduces to 115 °C. This is due to the formation of a small fraction (5.5 %) of S_n molecules with ring sizes larger or smaller than S_8. The molten fraction of S_8 was traditionally termed λ-sulfur and the non-S_8 fractions were termed π-sulfur (rings) and μ-sulfur (polymeric sulfur). Since polymeric sulfur is insoluble in CS_2, it can be obtained as residue after rapid cooling of a sulfur melt followed by washing with CS_2. When the temperature of a sulfur melt is increased, the viscosity increases due to the formation of more and longer polymer chains. After 159 °C the viscosity of the melt increases by several orders of magnitude reaching a maximum viscosity at 187 °C. However, the concentration of polymeric sulfur increases further from ca. 3.0 wt% at 159 °C to 28 wt% at 200 °C, and to 34.2 wt% at 220 °C. Other sources cite the maximum viscosity of sulfur melts to be at 248 °C.[8] The composition of the gas phase above 445 °C is a pressure and temperature dependent distribution containing S_8 – S_2 molecules. S_2 dominates already slightly above 700 °C, whereas sulfur atoms (S_1) only dominate above 2500 °C at very low pressures of 10^{-6} kPa (**Figure 3**).[4]

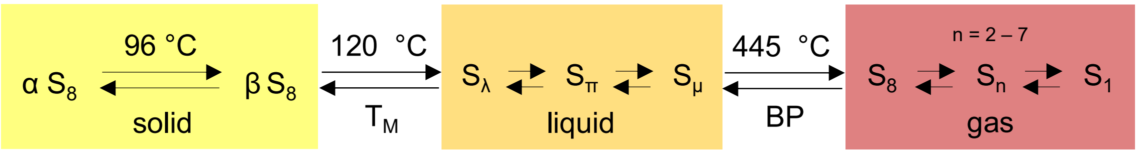

Figure 3. Thermal transitions of sulfur allotropes in the solid, liquid, and gas state.

Besides enantiotropic allotropes such as α-S_8 and β-S_8, some monotropic allotropes can be synthesized in a targeted way using a pentasulfido titanocene complex [Cp_2TiS_5] as a S_5-ligand transfer agent (**Figure 4**). A variety of rings, namely S_{10}, S_{15}, and S_{20} can be synthesized using the reaction of [Cp_2TiS_5] with SO_2Cl_2, whereas the rings S_6, S_7, and S_9, S_{11}, S_{12}, and S_{13} can be synthesized via reaction of [Cp_2TiS_5] with S_nCl_2. Some other sulfur rings were isolated from cooled sulfur melts, too, and thus cannot be considered monotropic allotropes.[9]

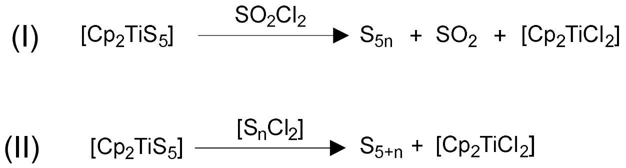

$$\text{(I)}\quad [Cp_2TiS_5] \xrightarrow{SO_2Cl_2} S_{5n} + SO_2 + [Cp_2TiCl_2]$$

$$\text{(II)}\quad [Cp_2TiS_5] \xrightarrow{[S_nCl_2]} S_{5+n} + [Cp_2TiCl_2]$$

Figure 4. Reaction equation for (I) the synthesis of S_{5n} (n = 1, 2, or 3) from $[Cp_2TiS_5]$ and SO_2Cl_2, and (II) the synthesis of S_{5+n} (n =1, 2, 4, 6, 7, and 8) from $[Cp_2TiS_5]$ and S_nCl_2.

Since there are various high-pressure allotropes of sulfur, the phase diagram of sulfur is still a subject of debate.[10]

1.1.3 Applications

In 2020, 78 million tons of sulfur had been produced according to the US Geological Survey (USGS) of which roughly 90 % were converted into sulfuric acid via the contact process.[4,11] Sulfuric acid serves as a strong acid in industrial processes for example in the production of phosphoric acid from phosphate minerals, which is used to synthesize phosphate fertilizers. Other applications of sulfur are the vulcanization of rubbers, and the production of chemicals such as sulfur halogenides (e.g., S_2Cl_2), phosphor sulfides (e.g., P_4S_{10}), or carbon disulfide (CS_2) (**Table 3**).[8,12,13] The sulfur chlorides and phosphor sulfides are used as sulfur donors for various organic compounds, whereas the main application of CS_2 is the solubilization of cellulose containing wood pulp in the production of cellophane. The hydroxy groups in cellulose react with CS_2 under basic conditions to dithiocarbonates (xanthates), to form a viscous solution. The solution is extruded into sulfuric acid, where the dithiocarbonates are converted back into hydroxy groups and CS_2 and pure cellulose is obtained, which is processed into fibers. Recent research in the field of green chemistry aims to enhance the scope of organic reactions in which sulfur can be used directly.[14]

Table 3. Industrial chemicals produced from elemental sulfur and their applications.

Sum formula	Structure	Application	Ref.
S_2Cl_2	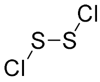	Synthesis of SCl_2, $SOCl_2$, SF_4, lubricating oils, cutting oils, thioindigo dyes, vulcanization of rubbers, catalyst in the chlorination of acetic acid	[3,7,8]
P_4S_{10}	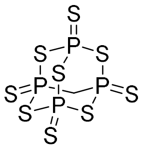	Synthesis of insecticides, zinc dialkyldithiophosphates, thiophenes, and thioamides.	[3,6]
CS_2	S=C=S	Synthesis of CCl_4, cellulose fibers (cellophane), dithiocarbamates, and fungicides, vulcanization of rubbers, solvent for phosphorus, sulfur, selenium, and waxes.	[3,6]

However, the annual need for elemental sulfur is surpassed by the annual production of sulfur, which is why excess amounts of around 5 – 10 Mt of sulfur are annually deposited in large landfilling sites. The deviation in the demand for phosphate fertilizers is the most influential factor on the price of sulfur, which dropped from around 140 \$ t^{-1} in January 2019 to about 46 \$ t^{-1} in October 2020.[11]

1.2 The sulfur-sulfur bond

To understand the chemical behavior of sulfur it is essential to understand the unique properties of sulfur-sulfur (S-S) bond. The S-S bonds show a high flexibility, with bond lengths between 1.8 – 3.0 Å, bond angles between 90 – 180° and dihedral angles between 0 – 180°. The force constant of the S-S bond can vary from 140 – 630 N m^{-1} as found from S-S stretching vibrations from 177 – 820 cm^{-1}. With a bond energy of 265 kJ mol^{-1}, the S-S bond ranks the third highest amongst homonuclear single bonds and is only exceeded by H-H bonds (435 kJ mol^{-1}) and C-C bonds (330 kJ mol^{-1}).[15] However, the chemistry of elemental sulfur is known for S-S bond dissociation into thiyl radicals and a dynamic change between various different ring sizes. To resolve this seeming contradiction, a deeper look into the nature of the S-S bond is necessary.

1.2.1 S-S in disulfides

The disulfide bond in H_2S_2 can serve as a reference bond because of the low steric and electronic influence of the two hydrogen atoms. H_2S_2 possesses the same geometry as its oxygen analogue H_2O_2. The S-S bond length in H_2S_2 is 2.055 Å, the S-S-H bond angle α is 91.3° and the dihedral angle φ is 90.6°. H_2S_2 molecules adopt a *gauche* conformation, since only for dihedral angles of 90° and 270° the non-binding p-electrons pairs are perpendicular to each other (**Figure 5**). The *cis* conformation is highest in energy due to the additional repulsion of the H atoms compared to the *trans* conformation.

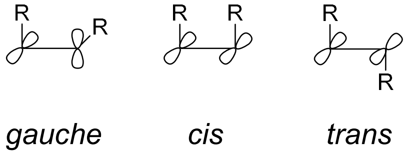

Figure 5. Structure of the *gauche*, *cis*, and *trans*-conformation for R_2S_2.

If the hydrogen atom is replaced with a methyl group (Me), the bond length decreases slightly to 2.03 Å, the S-S-H bond angle α increases to 103°, and the dihedral angle φ decreases to is 84° mainly because of the larger steric hindrance of the methyl group. For the bulky *tert*-butyl groups ($t\mathrm{Bu}_2S_2$) the dihedral angle increases to 97° (**Figure 6**). As the opposite extreme, if the dihedral angle is greatly decreased by incorporation of the disulfide group into a cyclic compound, the unfavorable interaction of the non-binding electron pairs results in an increase of the S-S bond length, which is why a typical value for the S-S bond length in four or five membered rings is around 2.10 Å. For example, φ is 27° and d is 2.097 Å for 1,2-dithiolane-4-carboxylic acid.[15]

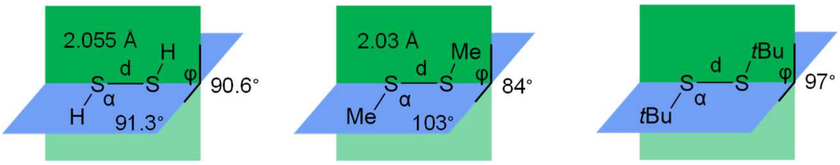

Figure 6. Structure of H_2S_2, Me_2S_2, and t-Bu_2S_2 with a S-S bond length d, a H-S-S bond angle α and a dihedral angle φ.

In a series of S_2X_2 with X being Br, Cl, and F, the S-S bond lengths found were 1.98, 1.931, and 1.888 Å, the S-S-X bond angles α were 105, 108.2, and 108.3°, and the dihedral angles φ were 83.5, 84.8, and 87.9°, respectively (**Figure 7**).[16-18] The electronegative substituents are believed to strengthen the S-S bond by withdrawing electrons from the two antibonding highest occupied molecular orbitals.[15] Theoretical calculations of sulfur halogenides confirm this hypothesis.[19]

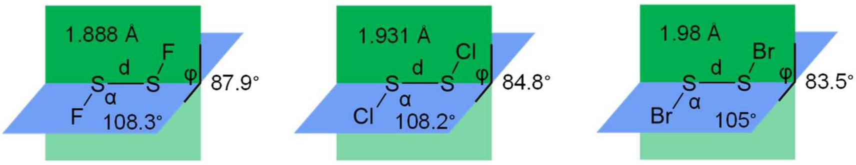

Figure 7. Structure of S_2F_2, S_2Cl_2, and S_2Br_2 with a S-S bond length d, a X-S-S bond angle α and a dihedral angle φ.

1.2.2 S-S in polysulfides

The S-S bond dissociation energies (BDE) of disulfides are higher than those of polysulfides. For example, the BDE of Me_2S_2 is around 281 kJ mol^{-1}, it is only 151 kJ mol^{-1} for the central S-S bond in the tetrasulfide Me_2S_4. In S_8 the BDE is even lower at 138 kJ mol^{-1}. This can be explained with the participation of thiyl radicals in π-bonds with neighboring S atoms. Consequently, the presence of sulfur radicals in liquid sulfur at 172 °C can be proven by electron spin resonance spectroscopy.[15,20]

Determination of Urey-Bredley force constants (k_r, k_{rr}) for S-S bond revealed that sulfur bonds in S_8 ($k_r = 237$ N m^{-1}) require significantly less energy to stretch than C-C bond ($k_r \approx 440$ N m^{-1}). However, the force constant k_{rr}, which describes the behavior of S-S bonds vicinal to the bond stretched is much larger for S_8 ($k_{rr} = 61$ N m^{-1}) than for vicinal C-C bonds in cyclohexane ($k_{rr} =$ 10 N m^{-1}). This means that a stretch of a S-S bond causes a contraction of the vicinal S-S bonds, which results in an even lower effective force constant ($k_{eff} \approx k_r - k_{rr}$), i.e., less energy is required to elongate or compress the S-S bond. This phenomenon can be understood by imagining that the border case of bond vibrations is bond dissociation, in which the thiyl radicals are stabilized by participation in π-bonds of vicinal sulfur atoms. Thus, it appears likely that this favorable interaction already takes place during the bond vibration (**Figure 8**).

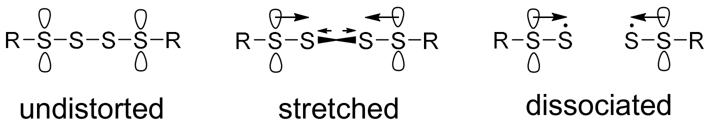
undistorted
stretched
dissociated

Figure 8. Schematic visualization of a vicinal π-electron interaction stabilizing the S-S bonds next to a stretched or homolytically dissociated S-S bond, i.e., thiyl radicals.

The high value of k_{rr} is a characteristic feature of cumulated S-S bonds and can explain why the BDE of sulfur chains is far lower than their bond energy, which is the arithmetic mean of all BDEs. The energy required to break a single S-S bond in a sulfur chain is compensated by a decrease in energy, i.e., a strengthening of vicinal S-S bonds. To further support this theory, investigation of the radical anion $S_3^{\bullet -}$ with Raman spectroscopy found a short S-S bond length of 1.95 Å, revealing the presence of π-bonds.[15,21]

1.3 Sulfur containing polymers

The polymer chemistry of sulfur can be subdivided into polymers containing sulfur in a side chain and polymers containing sulfur in their backbone. This chapter only deals with polymer containing sulfur in their backbone (**Figure 9**). Several functional groups containing sulfur can be incorporated into polymers. Amongst those, the most relevant functional groups can be grouped as polysulfides, thiocarbonyls, thioethers and their oxidized analogues sulfoxides and sulfones, as well as thiophenes.[22]

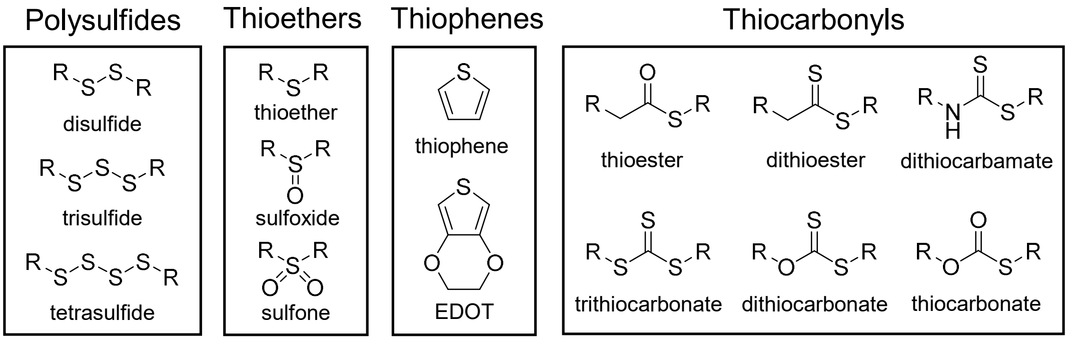
Polysulfides
Thioethers
Thiophenes
Thiocarbonyls
disulfide
trisulfide
tetrasulfide
thioether
sulfoxide
sulfone
thiophene
EDOT
thioester
dithioester
dithiocarbamate
trithiocarbonate
dithiocarbonate
thiocarbonate

Figure 9. Sulfur containing functional groups with relevance for sulfur containing polymers. EDOT = 3,4-ethylenedioxythiophene. R is an organic rest.

1.3.1 Polysulfides

The chemistry of “organic polysulfanes” of the general formula R-S_n-R (R = alkyl and aryl, $n \geq 2$) was comprehensively reviewed by STEUDEL.[23] Today, the use of the name polysulfanes is not encouraged since the suffix “-ane” is reserved for element-hydrogen compounds, such as alkanes or silanes. Instead, the preferrable IUPAC name for R-S_n-R (R = alkyl and aryl, $n \geq 2$) is polysulfides.[24]

Polysulfides are either chain- or ring-like molecules, with the length n of the sulfur chain R-S_n-R being 1 – 35. However, only R-S_n-R with 1 – 11 have been isolated in pure form.[23] They can be synthesized using different approaches: (i) the reaction of thiols (R-SH) with sulfur chlorides (SCl_2, S_2Cl_2), (ii) the reaction of a metal sulfide (MS_n) with a sulfur chloride (SCl_2, S_2Cl_2), (iii), the oxidation of thiols (R-SH) or (iv) the insertion of S_8 into disulfides (R-S_2-R) (**Figure 10**).[4] Disulfides play the largest role amongst polysulfides, due to their superior chemical and thermal stability.[25-27]

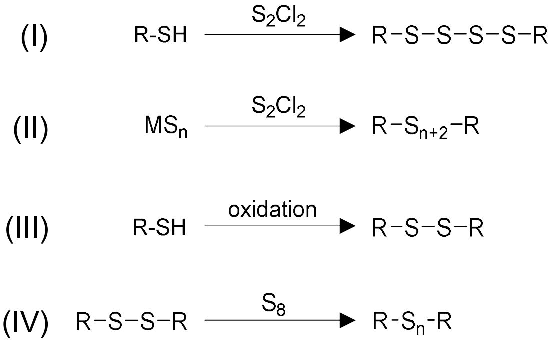
(I) R-SH $\xrightarrow{S_2Cl_2}$ R–S–S–S–S–R
(II) MS_n $\xrightarrow{S_2Cl_2}$ R–S_{n+2}–R
(III) R-SH $\xrightarrow{\text{oxidation}}$ R–S–S–R
(IV) R–S–S–R $\xrightarrow{S_8}$ R-S_n-R

Figure 10. Reaction equations for the formation of polysulfides R-S_n-R (R = alkyl and aryl, $n \geq 2$).

Industrially, mixtures of aliphatic chloroalkanes, e.g., bis(2-chloroethoxy)methane and 1,2-dichloroethane, are reacted with an aqueous solution of sodium polysulfide to form poly(disulfide)s. Historically, only 1,2-dichloroethane was reacted with sodium disulfide, but the resulting polymer had a bad smell. This problem was overcome by copolymerization with bis(2-chloroethoxy)methane.[28] A reduction of sulfide bonds to thiols is used to controllably shorten the chain lengths, whereas the use of a trifunctional chloroalkane, i.e., 1,2,3-trichloropropane, can be used to generate branches into the linear polymers. The terminal sulfide groups can later be oxidized back to disulfides to cure the liquid polymers into an elastomer (**Figure 11**). Due to their outstanding solvent resistance, they are used as sealants for airplane fuel tanks.[23] Their main use, however, remains the vulcanization of rubbers.[8]

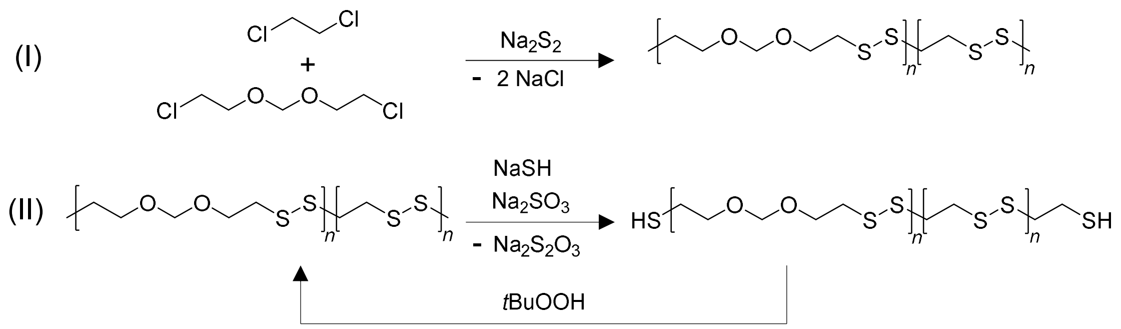
(I)
Cl
Cl
+
Cl
O
O
Cl
Na_2S_2
- 2 NaCl
O
O
S
S
n
S
S
n
(II)
NaSH
Na_2SO_3
- $Na_2S_2O_3$
HS
SH
tBuOOH

Figure 11. Reaction equation for (I) the formation of Thiokol type copolymers and (II) their selective reduction and oxidation.

1.3.2 Poly(thioether)s, poly(sulfoxide)s, and poly(sulfone)s

There are various established methods to synthesize poly(thioether)s such as the ring opening polymerization of ethylene sulfide, the thiol-ene or thiol-yne polyaddition of dithiols with dialkenes or alkynes, respectively, and the polycondensation of dithiols with dibromoalkanes (**Figure 12**).[29-31] The addition of S-H bonds onto C=C double bonds can occur as a radical addition or as a thiol-Michael addition. Both additions typically proceed as anti-Markovnikov addition.[32,33] More recent approaches showed the use of COS or the degradation of poly(monothiocarbonates) to synthesize poly(thioether)s.[34,35] Ultrafast polymerization times of one minute can be achieved by reacting electron deficient alkynes with 1,6-hexanedithiol and 1,5,7-triazabicyclo[4.4.0]dec-5-ene (TBD) as base catalyst at room temperature.[31,36] The thiol-ene reaction offers the possibility to synthesize fluorinated poly(thioether)s under mild conditions.[37] Poly(thioether)s possess a higher heat stability than poly(disulfides) while maintaining a high resistance to organic solvents. A proposed application for poly(thioethers) is thus as sealant for aeronautics.[38] A related class of polymers are poly(thioether ketone)s, which are the thio-analogues of the industrially relevant poly(ether ketone)s. They can be synthesized in a similar fashion as poly(thioether)s through the polycondensation of aromatic dihaloketons with aromatic dithiols.[39-41] Since their sulfur content is quite low, they are not discussed further.

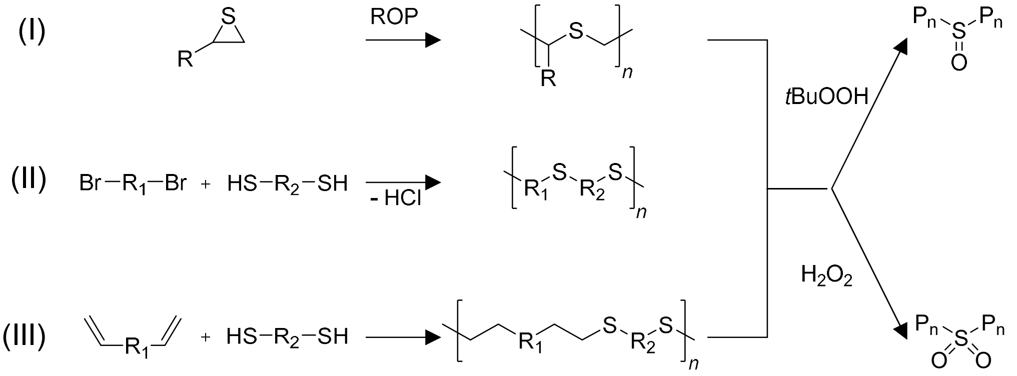

Figure 12. Reaction equation for the synthesis of poly(thioether)s via (I) ring opening polymerization (ROP) of ethylene sulfide derivatives, (II) polycondensation of alkylbromides, and (III) thiol-ene polyaddition. Selective oxidation yields the respective poly(sulfoxide)s or poly(sulfon)s.

Poly(sulfoxide)s and poly(sulfone)s can be obtained by selective oxidation of poly(thioether)s.[42-44] The poor solubility of poly(thioether)s typically requires a heterogeneous oxidation reaction making use of hydrogen peroxide (H_2O_2) or organic peroxides such as *tert*-butylhydroperoxide (*t*BuOOH). Upon oxidation of the poly(thioether), the polymer increasing solubility causes it to dissolve in the reaction solvent, which enables a high conversion.[43] The general term poly(sulfone)s is often used as synonym for poly(aryl ether sulfone)s, since these are the only poly(sulfone)s used commercially. They combine a high oxidative, hydrolytic, and thermal stability with high mechanical stability, which makes them useful as flame retardants and in membranes.[45-47] Poly(aryl ether sulfones) are synthesized via nucleophilic aromatic substitution of bis(4-chlorphenylsulfone)s and diphenols, but AB-type polymerizations have also been demonstrated.[48,49] Polyamides and polyimides containing sulfone and thioether functionalities along the polymer backbone have been extensively researched for applications as high refractive index polymers (HRIPs). Thioether or sulfone containing polyimides achieve high refractive indices around 1.72 – 1.77 (633 nm) with sulfur contents between ca. 15 – 30 wt%, and thioether or sulfone containing polyimides achieve refractive indices of around 1.73 – 1.77 with a sulfur content of ca. 20 wt%.[50-53]

1.3.3 Poly(thiophene)s

Poly(thiophene)s are a class of conductive polymers based on substituted thiophenes.[54] They can be obtained via oxidation of thiophenes with Fe^{3+} or through reduction of 2,5-dihalothiophenes with Rieke-Zn or reduction of 2-halothiophenes with lithium diisopropylamide (LDA) and a Ni catalyst.[55] While the oxidation of thiophenes is undoubtedly the more economic pathway, it typically leads to amorphous poly(thiophene)s with random head-to-tail, tail-to-tail, and head-to-head connection (**Figure 13**). For reductive polymerization, highly regioregular poly(thiophene)s can be obtained.[56] In the case of the most relevant polythiophene, poly(3,4-ethylendioxythiophen) (PEDOT), the regioregularity does not have to be considered since head and tail connection are identical. The high electrical conductivity, film forming ability, low absorbance of visible light, and mechanical flexibility of PEDOT make it the commercially most successful conductive polymer, with uses in solar cells, flexible electrodes, optoelectronic devices, and antistatic coatings.[57-59] In commercial products, PEDOT is often blended with poly(styrene sulfonate) (PSS), which acts as an acid and anionic surfactant to overcome the inherent poor solubility of PEDOT. PEDOT:PSS is sold as aqueous dispersion. Other potential applications of poly(thiophene)s are as sensors or as heat conductors.[60,61]

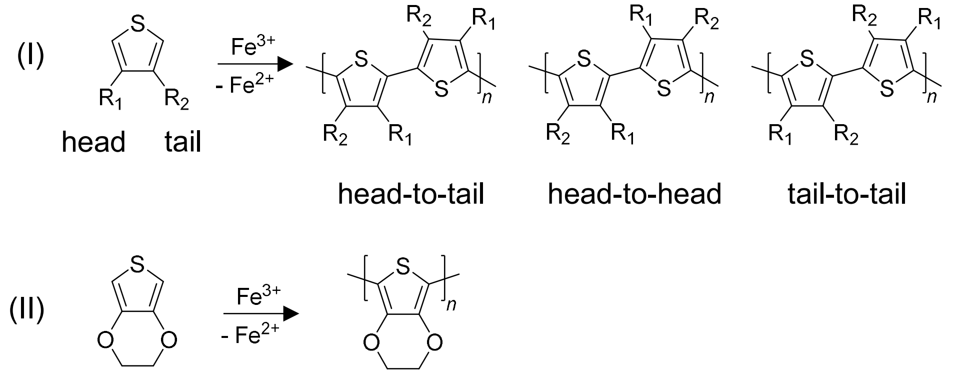

Figure 13. Reaction equation for the oxidation of a (I) 3,4-disubstituted thiophen and (II) 3,4-ethylendioxythiophen.

1.3.4 Poly(thioester)s and poly(thiocarbonate)s

Poly(thioester)s had attracted fairly little interest both industrially and academically, which is why the first review about this group of polymers dates back only to 2007.[62] Previously, the reaction of thioanhydrides with 2-methylethylene oxide and 2-methylethylene sulfide to synthesize poly(thioester)s with narrow molar mass distribution and a dispersity Đ of 1.3 had been unraveled.[63,64] Prior synthetic routes relied on the polyaddition of thiocarboxylic acids with alkenes, polycondensations of dithiols with diacids or diacid chlorides, ring opening polymerizations of thiolactone or thionolactone, and microbial pathways (**Figure 14**).[65-70]

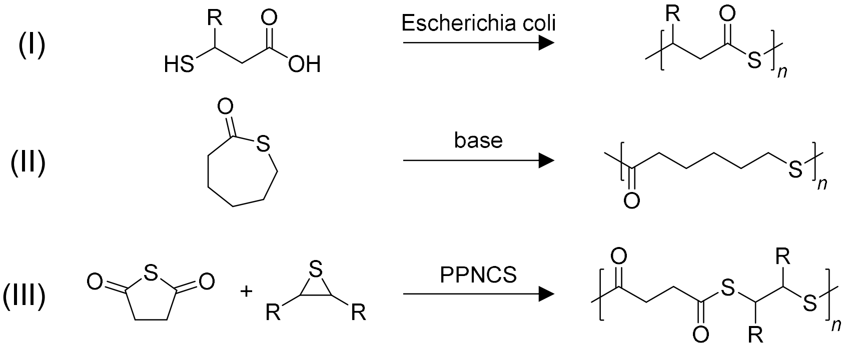

Figure 14. Synthesis of poly(thioester)s via (I) microbial polycondensation, (II) ring opening polymerization of ε-thiolactone, and (III) the reaction of a thioanhydride with substituted ethylene sulfide.

Poly(thiocarbonate)s, more exactly poly(monothiocarbonate)s, poly(dithiocarbonate)s, and poly(trithiocarbonate)s can be synthesized by reacting dialcohols or dithiols with phosgene or thiophosgene (**Figure 15**).[71-74] Another method is the use of ethylene sulfide or ethylene oxide derivatives and carbon disulfide (CS_2) or carbonyl sulfide (COS) as a C_1 building block.[75-78] Depending on the catalyst used for the reaction, the formation of unwanted low molar mass cyclic byproducts can be avoided.[79] Poly(propylene trithiocarbonate) synthesized from 2-methylethylene sulfide and CS_2 has a theoretical sulfur content of 64 wt%, which is presumably the highest sulfur content amongst all sulfur containing polymers with a well-defined repeating unit.[79] As a consequence of the high sulfur content of poly(propylene trithiocarbonate), the refractive index is very high, i.e., 1.78 at 633 nm.

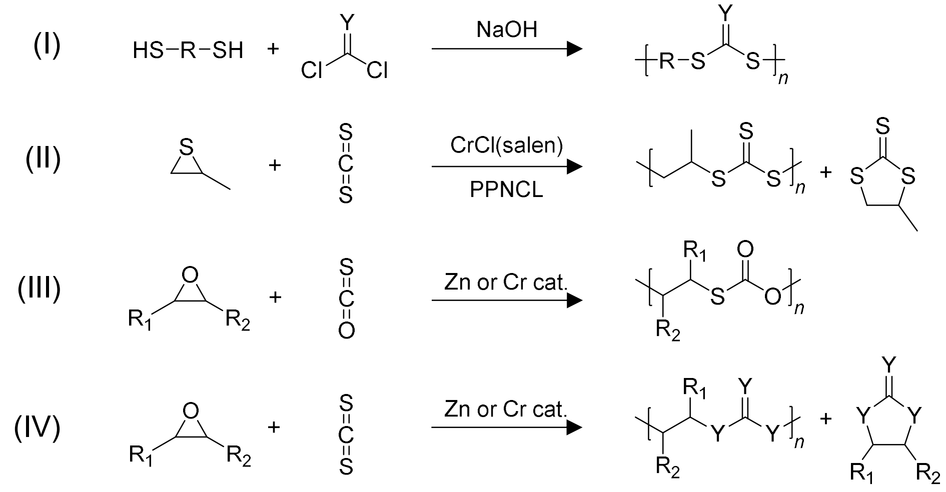

Figure 15. Synthesis strategies for poly(thiocarbonate)s. In (IV) there can be 1-3 sulfur or oxygen atoms in a repeating unit due to the oxygen-sulfur exchange reaction. In (III) the oxygen-sulfur exchange reaction is inhibited by using low temperatures. Y indicates either a sulfur or oxygen atom while R_1 and R_2 denote organic rests. PPNCL (bis(triphenylphosphoranylidene) ammonium chloride) is a co-catalyst.

In contrast to the immensely important poly(ester)s, poly(carbonate)s, or the related poly(urethane)s, their thio-counterparts did not reach commercial applications, nor did they find widespread academic interest. However, they might gain relevance due to the increasing relevance of polymer recycling, where thio-polymers might offer advantages over established poly(ester)s, poly(carbonate)s.[62,80]

1.4 Inverse vulcanization

The term inverse vulcanization was coined in 2013 by PYUN and describes the copolymerization of alkenes with molten sulfur at temperatures between 130 – 180 °C to form polysulfides.[81] The name inverse vulcanization refers to the vulcanization process invented by GOODYEAR in 1839 in which unsaturated polymers such as poly(isoprene) or *cis*-poly(buta-1,3-diene) are crosslinked with sulfur to form rubbers. Sulfur makes up around 0.5 – 4 wt% of vulcanized rubber.[82,83] In the inverse vulcanization, alkenes serve as crosslinkers for radical polysulfide chains present in melts of sulfur (**Figure 16**). The content of sulfur can be larger than the organic content, i.e., carbon and hydrogen. A core advantage of this reaction is the direct utilization of the waste product sulfur. Further advantages are experimental simplicity, a low price, and thus scalability. The incorporation of elemental sulfur can reach around 90 wt%, which is far more than for any other class of sulfur containing polymers.

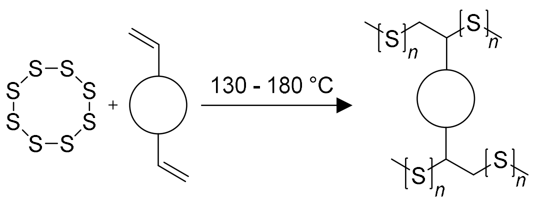

Figure 16. General reaction equation of the inverse vulcanization of a divinyl compound.

It must be noted that much before the term inverse vulcanization was coined similar or identical reactions had been performed from ca. 1950 – 1980, particularly with styrene or norbornenes.[84-99] Further, elemental sulfur was used as a retarder for free radical polymerizations of vinyl acetate and methyl acrylate.[100,101] However, studies about such ‘sulfur modified polymers’ were not motivated by ecological or green chemistry considerations and thus did not attract lasting interest.

Polymers prepared via inverse vulcanizations have been given three different names. ‘Organically modified chalcogenides (Ormochalks)’ by SANGHERA, as analogy to established ‘organically modified silicates (Ormosils)’, ‘chalcogenide hybrid inorganic/organic polymer (CHIP)’ by PYUN, and simply ‘inverse vulcanized polymers’, as preferred by HASELL.[102-105] The formally correct name polysulfide is problematic since it does not reveal the synthetic origin of the polymer. Thus, it does not allow a distinction from polysulfides prepared via inverse vulcanization from polysulfides prepared via the reaction of Na_2S_2 with dichloroalkanes. Further, the number of sulfur atoms in a R-S_n-R unit in polymers prepared via inverse vulcanization is usually neither constant nor known. For the author of this thesis the term inverse vulcanized polymer is preferred.

Initially, only highly reactive C=C double bonds like those of styrene or norbornene could be used. With the aid of catalysts and the so-called dynamic covalent polymerization, the monomer (i.e., crosslinker) pool could be expanded beyond highly reactive styrene or norbornene type C=C double bonds to vinyl siloxanes, methacrylates, or allyl ethers.[103-109] Since catalytic inverse vulcanization can be conducted at lower temperatures, the undesired formation of toxic and smelly H_2S can be reduced or avoided.

The first article about the inverse vulcanization published in 2013 caused a large surge in research to generate useful materials from elemental sulfur. Consequently, the field has been reviewed frequently since then, with a focus on synthetic approaches, green chemistry, and applications.[111-116] So far, proposed applications range from mercury, perfluorooctanoic acid, and oil remediation,[117-123] anti-microbial surfaces,[124,125] adhesives,[126] metal and particle templates,[127,128] infrared optics,[105,129-137] catalysis,[138] cathode materials,[139-144] healable or recyclable materials,[145,146] thermal insulators,[147,148] flame retardants,[149,150] or fertilizers.[151,152]

Despite the rapid advances and diverse research about the inverse vulcanization, there are several serious drawbacks that limit commercial application. Among those are the very limited understanding and control over the inverse vulcanization reaction, which causes the products to differ strongly based on the exact reaction procedure.[153] Further, the molar mass distributions of soluble inverse vulcanized polymers reveal the presence of mainly low molecular weight molecules, whereas insoluble, crosslinked inverse vulcanized polymers are typically glassy and brittle. In contrast to the well-established polymer chemistry of carbon, fundamental parameters of inverse vulcanized polymers, such as the molar mass, the solubility, or the thermomechanical properties, are not readily controlled. Initially, the sulfur rank was used as the main variation parameter to influence the properties of inverse vulcanized polymers, which showed to be insufficient to address a wide range of properties. HASELL developed ternary inverse vulcanizations, which induced control over the physical properties by means of the relative ratio of different alkenes or by employing alkenes with different reactivity to enable delayed curing.[110,154,155] However, the exact influence of the alkene on the inverse vulcanized polymer are hard to predict. The most recent strategy to prepare polymers with tailored mechanical properties includes the inverse vulcanization of post-curable moieties followed by a post-curing step. Based on the addition reaction of alcohols with diisocyanates to form urethane crosslinks, HASELL and PYUN demonstrated inverse vulcanized polymers with the most intriguing mechanical properties reported so far, i.e., high strength and elasticity.[149,156] Achieving both a high stress (> 10 MPa) and strain (> 300 %), however, required a reduction of the sulfur content to only 20 wt%.[149] Further, the procedure required a complex mixture of 10-undecen-1-ol, methylendiphenylisocyanate, 1,4-butanediol, vinyl capped polydimethylsiloxane or diisopropenylbenzene, and N,N′-dimethylformamide as a solvent. So far, the partial crosslinking of alcohols with isocyanates to form urethane bonds has been the only reported post-curing strategy compatible with the inverse vulcanization to produce thermosets and thermoplastics with tunable properties.

1.5 Organosilicon chemistry

Organosilicon compounds are molecules containing between one and four carbon-silicon bonds. As such, they have fairly similar properties to alkanes in terms of polarity and reactivity. Their large commercial relevance stems from the high affinity of silicon to oxygen, which enables the formation of Si-O-Si bond containing poly(organosiloxane)s or allows them to serve as mediators between organic and inorganic matter (organic-Si-O-inorganic).

As a purely synthetic class of molecules, they must be formed from silicon, which is obtained by reduction of silicon oxide (SiO_2) and silicates ($M^{2+}SiO_4^{2-}$). Since silicon and oxygen are the most abundant elements and amount to ca. 75% of the elements in Earth's crust, the silicon supply can be regarded as infinite. Industrially, the reduction of SiO_2 is achieved via reduction with carbon at a temperature of 2000 °C.[8] Elemental silicon is reacted with methyl chloride in the MÜLLER-ROCHOW process to form mainly dimethyldichlorosilane, and further methyltrichlorosilane, trimethylchlorosilane, and other silanes.[157] Historically, the first organosilicon molecule was synthesized by FRIEDEL and CRAFTS in 1863, who prepared tetraethylsilane by reaction of tetrachlorosilane with diethylzinc.[157]

For the use of silicon as semiconductor the purity of raw silicon obtained via reduction of quartz is not sufficient. Thus, raw silicon is oxidized with HCl to form the volatile $HSiCl_3$, which can be purified by distillation. The purified $HSiCl_3$ is reduced with H_2 and crystalized using a seed crystal to form monocrystalline silicon (CZOCHRALSKI process).[158] The need for high purity silicon for the solar cell and semiconductor industries grants affordable access to $HSiCl_3$, which can be used to synthesize a range of organosilicon compounds. In the following, only organosilicon compounds of relevance for the chemistry of poly(siloxane)s are addressed. For information about the incredibly rich chemistry of organosilicons the reader is referred to comprehensive textbooks.[159,160]

1.5.1 Alkoxy- and chlorosilanes

Alkoxy- and chlorosilanes are organosilicon compounds containing at least one alkoxy or chloro-substituent bound to the silicon. Typically, they carry 1 – 3 organic groups and 3 – 1 chloro- or alkoxy-substituents, respectively. Notable exceptions are tetraalkoxysilanes, such as tetraethoxysilane or tetramethoxysilane, which are used for the controlled synthesis of silica (nano-) particles via the STÖBER method or for aerogels.[161,162]

A large range of alkoxysilanes can be synthesized from the industrial $HSiCl_3$ in few steps (**Figure 17**). The Si-H bond can be added to C=C double bonds via hydrosilylation using KARSTEDTs catalyst.[163] The addition typically proceeds as anti-Markovnikov addition.[164] The resulting trichlorosilane ($R\text{-}CH_2CH_2\text{-}SiCl_3$) can be reacted with alcohols (R-OH) to form alkoxysilanes ($R\text{-}CH_2CH_2\text{-}SiOR_3$). Additional Si-C bonds can be formed using lithium or magnesium organyls (RLi, RMgX). If only mono or disubstitution is desired, the metal organic reagent should be added slowly to avoid oversubstitution.[165] Due to environmental concerns, recent advances in alkoxysilane synthesis have been devoted to routes that do not lead to the release of HCl.[166]

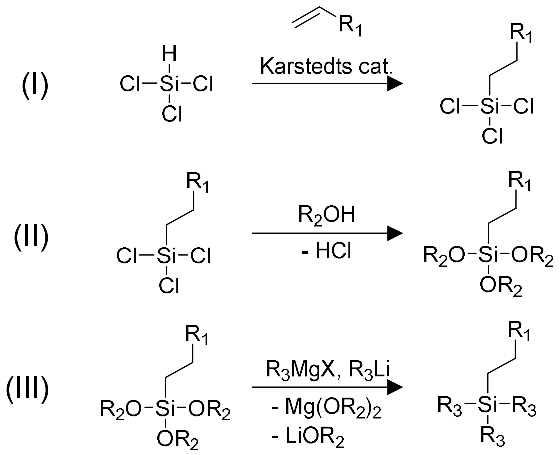

Figure 17. Synthetic route from trichlorosilane to functional alkoxysilanes. (I) Hydrosilylation, (II) alcoholysis, and (III) substitution with metal organyls (RLi, RMgX). R_1 can be aryl or alkyl, R_2 is mostly methyl- or ethyl-, R_3 can be alkyl or aryl.

1.5.2 Polycondensation of alkoxy- and chlorosilanes

Both alkoxy- and chloro-substituents of the general formula R_nSiX_{4-n} (X = Cl, OMe, OEt) can be hydrolyzed to yield silanols (Si-OH) which condensate into (poly-) organosiloxanes (Si-O-Si). Depending on the amount of hydrolysable groups, different (poly-) organosiloxanes are obtained, which are termed M ($SiO_{0.5}$), D (SiO_1), and T ($SiO_{1.5}$) (poly-) organosiloxanes. Q (SiO_2) siloxanes are obtained from hydrolysis and polycondensation of silanes containing four hydrolysable substituents and thus do not contain any organic moieties after polycondensation (**Figure 18**). M siloxanes are small molecules, D siloxanes possess a chain or ring like structure, T siloxanes possess a (open) cage structure, i.e., polyhedral oligomeric silsesquioxanes (POSS), or polymeric network structure. Q siloxanes are synthetic analogues of quartz (SiO_2). Silanes containing one hydrolysable substituent are used as protective group for alcohols and as capping agent for poly(organosiloxanes) polymerization.[167,168] Silanes with two hydrolysable groups are used for the synthesis of linear polymers and cyclosiloxanes.[169,170] Silanes containing three hydrolysable groups find use in coatings (mono- and multilayer) or for the synthesis of POSS.[171,172] Silanes containing four hydrolysable groups can be converted to synthetic silica (nano-) particles and zeolites.[173,174]

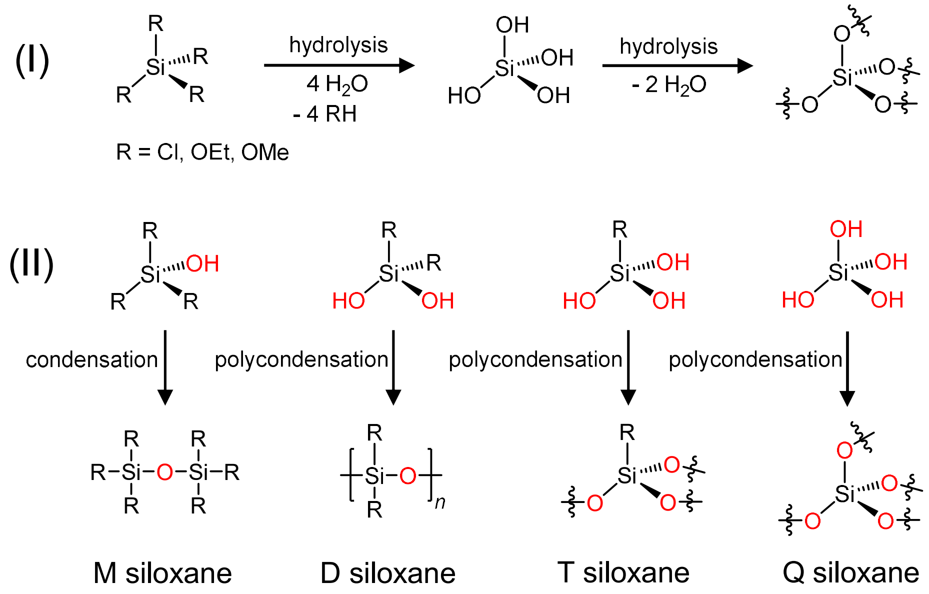

Figure 18. Reaction equation of the (I) hydrolysis and polycondensation of a silane containing four hydrolysable groups (simplified) and (II) the formation of M, D, T, and Q siloxanes.

The most relevant hydrolysable silane is dimethyldichlorosilane, which is produced in the MÜLLER-ROCHOW process and can be directly polycondensated into poly(dimethylsiloxane) (silicone oil).[167] Silicone oils possess excellent heat stability and low UV susceptibility due to the strength and low UV absorbance of the Si-O bond, respectively.[167] The viscosity of PDMS oils can be tuned in a wide range via the molar mass. Their inertness, hydrophobicity, and low surface tension make them useful in industrial applications as hydraulic oils, defoamers, parting agents, spreading agents, lubricants, and in cosmetics.[167]

The reactivity of hydrolysable groups decreases in the order chloro >> methoxy > ethoxy. For alkoxysilanes, an acid or base is required as catalyst, whereas chlorosilanes form HCl upon hydrolysis.[175] Further, tin catalyst are commonly employed.[176-178] Some alkoxysilanes, such as 3-(aminopropyl)trimethoxysilane (APTES) do not require an external catalyst, since the amino group in APTES is sufficiently basic to catalyze the hydrolysis and polycondensation.[179]

The polycondensation of alkoxy- and chlorosilanes is a complex equilibrium of non-hydrolyzed, partly hydrolyzed, and fully hydrolyzed silanes as well as non-condensated, partly condensated, and fully condensated siloxanes (**Figure 19**). In principle, each species in the equilibrium has its own set of rate constants. For example, the rate of condensation generally increases with an increasing number of silanol groups at the same silicon atom. This is reflected by the fact that monomeric silanols can be bench stable.[180] Siloxane bond formation can occur via condensation of two silanol groups (-H_2O) or via condensation of a silanol group with an alkoxy group (-MeOH).

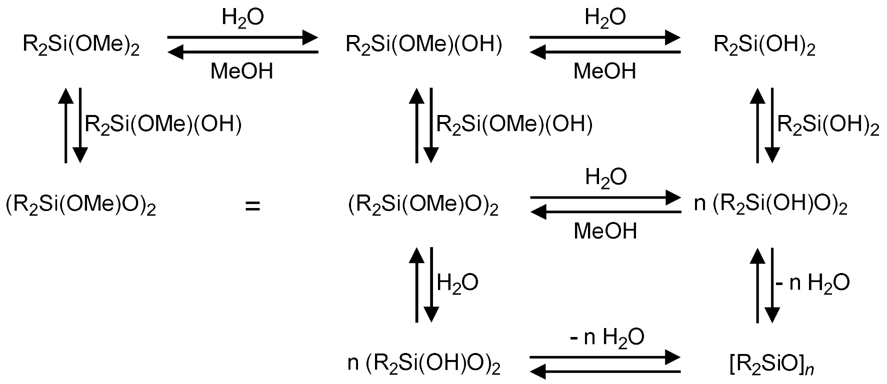

Figure 19. Reaction equations of some of the possible equilibria occurring during the polycondensation of a diorganodimethoxysilane.

Due to the complex equilibria involved in their synthesis, there is no generally applicable method for the synthesis for poly(organosiloxanes)s. However, a various kinetic trends have been unraveled. For example, it was found that the hydrolysis of trialkoxysilanes is fast using acid catalysts and slow using base catalysts, whereas the inverse is true for the condensation.[180] Electron donating organic substituents increase the rate of hydrolysis in acidic media and decrease it in basic media, whereas a larger steric hindrance of the organic moiety generally decreases the rate of hydrolysis. Protic solvents were found to increase the rate of polycondensation when using an acid catalyst, whereas a decrease was observed with basic catalysts. The opposite was found for aprotic solvents, which explains the popularity of alcohols as a solvent in combination with a mineral acid as catalyst.[175] An increase of the water content increases the rate of hydrolysis, until the reduction of the solubility of the silane causes the adverse effect. For T siloxanes, the share of higher condensated species can decrease with increasing water content.[175] Industrially, the preparation of silicon oils is conducted in a two-step process, in which a low molar mass ‘hydrolysate’ is formed by hydrolysis of a dichlorodiorganosilane. In a second step, the equilibrium is then driven towards the polycondensate utilizing elevated temperatures, removal of water, and condensation catalysts.[169]

1.5.3 Cyclosiloxanes

Cyclosiloxanes are obtained by hydrolysis and condensation of dichlorodiorganosilanes, where they are typically a side product of the desired long poly(organosiloxanes)s chains (**Figure 20**). Typically, a distribution of different ring sizes is obtained, with most rings being either cyclotrisiloxanes (D_3) or cyclotetrasiloxanes (D_4). If the organic rest is sufficiently small, the rings can be separated from each other via vacuum distillation. Another synthetic route is the oxidation of diorganosilanes (R_2SiH_2). Functionalization of Si-H bond containing cyclosiloxanes can be conveniently done via Pt catalyzed hydrosilylation.[181,182] Cyclosiloxanes serve as monomers for the ring opening polymerization to prepare poly(organosiloxane)s with controllable molar mass

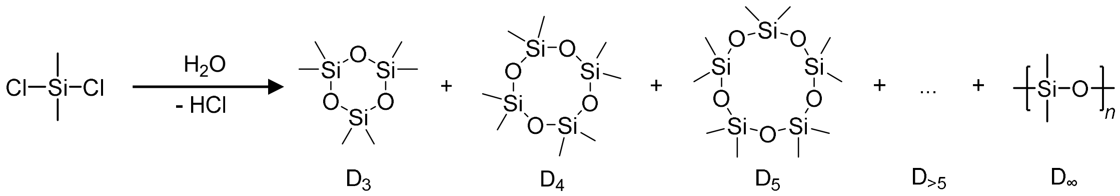

Figure 20. Hydrolysis and polycondensation of dichlorodimethylsilane to form a mixture of ring molecules and linear chains.

1.5.4 Ring opening polymerization of cyclosiloxanes

The ring opening polymerization (ROP) of cyclosiloxanes can be distinguished in kinetically and thermodynamically controlled ROP and can be conducted for strained (D_3) and non-strained rings (D_{4-6}) using anionic or cationic initiators (**Figure 21**). Due to its higher costs compared to the hydrolysis and polycondensation approach it is mainly used for specialty applications, where the molar mass must be controlled finely.[169] To obtain high molar mass polymers with a narrow molar mass distribution, the kinetically controlled anionic ROP of cyclotrisiloxanes (D_3) is used. The kinetically controlled ROP exploits that the ring opening polymerization proceeds faster than side reactions such as backbiting or chain transfer, which leads to the initial formation of high molar mass poly(organosiloxane)s. To control the molar mass, disiloxanes can be used as end-capping agents.[169] For the thermodynamically controlled ROP, cyclosiloxanes are obtained as side products and the molar mass is lower than for the kinetically controlled ROP. Since the thermodynamically controlled product is identical for all ring sizes, mostly cyclotetrasiloxane (D_4) as the cheapest rings are used. Thus, the thermodynamically controlled cationic polymerization of cyclotetrasiloxanes (D_4) has commercial relevance, too.[169]

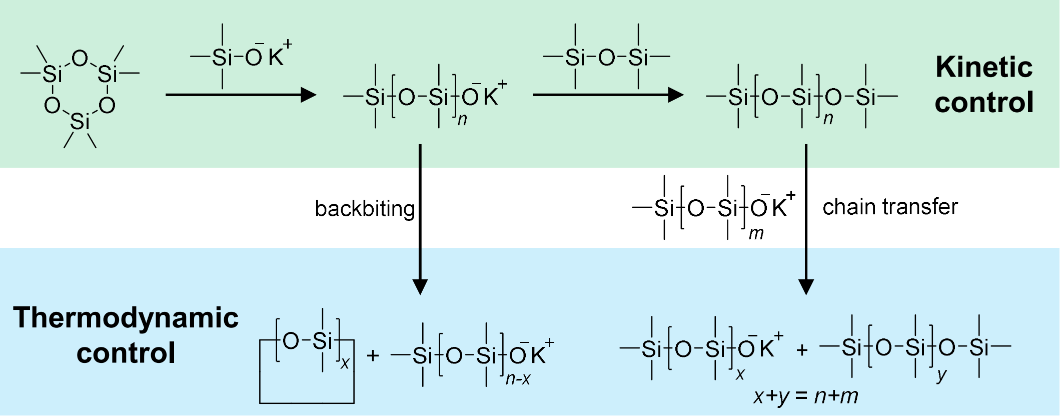

Figure 21. Reaction equations of the kinetically (green) or thermodynamically (blue) controlled anionic ROP of 2,2,4,4,6,6-hexamethylcyclotrisiloxane using potassium trimethylsilanolate as an initiatior and 1,1,1,3,3,3-hexamethyldisiloxane as an end capping agent.

For the cationic ROP of cyclosiloxanes, mineral acids such as sulfuric acid or heterogeneous catalysts carrying sulfonic acid groups are used. A heterogeneous acid catalyst offers the advantage of trivial separation from the poly(organosiloxanes) by filtration.[183,184] The use of triflic acid as catalyst is also popular since it is soluble in organic solvents and enables rapid reactions.[185] The cationic ROP of cyclosiloxanes has the advantage that base sensitive functional groups such Si-Cl can be polymerized.[169] Anionic ROPs are conducted using strong bases such as KOH or potassium silanolates. Further, the use of phosphazene superbases has been explored due to the very fast reaction times.[186] Generally, less electrophilic countercations will increase the rate of propagation, e.g., $Na^+ < Ka^+ < Et_4N^+ < Et_4P^+$, since they do not tend to form dormant aggregates with the propagating anion.[169] For unstrained siloxane rings ($D_{>3}$), the ROP is an entropy driven process, which is due to the higher conformational freedom of open polysiloxane chains in comparison with cyclosiloxanes. Since this entropy gain decreases with the size and polarity of the organic substituents the yield of the polymer in the equilibrium decreases strongly.[170]

1.5.5 The silicon-oxygen bond

The unique properties of the silicon-oxygen bond are the reason for the fascinating properties of poly(organosiloxane)s, such as the extremely low glass transition temperatures (T_G), the high thermal and oxidative stability, the large binding angles, and the small rotational barrier of the organic substituents around the silicon atom.

From the large difference (1.7) in the electronegativity of oxygen (3.5) and silicon (1.8) a partially ionic covalent bond was already postulated in the 1930s, with the ionic and covalent contributions amounting to ca. 50 % each. Henceforth, the nature of the silicon-oxygen bond has been a subject of debate, even involving Nobel laureate Linus Pauling, who formulated the electronegativity scale in 1932 and authored several books about the nature of chemical bonds.[187] In 1980, Pauling wrote an article to refute a postulate by DONNAY and DONNAY in 1978, who argued that the distribution of ionic and covalent shares in the silicon-oxygen bond are 25 and 75 %, respectively.[188] According to Pauling, this conclusion is based on the false assumption of silicon atoms with four Si-O single bonds being present in quartz (SiO_2). Based on the determination of the electron density at Si and O in quartz, a charge of +1 can be assigned to each Si atom and -0.5 to each oxygen atom. For four covalent Si-O bonds this would result in an ionic share of only 25 %. However, the Si-O bond length in silicates is around 1.6 Å, which is about 0.2 Å less than the sum of the single bond radii of oxygen and silicon. Pauling argues that from a comparison with other tetrahedral silicates a bond order of 1.55 can be assumed. The binding situation in quartz can thus be described by two oxygen atoms donating one electron to Si resulting in Si^{2-}, which can form six resonating bonds, i.e., two Si=O double bonds and two Si-O single bonds. Only when an ionic character of 50 % is assumed for each bond, the charge of the Si atom reduces to a value of +1 (Si^{1+}), which complies with Pauling's electroneutrality principle.[189,190] Recent calculations and crystallographic studies, however, do not find evidence for the involvement of the empty d-orbitals of silicon but rather involvement of negative hyperconjugation from oxygen p-orbitals into antibonding σ*-orbitals between Si and its substituents (Si-R).[191,192]

The high ionic share of the Si-O bond can explain the very low barrier of rotation around the Si-O axis of ca. 2.5 kJ mol^{-1} in 1,1,1,3,3,3-hexamethyldisiloxane ($(Me_3SiO)_2$) and the very low barrier for linearization, i.e., a Si-O-Si bond angle of 180 °, of ca. 1.3 kJ mol^{-1}. Consequently, Si-O-Si binding angles are typically around 130 – 170 ° which is much wider than the tetrahedral angle of 109.5 °. Ethers as the carbon analogues of disiloxanes show angles close to the tetrahedral angle, e.g., ca. 112 ° for dimethylether.[193,194] The wide angles result in a lower Lewis basicity of siloxanes compared to ethers, since the high partial positive charge of the silicon atoms repels the positive charge of electrophiles more efficiently.[195] The flexibility of the poly(organosiloxane) chains is further supported by the fact, that substituents appear only at every second atom.

Importantly, the high flexibility and rotational freedom in poly(organosiloxane)s is the entropic driving force for the ring opening polymerization of non-strained cyclosiloxanes ($D_{>3}$). This has the consequence, that the thermodynamically controlled ROP of cyclosiloxanes with bulky organic substrates will lead to a larger share of small rings compared to long chains in the equilibrium state.[170]

2 Motivation

Sulfur is produced annually on the megaton scale due to being a side product of natural oil and gas refining. While most of the sulfur production can be utilized to synthesize sulfuric acid for fertilizers, a large amount of sulfur remains unused and ends up being landfilled. Elemental sulfur is not toxic but can pose a large environmental threat when incinerated due to the uncontrolled formation of SO_2, which causes acid rain. Thus, there is an ecological and economical imperative to convert sulfur into useful materials. The most stable allotrope of sulfur at room temperature, α-S_8, is a highly brittle material due to its crystallinity and the weak attractive forces between the *cyclo*-octasulfur molecules in the crystal. The polymeric allotrope μ-sulfur possesses elastic properties but it is not stable at room temperature and will degrade back to *cyclo*-octasulfur.[196] By preventing the sulfur chains from degrading back into *cyclo*-octasulfur, sulfur polymers can be stabilized.

Modern life relies on carbon-based polymers. They serve in a multitude of applications such as packaging, coatings, construction materials, insulators, and many more. Nearly all carbon-based polymers are synthesized from fossil fuel derived chemicals, which are a finite feedstock. Sulfur-based polymers have the advantage of being derived from a waste material, which reduces the energy required for the synthesis of the monomer to zero. The unique properties of S-S bonds in polysulfides, such as their low dissociation energy, could lead to polymers with a much greater recyclability than that of polyolefins or state-of-the-art thermosets by virtue of dynamic covalent chemistry. At the end of their lifecycle, sulfur polymers could be controllably oxidized to SO_2 to produce sulfuric acid and fertilizers.

The inverse vulcanization, the reaction of molten sulfur with alkenes, allows the conversion of sulfur into stable polymers. Inverse vulcanized polymers have been shown to be inexpensive and promising materials for applications in optics or water purification. However, inverse vulcanized polymers suffer from a lack of control over basic polymer parameters, such as the solubility or the molar mass. Apart from design principles abbreviated by HASELL and CHALKER to alter the thermomechanical properties of certain inverse vulcanized polymers via the type and stoichiometry of the comonomers, there is no generally applicable strategy to tailor the properties of inverse vulcanized polymers.[154] The poor control over the properties of inverse vulcanized polymers limits their applications, as no targeted product development can be done. Further development of inverse vulcanized polymers by means of product engineering and materials science require profound chemical variation parameters to allow rapid and scalable prototyping of materials and products. Ideally, no drastic compositional changes of the sulfur or comonomer content should be required for prototyping. Instead, fine chemical screws should regulate the properties of inverse vulcanized polymers in a way it has been established for carbon-based polymer engineering.

The objective of this thesis is to introduce and establish chemical strategies to overcome existing limitations of the inverse vulcanization in terms of control over molecular and macromolecular properties. In contrast to previous attempts, a genuinely systematic and predictable approach was sought. It was hypothesized that a well-defined post-modification reaction could be used to crosslink inversed vulcanized polymers to control their molecular and macroscopic properties by subtle variations of the amount and type of crosslinking. The requirements for the post-modification reaction pose a chemical challenge. First, the functional moieties incorporated into the sulfur prepolymer must remain unchanged under the harsh conditions of the inverse vulcanization, i.e., temperatures around 130 – 160 °C and the presence of thiyl radicals. Second, the chemical trigger to induce post-modification must not react with the polysulfide chains of inverse vulcanized polymers. Third, neither the functional comonomer nor the chemical trigger can be expensive. Fourth, no solvent is required for the post-modification step. As of the end of 2021, only two post-crosslinking strategies for the inverse vulcanization are known. One is the use of alkenes containing hydroxy groups as comonomers and isocyanates as post-crosslinker to form urethanes, as developed independently by HASELL and PYUN. The other one is the use of organosilicon chemistry described in this thesis.

Marrying organosilicon chemistry with the inverse vulcanization deemed to be a powerful chemical toolbox to extend the boundaries of inverse vulcanization chemistry. Chloro- and alkoxysilanes appeared interesting as comonomers for the inverse vulcanization since they can form siloxane bonds between each other using only water as a reagent. Further, chloro- and alkoxysilanes are cheap, temperature stable, and have high boiling points. As compounds of large academic and industrial relevance, a broad range of chloro- and alkoxysilanes is economically available, which ensures the scalability of strategies to control the inverse vulcanization via chloro- and alkoxysilane chemistry.

A promising future application for inverse vulcanized polymers in the future is the treatment of wastewater by remediation of metal ions, perfluorinated compounds, or oil. Such applications require and benefit from a defined surface chemistry, such as a covalent attachment of the polymer to the substrate or the control of the solubility of the coating. Thus, it was aimed to develop a high-sulfur content coating by marrying the chemistry of the inverse vulcanization with the chemistry of alkoxysilanes (Chapter 3.1).

Controlling the molar mass of inverse vulcanized polymers while retaining their solubility and their sulfur content has not been demonstrated yet. Synthetic strategies to control the properties of soluble inverse vulcanized polymers are crucial to study the fundamental influence of the molar mass on their macroscopic properties. It was assumed that a fine adjustments of the amount of siloxane crosslinks in an inverse vulcanized polymer would allow for the control over the molar mass without disturbing the elemental composition of the polymers (Chapter 3.2).

Inverse vulcanized polymers suffer from a tradeoff between flexibility and strength. Many inverse vulcanized polymers are glassy and brittle materials, which might arise from the rigidity of the comonomers they were synthesized from. The siloxane bond possesses a high degree of rotational freedom and a very low energy barrier of linearization. It was hypothesized that inverse vulcanized polymers containing flexible siloxane bonds could be inherently flexible polymers (Chapter 3.3).

3 Results and Discussion

3.1 Inverse Vulcanization of Styrylethyltrimethoxysilane

3.1.1 Disclaimer

The content of this chapter has been published in Angewandte Chemie International Edition from Wiley-VCH GmbH (Weinheim, Germany).[197] The complete authors list in the original order is Johannes M. Scheiger, Chatrawee Direksilp, Patricia Falkenstein, Alexander Welle, Meike Koenig, Stefan Heissler, Joerg Matysik, Pavel A. Levkin, and Patrick Theato. Johannes M. Scheiger is the first author of the article.

The author contributions were as follows: J. M. S. proposed the original idea, performed the experiments, curated, and analyzed the data, and wrote the paper (lead). C. D. acquired XPS data (lead). P. F. acquired ^{29}Si NMR data (lead). A. W. acquired and analyzed ToF-SIMS data (lead), M. K. acquired and analyzed ellipsometry data (lead). S. H. helped with RAMAN and ATR FT-IR spectroscopy (supporting). A. G., K. U., and T.S. helped with experiments and analysis of the data (supporting). J. M., P. A. L., and P. T. acquired funding and corrected the manuscript (lead).

3.1.2 Nomenclature

3.1.2.1 Monomer

The monomer used in this chapter is a mixture of four constitutional isomers, whose IUPAC names are trimethoxy(3-vinylphenethyl)silane, trimethoxy(4-vinylphenethyl)silane, trimethoxy(1-(3-vinylphenyl)-ethyl)silane, and trimethoxy(1-(4-vinylphenyl)ethyl)silane. Since each of these isomers has the same structural motifs, i.e., a styryl, an ethyl, and a trimethoxysilane moiety, the trivial name styrylethyltrimethoxysilane was formed, and StyTMS was chosen as an acronym. Commercial StyTMS contains an impurity of four constitutional isomers, whose IUPAC names are trimethoxy(3-ethylphenethyl)silane, trimethoxy(4-ethylphenethyl)silane, trimethoxy(1-(3-ethylphenyl)-ethyl)silane, and trimethoxy(1-(4-ethylphenyl)ethyl)silane. Since each of these isomers has the same structural motifs, i.e., an ethylphenyl and an ethyltrimethoxysilane moiety, the trivial name ethylphenethyltrimethoxysilane was formed to represent all four isomers, and EPTMS was chosen as an acronym.

3.1.2.2 Polymer

The product of the inverse vulcanization of StyTMS with sulfur was termed poly(S_n-*r*-StyTMS) in accordance with the published literature. The index *n* stands for the weight percentage (wt%) of sulfur in the polymer and *r* indicates the random sequence of sulfur and StyTMS repeating units.

The product of the hydrolysis and polycondensation of poly(S_n-*r*-StyTMS) was termed *net*-poly(S_n-*r*-StyTMS). The suffix *net* indicates the insolubility and the network structure of the polymer, arising from siloxane crosslinking.

3.1.3 Introduction

No strategy of a solution processable inverse vulcanized polymer which can be mildly cured into an insoluble thermoset had been introduced yet. For surface applications such as wastewater remediation or membranes the interface and not the bulk of a substrate is decisive for its properties. Thus, solution-based coating strategies for inverse vulcanized polymers are sought to allow for the preparation of coated substrates. It is not sufficient to apply solutions of inverse vulcanized to substrates, since this does not result in a covalent attachment of the inverse vulcanized polymer to the surface the leaching or dissolution of the coating by organic solvents cannot be prevented. To develop stable and solvent resistant coatings, the curing step must occur after the application of the inverse vulcanized polymer, which had not been demonstrated yet.

It was hypothesized that the inverse vulcanization of a vinylalkoxysilane would allow the formation of a high-sulfur content polysulfide bearing alkoxysilane groups, which would enable a mild post-condensation chemistry. The alkoxy groups were expected to be preserved after the harsh conditions of an inverse vulcanization reaction, i.e., high temperatures and the presence of thiyl radicals. A post-polycondensation of a soluble polysulfide bearing alkoxysilane groups was expected to give access to crosslinked high-sulfur content poly(organosiloxanes)s. Styrylethyltrimethoxysilane (StyTMS) was selected as vinyl alkoxsilane since styrene was already known to undergo inverse vulcanization reactions.[141]

3.1.4 Synthesis of poly(S_n-*r*-StyTMS) and *net*-poly(S_n-*r*-StyTMS)

Styrylethyltrimethoxysilane (StyTMS) was reacted with elemental sulfur in bulk at 130 °C for 8 h and the product of the inverse vulcanization, poly(S_n-*r*-StyTMS), could undergo hydrolysis and polycondensation to *net*-poly(S_n-*r*-StyTMS) in the form coated surfaces and particles as well as crosslinked materials with a maximum sulfur content of 35 wt% (**Figure 22**).

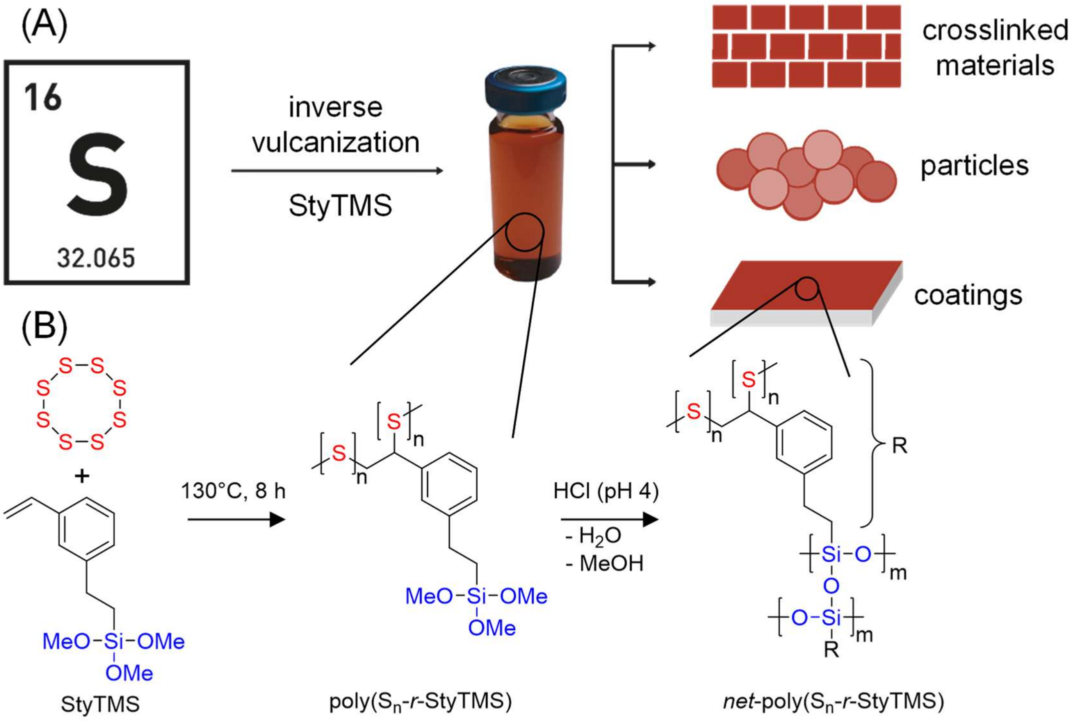
(A)
16
S
32.065
inverse vulcanization
StyTMS
crosslinked materials
particles
coatings
(B)
S S S S S S S S
+
130°C, 8 h
HCl (pH 4)
- H2O
- MeOH
MeO-Si-OMe
OMe
StyTMS
S
n
poly(Sn-r-StyTMS)
R
Si-O
m
O
O-Si
net-poly(Sn-r-StyTMS)

Figure 22. (A) Schematic reaction of sulfur with styrylethyltrimethoxysilane (StyTMS) to form a soluble prepolymer which can be hydrolyzed and polycondensated to yield high sulfur content coatings on surfaces and particles as well as crosslinked bulk *net*-poly(S_n-*r*-StyTMS). (B) Reaction equation of the inverse vulcanization of sulfur with styrylethyltrimethoxysilane (StyTMS) and the subsequent hydrolysis and polycondensation of the formed poly(S_n-*r*-StyTMS) to yield *net*-poly(S_n-*r*-StyTMS).

Commercial StyTMS is a mixture of *para*- and *meta*-isomers as well as the respective Markovnikov and anti-Markovnikov products of the hydrosilylation of (*m*, *p*)-divinylbenzene and trichlorosilane, adding up to a total of four different isomers (**Figure 23 A**). StyTMS is synthesized via the Pt(0) catalyzed hydrosilylation of divinylbenzene with trichloro- or trimethoxyvinylsilane. An impurity in commercial divinylbenzene are (*m*, *p*)-ethylstyrene, which results in four constitutional isomers of ethylphenethyltrimethoxysilane (EPTMS) upon hydrosilylation with trichloro- or trimethoxyvinylsilane (**Figure 23 B**). Thus, it was important to investigate the ^{1}H NMR spectrum of commercial StyTMS to determine the amount of the EPTMS impurity, since EPTMS is unreactive in the inverse vulcanization reaction.

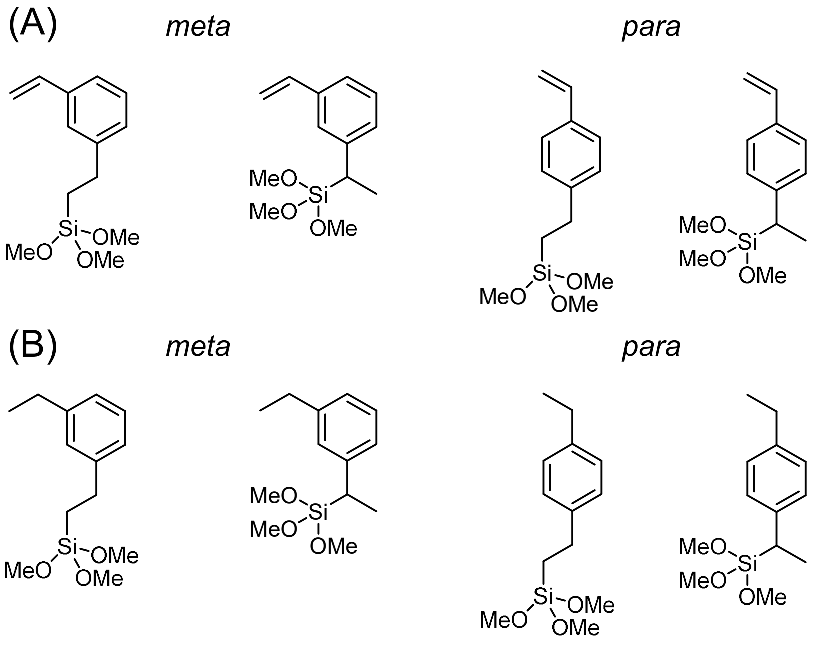

Figure 23. Molecular structures of the four constitutional isomers of (A) StyTMS and (B) EPTMS. The respective *meta* and *para* isomers are grouped. In each group of *meta* and *para* isomers, the left structure is the product of an anti-Markovnikov addition, whereas the right structure is the product of a Markovnikov addition.

Commercial StyTMS was investigated with ^{1}H NMR to shed light on the relative distribution of constitutional isomers and the quantity of EPTMS isomers and other impurities (**Figure 24 A**). Peaks in the ^{1}H NMR spectra of commercial StyTMS at 3.49 ppm (s) and at 1.54 ppm (s) were assigned to MeOH and H_2O, respectively, whereas peaks 2.67-2.60 ppm (m), 1.26-1.21 ppm (m) could be assigned to EPTMS. The amount of unreactive EPTMS was calculated to be 27 % based on the integral ratio of the isolated peak at 2.67-2.60 ppm of ethylphenethyltrimethoxysilane (dq, Ar-$\mathbf{CH_2}$-CH_3) relative to the peak at 2.71 ppm shared by all anti-Markovnikov products (m, Si-CH_2-$\mathbf{CH_2}$-Ar). This finding contradicted the value provided by the manufacturer Gelest, who stated an EPTMS content of only 10%. Based on the integral ratio between the signals at 2.77-2.70 ppm (m, Ar-C$\mathbf{H}_2$-CH_2-Si, anti-Markovnikov product) and 2.40-2.34 ppm (m, Ar-C**H**-(CH_3)Si, Markovnikov product), the ratio between anti-Markovnikov and the Markovnikov adduct of StyTMS was found to be ca. 7:1. The relative amounts of the *meta* and *para* isomers cannot be determined due to the overlap of peaks but is presumably the same as the *meta* to *para* ratio of commercial divinylbenzene, which is ca. 2:1.

The reaction of StyTMS with elemental sulfur afforded poly(S_n-*r*-StyTMS). The successful synthesis of poly(S_n-*r*-StyTMS) was concluded from ^{1}H NMR spectroscopy based on the disappearance of proton peaks assigned to the vinyl groups, the presence of peaks indicative for C-S bonds, and the retention of peaks assigned to the methoxy groups (**Figure 24 B**).

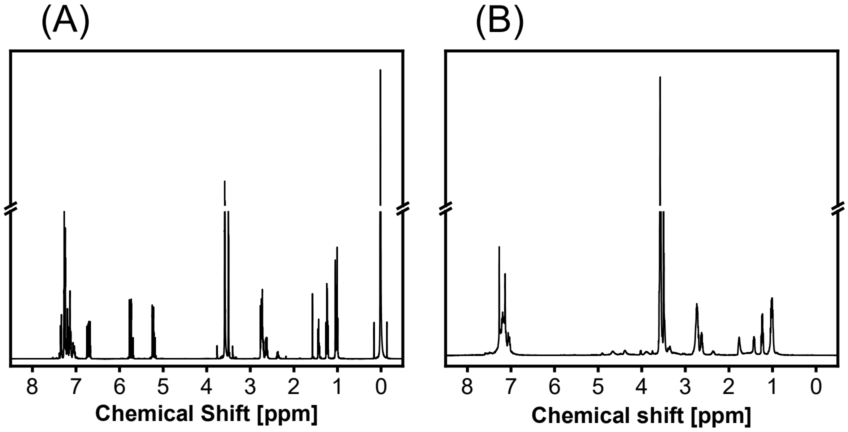

Figure 24. ^{1}H NMR spectrum of (A) StyTMS and (B) poly(S_n-*r*-StyTMS) in $CDCl_3$. The $CDCl_3$ in (A) contained 0.03 vol% TMS as a reference.

In the ^{1}H NMR spectrum of poly(S_n-*r*-StyTMS) all peaks assigned to vinyl groups of StyTMS at 6.75-6.68 (m, Ar-C**H**=CH_2), 5.77-5.73 (d, *cis*-vinyl H), and 5.25-5.22 ppm (d, *trans*-vinyl H) disappeared. Thus, all four isomers of StyTMS (*meta*, *para*, and the respective Markovnikov and anti-Markovnikov addition products) are reactive in the inverse vulcanization reaction. The ^{29}Si satellites of the methoxy peak at 3.58 ppm (s, SiO**CH_3**) in StyTMS were retained in the spectrum poly(S_n-*r*-StyTMS), indicating that the methoxy groups were still connected to the silicon atom after the inverse vulcanization. The emergence of peaks at 4.67, 4.39, and 3.90 ppm showed the formation of C-S bonds. The peak at 1.75 ppm indicated formation of a terminal -CH_3 microstructure as previously observed for styrene. Since all four isomers of StyTMS reacted with sulfur and beach of them can theoretically form a linear and a terminal product, eight different microstructures can be proposed (**Figure 25**).[141] The linear microstructure forms when thiyl radicals attach to both carbons of the styryl double bond. The terminal microstructure forms when styryl radicals abstract benzylic hydrogens. Peaks of impurities in the ^{1}H NMR spectrum of poly(S_n-*r*-StyTMS) at 3.76 and 1.86 ppm were assigned to THF, peaks at 3.49 and 1.59 ppm were assigned to MeOH and H_2O, respectively, and peaks at 2.67-2.60, and 1.26-1.21 ppm were assigned to EPTMS.

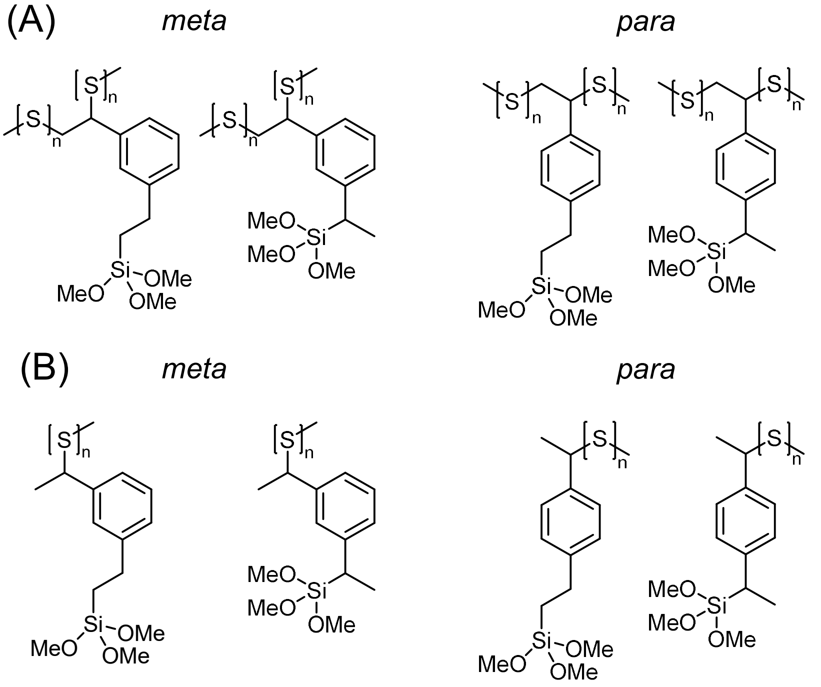

Figure 25. Molecular structures of the constitutional isomers of poly(S_n-*r*-StyTMS) for a (A) linear and a (B) terminal micrstructure. The respective *meta* and *para* isomers are grouped. In each group of *meta* and *para* isomers, the left structure is the product of an anti-Markovnikov addition, whereas the right structure is the product of a Markovnikov addition.

The product of the inverse vulcanization reaction, poly(S_n-*r*-StyTMS) was found to be a viscous, low molar mass oligomer, which was well soluble in THF (**Figure 26**). To test the influence of the reaction time and the feed ratio of sulfur and StyTMS on the molar mass, GPC measurements were conducted. The use of higher amounts of sulfur led to slightly higher molar masses after 8 h of reaction time for sulfur feed ratios increasing from 50 (M_N = 500 g mol^{-1}, M_W = 800 g mol^{-1}), to 60 (M_N = 500 g mol^{-1}, M_W = 900 g mol^{-1}), and to 70 wt% (M_N = 600 g mol^{-1}, M_W = 1200 g mol^{-1})

Despite this finding, the sulfur weight content of samples aged for two months did not exceed 35 wt% as determined with elemental analysis, thus the sulfur feed ratio was kept at 50 wt% for further experiments. The obtained elemental composition of *net*-poly(S_n-*r*-StyTMS) was 40.4 ± 0.04 wt% C, 4.00 ± 0.03 wt% H, 34.6 ± 0.25 wt% S. When the reaction time was increased from 8 h to 24 h, the molar mass did not change significantly (M_N = 500 g mol^{-1}, M_W = 800 g mol^{-1} to M_N = 600 g mol^{-1}, M_W = 800 g mol^{-1}, respectively), but the amount of the low molar mass species decreased. The remaining low molar mass species can be partly attributed to the presence of ethylphenethyltrimethoxysilane, which cannot react with sulfur. The dispersity (Đ) was not considered a meaningful parameter for multimodal molar mass distributions and was thus not calculated.

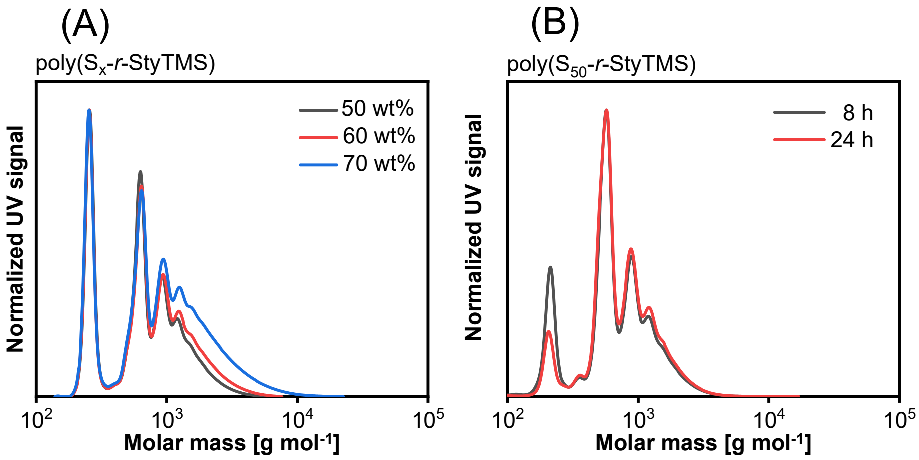

Figure 26. GPC traces of poly(S$_x$-r-StyTMS) for varying ratios of sulfur (A) and different reaction times (B). The index *x* instead of *n* refers to the feed ratio and not to the factual content of sulfur.

Addition of 5 vol% of dilute HCl (pH 4) to a solution of poly(S$_n$-*r*-StyTMS) in THF caused hydrolysis of the methoxy groups and initiated a polycondensation reaction. As a result, the molar mass of the soluble polymer increased (M_N = 1600 g mol^{-1}, M_W = 5500 g mol^{-1}). Equal masses of sulfur and StyTMS were reacted for 8 h at 130 °C, the product was extracted with 5 mL of THF and 5 vol% of HCl (pH 4) were added. The vial was sealed for three months, after which the volume of THF was reduced to ½ of the initial volume. A phase separation of the former clear orange solution into a red oil of partially polycondensated *branch*-poly(S$_{35}$-*r*-StyTMS) and a transparent THF phase occurred. The molar mass of the partially polycondensated *branch*-poly(S$_{35}$-*r*-StyTMS) was determined with GPC (**Figure 27**).

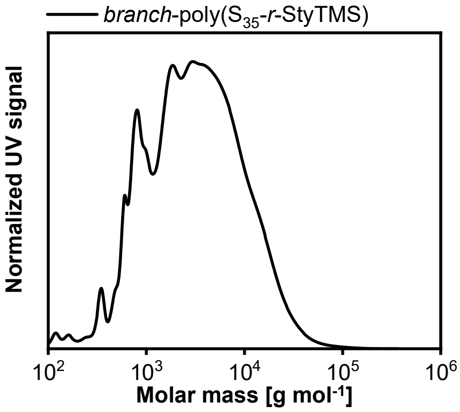

Figure 27. GPC traces of partially polycondensated poly(S$_n$-*r*-StyTMS). M_N = 1600 g mol^{-1}, M_W = 5500 g mol^{-1}, Đ = 3.4.

Longer durations of storage of hydrolyzed poly(S$_n$-*r*-StyTMS) resulted in the phase separation of a transparent THF phase and an insoluble, red precipitate. Removal of volatiles accelerated the polycondensation as indicated by the formation of an orange-red *net*-poly(S$_{35}$-*r*-StyTMS) powder, which was insoluble in THF, toluene, hexanes, and CS_2 because of covalent Si-O-Si crosslinking. This was observed for all weight ratios of sulfur tested (17-35 wt% by elemental analysis), which is different from most reports, where insolubility occurs only for high sulfur contents (>50 wt%).[81,141]

The highest sulfur content in crosslinked *net*-poly(S_n-*r*-StyTMS) was 35 wt% as determined by elemental analysis, independent of the feed ratio of sulfur and StyTMS used for the inverse vulcanization. This is below the highest values reported for materials made via inverse vulcanization of ca. 90 wt% sulfur but is still remarkable for a polymeric material.[15] Considering that there is a large share of EPTMS impurity amounting to ca. 27 mol% in commercial StyTMS, which does not contribute to sulfur fixation, the weight ratio of bound sulfur could presumably be increased to ca. 50% by using pure StyTMS.

3.1.5 Stability of *net*-poly(S_{35}-*r*-StyTMS) against degradation

The long-term stability of *net*-poly(S_{35}-*r*-StyTMS) against depolymerization into sulfur was confirmed with differential scanning calorimetry (DSC) and powder x-ray diffractometry (PXRD). To demonstrate the stability of *net*-poly(S_{35}-*r*-StyTMS) against depolymerization into elemental sulfur, *net*-poly(S_{35}-*r*-StyTMS) was milled into a powder and washed with THF and CS_2. The PXRD patterns of (S_{35}-*r*-StyTMS) powders aged for two months did not show any of the characteristic reflexes present in the diffraction pattern of crystalline sulfur. Thus, *net*-poly(S_{35}-*r*-StyTMS) can be considered amorphous (**Figure 28 A**). The DSC thermograms of (S_{35}-*r*-StyTMS) powders aged for two months did not show a melting peak of sulfur, which would be expected around 115°C. For DSC measurements, the temperature was ramped up from 40 °C to 180 °C, decreased to -60 °C, and increased to 180 °C at a heating rate of 10 K min^{-1}. The first ramp from 40 °C to 180 °C was used to examine the presence of crystalline sulfur, whereas the second ramp from -85 °C to 180 °C was used to examine the thermal properties of *net*-poly(S_{35}-*r*-StyTMS). No glass transition temperature (T_G) could be determined, presumably because the network is too densely crosslinked to allow any chain mobility (**Figure 28 B**). The absence of a detectable T_G due to siloxane crosslinking explained the brittleness of *net*-poly(S_{35}-*r*-StyTMS).

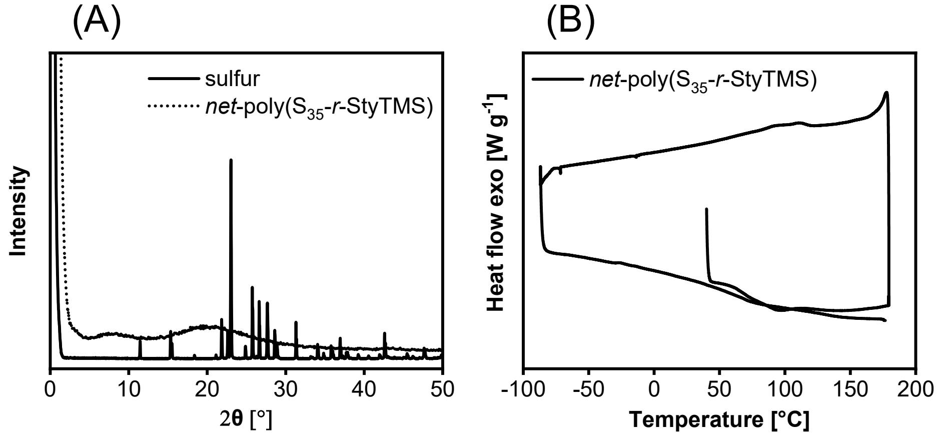

Figure 28. (A) PXRD patterns of *net*-poly(S_{35}-*r*-StyTMS) powder aged for two months. Elemental sulfur was used as a reference. (B) DSC thermograms of *net*-poly(S_{35}-*r*-StyTMS) powder aged for two months.

The thermal stability and the thermal degradation of *net*-poly(S_{35}-*r*-StyTMS) was investigated with thermogravimetric analysis coupled with mass spectrometry (TGA-MS). In this method, a sample is heated up above the decomposition temperature of a substance and the gaseous degradation products are ionized to determine their mass. Powdered *net*-poly(S_{35}-*r*-StyTMS) was stable until ca. 220 °C in the presence of oxygen, as indicated by a 5 wt% decomposition temperature ($T_{5\%}$) of 227 °C (**Figure 29 A**). The TGA curve of *net*-poly(S_{35}-*r*-StyTMS) showed a significant loss of ca. 30% of the initial mass between 220 – 300 °C, which is roughly the same as the sulfur content in *net*-poly(S_{35}-*r*-StyTMS). A further weight loss of 15 wt% until 500 °C could be attributed to the loss of organic moieties. A mixture presumably containing carbon and siloxane moieties remained as ash fraction at 500 °C. The coupling of mass spectrometry with TGA allowed a chemical analysis and confirmation of the assumed degradation products (**Figure 29 B**). TGA-MS showed a maximum of SO_2 and H_2O formation at 270 °C as well as a local maximum of CO_2 formation. Molecules were identified by their masses of 18, 44, and 60 g mol^{-1}, respectively. From 350 °C to 400 °C a steep increase in the formation of CO_2 could be observed, which reduced until ca. 470 °C after which it increased again. The graph shows the relative ion stream of a specific molecule and thus does not allow a quantitative comparison of the relative formation of SO_2, H_2O, or CO_2.

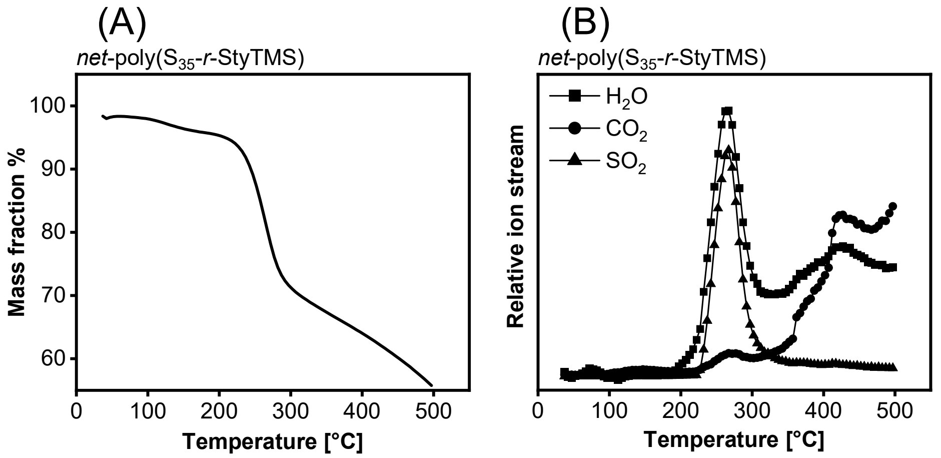

Figure 29. (A) TGA thermogram of *net*-poly(S_{35}-*r*-StyTMS) from 50 to 500 °C. (B) Formation of SO_2, H_2O, and CO_2 in dependence of the temperature as determined with a mass spectrometer coupled to the TGA.

3.1.6 Coatings of *net*-poly(S_{35}-*r*-StyTMS)

To explore future applications of sulfur containing polymers, strategies to bind high sulfur content materials to surfaces are required and relevant.

3.1.6.1 Solution casting, spin-coating, and dip-coating of *net*-poly(S_{35}-*r*-StyTMS)

Solutions of hydrolyzed poly(S_n-*r*-StyTMS) were prepared by dissolving and hydrolyzing poly(S_n-*r*-StyTMS) in THF with 5 vol% of dilute HCl (pH 4). This solution was then employed for different coating techniques and substrates. To compare the different coating methods, glass substrates were coated via spin-coating, dip coating, and solution casting (**Figure 30**). The obtained topologies differed strongly for the different coating techniques and concentrations used. Polymerization induced phase separation was observed in solution and is believed to influence the surface topology. Solution casting led to a micro-rough surface topology, whereas smoother surfaces were obtained for spin-coating and dip coating.

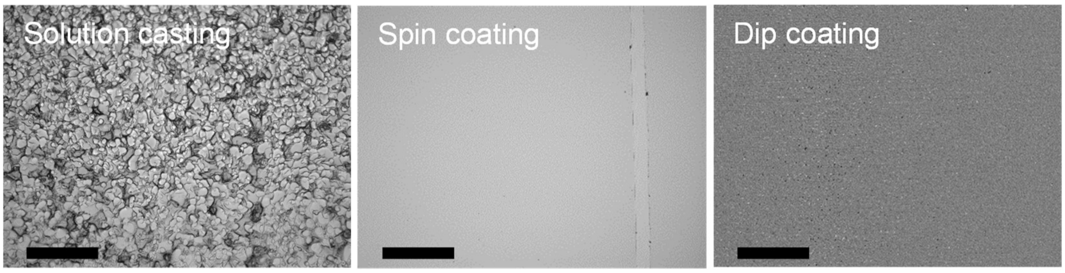

Figure 30. Microscopy images of glass surfaces coated with *net*-poly(S_{35}-*r*-StyTMS) with different coating techniques. The spin-coated surface was scratched with a needle to visualize the presence of a coating. An "Emboss (strong)" filter was used for the dip coated sample, to enhance the visibility of the micropores on the surface. Scalebars are 200 µm.

For dip coating, the topology depended strongly on the speed of substrate removal from the silanization solution (**Figure 31 A**). Substrates were immersed into a THF solution of hydrolyzed poly(S_n-*r*-StyTMS) for 5 min and were then removed with a defined speed of 40-, 45-, 125-, and 760 mm min^{-1} using a dip-coating machine. Dip-coated surfaces showed elongated features with widths of several micrometers and heights increasing from 24 to 70 nm with increasing substrate removal speed as determined with atomic force microscopy (**Figure 31 B**). As general trends, the height of features seemed to decrease with increasing removal speed, whereas the number of pores increased.

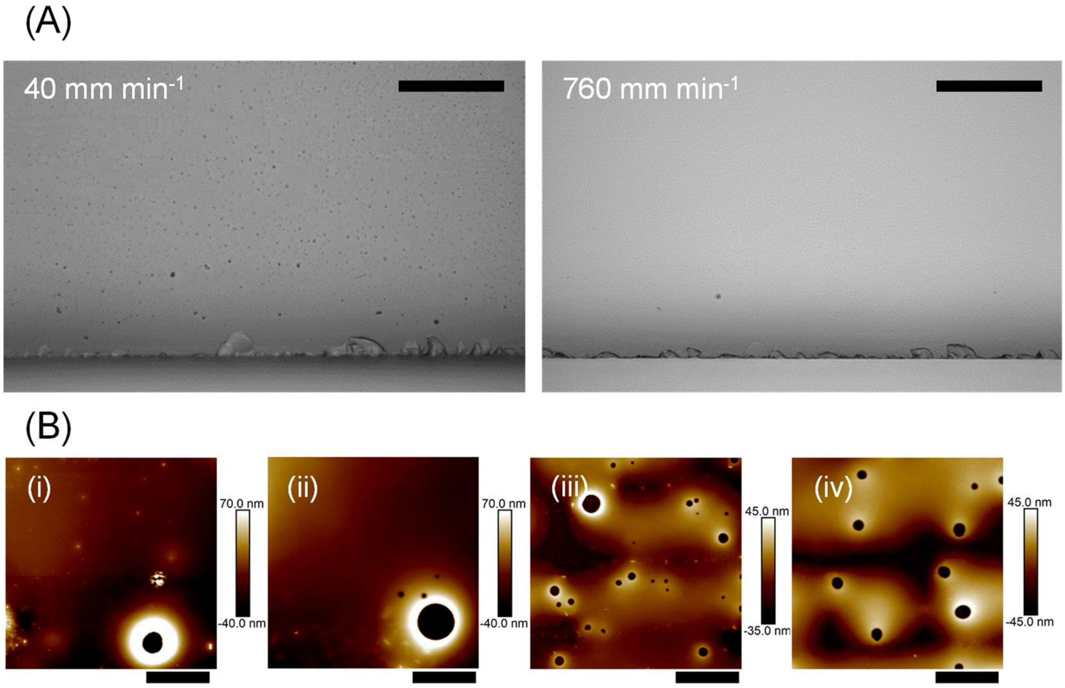

Figure 31. (A) Microscopy images of glass slides dip-coated via slow (40 mm min^{-1}) and fast (760 mm min^{-1}) removal of the glass slide from a hydrolyzed poly(S_{35}-*r*-StyTMS) solution. The slow-removal surface appeared to contain many micropores, whereas the fast-removal surface appeared to be smooth. (B) AFM images of glass slides being removed from a poly(S_{35}-*r*-StyTMS) solution with a speed of (i) 40, (ii) 45, (iii) 125, and (iv) 760 mm min^{-1}, respectively. The heights of the *net*-poly(S_{35}-*r*-StyTMS) features were 26, 24, 45, and 70 nm for (i)-(iv), respectively. Scalebars are 3 µm.

3.1.6.2 Surface topology of *net*-poly(S_{35}-*r*-StyTMS) coatings on silicon, gold, and glass substrates

Spin-coating on glass yielded homogeneous micro- and nano-porous films on silicon, gold, and glass depending on the concentration of the poly(S_{35}-*r*-StyTMS) solution and the number of spin-coating cycles (**Figure 32**). For gold and silicon surfaces, periodical features and pores were observed, whose size decreased with decreasing concentration of poly(S_{35}-*r*-StyTMS). For glass, micro sized pores in the surface were observed to decrease in radius with decreasing concentration of poly(S_{35}-*r*-StyTMS).

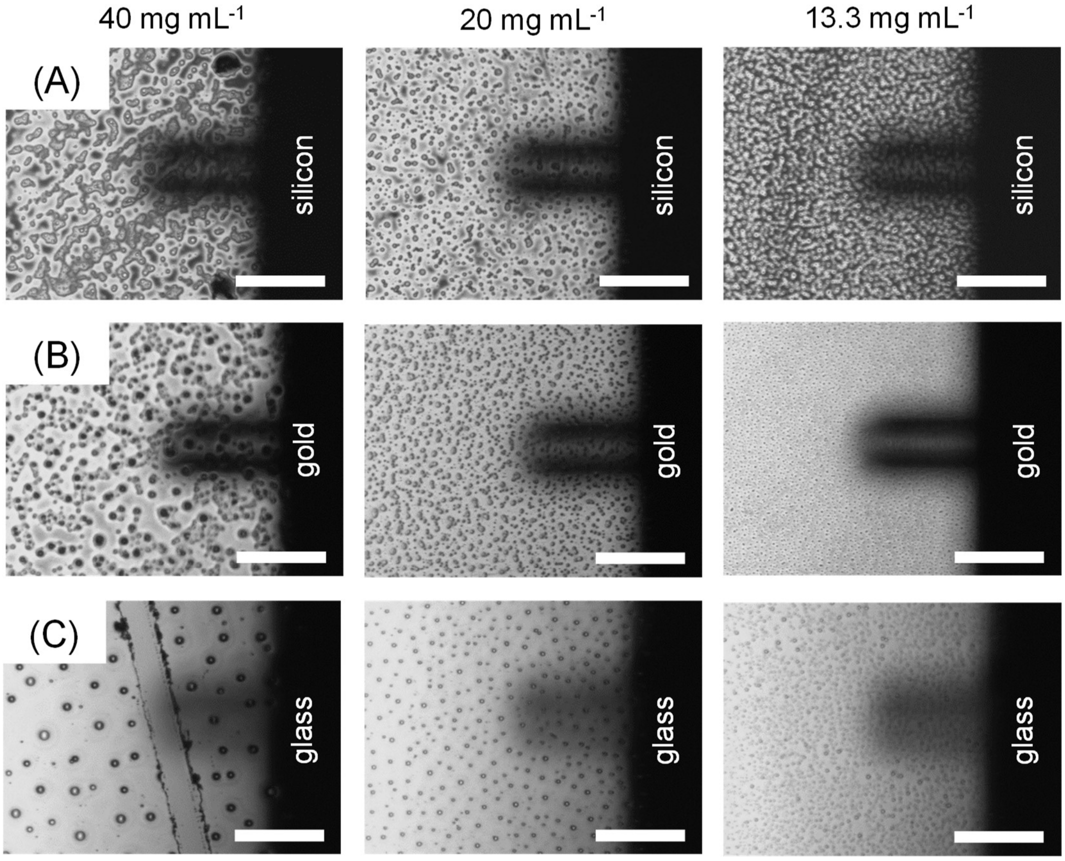

Figure 32. Digital microscope images of surfaces spin-coated with three different concentrations of poly(S_n-*r*-StyTMS), i.e., 40, 20, and 13.3 mg mL^{-1}. The AFM cantilever and tip can be seen on the right side of the pictures. Scalebars are 100 µm.

To investigate the influence of the number of spin-coating cycles and the concentration of the poly(S_{35}-*r*-StyTMS) solution on the surface topology, glass slides were coated for one, two, and three spin-coating cycles and were imaged with AFM (**Figure 33**). A concentration of 40 mg mL^{-1} poly(S_{35}-*r*-StyTMS) in THF led to the formation of micropores, presumably due to poly-condensation induced self-assembly and insolubility as well as THF evaporation. A decrease in the pore size from ca. 6-7 µm to ca. 1-2 µm was observed when the concentration of poly(S_n-*r*-StyTMS) was decreased from 40.0 to 13.3 mg mL^{-1}. For three spin-coating cycles with a poly(S_n-*r*-StyTMS) concentration of 13.3 mg mL^{-1}, the formation of nanopores down to ca. 200 nm was observed. The micropores formed initially after one spin-coating cycle were partially filled up after three spin-coating cycles and the widespread formation of nanopores can be observed well in the amplitude error image.

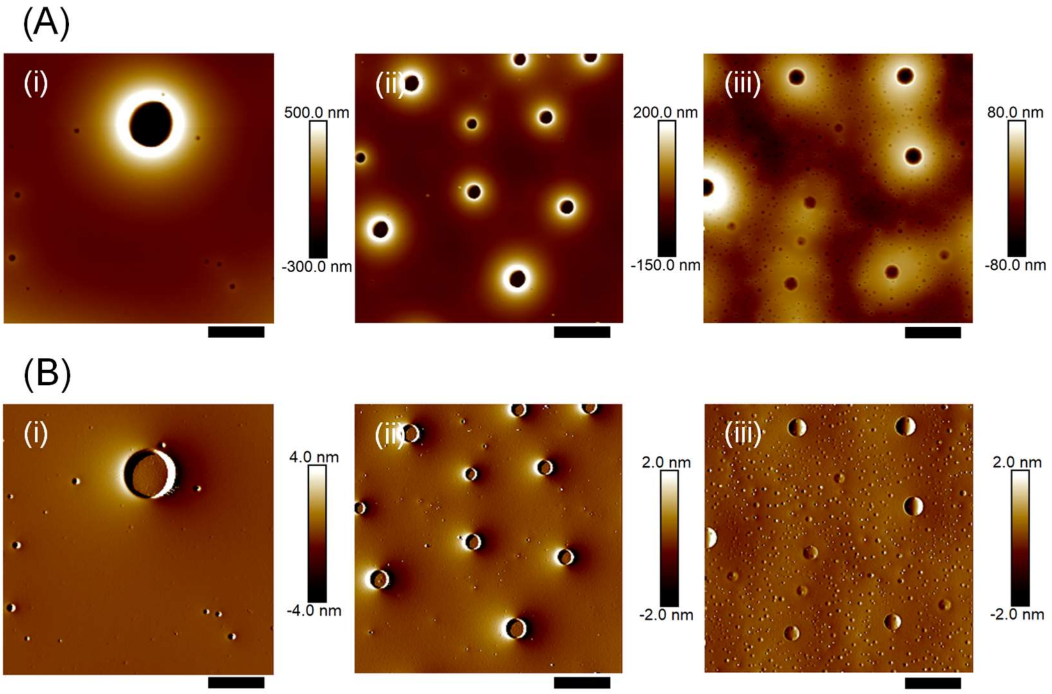

Figure 33. AFM (A) height images and (B) amplitude error images of *net*-poly(S_{35}-*r*-StyTMS) coatings on glass prepared with a concentration of (i) 40 mg mL^{-1} and (ii) 13.3 mg mL^{-1} of hydrolyzed poly(S_n-*r*-StyTMS) for one spin-coating cycle, and (iii) 13.3 mg mL^{-1} of hydrolyzed poly(S_n-*r*-StyTMS) for three spin-coating cycles. Scalebars are 8 µm.

3.1.6.3 Thickness of *net*-poly(S_{35}-*r*-StyTMS) coatings on silicon, gold, and glass

The thickness is a key parameter for surface coatings. To achieve control over the thickness of *net*-poly(S_{35}-*r*-StyTMS) coatings, two strategies were tested: Varying the concentration of hydrolyzed poly(S-*r*-StyTMS) solution and spin-coating with different numbers of spin-coating cycles. The resulting coating thickness was determined with AFM scratch analysis (**Figure 34**). The scratches were first localized with a digital microscope and AFM scans were conducted perpendicular to the direction of the scratches. To calculate the thickness of the *net*-poly(S_{35}-*r*-StyTMS) coating, the difference between the height of the scratch and the coating was determined. By averaging an area of at least 3 × 5 µm in the lower level (scratch) and the upper level (*net*-poly(S_{35}-*r*-StyTMS) coating), respectively, the height difference (thickness) could be obtained. Large artifacts on the surface resulting from the scratches were not excluded from the analysis.

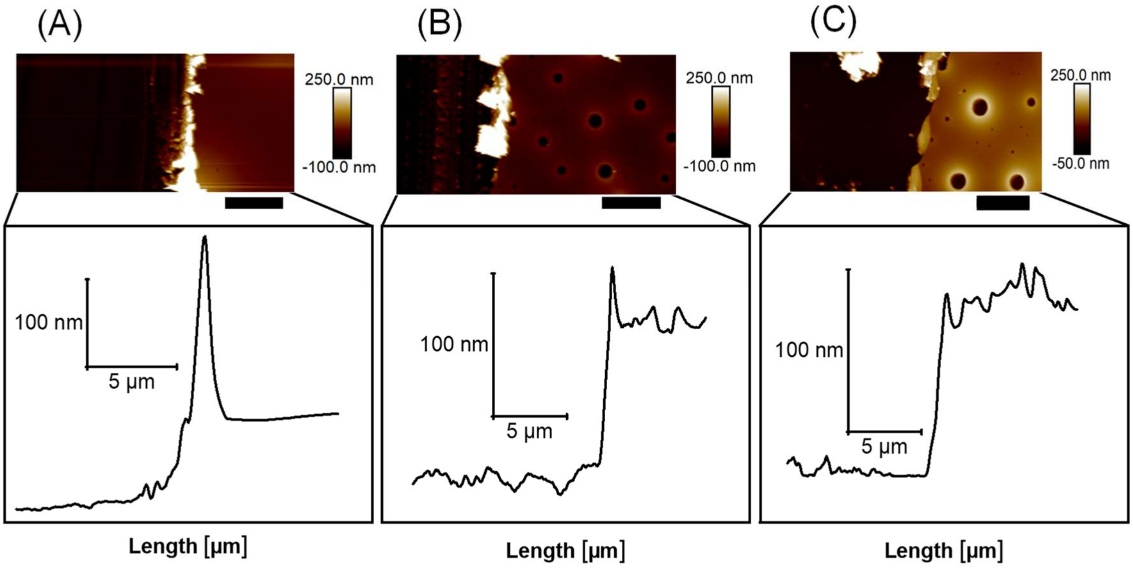

Figure 34. Top row: Examples for AFM scratch analysis for surfaces prepared via spin-coating of 13.3 mg mL-1 hydrolyzed poly(S-*r*-StyTMS) solution on (A) glass, (B) gold, and (C) silicon. Bottom row: Graphs showing the average height along the cross-section. The respective step heights were analyzed with the software NanoScope Analysis. Scalebars are 4 µm.

Both strategies chosen, i.e., increasing the number of spin-coating cycles as well as varying the concentration of the hydrolyzed poly(S-*r*-StyTMS) solution allowed control over the film thickness. For one, two, and three spin-coating cycles the height of *net*-poly(S_{35}-*r*-StyTMS) on glass increased almost linearly from 89 ± 5, to 175 ± 4, to 265 ± 7 nm as determined with AFM (**Figure 35**). For concentrations of 40, 20, and 13.3 mg mL^{-1} of poly(S-*r*-StyTMS), the thicknesses 99 ± 1, 160 ± 6, and 314 ± 5 nm for glass, 108 ± 4, 155 ± 1, and 321 ± 5 nm for gold, and 110 ± 7, 142 ± 10, and 325 ± 8 nm for silicon were obtained, respectively. Thus, *net*-poly(S_{35}-*r*-StyTMS) coatings on all substrates showed the expected decrease of the coating thickness with decreasing concentration, despite not displaying a linear behavior. The thickness of *net*-poly(S_{35}-*r*-StyTMS) coatings is fairly substrate independent, as apparent by the small differences between different substrates for the same concentration of poly(S-*r*-StyTMS), i.e., 99 – 110, 142 – 160 nm, and 314 – 325 nm. Each value represents an average and its standard deviation based on the analysis of three independent scratches. In conclusion, the thickness of the *net*-poly(S_{35}-*r*-StyTMS) coating can be controlled on the nanoscale by the choice of concentration and the number of spin-coating cycles.

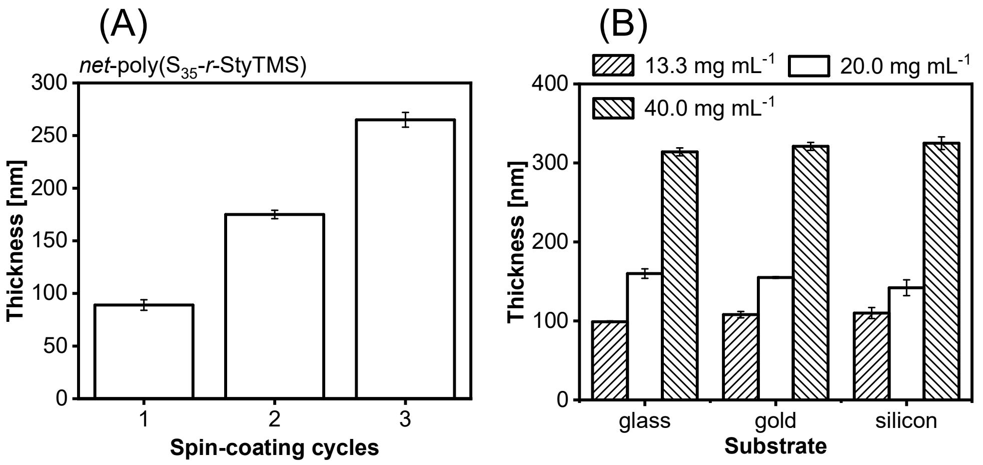

Figure 35. (A) Influence of the number of spin-coating cycles on the film thickness on glass. (B) Influence of the poly(S-*r*-StyTMS) concentration on the film thickness on different substrates via spin-coating (glass, silicon, gold). Error bars are standard deviations (N=3).

3.1.6.4 Thin-film interference of *net*-poly(S_{35}-*r*-StyTMS) coatings on silicon

Polymers prepared via inverse vulcanization naturally have a strong yellow, orange, red, brown, or black color and no other color such as green or blue has been obtained yet. The reason for the yellow-black color of inversely vulcanized polymers is their strong absorption of blue light. Poly(S-*r*-StyTMS) is no exemption from this as apparent from the red color of poly(S-*r*-StyTMS) solutions and solid *net*-poly(S-*r*-StyTMS) films. Solid films of *net*-poly(S-*r*-StyTMS) were obtained as flexible films by solution casting of hydrolyzed poly(S_n-*r*-StyTMS) in a Teflon mold. Upon drying the films at room temperature overnight, they became brittle, which indicated a completion of the crosslinking via polycondensation. The UV-vis spectrum of poly(S-*r*-StyTMS) in THF revealed a very strong UV absorbance, which sharply decreases from 1.46 to 0.04 between 300 – 400 nm and slowly approaches an absorbance of 0 above 500 nm (**Figure 36**). Due to the absorption of violet-blue-cyan light between 380 – 500 nm the solution is perceived as red.

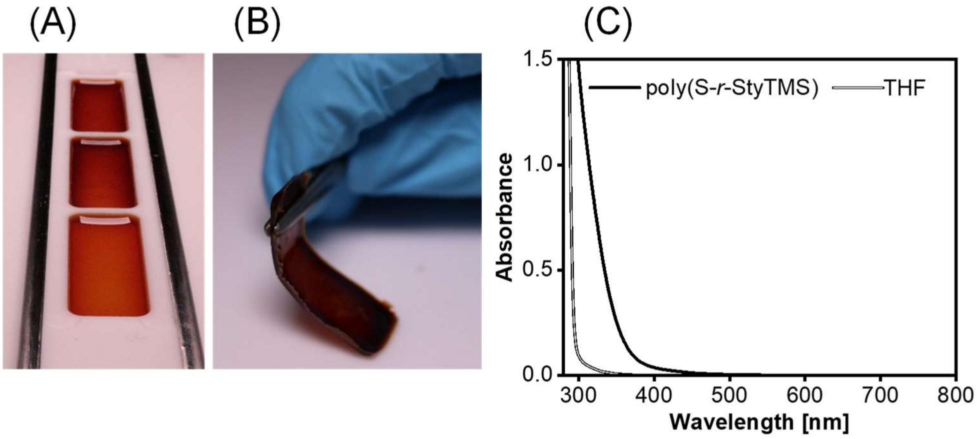

Figure 36. Digital images of (A) a poly(S-*r*-StyTMS) solution in THF in a Teflon mold and (B) a solution casted film of *net*-poly(S-*r*-StyTMS). (C) UV-vis spectrum of poly(S-*r*-StyTMS) in THF. The concentration of poly(S-*r*-StyTMS) was 0.16 µg mL^{-1}.

According to the BEER-LAMBERT law, the light intensity decreases exponentially in an absorbing medium, which is why the absorption color becomes more pronounced with an increasing thickness of the respective solids or liquid. For thin films, however, refraction effects can generate a color impression different from the absorbance color. A simple example for this is a drop of oil spread on the surface of water, which appears in the colors of a rainbow upon despite being a colorless liquid in bulk, i.e., despite not absorbing visible light.

To investigate whether the same effect can be observed for an inverse vulcanized polymer, a series of silicon wafers coated with different thicknesses were prepared by spin-coating using different concentrations of hydrolyzed poly(S_n-*r*-StyTMS). To improve the homogeneity of the coatings relative to the samples investigated with AFM, the rotation speed during spin-coating was increased to 6000 rpm. The difference in the thickness of *net*-poly(S_{35}-*r*-StyTMS) coatings was apparent with bare eyes because of the thin-film interference effect on the reflective silicon surfaces (**Figure 37 A**). By varying the coating thickness on the nanoscale, different interference colors such as yellow, yellow-green, orange, amber, red, purple, pink, light blue, and dark blue could be obtained. The surfaces were compared with a calculated thin film interference pattern for validation (**Figure 37 B**). The close match between calculated and obtained interference colors proved that the color of *net*-poly(S_{35}-*r*-StyTMS) surfaces could be accurately predicted and predetermined. Hence, the disadvantageous intrinsic coloration of polysulfides can be overcome by exploiting thin film interference, which could be of interest for applications in optical coatings (e.g., effect lacquers).

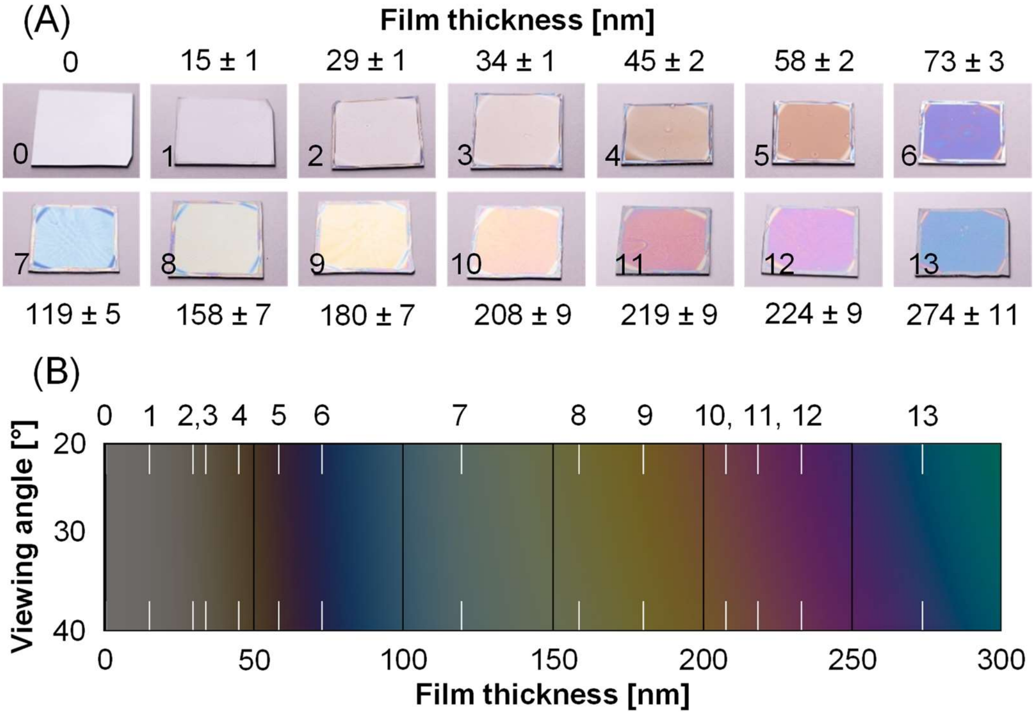

Figure 37. (A) Digital images of silicon wafers (0 – 13) spin-coated with *net*-poly(S_{35}-*r*-StyTMS) taken at a viewing angle of ca. 30 ° relative to the surface normal. (B) Calculated thin film interference colors in dependence of the film thickness and the viewing angle. Parameters required for the calculation were based on the Cauchy model with absorbance corrections. The thicknesses of the *net*-poly(S_{35}-*r*-StyTMS) coatings are indicated by the sample numbers (0 – 13) and are marked as white stripes.

The optical parameters necessary to calculate the thin film interference pattern of *net*-poly(S_{35}-*r*-StyTMS), i.e., the wavelength dependent refractive index and extinction coefficient, as well as the thickness of *net*-poly(S_{35}-*r*-StyTMS) coatings were obtained by ellipsometry (**Figure 38**). A stepwise decrease of the relative concentration of poly(S-*r*-StyTMS) from 100 % (40 mg mL^{-1}) to 8.3 % (3.3 mg mL^{-1}) led to a linear decrease of the coating thickness from 274 ± 11 to 15 ± 1nm with a slope of 2.57 ± 0.07 nm $\%^{-1}$. The refractive index n(λ) was measured from 300 – 1000 nm and fitted with a Cauchy fit to obtain $n = 1.591 + 0.01935\ nm^{-2}$. From the measurement of the complex refractive index the extinction coefficient was obtained via the KRAMERS-KRONIG relation. The sharp decline of the extinction coefficient between 300 – 400 nm is like the decline of the light absorbance of poly(S-*r*-StyTMS) in the same area as determined via UV-vis spectroscopy.

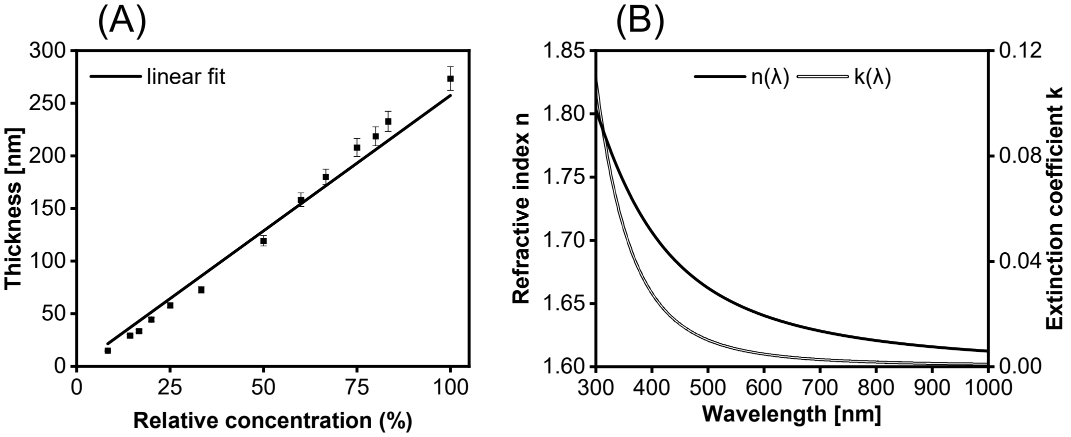

Figure 38. (A) Thickness of *net*-poly(S_{35}-*r*-StyTMS) coatings in dependence of the relative concentration of poly(S_n-*r*-StyTMS), with 40 mg mL^{-1} in THF corresponding to 100 %. Error bars represent the 90% confidence value. Linear fit: $y = 2.57x \pm 0.07$, $R^2 = 0.992$. (B) Refractive index n and the extinction coefficient k in dependence of the wavelength. Cauchy fit: $n = 1.591 + 0.01935\ nm^{-2}$ and $k = 0.02425 + 0.1552\ nm^{-2}$.

3.1.6.5 Chemical analysis of *net*-poly(S_{35}-*r*-StyTMS) coatings with EDX, XPS, ATR FT-IR, ToF-SIMS, and ^{29}Si NMR

To provide evidence for the presence of a polysiloxane coating containing a high content of covalently bound sulfur, different analysis methods were employed. The *net*-poly(S_{35}-*r*-StyTMS) coated surfaces were analyzed with energy dispersive x-ray spectroscopy (EDX), x-ray photoelectron spectroscopy (XPS) and time-of-flight secondary ion mass spectrometry (ToF-SIMS). All three methods conclusively and independently proved the presence of sulfur in the coating. Prior to the measurements, surfaces were washed with excess CS_2 and THF to remove traces of elemental sulfur. EDX confirmed the presence of the expected elements sulfur and silicon in the *net*-poly(S_{35}-*r*-StyTMS) coating, while XPS revealed the presence of various sulfur-carbon binding states (**Figure 39**). Elemental sulfur powder was used as a reference for XPS. The obtained peak maximum energy of 164.1 eV was referenced to the literature value of 163.9 eV and the same shift (- 0.2 eV) was applied to the obtained XPS spectra of the *net*-poly(S_{35}-*r*-StyTMS) coated sample. In the spectrum of elemental sulfur, the 2p-electron energy levels were distinctly split up into a characteristic doublet due to spin-orbit coupling. For the *net*-poly(S_{35}-*r*-StyTMS) coated sample, a broadened energy distribution was observed, which was attributed to the presence of sulfur in many different but similar binding states, i.e., C-S_n-C with $n = \mathbb{N} > 0$. An energy distribution shift to higher binding energies from 163.9 eV (sulfur) to 164.6 eV *net*-poly(S_{35}-*r*-StyTMS) was observed, which indicated the presence of C-S bonds. Attempts to gain an improved understanding of the S-S species with Raman spectroscopy failed due to sample fluorescence (**Appendix 1**).

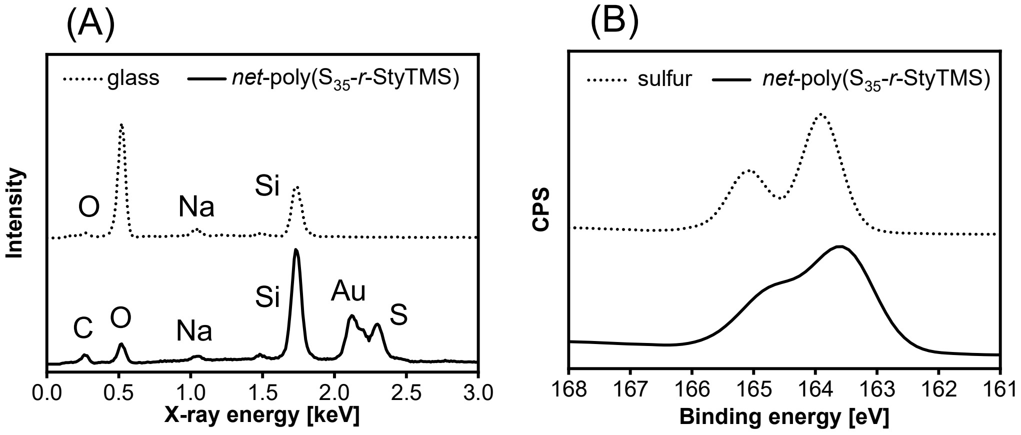

Figure 39. (A) EDX spectra of glass and glass coated with *net*-poly(S_{35}-*r*-StyTMS). (B) XPS spectra of elemental sulfur and glass coated with *net*-poly(S_{35}-*r*-StyTMS).

ATR FT-IR could confirm the presence of the organic and siloxane moieties (**Figure 40 A**). To ensure that the spectrum of *net*-poly(S_{35}-*r*-StyTMS) was not disturbed by the very intense siloxane bands of glass or silicon substrates, powdered *net*-poly(S_{35}-*r*-StyTMS) was used. In the spectrum *net*-poly(S_{35}-*r*-StyTMS), characteristic vibrations C-H stretching vibrations for both aromatic (3055, 3018 cm^{-1}) and aliphatic (2957, 2925, and 2867 cm^{-1}) C-H bonds were found. The siloxane band (Si-O-Si) was at 1031 cm^{-1}. A broad band between 3500 – 3050 cm^{-1} and a band at 1180 cm^{-1} revealed the presence of residual silanol (SiOH) and methoxysilane ($SiOCH_3$) groups.

ToF-SIMS (time-of-flight secondary ion mass spectrometry) was employed to confirm the presence of polysulfide chains on the surface (**Figure 40 B**). The distribution of sulfur associated ions (i.e., S_n^-) was homogeneous within the examined surface area for all examined ions (S_n^- for n = 1 – 8). ToF-SIMS experiments with elemental sulfur powder were conducted under the same ionization conditions to gain insight into the fragmentation patterns of sulfur-sulfur bonds. For elemental sulfur, fragments up to S_8^- were detected, while for the *net*-poly(S_{35}-*r*-StyTMS) no polysulfide fragment heavier than S_4^- could be traced. The most dominant fragment was S_3^- for both elemental sulfur and the *net*-poly(S_{35}-*r*-StyTMS) surfaces. Thus, it could be concluded that the fragmentation pattern is not representative for the abundance of a sulfur species. The obtained mass distribution in the *net*-poly(S_{35}-*r*-StyTMS) coating indicated that the sulfur chains were shorter than S_8 and presumably between S_1-S_5. Due to the high C-S bond energy of ca. 370 kJ mol^{-1} it is reasoned that the central S-S bonds or α-C-S bonds break faster upon ion bombardment, since the S-S bond energy in disulfides and *cyclo*-octasulfur is ca. 270 kJ mol^{-1} and 174 kJ mol^{-1}, respectively).[198,199] Such an effect would cause a decrease in the observable length of the polysulfide fragments. The S^{3-} ions were generated homogeneously throughout the examined surface area, indicating a chemically homogeneous coating (**Figure 40 C**).

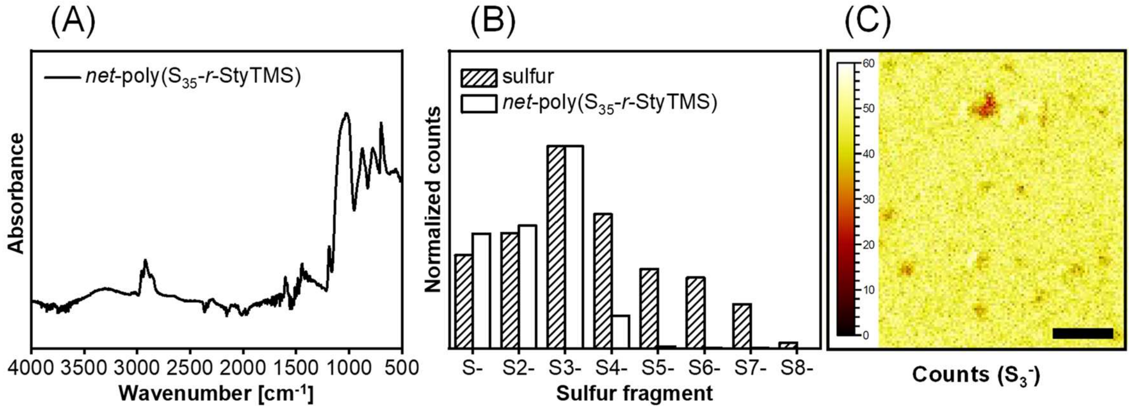

Figure 40. (A) FTIR IR spectrum of *net*-poly(S_{35}-*r*-StyTMS) coated on a gold surface. (B) Relative distribution of polysulfide fragments (S_n^-) for *net*-poly(S_{35}-*r*-StyTMS) coating as determined with ToF-SIMS. Elemental sulfur was used as a reference. (C) Map of S_3^- ion counts as detected with ToF-SIMS. A surface area of 500 × 500 µm (0.025 mm²) was examined. Scalebar is 100 µm.

To investigate the binding states of silicon after the inverse vulcanization and polycondensation, ^{29}Si NMR was conducted in solution and solid state (**Figure 41 A-B**). In the ^{29}Si NMR spectrum of StyTMS eight different silicon species were found, which correspond to the four constitutional isomers of StyTMS (-42.5, -42.8, -49.4, and -49.5 ppm) and the EPTMS impurity (-42.6, -42.6 -49.0, and -49.2 ppm), respectively. Upon reaction with sulfur, peaks associated to StyTMS broadened strongly due to polymerization, whereas the peaks associated to EPTMS isomers remained unchanged. ^{29}Si cross polarization (CP) magic-angle spinning (MAS) NMR spectra of the solid, powdered *net*-poly(S_{35}-*r*-StyTMS) revealed peaks at -49.5, -58.2, and -68.0 ppm, indicating the silicon atoms to be in T_1, T_2, and T_3 binding states, respectively. Line fit integration of both CP and high power decoupled (HPDEC) MAS NMR peaks resulted in an average of 1.8 Si-O-Si bonds per silicon center, which deviates from a fully crosslinked T siloxane (3.0 Si-O-Si bonds per silicon center) and is closer to a linear polysiloxane (2.0 Si-O-Si bonds per silicon center). Most silicon atoms were found to be in a T_2 ($(SiR_1(OR_2)O)_n$) binding state (R_1 = Ar, $Ar(S_n)_2$, ArS_n, R_2 = -OH, -OMe, or -OSi) according to the integral ratios 4.5 (T_1), 10.6 (T_2), and 1.0 (T_3), respectively. Since only solids were obtained after polycondensation, it can be concluded that the contribution of sulfur crosslinking to the network structure is essential. An unknown Q species between -100-(-)120 ppm was attributed to the rotor, since it was also present in a control NMR experiment without sample (**Figure 41 C**).

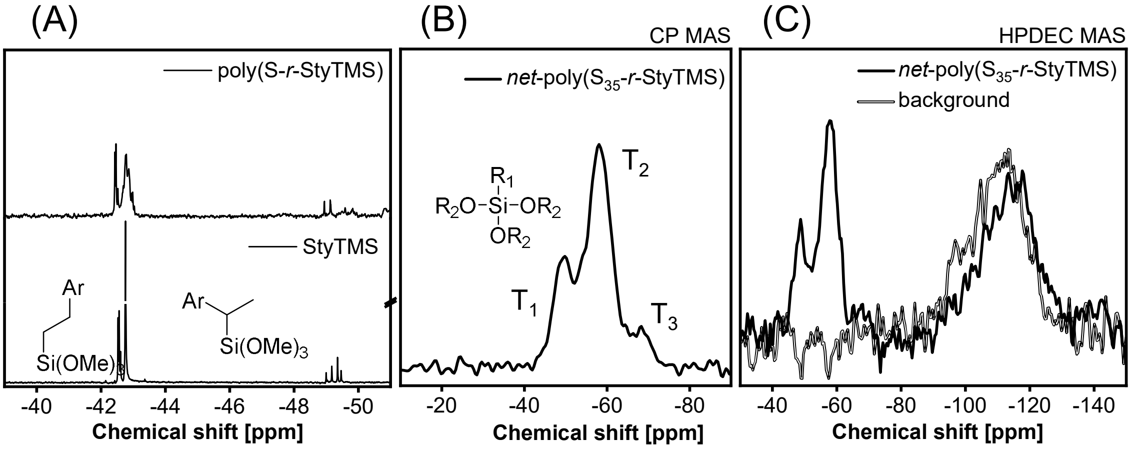

Figure 41. (A) ^{29}Si NMR spectra of StyTMS (bottom) and poly(S-*r*-StyTMS) (top) in $CDCl_3$. Ar denotes a styryl or ethylphenyl substituent, respectively. (B) ^{29}Si NMR CP-MAS spectrum of powdered *net*-poly(S_{35}-*r*-StyTMS) showing Si in T_1, T_2, and T_3 siloxane binding states. (C) ^{29}Si HPDEC-MAS NMR spectrum of powdered *net*-poly(S_{35}-*r*-StyTMS) showing Si in T_1, T_2, and T_3 siloxane binding states after the polycondensation and a background spectrum (rotor).

3.1.6.6 Filters and particles coated with *net*-poly(S_{35}-*r*-StyTMS)

With the developed method, *net*-poly(S_{35}-*r*-StyTMS) could be conveniently and homogeneously coated onto various commonly used filter materials, such as cellulose, silica particles or glass fibers (**Figure 42**). The successful modification of the pristine filter materials was apparent from their change in color from white to red as well as an increase in their surface hydrophobicity. Washing the *net*-poly(S_{35}-*r*-StyTMS) coated filter materials with excess THF and CS_2 afforded colorless washings. The insolubility of *net*-poly(S_{35}-*r*-StyTMS) in organic solvent such as THF, hexanes, toluene, and CS_2 is an inherent advantage of *net*-poly(S_{35}-*r*-StyTMS) over previously reported inverse vulcanized polymer filters since the coating does not wash off when organic solvents are present. This can be important for practical applications such as mercury removal from petroleum.[200]

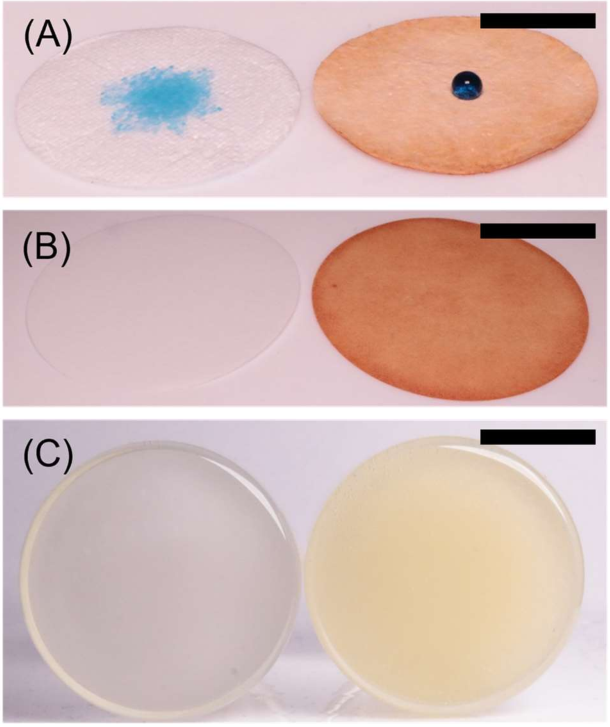

Figure 42. Digital images of a (A) glass fiber filter, a (B) cellulose filter, and (C) silica gel before (left) and after (right) coating with *net*-poly(S_{35}-*r*-StyTMS). The hydrophobicity of the filter surfaces were increased after coating with *net*-poly(S_{35}-*r*-StyTMS) as seen from the formation of a water droplet (dyed blue) blue dye) instead of spreading of the droplet. Scalebars are 1, 3, and 1 cm, respectively.

The surface of a cellulose filter was imaged with secondary electron microscopy (SEM) before and after being coated with *net*-poly(S_{35}-*r*-StyTMS) to investigate whether the *net*-poly(S_{35}-*r*-StyTMS) coating influences the microstructure of the substrate, Due to the low thickness of the coating, the fibrous micro-structure of the cellulose filters remained unchanged, whereas the presence of the *net*-poly(S_{35}-*r*-StyTMS) could be concluded from the presence of the elements silicon and sulfur as detected by EDX (**Figure 43**). To prove the successful surface modification of silica particles beyond the apparent color change from white to pale yellow, dynamic light scattering (DLS) was used. Silica nanoparticles were used as a model system to mimic silica microparticles, which are too big to be measured with DLS. The successful modification of the silica particle surfaces could be confirmed by the increase of the particle radius determined in a THF dispersion. After immersing silica nanoparticles in hydrolyzed poly(S_n-*r*-StyTMS) for 2 h at rt, their radius increased by 30 nm from 270 to 300 nm. Another coating process involving silica was published by the group of HASELL, who coated silica particles with a soluble limonene-based polysulfide.[34] The limonene-based polysulfide, however, remains soluble as a coating and is thus presumably more prone to dissolution and leaching. Very recently, in October 2021, a strategy based on the sequential inverse vulcanization of dicyclopentadiene for a soluble, but curable, inverse vulcanized polymer has been reported. Since the work described in this chapter has been published more than one year prior to that, it is likely to have stimulated research on inverse vulcanized coatings for mercury remediation.[201]

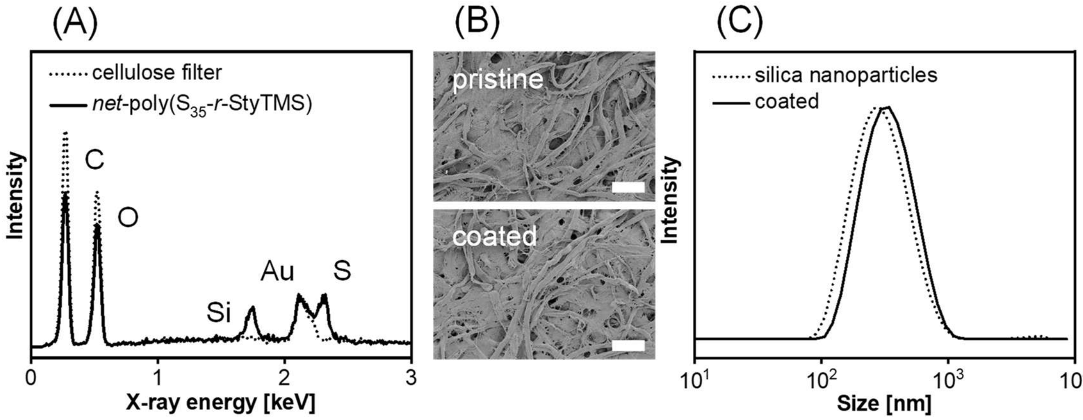

Figure 43. (A) EDX spectrum of a pristine and a cellulose filter coated with *net*-poly(S_{35}-*r*-StyTMS). (B) SEM images of a cellulose filter before and after coating with *net*-poly(S_{35}-*r*-StyTMS). Scalebars are 100 µm. (C) DLS measurements of SiO_2 nanoparticles before (270 nm) and after functionalization (300 nm) with *net*-poly(S_{35}-*r*-StyTMS). Each curve represents the average of three measurements.

3.1.6.7 Hg(II) uptake of *net*-poly(S_{35}-*r*-StyTMS) coated silica

To demonstrate the enhanced utility of filter materials coated with a high sulfur content polymer, silica microparticles were functionalized with *net*-poly(S_{35}-*r*-StyTMS) and their change in mercury remediation properties was tested. The mercury uptake was tested by stirring 200 mg of *net*-poly(S_{35}-*r*-StyTMS) coated silica microparticles in 10 mL of aqueous $HgCl_2$ solution (15 mg L^{-1}) for one hour. The solution was filtered and the Hg^{2+} concentration of the filtrate was determined by hydride generation atom absorption spectroscopy (hydride-AAS) according to a method reported previously.[202] As a control, pristine silica microparticles were used (**Figure 44**). The concentration of Hg^{2+} decreased by 97% from 11.79 mg L^{-1} to mg 0.41 mg L^{-1} after remediation with *net*-poly(S_{35}-*r*-StyTMS) coated silica microparticles, whereas the silica control could remove 74% to a concentration of 3.02 mg L^{-1}. The performance of particles coated with poly(S-*r*-StyTMS) compared well to other materials prepared via inverse vulcanization reported previously.[121,203] Due to the polar siloxane and silanol groups, pristine silica microparticles can remediate Hg^{2+}, too.[121,204] The difference between pristine silica microparticles and *net*-poly(S_{35}-*r*-StyTMS) coated silica microparticles became more pronounced for higher initial concentrations of Hg^{2+}, which is in accordance with the observations of the group of HASELL (Figure 4A). While *net*-poly(S_{35}-*r*-StyTMS) coated microparticles were able to remediate > 97 % of Hg^{2+} cations throughout the tested Hg^{2+} concentration range, the remediation capability of pristine silica microparticles sharply decreased for an initial concentration of 100 mg L^{-1} $HgCl_2$ (52 %). It should be noted that the content *net*-poly(S_{35}-*r*-StyTMS) as the functional compound attributed to less than 8 wt% of the coated particles weight, highlighting the value and efficiency of defined surface chemistries.

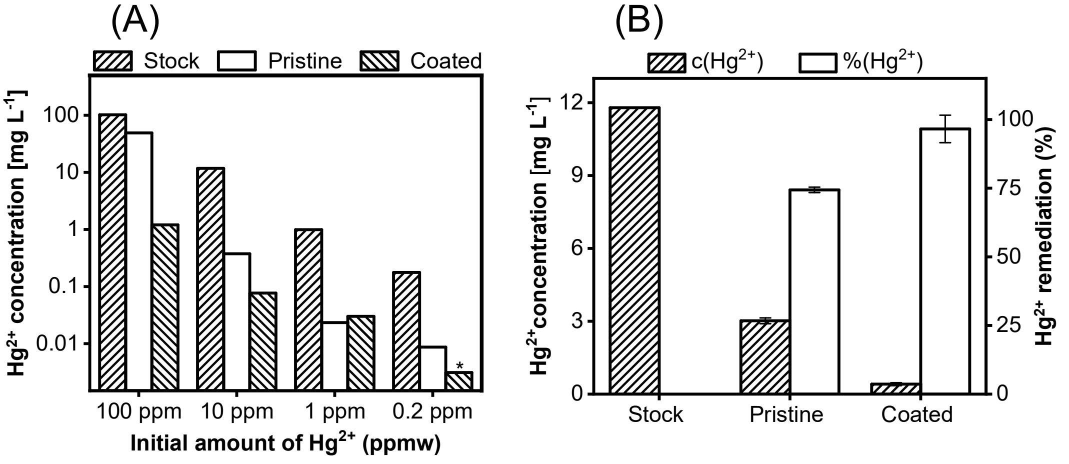

Figure 44. Mercury remediation experiments evaluated with hydride-AAS for different initial concentrations of Hg^{2+}. Stock refers to the Hg^{2+} stock solution, pristine refers to silica microparticles, and coated refers to silica microparticles coated with *net*-poly(S_{35}-*r*-StyTMS). (A) Mercury remediation experiments using different initial Hg^{2+} concentrations. (B) Mercury remediation experiments for an initial Hg^{2+} concentration of ca. 10 ppmw. Values are given as the average of three measurements with the error bars being the standard deviation.

3.1.7 Summary

The inverse vulcanization reaction of styrylethyltrimethoxysilane (StyTMS) with sulfur was described. The obtained poly(S_n-*r*-StyTMS) could undergo hydrolysis and polycondensation, which could be used to coat surfaces and particles. The sulfur content in *net*-poly(S_n-*r*-StyTMS) could reach 35 wt%, which is a remarkable amount for a solution processable and room-temperature curable coating material. After curing, coatings and crosslinked materials were insoluble in organic solvents such as THF or CS_2, extending the range of potential applications of polymers from inverse vulcanization. The thickness of spin-coated films could be controlled on the nanoscale. Due to the thin-film interference effect, the coatings could appear in colors such as light blue, dark blue, and purple, which is different from the typical red color of inverse vulcanized materials. Silica particles coated with *net*-poly(S_n-*r*-StyTMS) improved their Hg^{2+} adsorption performance from 74 % to 97 % for an initial concentration of 11.8 mg L^{-1} $HgCl_2$.

3.2 Inverse Vulcanization of Norbornenylsilanes

3.2.1 Disclaimer

The content of this chapter is the basis for a manuscript that has been accepted for publication in Angewandte Chemie International Edition from Wiley-VCH GmbH (Weinheim, Germany). The list of authors is as follows: Johannes M. Scheiger, Maxi Hoffmann, Patricia Falkenstein, Zhenwu Wang, Mark Rutschmann, Valentin W. Scheiger, Alexander Grimm, Klara Urbschat, Tobias Sengpiel, Jörg Matysik, Manfred Wilhelm, Pavel A. Levkin, and Patrick Theato. Johannes M. Scheiger is the first author of the manuscript.

The author contributions were as follows: J. M. S. proposed the original idea, performed the experiments, curated, and analyzed the data, and wrote the paper (lead). M. H. acquired rheometry data (lead). P. F. acquired ^{29}Si NMR data (lead). Z. W. acquired data for mechanical analysis (lead), M. R. acquired PXRD data (lead). V. W. S. wrote the script to model the chain growth mechanism (lead). A. G., K. U., and T.S. helped with experiments and analysis of the data (supporting). J. M., M. W., P. A. L., and P. T. acquired funding and corrected the manuscript (lead).

3.2.2 Nomenclature

3.2.2.1 Monomers

The complex names of alkoxysilanes, chlorosilanes, and siloxanes were not used in full to improve the readability of the text. The IUPAC names of the respective chemicals were simplified, and acronyms were formed. The simplified names were derived from the number (i.e., mono, di, and tri) and type of hydrolysable substituents (i.e., chloro- or ethoxy) of the silicon atom. Methyl substituents were excluded from the simplified names, except when three methyl substituents and no hydrolysable substituents were bound to the silicon atom. In case three methyl substituents were bound to the silicon atom, "trimethyl" was used as a prefix. The bicyclo[2.2.1]hept-5-enyl substituent was referred to as "norbornenyl" (**Table 4**).

Table 4. Nomenclature of ethoxy- and chlorosilanes used in this thesis.

IUPAC name	Simplified name	Acronym
Bicyclo[2.2.1]hept-5-en-2-yltrimethylsilane	Trimethylnorbornenylsilane	TMNBS
Bicyclo[2.2.1]hept-5-en-2-yl(ethoxy)dimethylsilane	Monoethoxynorbornenylsilane	MENBS
Bicyclo[2.2.1]hept-5-en-2-yldiethoxy(methyl)silane	Diethoxynorbornenylsilane	DENBS
Bicyclo[2.2.1]hept-5-en-2-yldichloro(methyl)silane	Dichloronorbornenylsilane	DCNBS
Bicyclo[2.2.1]hept-5-en-2-yltriethoxysilane	Triethoxynorbornenylsilane	TENBS
Bicyclo[2.2.1]hept-5-en-2-yltrichlorosilane	Trichloronorbornenylsilane	TCNBS

3.2.2.2 Polymers

The products of the inverse vulcanization were termed poly(S-*r*-NBS_x) in accordance with previous reports on the inverse vulcanization. NBS represents a norbornenylsilane, i.e., TMNBS, MENBS, DENBS, DCNBS, TENBS, or TCNBS. NBS_x represents a binary mixture of a hydrolysable norbornenylsilane, i.e., MENBS, DENBS, DCNBS, TENBS, and TCNBS with TMNBS in which the index *x* denotes the mass fraction of the respective hydrolysable silane in the binary mixture. The sulfur content of polymers in this thesis was kept at 50 wt% unless stated differently. For example, poly(S-*r*-$MENBS_{30}$) refers to a polymer prepared via inverse vulcanization of 50 wt% sulfur and 50 wt% of a NBS mixture composed of 30 wt% MENBS and 70 wt% TMNBS. During the polycondensation of poly(S-*r*-NBS_x), siloxane bonds between poly(S-*r*-NBS_x) molecules form. The partial crosslinking of poly(S-*r*-NBS_x) with siloxane bonds results in branching. The products of the polycondensation of poly(S-*r*-NBS_x) are thus termed *branch*-poly(S-*r*-NBS_x). Insoluble or partially soluble products of *branch*-poly(S-*r*-NBS_x) are referred to as *net*-poly(S-*r*-NBS_x) analogue to the previous work on insoluble *net*-poly(S-*r*-StyTMS) polymers (**Table 5**).

Table 5. Nomenclature and composition of *branch*-poly(S_y-*r*-NBS_x) polymers discussed in this chapter.

Name	S (wt%)[a]	NBS_x total (wt%)	NBS_x relative (wt%)	Soluble
branch-poly(S_y-*r*-NBS_x)	y	100-y	x:100-x NBS:TMNBS	-
poly(S-*r*-$TMNBS_{100}$)	50	50	100 TMNBS	Yes
branch-poly(S-*r*-$MENBS_{10}$)	50	50	10:90 MENBS:TMNBS	Yes
branch-poly(S_{30}-*r*-$DENBS_{20}$)	30	70	20:80 DENBS:TMNBS	Yes
net-poly(S-*r*-$TENBS_{30}$)	50	50	30:70 TENBS:TMNBS	No

[a] If no index for the sulfur content is given, the sulfur content is 50 wt%.

3.2.3 Introduction

Control over fundamental properties such of inverse vulcanized polymers, such as the molar mass or the solubility of polymers, is not well established and existing strategies lack predictability, scalability, or variability. Systematic design principles are thus sought to allow a targeted design of materials. The inverse vulcanization, hydrolysis and polycondensation of styrylethyltrimethoxysilane (StyTMS) yielded room-temperature curable high sulfur content coatings. Polycondensation of trialkoxysilanes naturally results in cross-linked, insoluble siloxane networks, and is thus not a suitable strategy to prepare soluble bulk polymers. However, it was hypothesized that the inverse vulcanization of sulfur with hydrolysable silanes can be exploited to control the molecular properties of the polymer when the average number of hydrolysable groups per silane is low enough to circumvent crosslinking and insolubility. A low number of hydrolysable groups should lead to fewer siloxane binding between polymer chains and enable the formation of soluble, branched polymers.

This chapter deals with the inverse vulcanization of norbornenylsilanes (NBS), which differ in the number of their hydrolysable functional groups. Norbornenylsilanes (NBS) carry C=C double bonds which are known to react with sulfur at elevated temperatures.[110] The chosen NBS contain a norbornenyl substituent and a different number of hydrolysable chloro- or ethoxy substituents, allowing them to form M, D, or T siloxane bonds upon polycondensation. Control over the properties of high sulfur content polymers is achieved by mixing different NBS before reacting them with sulfur. The sulfur content can be kept constant, while altering the polymers properties significantly. Importantly, NBS can be produced from commodity chemicals that are available on an industrial scale (vinyltrialkoxysilanes and cyclopentadiene, or norbornadiene and $HSiCl_3$), rendering the strategy proposed herein is scalable. Inverse vulcanization of mixtures of NBS followed by polycondensation yielded soluble high sulfur content polymers (50 wt% S) with controllable weight average molar mass (M_W), glass transition temperature (T_G), or zero-shear viscosity (η_0). Polycondensation was conducted in melt using HCl, abolishing the need for a solvent. Purification by precipitation afforded polymers (40 wt% S) free from low molar mass species.

3.2.4 Synthesis of TMNBS

Inverse vulcanization reactions consisting of sulfur as monomer, the non-hydrolysable trimethylnorbornenylsilane (TMNBS) as a comonomer, and a hydrolysable norbornenylsilane (NBS) as a termonomer were conducted. Since trimethylnorbornenylsilane (TMNBS) is not commercially available, it was synthesized from the reaction of MENBS with MeLi (**Figure 45**).

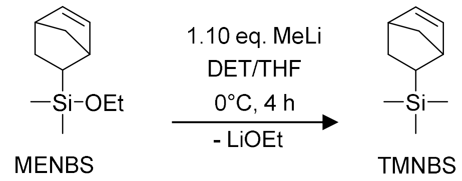

Figure 45. (A) Reaction equation for the synthesis of TMNBS.

TMNBS was characterized with ATR FT-IR spectroscopy, and ^{1}H, ^{13}C, and ^{29}Si NMR spectroscopy (**Figure 46**). The ^{1}H NMR and ^{13}C NMR spectra of MENBS and TMNBS are complex due to the presence of both *exo*- and *endo*-isomers. However, the successful substitution of the ethoxy group of MENBS with a methyl group to yield TMNBS can be easily seen from the disappearance of the multiplet at 3.65 assigned to the ethoxy groups of *exo*- and *endo*-MENBS (Si-OC**H**$_2$-CH$_3$). The methyl groups in TMNBS are identical as evidenced by two large singlets with ^{29}Si satellite peaks in the spectrum of TMNBS at 0.00 and -0.09 ppm. Five $SiCH_3$ peaks were found in the spectrum of MENBS at 0.11 (doublet), 0.07 (singlet), 0.04 (singlet), 0.00 (singlet) and -0.09 ppm (singlet), respectively, which is presumably caused by a rotational barrier arising from the norbornenyl bridgehead and the ethoxy group. From the integral ratios of the two $SiCH_3$ peaks in the spectrum of TMNBS, the ratio of *exo*- and *endo*-TMNBS could be calculated as 45 to 55 %, respectively. Importantly, the alkene hydrogen atoms found in the spectrum of MENBS at 6.15 and 5.95 ppm were retained in the spectrum of TMNBS but experienced a slightly different chemical shift of 6.15 and 5.94 ppm, respectively. Similar observations were made in the ^{13}C NMR spectra of MENBS and TMNBS, such as the disappearance of the ethoxy peak at 58.4 ppm, the retention of norbornene alkene peaks around 135 ppm, and a reduction from four $SiCH_3$ peaks in MENBS to two $SiCH_3$ peaks in TMNBS. The ^{29}Si NMR spectra of MENBS and TMNBS showed the expected upfield shift of two peaks from 17.8 and 17.1 ppm to 3.2 and 2.7 ppm, which correspond to the *exo*- and *endo*-isomers of MENBS and TMNBS, respectively. ATR FT-IR could confirm the quantitative removal of ethoxy groups as apparent from the disappearance of characteristic $SiOCH_2CH_3$ vibrations at 1165, 1107, 1078, and 945 cm^{-1}. Full spectra can be found in **Appendix 3** and **Appendix 6**.

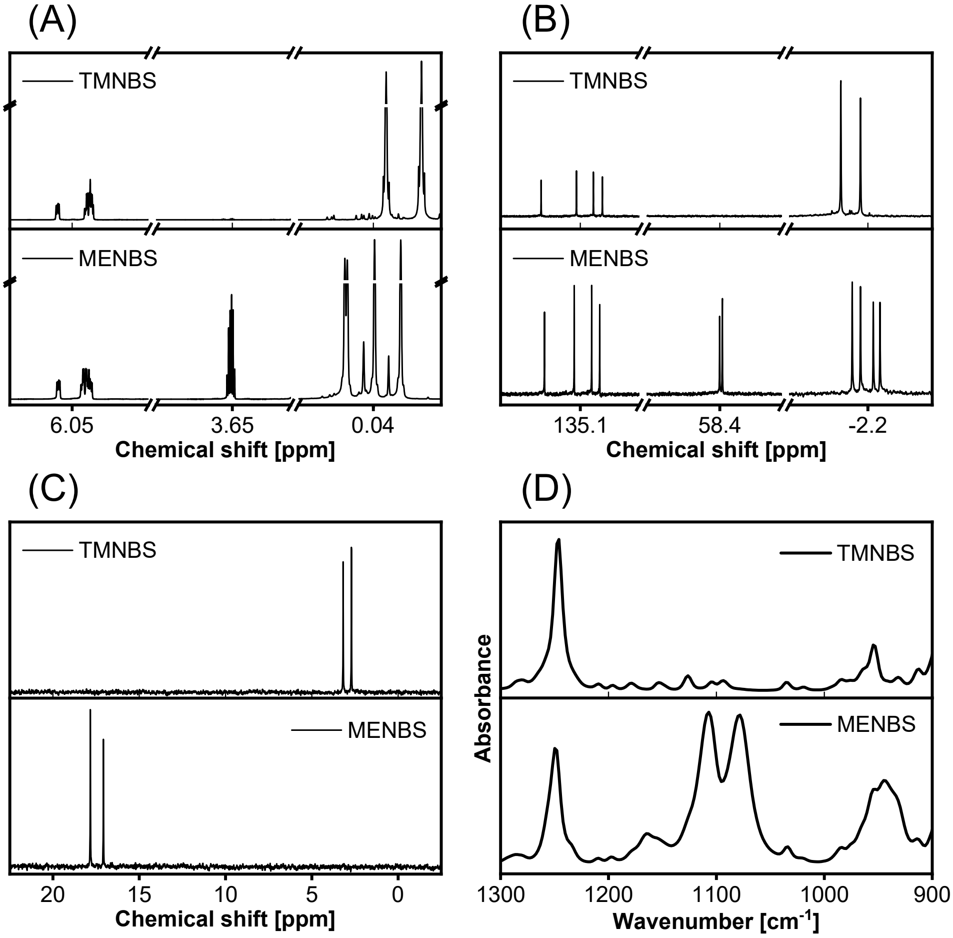

Figure 46. Insets in the (A) ^{1}H NMR, (B) ^{13}C NMR, and (C) ^{29}Si NMR spectra of MENBS and TMNBS in $CDCl_3$ as well as an inset in the (D) ATR FT-IR spectra of TMNBS and MENBS. The insets highlight areas or peaks relevant for the substitution of the ethoxy group in MENBS with a methyl group in TMNBS.

3.2.5 Inverse vulcanization of NBS_x

Inverse vulcanizations with varying ratios of TMNBS and a hydrolysable NBS were carried out, whereas the sulfur content was kept constant. A mixture of TMNBS and NBS is termed NBS_x, with NBS referring to the name of the hydrolysable NBS and the index x referring to the weight percentage of the hydrolysable NBS relative to the total mass the NBS and TMNBS.

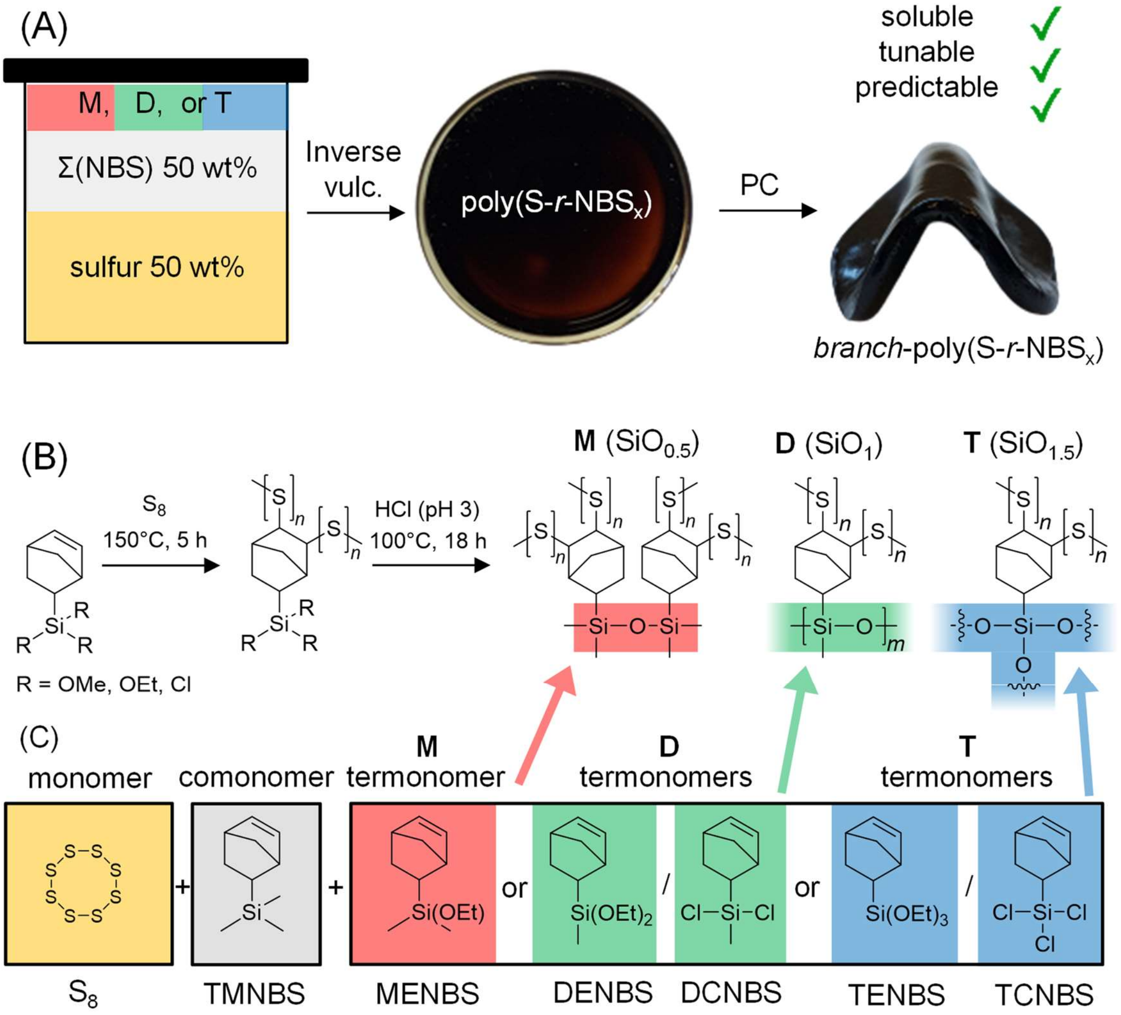
(A)
M, D, or T
Σ(NBS) 50 wt%
sulfur 50 wt%
Inverse vulc.
poly(S-r-NBSx)
PC
soluble
tunable
predictable
branch-poly(S-r-NBSx)
(B)
S8
150°C, 5 h
HCl (pH 3)
100°C, 18 h
R = OMe, OEt, Cl
M (SiO0.5)
D (SiO1)
T (SiO1.5)
(C)
monomer
comonomer
M termonomer
D termonomers
T termonomers
Si(OEt)
or
Si(OEt)2
Cl–Si–Cl
Si(OEt)3
S8
TMNBS
MENBS
DENBS
DCNBS
TENBS
TCNBS

Figure 47. (A) Schematic of the inverse vulcanization and polycondensation (PC) of mixtures of norbornenylsilanes (NBS$_x$). NBS$_x$ containing of a M, D, or T siloxane precursor and TMNBS react with sulfur to form poly(S-*r*-NBS$_x$), which polycondensates to yield *branch*-poly(S-*r*-NBS$_x$). (B) Generalized reaction equation of the inverse vulcanization and polycondensation of sulfur with NBS$_x$. The *branch*-poly(S-*r*-NBS$_x$) can contain either M, D, or T siloxane bonds. (C) Chemical structures, acronyms, and designated color of NBS serving as comonomer (TMNBS) or termonomers (MENBS, DENBS, DCNBS, TENBS, and TCNBS.

Equal masses of sulfur and NBS$_x$ were reacted at 150°C for 5 h to obtain polymers of the general formula poly(S-*r*-NBS$_x$). Melt polycondensation of poly(S-*r*-NBS$_x$) resulted in the formation of soluble *branch*-poly(S-*r*-NBS$_x$) polymers with controllable molecular and macroscopic properties, depending on the exact composition of the NBS mixture (**Figure 47 A**). This is due to the introduction of either M, D, or T siloxane binding motifs into the polymers (**Figure 47 B**). A typical NBS$_x$ mixture consisted of 90 – 50 wt% of TMNBS and 10 – 50 wt% of a hydrolysable NBS. As hydrolysable NBS, the M siloxane precursor monoethoxynorbornenylsilane (MENBS), the D siloxane precursors diethoxynorbornenylsilane (DENBS) or dichloronorbornenylsilane (DCNBS), or the T siloxane precursors triethoxynorbornenylsilane (TENBS) or trichloronorbornenylsilane (TCNBS) were used (**Figure 47 C**).

The hydrolysable ethoxy group should remain unaffected by the harsh conditions of the inverse vulcanization. To test this, DENBS, containing two ethoxy substituents, was reacted with equal masses of sulfur at 150°C for 1, 2, 4, and 8h, respectively. The resulting poly(S-*r*-DENBS$_{100}$) were investigated with ATR FT-IR and compared to the spectrum of the DENBS (**Figure 48**). The characteristic peaks associated with the vibrations of the ethoxy groups in the ATR FT-IR spectrum of DENBS were assigned at 1164, 1103, 1074, and 948 cm^{-1}. The intensity and position of the characteristic ethoxy peaks does not change significantly in the spectra of poly(S-*r*-DENBS$_{100}$), indicating a full retention of ethoxy groups even after 8 h. The intensity of peaks associated with the norbornene C=C double bond, i.e., 3057 cm^{-1} (C=C-H$_{\text{stretch}}$), 1568 (C=C$_{\text{stretch}}$), 890 (C=C$_{\text{bend}}$), and 717 cm^{-1} (C-H$_{\text{wag}}$) were reduced drastically after 1 h and disappeared after 2 h, indicating full conversion of C=C double bonds after 1 – 2 h.

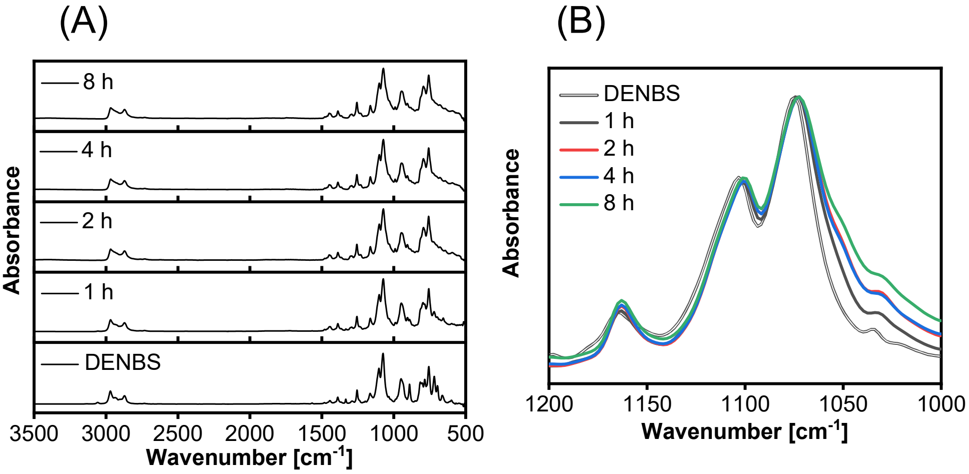

Figure 48. (A) ATR FT-IR spectra of poly(S-*r*-DENBS$_{100}$) formed by reacting equal masses of sulfur and DENBS at 150°C for 1, 2, 3, 4, and 8 h, respectively. (B) Inset of the normalized ethoxy bands between 1200 – 1000 cm^{-1}.

To ensure that the reaction of NBS mixtures with sulfur does not lead to sole consumption of just one of the NBS, kinetic experiments of the inverse vulcanization of TMNBS, MENBS, DENBS, and TENBS were performed. Equal masses of sulfur were reacted with TMNBS, MENBS, and DENBS at 150°C for 1, 2, 3, and 5 h, respectively. After 1 h, the reaction products were heterogeneous and residual sulfur could be seen for all monomers except TMNBS, which formed a deep red liquid of low viscosity. Longer reaction times led to a homogenization of the reaction products and to an increase in the viscosity (**Figure 49**).

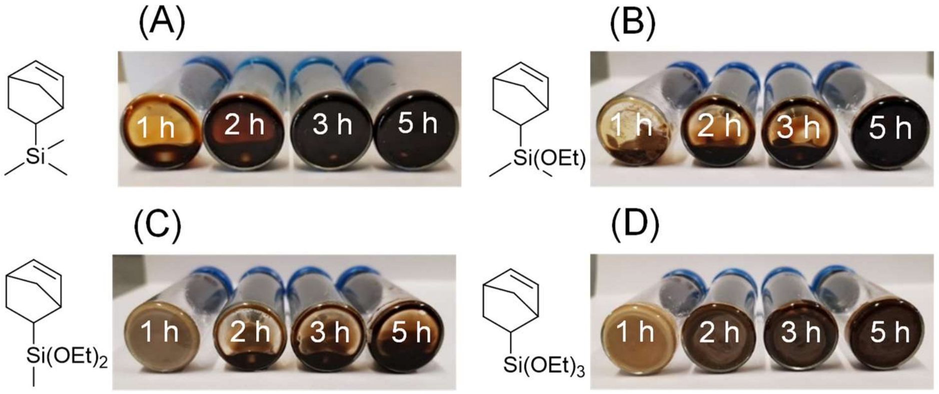

Figure 49. Digital image showing the products of the inverse vulcanization of sulfur with equal amounts of (A) TMNBS, (B) MENBS, (C) DENBS, and (D) TENBS for different reaction times. The total mass of each sample 1 g.

The products of the inverse vulcanizations of equal amounts of sulfur and TMNBS, MENBS, DENBS, and TENBS were examined for residual sulfur and C=C double bonds after 1, 2, 3, and 5 h. For all monomers, the conversion of C=C double bonds was complete after 2 h, as determined by ^{1}H NMR spectroscopy (**Figure 50**). The conversion of sulfur was complete after 5 h for all monomers, as investigated with DSC (**Figure 51**). Generally, the conversion of sulfur was faster for the less polar TMNBS than for the more polar DENBS and TENBS, which was attributed to the differences in polarity and thus the solubility of the respective NBS in molten sulfur. For example, in the DSC thermograms of poly(S-*r*-DENBS) and poly(S-*r*-TENBS) after 1 and 2 h the presence of a melting process at 115°C is clear evidence for the presence of crystalline sulfur. From the quantitative consumption of C=C double bonds and sulfur during the inverse vulcanization of TMNBS, MENBS, DENBS, and TENBS after 5 h, it was concluded that the reactivity of all NBS was sufficiently similar to conduct the inverse vulcanization as a ternary mixture of sulfur as monomer, TMNBS as comonomer, and a M, D, or T siloxane precursor as a termonomer.

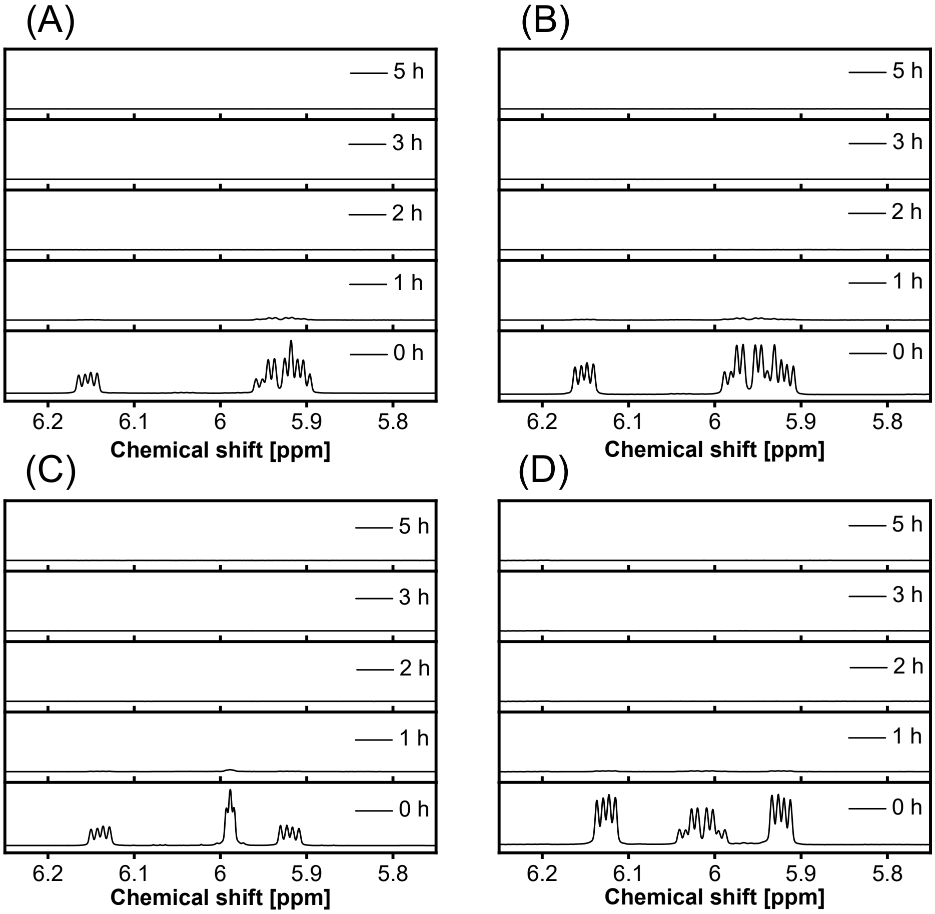

Figure 50. Inset of ^{1}H NMR spectra showing the consumption of norbornene C=C double bonds for the inverse vulcanization of sulfur with equal amounts of either (A) TMNBS, (B) MENBS, (C) DENBS, or (D) TENBS after different reaction times.

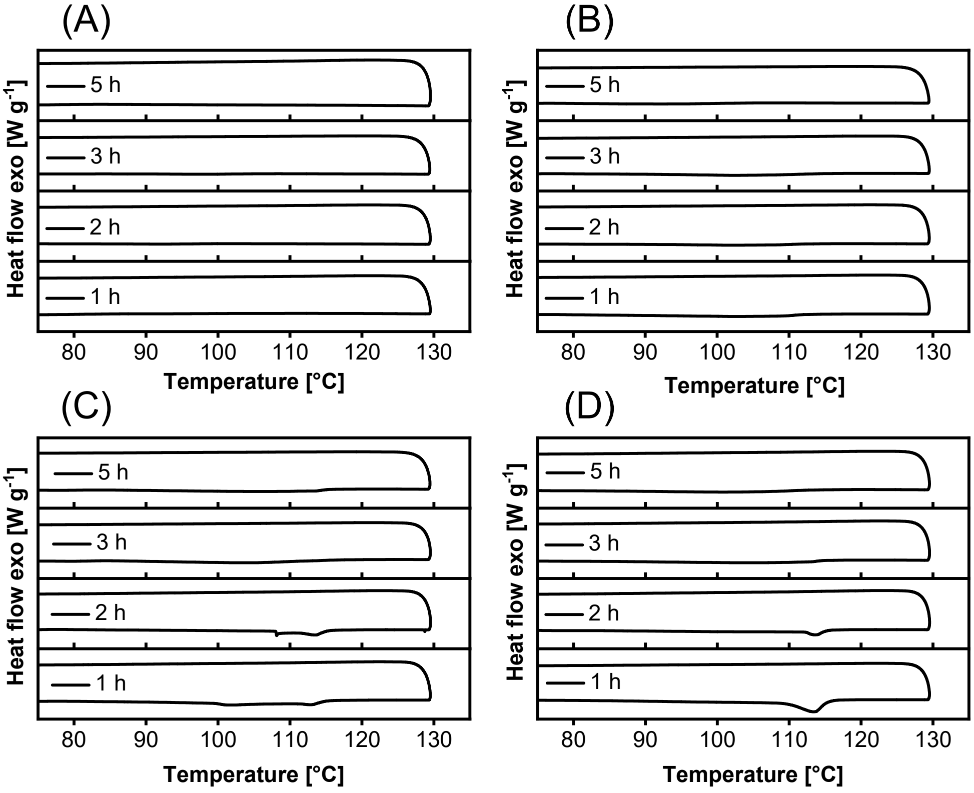

Figure 51. DSC thermograms (75 – 130°C) of the products of the inverse vulcanization of (A) TMNBS, (B) MENBS, (C) DENBS, and (D) TENBS after different reaction times. The masses of sulfur and the respective NBS was 500 mg.

3.2.6 Melt polycondensation of poly(*S*-*r*-NBS$_x$)

The products of the inverse vulcanization of sulfur and NBS$_x$, poly(S-*r*-NBS$_x$), were kept in a molten state at 100°C and were hydrolyzed for 18 h with 20 eq. of HCl solution (pH 3) relative to the hydrolysable ethoxy group. For the hydrolysis of the chloro-substituted poly(S-*r*-DCNBS) and poly(S-*r*-TCNBS), deionized water (pH 7) was used since the hydrolysis of chlorosilanes generates HCl. The hydrolyzed poly(S-*r*-NBS$_x$) was heated in an oven at 80°C for 5 days and in a vacuum oven at 40°C overnight to quantitatively drive the polycondensation towards the siloxane. The resulting polymers of the general formula *branch*-poly(S-*r*-NBS$_x$) were precipitated in methanol to yield thick flakes that turned into grey granules after drying (**Figure 52**). The granules were not sticky and could be molded and formed into different shapes.

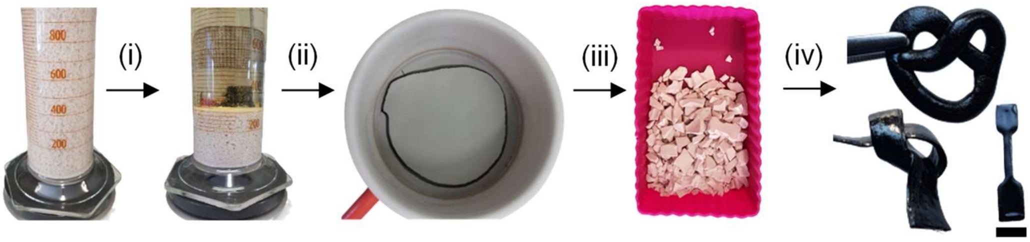

Figure 52. Digital images of the purification of *branch*-poly(S-*r*-NBS$_x$) after precipitation. (i) Sedimentation, (ii) vacuum filtration, (iii) vacuum oven drying and (iv) molding. The shown *branch*-poly(S-*r*-MENBS$_{20}$) were ductile but not sticky. Scalebar is 5 mm.

The precipitation helped to significantly decrease the content of low molar mass oligomers as recently also described by PYUN.[149] GPC elugrams of crude and precipitated *branch*-poly(S-*r*-MENBS$_{20}$) show the efficiency of the precipitation (**Figure 53**). In the elugram of crude *branch*-poly(S-*r*-MENBS$_{20}$), the UV signal of the low molar mass fraction is twice as high as the maximum UV signal of the polymer fraction. The signal of the low molar mass fraction after the precipitation is much smaller than the signal of the polymer fraction. For precipitations, the mass concentration of the crude polymer in THF was typically 20 mg mL^{-1}. The solution was added dropwise into methanol and the amount of methanol was typically 1 mL per mg of crude polymer. To test the influence of the reaction time on the polycondensation of poly(S-*r*-MENBS$_{25}$), three polycondensations of poly(S-*r*-MENBS$_{25}$) were conducted using identical conditions, i.e., 100°C and use of 20.0 eq. of HCl (pH 3) relative to number of ethoxy groups. The resulting *branch*-poly(S-*r*-MENBS$_{25}$) polymers were investigated with GPC. With increasing reaction time, the amount of low molar mass products decreased, and the M_W increased after 2, 4 and 18 h (3600, 4200, to 5200 g mol^{-1}). Thus, the heterogenic melt polycondensation of poly(S-*r*-NBS$_x$) polymers has the drawback of long reaction times but has the advantage of not requiring a solvent. Alternatively, it is possible to conduct the polycondensation of poly(S-*r*-NBS$_x$) in solution, too.

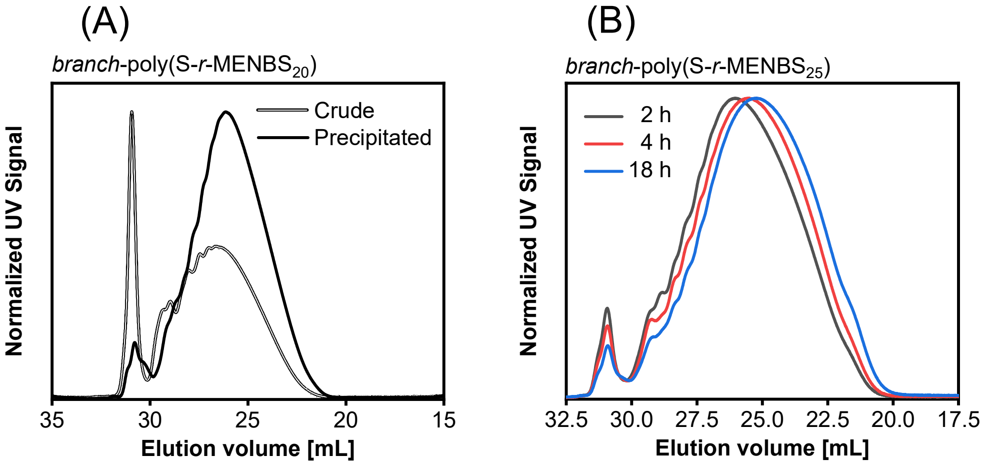

Figure 53. (A) GPC elugram of *branch*-poly(S-*r*-MENBS$_{20}$) before and after precipitation from THF into MeOH. (B) GPC elugrams of *branch*-poly(S-*r*-MENBS$_{25}$) for different reaction times.

3.2.7 Solution polycondensation of poly(S-*r*-NBS$_x$)

The polycondensation of poly(S-*r*-NBS$_x$) was examined in different solvents and for different amounts of water since these parameters are known to influence the complex interplay of hydrolysis and polycondensation.[175] HCl was chosen as acid catalyst because experiments using bases as catalyst (NH_3, $NaCO_3$) led to the precipitation of elemental sulfur. Tetrahydrofuran (THF) was the first choice of solvent due to the high solubility of all poly(S-*r*-NBS$_x$). DENBS was chosen as a model NBS, since the polycondensation of poly(S-*r*-NBS$_{100}$) was expected to result in a stronger increase of the molar mass in comparison to poly(S-*r*-MENBS$_{100}$) and was expected to yield a material with a better solubility than the product of the polycondensation of poly(S-*r*-TENBS$_{100}$).

Equal masses (500 mg) of DENBS and sulfur were reacted at 150°C for 5 h. The poly(S-*r*-DENBS$_{100}$) was dissolved in 5 mL of THF. To investigate the influence of the water content used for the hydrolysis of poly(S-*r*-DENBS$_{100}$) on the molar mass of the resulting polymer, different amounts, i.e., 1, 10, 15, and 20 vol% of HCl (pH 4) relative to volume of THF were added. The sealed reaction vials were stirred at 60°C for 2 h. Volatiles were removed under reduced pressure and the crude product was dried in a vacuum oven prior to GPC analysis. A clear decrease of the molar mass with an increasing volumetric ratio of HCl solution could be observed (**Figure 54**). It seems unlikely that higher concentrations of water inhibit the hydrolysis of poly(S-*r*-DENBS$_{100}$). Thus, it was hypothesized that a high content of water inhibits the polycondensation of poly(S-*r*-DENBS$_{100}$) during the removal of volatiles and vacuum drying according to CHATELIERS principle.

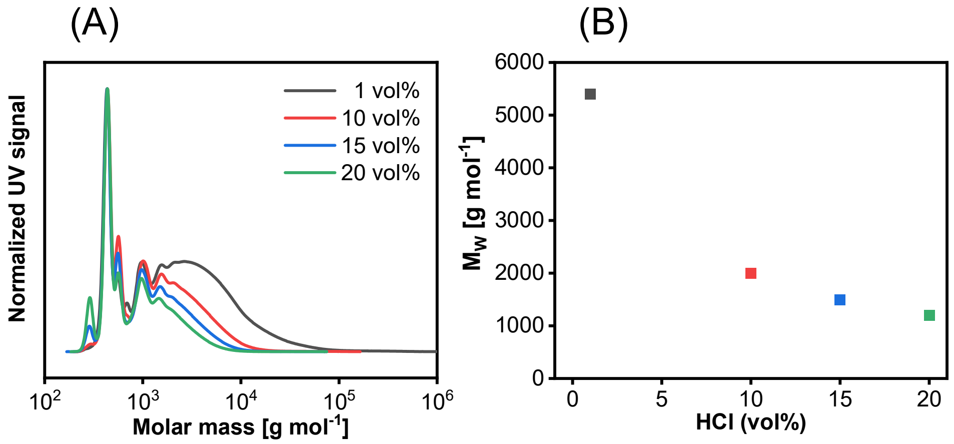

Figure 54. (A) GPC traces and (B) analysis of the molar mass of poly(S-*r*-DENBS$_{100}$) prepared in THF solution using different volume ratios of HCl (pH 4). Molar mass: 1 vol% (M_N = 1200 g mol^{-1}, M_W = 5400 g mol^{-1}), 10 vol% (M_N = 900 g mol^{-1}, M_W = 2000 g mol^{-1}), 15 vol% (M_N = 800 g mol^{-1}, M_W = 1500 g mol^{-1}), and 20 vol% (M_N = 700 g mol^{-1}, M_W = 1200 g mol^{-1}).

To examine the influence of each reaction step onto the molar mass of poly(S-*r*-DENBS$_{100}$) sequentially, GPC analysis was conducted after the inverse vulcanization, after the hydrolysis, after removal of volatiles (solvent), and after vacuum drying of the product (**Figure 55**). A volume of 1 vol% of HCl solution (pH 4) was used since it gave the highest molar mass amongst the volumes tested. GPC analysis revealed a minor increase in the molar mass after the hydrolysis of poly(S-*r*-DENBS$_{100}$) (M_W = 1400 g mol^{-1}) relative to poly(S-*r*-DENBS$_{100}$) after the inverse vulcanization (M_W = 1300 g mol^{-1}). The removal of volatiles caused a further moderate increase of the molar mass (M_W = 1800 g mol^{-1}), whereas the final step of drying in a vacuum oven showed the largest increase of the molar mass (M_W = 5400 g mol^{-1}). Typically, the polycondensation of silanols happens at the same time as the hydrolysis of alkoxysilanes to silanols and the respective alcohol, resulting in a complex equilibrium of hydrolyzed and condensated species.[175] The different behavior of hydrolyzed poly(S-*r*-DENBS$_{100}$) is attributed to the large steric hindrance of the norbornenyl-substituent causing the condensation to proceed far slower than the hydrolysis. Thus, a strong driving force such as the removal of water from the equilibrium is required to drive the formation of siloxane bonds.

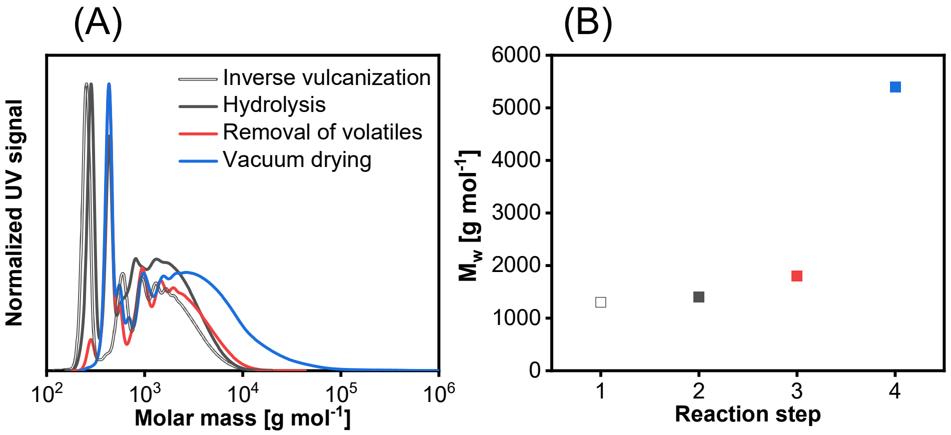

Figure 55. (A) GPC traces and (B) analysis of the molar mass of poly(S-*r*-DENBS$_{100}$) after different reaction or work-up steps. Molar mass: (1) Inverse vulcanization (M_N = 600 g mol^{-1}, M_W = 1300 g mol^{-1}), (2) hydrolysis (M_N = 600 g mol^{-1}, M_W = 1400 g mol^{-1}), (3) removal of volatiles (M_N = 800 g mol^{-1}, M_W = 1800 g mol^{-1}), and (4) vacuum drying (M_N = 1200 g mol^{-1}, M_W = 5400 g mol^{-1}).

It has been reported that the combination of aprotic solvents and acid catalysts can have adverse effects on the rate of polycondensation due to coordination and inactivation of the catalysts positive charge by the lone electron pairs of the solvent.[175] For this reason, the polar aprotic THF might not be an ideal choice of solvent with HCl as a catalyst. To investigate the influence of the type of solvent, toluene as non-polar solvent, 1-butanol as non-polar protic solvent, and 2-propanol as polar protic solvent were chosen (**Figure 56**). The polycondensations in different solvents were performed using the same conditions (1 vol% HCl, 5 mL of solvent, 60°C, 2 h), except for toluene for which 110°C were chosen as the reaction temperature. GPC analysis revealed that the solvent had a large influence on the molar mass of the product of polycondensation. For the polycondensation attempt in toluene a degradation of the polymer was observed, as apparent by the precipitation of sulfur and the GPC traces (M_N = 300 g mol^{-1}, M_W = 400 g mol^{-1}). The polycondensation in 1-butanol yielded a low molar mass polymer (M_N = 700 g mol^{-1}, M_W = 1600 g mol^{-1}). Use of the polar aprotic THF yielded a higher molar mass (M_N = 1200 g mol^{-1}, M_W = 5400 g mol^{-1}) and use of the polar protic 2-propanol afforded the polymer with the highest molar (M_N = 900 g mol^{-1}, M_W = 9000 g mol^{-1}). However, the alcohols 1-butanol and 1-propanol suffered from a limited solubility of poly(S-*r*-DENBS$_{100}$), limiting the yield.

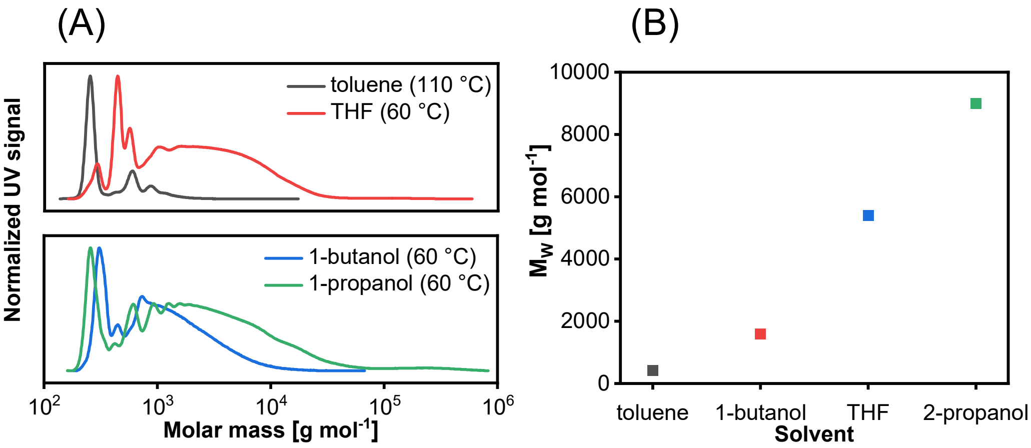

Figure 56. (A) GPC traces and (B) analysis of the molar mass of poly(S-*r*-DENBS$_{100}$) polycondensated in different solvents. Molar mass: toluene (M_N = 300 g mol^{-1}, M_W = 400 g mol^{-1}), 1-butanol (M_N = 700 g mol^{-1}, M_W = 1600 g mol^{-1}), THF (M_N = 1200 g mol^{-1}, M_W = 5400 g mol^{-1}), 2-propanol (M_N = 900 g mol^{-1}, M_W = 9000 g mol^{-1}). Poly(S-*r*-DENBS$_{100}$), the alcohols 1-butanol and 1-propanol suffered from a limited solubility of poly(S-*r*-DENBS$_{100}$).

For all polycondensations, a considerable amount of low molar mass species was found. Attempts to purify hydrolyzed poly(S-*r*-DENBS$_{100}$) via precipitation from 2-propanol solution in ethanol, methanol, or even water failed due to the formation of solutions of hydrolyzed poly(S-*r*-DENBS$_{100}$) in the resulting solvent mixtures (methanol, ethanol) or the formation of a nano-dispersion (water). The formation of colloidal particles containing poly(S-*r*-DENBS$_{100}$) particles could be visualized using the TYNDALL effect. A light source shined into the aqueous dispersion from above revealed a white turbidity, which is due light scattering of the particles. The farther the light reached into the dispersion, more blue and green light was absorbed, and only yellow light was scattered. The formation of uniform poly(S-*r*-DENBS$_{100}$) nanoparticles with a size of 132.2 ± 0.1 nm was confirmed with dynamic light scattering (**Figure 57**).

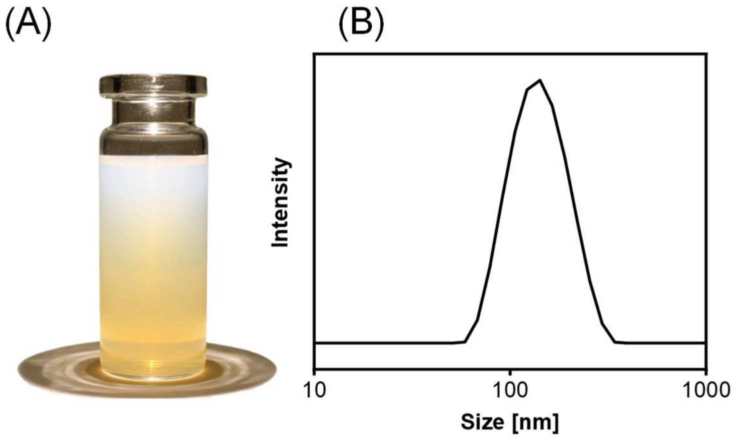

Figure 57. (A) Digital image of a nano-dispersion of hydrolyzed poly(S-*r*-DENBS$_{100}$) in water. (B) Differential light scattering of the poly(S-*r*-DENBS$_{100}$) dispersion. The size of the particles was 132.2 ± 0.1 nm (N=3).

In conclusion, the polycondensation of poly(S-*r*-NBS$_x$) in solution were investigated thoroughly using poly(S-*r*-DENBS$_{100}$) as a model polymer. However, the heterogeneous melt polycondensation was preferable under practical and green chemistry aspects.

3.2.8 Chemical analysis of *branch*-poly(S-*r*-NBS$_x$)

Granulated *branch*-poly(S-*r*-NBS$_{20}$) could be molded into different shapes by heating to 80°C overnight (**Figure 58**). Upon molding, the grey granules turned into black polymer melts, which is due to the reduction of light scattering. The molding behavior of *branch*-poly(S-*r*-MENBS$_{20}$), *branch*-poly(S-*r*-DCNBS$_{20}$), and *branch*-poly(S-*r*-TCNBS$_{20}$) differed drastically. After 2 hours in an oven at 80°C, *branch*-poly(S-*r*-MENBS$_{20}$) spread as a viscous melt, *branch*-poly(S-*r*-DCNBS$_{20}$) formed droplets, and *branch*-poly(S-*r*-TCNBS$_{20}$) only showed a color change from grey to black, due to the loss of surface porosity. While *branch*-poly(S-*r*-MENBS$_{20}$) and *branch*-poly(S-*r*-DCNBS$_{20}$) adopted the shape of the mold, *branch*-poly(S-*r*-TCNBS$_{20}$) was rubbery at 80°C and did not fully adopt the shape of the mold. The drastically different molding behavior is caused by the different types of siloxane bonds in the polymers, i.e., M, D, and T siloxane bonds.

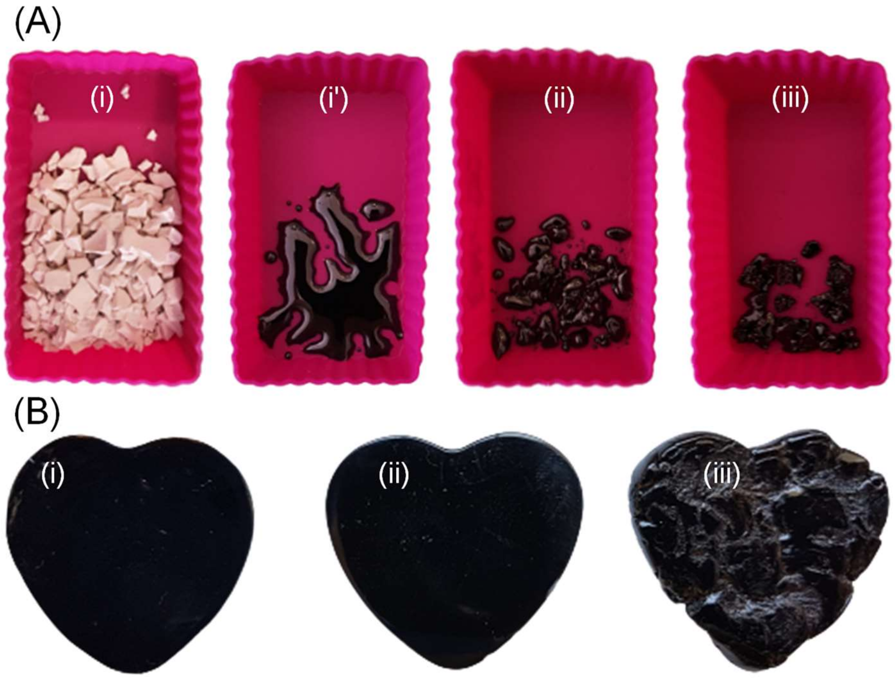

Figure 58. (A) Melting behavior of *branch*-poly(S-*r*-NBS$_{20}$) containing different siloxane bonds. Granules of b*ranch*-poly(S-*r*-MENBS$_{20}$) before (i) and after 2 h (i') at 80°C. Granules of (ii) *branch*-poly(S-*r*-DCNBS$_{20}$) and (iii) *branch*-poly(S-*r*-TCNBS$_{20}$) after 2 h at 80°C. (B) Molded objects made from 2 g of *branch*-poly(S-*r*-NBS$_{20}$) at 80°C overnight.

The *branch*-poly(S-*r*-NBS$_{20}$) polymers were homogeneous materials, which could be concluded from the optical transparency of thin films (**Figure 59 A**). UV-vis spectroscopy of a film of *branch*-poly(S-*r*-NBS$_x$) revealed that its black color stems from an absorption band that decreases monotonously throughout the visible light spectrum (**Figure 59 B**).

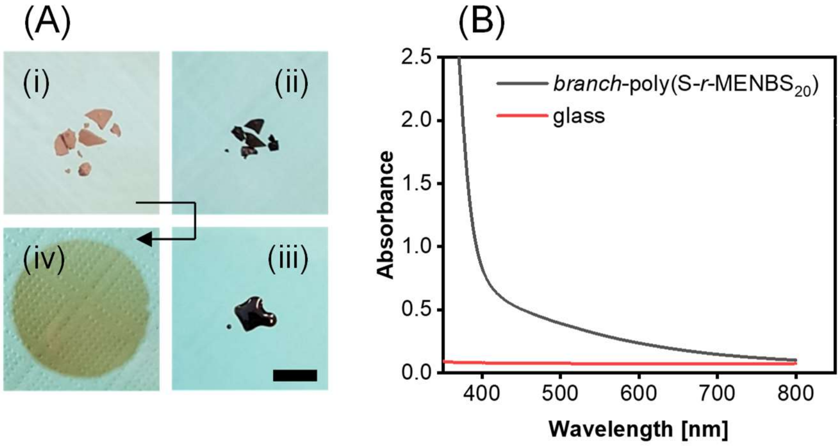

Figure 59. (A) Digital images showing the melting of *branch*-poly(S-*r*-MENBS$_{20}$) granules into a transparent film). (i) granulated *branch*-poly(S-*r*-MENBS$_{20}$) on a glass slide after (ii) 2 min, (iii) and 10 min at 80°C. (iv) Molten *branch*-poly(S-*r*-MENBS$_{20}$) in between two glass slides. Scalebar is 5 mm. (A) UV-vis spectrum from 250 – 800 nm of a thin film of *branch*-poly(S-*r*-MENBS$_{20}$).

To prove the presence of M, D, and T siloxane bonds in the *branch*-poly(S-*r*-NBS$_{20}$) polymers, ^{29}Si cross polarization magic-angle spinning (CP MAS) NMR spectroscopy was used (**Figure 60**). Peaks at 1.4 ppm in all spectra correspond to the trimethyl-substituted silicon atom from TMNBS. The M siloxane bonds of *branch*-poly(S-*r*-MENBS$_{20}$) are confirmed by the peak found at 6.6 ppm.[205] For *branch*-poly(S-*r*-DENBS$_{20}$), two peaks at -11.4 and -22.2 ppm were observed, which correspond to short chains or cyclic siloxanes (MDM, D_3) and larger cyclic and linear oligomers ($MD_{>2}M$, $D_{>3}$), respectively.[205,206] The peaks found for *branch*-poly(S-*r*-TENBS$_{20}$) at -59.1 and -69.8 ppm are in the expected range for alkyl-substituted T siloxanes.[205,207] Due to the broad peaks in the spectrum of *branch*-poly(S-*r*-TENBS$_{20}$) and the variety of possible chemical structures for T-siloxanes (heterogeneous broadening), no further assignment was done.

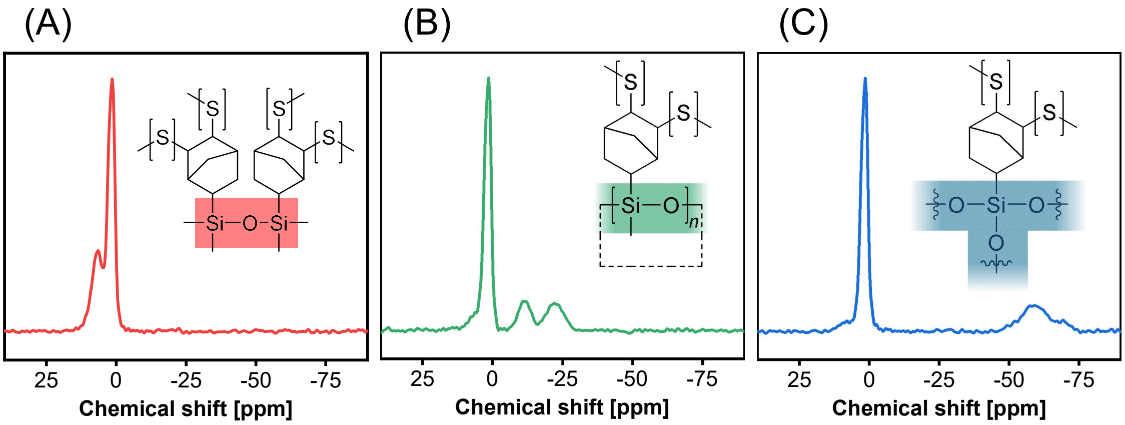

Figure 60. ^{29}Si CP/MAS NMR spectra of (A) *branch*-poly(S-*r*-MENBS$_{20}$), (B) *branch*-poly(S-*r*-DENBS$_{20}$), and (C) *branch*-poly(S-*r*-TENBS$_{20}$). The peak appearing in each spectrum at 1.4 ppm corresponds to the $-SiMe_3$ group from TMNBS.

To provide further evidence for the conversion of the hydrolysable ethoxy and chloro groups into siloxane bonds, *branch*-poly(S-*r*-NBS$_{20}$) polymers were investigated with infrared spectroscopy and compared to their monomers (**Figure 61**). The quantitative conversion of chloro substituents during the formation of *branch*-poly(S-*r*-DCNBS$_{20}$) and *branch*-poly(S-*r*-TCNBS$_{20}$) could be observed from the disappearance of the Si-Cl vibration bands at 537 cm^{-1} and 562 cm^{-1}, and from the appearance of a siloxane (Si-O-Si) band at 1136 – 956 cm^{-1} and 1164 – 956 cm^{-1}, respectively. For MENBS, the strong doublet of the ethoxy group at 1107 and 1078 cm^{-1} disappeared and a siloxane band from 1092 – 999 cm^{-1} appeared for *branch*-poly(S-*r*-MENBS$_{20}$). The doublets of the ethoxy groups in DENBS at 1103 and 1074 cm^{-1} and in TENBS at 1101 and 1074 cm^{-1} transformed into siloxane bands from 1136 – 956 cm^{-1} for *branch*-poly(S-*r*-DENBS$_{20}$) and *branch*-poly(S-*r*-TCNBS$_{20}$) 1179 – 979 cm^{-1}, respectively.

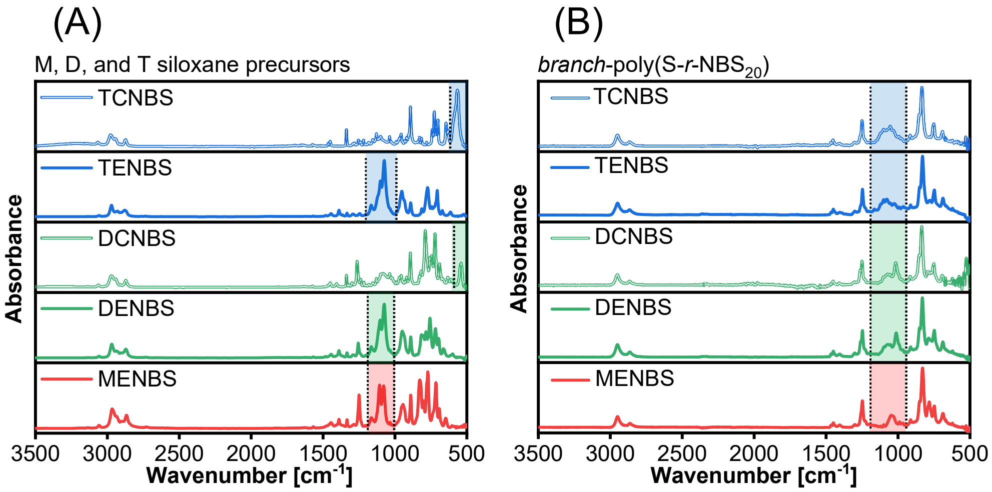

Figure 61. ATR FT-IR spectra of the (A) M, D, and T siloxane forming termonomers and (B) of *branch*-poly(S-*r*-NBS$_{20}$) for different termonomers. Dashed lines highlight peaks corresponding to hydrolysable ethoxy- (MENBS, DENBS, TENBS) or chlorosilane (DCNBS, TCNBS) vibrations (left) and characteristic siloxane vibrations (right).

Despite being derived from different hydrolysable groups (i.e., ethoxy and chloro), the siloxane bonds in *branch*-poly(S-*r*-DENBS$_{20}$) and *branch*-poly(S-*r*-DCNBS$_{20}$) as well as *branch*-poly(S-*r*-TENBS$_{20}$) and *branch*-poly(S-*r*-TCNBS$_{20}$) are naturally similar due to being D and T siloxanes, respectively. Based on a comparison with a spectrum of commercial linear poly(dimethylsiloxane) (PDMS, 10 cSt), both *branch*-poly(S-*r*-DENBS$_{30}$) and *branch*-poly(S-*r*-DCNBS$_{30}$) polymers contain cyclic and linear siloxane binding motifs (**Figure 62**).

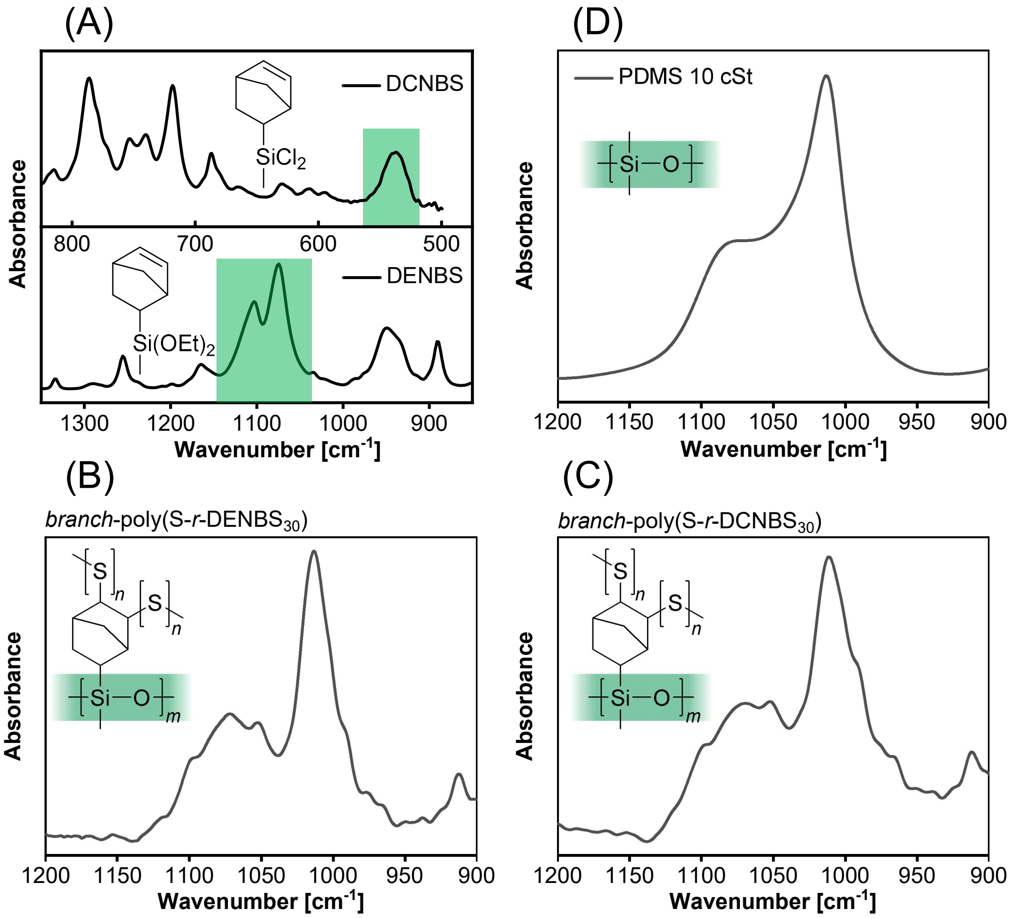

Figure 62. Insets of the ATR FT-IR spectra of (A) DCNBS and DENBS termonomers. Diagnostic chloro- (DCNBS) and ethoxysilane (DENBS) vibrations are highlighted in green. Insets highlighting the siloxane vibration peaks in the ATR FT-IR spectra of (B) *branch*-poly(S-*r*-DENBS$_{30}$), (C) *branch*-poly(S-*r*-DCNBS$_{30}$), and (D) PDMS (10 cSt) as reference.

The proposed underlying control mechanism for high sulfur content *branch*-poly(S-*r*-NBS$_x$) polymers is the finely tunable increase of siloxane bonding between polymer chains. This allowed keeping the elemental composition of all *branch*-poly(S-*r*-MENBS$_{10}$) polymers essentially the same, as demonstrated by elemental analysis (**Table 6**). The *branch*-poly(S-*r*-NBS$_x$) polymers contained, on average, 36.1 ± 0.9 wt% C, 4.8 ± 0.6 wt% H, and 49.9 ± 1.1 wt% S. The feed ratio of sulfur has thus been fully incorporated. This can be attributed to two compensating mechanisms: The loss of sulfur via sublimation during the inverse vulcanization and the increase of the relative sulfur content due to the loss of water and ethanol or HCl from the hydrolysable NBS.

Table 6. Elemental analysis of poly(S-*r*-TMNBS) and *branch*-poly(S-*r*-NBS$_x$) with varying contents of M, D, and T building blocks.

Name	C (wt%)[a]	H (wt%)[a]	S (wt%)[a]
poly(S-*r*-TMNBS)	38.8	5.6	48.6
branch-poly(S-*r*-MENBS$_{10}$)	35.9	4.9	51.1
branch-poly(S-*r*-MENBS$_{20}$)	35.2	4.9	50.6
branch-poly(S-*r*-MENBS$_{30}$)	35.1	4.7	52.0
branch-poly(S-*r*-MENBS$_{50}$)	34.9	4.6	49.9
branch-poly(S-*r*-DENBS$_{10}$)	36.3	3.7	50.5
branch-poly(S-*r*-DENBS$_{20}$)	35.6	3.7	49.7
branch-poly(S-*r*-DENBS$_{30}$)	35.3	4.0	49.7
branch-poly(S-*r*-DCNBS$_{10}$)	37.5	5.7	47.8
branch-poly(S-*r*-DCNBS$_{20}$)	37.7	5.7	48.4
branch-poly(S-*r*-DCNBS$_{30}$)	37.7	5.7	48.9
branch-poly(S-*r*-TENBS$_{10}$)	36.0	4.9	50.8
branch-poly(S-*r*-TENBS$_{20}$)	35.5	4.8	51.1
branch-poly(S-*r*-TCNBS$_{10}$)	36.8	5.2	49.1
branch-poly(S-*r*-TCNBS$_{20}$)	36.0	4.9	49.1

[a]Values represent an average of two measurements which did not differ by more than 1 wt%.

3.2.9 Molar mass analysis of *branch*-poly(S-*r*-MENBS$_x$)

The molar mass is arguably the most fundamental and relevant molecular property of polymers. While there are various strategies for carbon-based polymerizations to control the molar mass, there are few systematic approaches for polymers prepared via inverse vulcanization.[149,156] The siloxane approach presented herein allows control over M_W via the relative amount and the type (i.e., M, D, T) of the siloxane precursor added. Six different *branch*-poly(S-*r*-NBS$_x$) polymers with increasing amounts of MENBS from 0, 10, 20, 30, 50, to 100 wt% (relative to the total mass of the NBS mixture) were prepared. Poly(S-*r*-TMNBS$_{100}$) without MENBS (0 wt%) was used as a reference and treated the same as the MENBS containing polymers. The obtained polymers were investigated with GPC (**Figure 63 A**). It was found that M_W increased with an increasing content of MENBS in the NBS mixture, whereas the M_N increased only slightly. This could be explained with the discriminating mechanism of polymer chain formation. In brief, long polymer chains formed after the inverse vulcanization of a NBS$_x$ mixture have a higher chance to contain one or more MENBS units than short ones. Only chains containing at least one MENBS unit can form siloxane among each another, leading to a preferential growth of long chains.

To prove that the increase of the MENBS content in the NBS$_x$ mixture led to a factual increase in M siloxane bonding of *branch*-poly(S-*r*-MENBS$_x$) polymers, ATR FT-IR was used (**Figure 63 B**). A comparison of the siloxane vibration bands between 1092 and 999 cm^{-1} revealed integral ratios of 1.95, 3.14, and 4.86 between *branch*-poly(S-*r*-MENBS$_{10}$) and *branch*-poly(S-*r*-MENBS$_{20}$), *branch*-poly(S-*r*-MENBS$_{30}$), and *branch*-poly(S-*r*-MENBS$_{50}$), respectively, which is close to the expected values 2, 3, and 5. It can be concluded that the increase of

MENBS in the feed ratio of the NBS_x mixture leads to a linearly proportional increase of M siloxane bonds in the final *branch*-poly(S-*r*-$MENBS_x$) polymer.

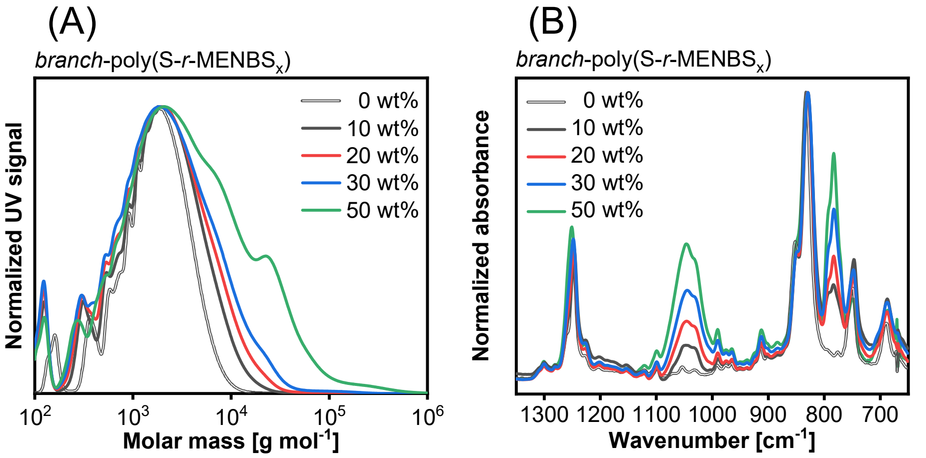

Figure 63. (A) GPC traces and (B) ATR FT-IR spectra of *branch*-poly(S-*r*-$MENBS_x$) with x being 0, 10, 20, 30, and 50 wt%.

Notably, the obtained molar mass distributions of *branch*-poly(S-*r*-$MENBS_x$) polymers contained fewer low molar mass species than those of other inverse vulcanization polymers such as poly(S-*r*-diisopropenylbenzene) or poly(S-*r*-styrene) (**Figure 64**).[81,141]

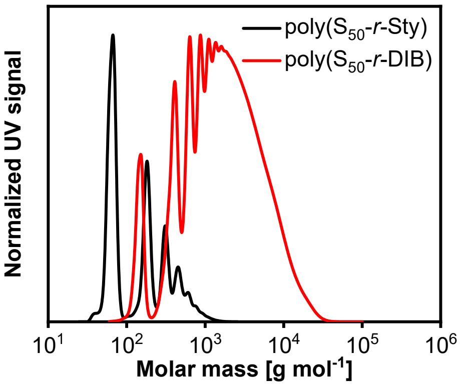

Figure 64. GPC traces of poly(S-*r*-Sty) and poly(S-*r*-DIB) prepared with 50 wt% of sulfur according to reported procedures. M_N = 100 g mol^{-1}, M_W = 200 g mol^{-1}. for poly(S-*r*-Sty) and M_N = 100 g mol^{-1}, M_W = 200 g mol^{-1} for poly(S-*r*-DIB). Sty is an abbreviation for styrene. DIB is an acronym for diisopropenylbenzene.

3.2.10 Theoretical considerations of *branch*-poly(S-*r*-MENBS$_x$) formation

When increasing the content of MENBS in *branch*-poly(S-*r*-MENBS$_x$) polymers M_W was found to increase whereas the number average molar mass (M_N). To understand this behavior, the formation of *branch*-poly(S-*r*-MENBS$_x$) chains must be understood on a theoretical level. The inverse vulcanization and polycondensation of mixtures of MENBS and TMNBS can be mimicked using a simple building block model:

A pool of red (MENBS) and grey (TMNBS) building blocks is assumed. The red and grey blocks are randomly assembled into chains with a length of 1 – 11 blocks. The probability of chain lengths follows a Poisson distribution. The maximum of the distribution is found at $P(x=\mu)$ and $P(x=0)$ resembles a chain length of 1, i.e., one block. Chains containing a red building block are fused together by connecting the two red blocks. The resulting fused chains contain two paired red blocks and potentially more unpaired red building blocks. Fused chains containing more than two red building blocks fuse together again with their unpaired red blocks. Further fusing of chains, e.g., when a doubly fused chain contains more than six red building blocks were not considered. This is due the very low probability of a single fused chain to contain three red building blocks and due to the possibility of intra-chain fusing, which could not be considered explicitly in this model. The final distribution of chains thus consists of primary chains, containing only grey building blocks, chains that fused together once, containing two red building blocks, and chains that fused together twice, containing six or more red building blocks.

The model is based on the following assumptions:

1.) The chain length after the inverse vulcanization follows a Poisson distribution.
2.) The incorporation of TMNBS and MENBS into poly(S-*r*-MENBS$_x$) is random.
3.) The chain length, as defined by the number of TMNBS or MENBS in poly(S-*r*-MENBS$_x$), is independent of the previous incorporation of TMNBS and MENBS.
4.) The maximum chain length after the inverse vulcanization is low, i.e., the probability of chains containing more than 11 building blocks is zero.
5.) There is no intramolecular formation of M-siloxane bonds for chains containing two MENBS units.

As an example, a pool of 10 % red blocks and 90 % grey blocks randomly assembles into chains containing between 1 – 11 blocks (**Figure 65**). The chain length distribution, as defined by the total numbers of blocks in a chain, follows a Poisson distribution with the highest probability being at the expected value $\mu = 4$. Only 40 % of the chains contain at least one red building block, whereas the residual 60 wt% contain only grey blocks. The chains containing red blocks then bind together in pairs of two, reducing the total amount of chains to 80 % relative to the previous step. The number of fused chains thus amounts to 25 % and chains containing only grey blocks amount to 75 %. Some of the fused chains still contain unpaired red blocks, since in the first fusing step only one red block per chain was fused. Chains containing unfused red blocks fuse again, and the final chain length distribution is obtained. In summary, the total amount of chains reduces from 100 % (assembly of primary chains) to 80 % (first fusing step) and finally to 76 % (second fusing step). Chains containing only grey blocks do not fuse and thus their relative amount increases from 60 % (assembly of primary chains) to 76 % (first fusing step) and finally to 79 % (second fusing step). The relative amount of chains containing red blocks reduces from 40 % (assembly of primary chains) to 25 % (first fusing step) and finally to 21 % (second fusing step). Among the fused chains, 16 % contain exactly two red blocks (fused once) and 5 % contain at least six red blocks. In this example, i.e., 10 % red blocks in the initial pool of building block and μ = 4, only 5 % of percent of chains could fuse twice and thus grew strongly, whereas 79 % of the chains in the final distribution were not affected by the fusing mechanism.

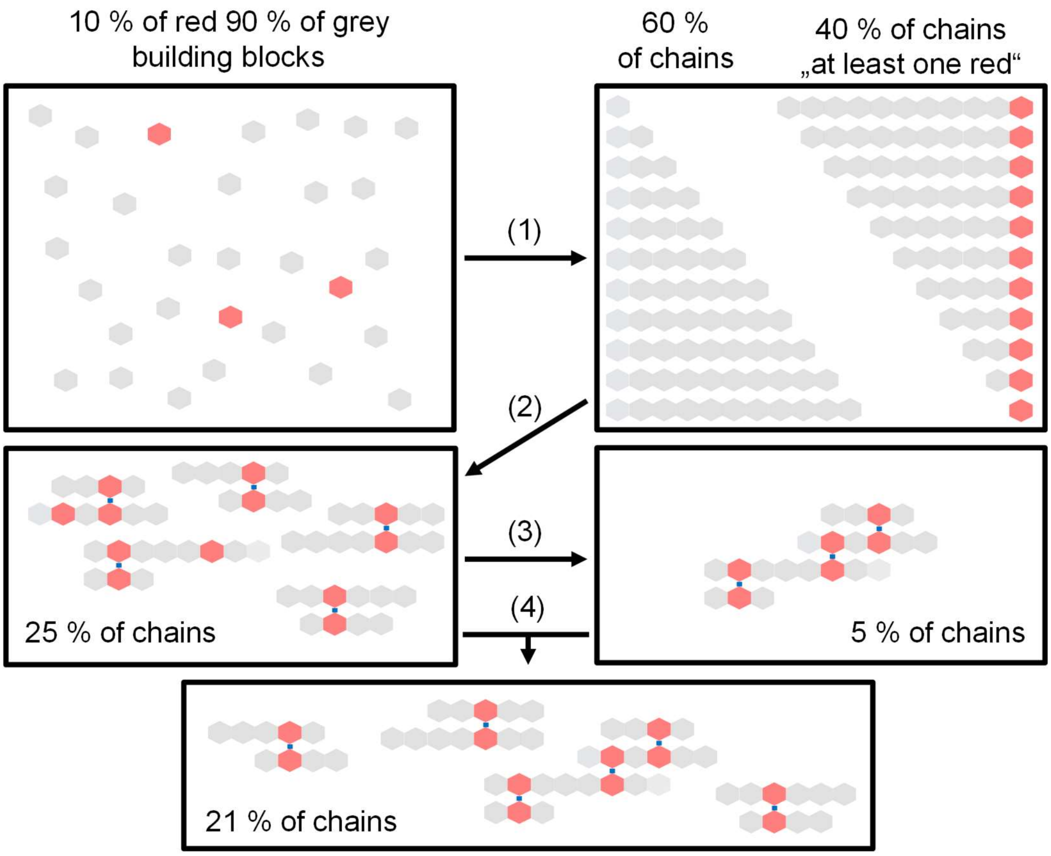
10 % of red 90 % of grey building blocks
60 % of chains
40 % of chains „at least one red“
(1)
(2)
(3)
(4)
25 % of chains
5 % of chains
21 % of chains

Figure 65. Schematic explanation of the model used to simulate the chain length distributions of *branch*-poly(S-*r*-MENBS$_x$) polymers. The steps are (1) random assembly of red and grey blocks into chains, (2) fusing chains containing at least one red block, (3) fusing of chains containing at least one unpaired block, (4) blending of chains to obtain a final distribution of chains. Percentages are relative to the total amount of chains after each respective step (1-4).

Based on this model, the chain length distribution was simulated for combinations of two parameters: The ratio of red and grey blocks, which corresponds to the ratio of MENBS and TMNBS in the experiment, and the expected value μ for the Poisson distribution, mimicking the chain length distribution after the inverse vulcanization. In accordance with the experiment, the ratio of red to grey blocks was chosen 0:100, 10:90, 20:80, 70:30, 60:40, and 50:50, respectively. The expected value μ was chosen to be 1, 2, 4, and 8, to compare different chain length distributions resulting from the inverse vulcanization of MENBS and TMNBS (**Figure 66**).

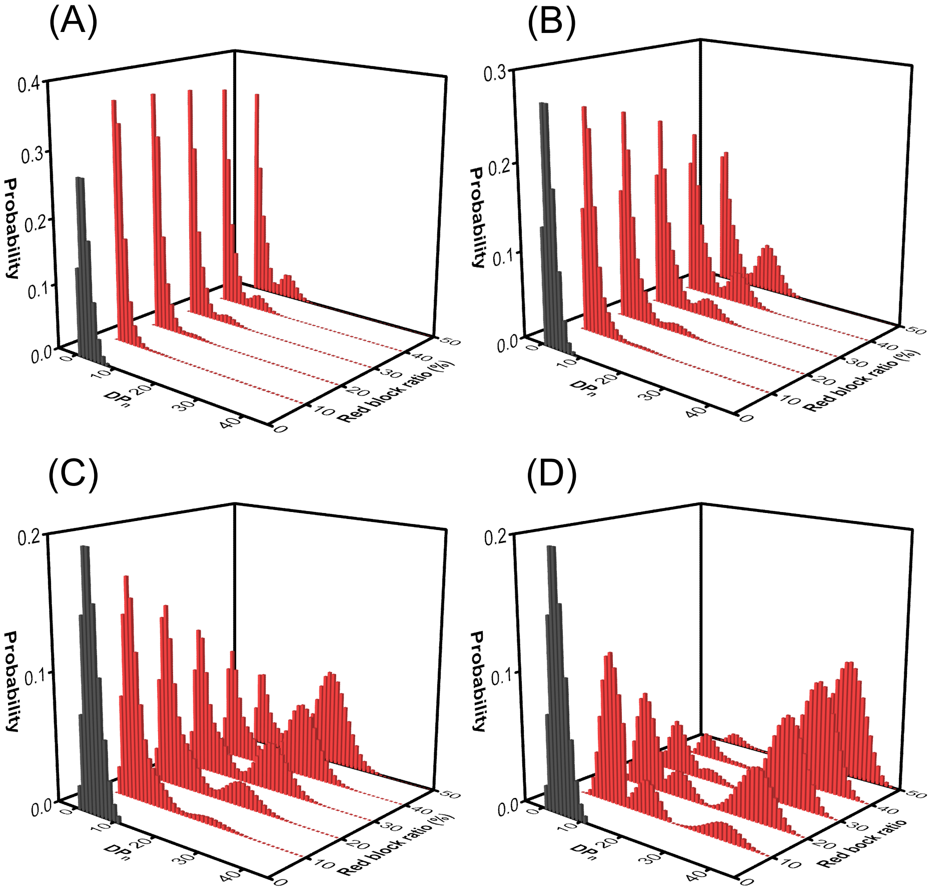

Figure 66. Simulated chain length distributions (DP_n) for different primary chain length distributions (grey) and for different ratios of red blocks. The primary distribution (grey) was approximated as a Poisson distribution with an expected value of (A) μ = 1, (B) μ = 2, (C) μ = 4, and (D) μ = 8.

An increase in the ratio of red blocks and an increase of μ generally increased the chain length and enabled the formation of longer chains. However, the monomodal Poisson distribution transformed into a bimodal or a multimodal distribution. When μ was chosen low (μ = 1 or 2), most chains in the simulated chain distribution remained small. For red block ratios of 20 % or higher, the chain length distribution became bimodal. A content of at least 20 % of red blocks is required to obtain a significant amount of long chains. This is because a small average chain length after the random assembly of red and grey blocks decreases the chance of a chain to contain one or more red blocks, which prevents further growth by pairing red blocks. For μ = 4, the same trend is observed, however the probability of obtaining higher chain lengths increases stronger with an increasing ratio of red blocks than it does for μ = 1 or 2. A bimodal distribution is thus observed already for a red block ratio of 10%. However, in the bimodal distributions the maxima at high chain lengths are less probable than the maxima at low chain lengths until the red block ratio reaches 50 %. When μ = 8 was assumed, only a small content of red blocks is required to significantly shift the chain length distribution to high chain lengths. For red block ratios of 10, 20, and 30 %, multimodal chain length distributions were obtained, whereas for red block ratios of 40 and 50 % two distinct distributions were obtained, in which most chains were found in the distribution containing larger chains. A high average chain length after the initial assembly of chains increases the chance of a chain to contain multiple red blocks while it drastically decreases the chance of a chain to not contain red blocks. Thus, large chains quickly dominate the distribution.

Experimental GPC data for *branch*-poly(S-*r*-MENBS$_x$) has most resemblance with the model for μ = 1 and μ = 2, which indicates that the inverse vulcanization of MENBS and TMNBS mostly leads to short chain oligomers with very few TMNBS and MENBS repeating units. Such a behavior is typical for the inverse vulcanization of monoalkenes. This simulation further highlights the importance of finding strategies to increase the average chain length after the inverse vulcanization, since it would make post-polymerization a much more efficient strategy to generate high molar mass polymers or weakly crosslinked elastomers.

3.2.11 Molar mass analysis of *branch*-poly(S-*r*-NBS$_x$)

To investigate the influence of the different siloxane precursors, i.e., M, D, and T precursors, as well as the influence of the hydrolysable functional group, i.e., ethoxy- and chloro groups, on the molar mass, *branch*-poly(S-*r*-NBS$_{20}$) polymers were synthesized using MENBS, DENBS, DCNBS, TENBS, and TCNBS. GPC analysis of the *branch*-poly(S-*r*-NBS$_{20}$) revealed that the M$_W$ increased from M, to D, to T siloxane bond containing polymers (Figure 67). Polymers made from ethoxy-substituted DENBS yielded a higher molar mass than those prepared from the chloro-substituted DCNBS. This might be due to a preferential formation of small cyclosiloxane rings resulting from the faster hydrolysis of chlorosilanes compared to ethoxysilanes. For *branch*-poly(S-*r*-DENBS$_{30}$) and *branch*-poly(S-*r*-DCNBS$_{30}$), however, no such effect was observed, and both had very similar molar mass. The molar mass distribution of the T-siloxane containing polymer *branch*-poly(S-*r*-TCNBS$_{20}$) split up into a high and low molar mass distribution, but with an average molar mass far higher than that of *branch*-poly(S-*r*-TENBS$_{30}$). This was attributed to the lesser steric hindrance and higher reactivity of trichlorosilanes towards hydrolysis compared to triethoxysilanes, which could cause extreme local growth of the polymer due to the heterogeneity of the polycondensation. It can be ensured that the high molar mass distribution observed in the GPC traces of *branch*-poly(S-*r*-TENBS$_{20}$) is not a homopolymer of polycondensated TCNBS, since aliphatic poly(siloxane)s do not absorb UV light (**Appendix 4**).

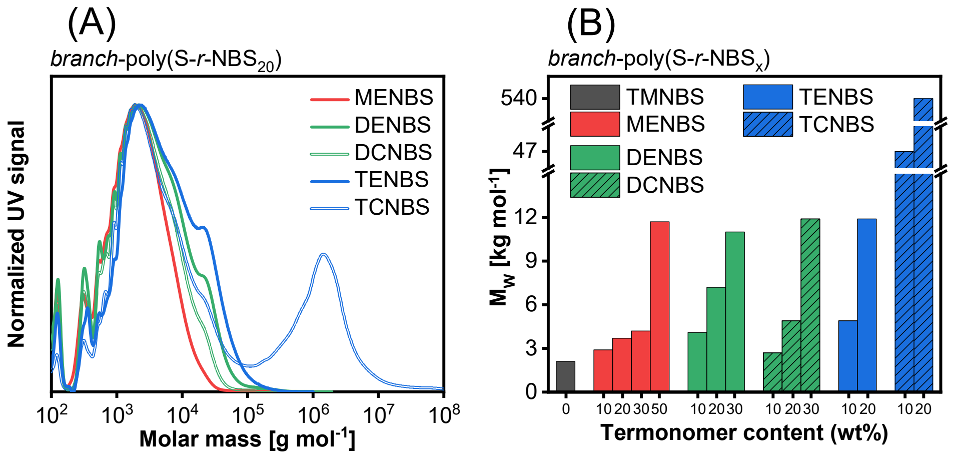

Figure 67. (A) GPC traces of *branch*-poly(S-*r*-NBS$_{20}$) with NBS being either MENBS, DENBS, DCNBS, TENBS, or TCNBS. (B) Comparison of M_W for different *branch*-poly(S-*r*-NBS$_x$).

The maximum molar mass of fully soluble *branch*-poly(S-*r*-NBS$_x$) polymers was determined by synthesizing *branch*-poly(S-*r*-NBS$_x$) polymers with varying contents of MENBS, DENBS, DCNBS, TENBS, and TCNBS, followed by a determination of their molar mass with GPC (**Figure 67 A**). As a general trend, the M_W of all *branch*-poly(S-*r*-NBS$_x$) increased with increasing amounts of the respective siloxane precursor (**Figure 67 B**). *Branch*-poly(S-*r*-MENBS$_x$) polymers derived from the inverse vulcanization and polycondensation of NBS mixtures exceeding either 50 wt% of MENBS, 30 wt% of DENBS or DCNBS, and 20 wt% of TENBS or TCNBS, were not fully soluble in tetrahydrofuran, dichloromethane, or chloroform. The molar mass (M_N, M_W) and dispersity (Đ) of soluble *branch*-poly(S-*r*-NBS$_x$) was tabulated (**Table 7**).

Table 7. Molar masses (M_N, M_W) and dispersity (Đ) of *branch*-poly(S-*r*-NBS$_x$) with varying contents of M, D, and T siloxane bonds.

Name	M_N [gmol^{-1}]	M_W [gmol^{-1}]	Đ
poly(S-*r*-TMNBS)	1100	2100	1.9
branch-poly(S-*r*-MENBS$_{10}$)	900	2900	3.2
branch-poly(S-*r*-MENBS$_{20}$)	900	3700	4.1
branch-poly(S-*r*-MENBS$_{30}$)	900	4200	4.7
branch-poly(S-*r*-MENBS$_{50}$)	1200	11700	9.8
branch-poly(S-*r*-DENBS$_{10}$)^a	1100	4100	3.7
branch-poly(S-*r*-DENBS$_{20}$)	1100 ± 100^b	7600 ± 700^b	6.5
branch-poly(S-*r*-DENBS$_{30}$)^a	1100	11000	10.0
branch-poly(S-*r*-DCNBS$_{10}$)^a	900	2700	3.0
branch-poly(S-*r*-DCNBS$_{20}$)	1100	4900	4.5
branch-poly(S-*r*-DCNBS$_{30}$)^a	1100	11900	10.1
branch-poly(S-*r*-TENBS$_{10}$)^a	1900	8600	4.5
branch-poly(S-*r*-TENBS$_{20}$)	1900	11000	5.8
branch-poly(S-*r*-TCNBS$_{10}$)^a	800	47000	59
branch-poly(S-*r*-TCNBS$_{20}$)	1400	540000	386

^{a}GPC traces can be found in **Appendix 5**. ^{b}Average and SD (n=3)

The M_N of three independently prepared *branch*-poly(S-*r*-DENBS$_{20}$) polymers was 1100 ± 100 g mol^{-1} and the M_W was 7600 ± 700 g mol^{-1}, demonstrating an acceptable reproducibility (**Figure 68**).

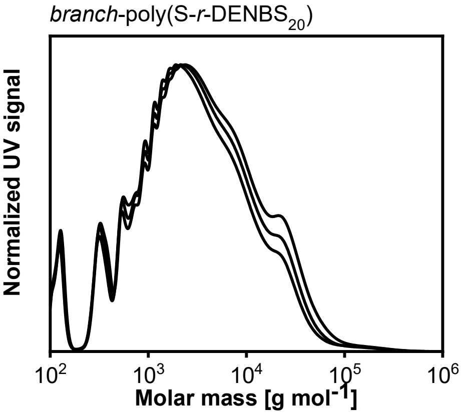

Figure 68. GPC traces for three independently prepared samples of *branch*-poly(S-*r*-DENBS$_{20}$) to investigate the reproducibility of the obtained molar mass. M_N = 1100 ± 100 g mol^{-1}, M_W = 7600 ± 700 g mol^{-1}.

The incorporation of increasing amounts of D, and T siloxanes bonds in *branch*-poly(S-*r*-NBS$_x$) polymers was confirmed with ATR FT-IR (**Figure 69**). In the spectra of *branch*-poly(S-*r*-DENBS$_x$), no peaks assigned to the norbornene C=C double bond (1333, 891, and 717 cm^{-1}) or ethoxy substituents (1164, 1103, 1074, and 948 cm^{-1}) groups of DENBS were found, indicating quantitative conversion of these functional groups during the inverse vulcanization and polycondensation, respectively. Instead, broad D siloxane peaks emerged at 1069, 1052, and 1012 cm^{-1}, which increase from *branch*-poly(S-*r*-DENBS$_{10}$) to *branch*-poly(S-*r*-DENBS$_{20}$), to *branch*-poly(S-*r*-DENBS$_{30}$). In the spectra of *branch*-poly(S-*r*-DCNBS$_x$), no peaks assigned to the norbornene C=C double bond (1335, 891, and 718 cm^{-1}) or chloro substituents (537 cm^{-1}) groups of DCNBS were found, indicating quantitative conversion of these functional groups during the inverse vulcanization and polycondensation, respectively. Instead, broad D siloxane peaks emerged at 1071, 1052, and 1014 cm^{-1}, which increase from *branch*-poly(S-*r*-DCNBS$_{10}$) to *branch*-poly(S-*r*-DCNBS$_{20}$), to *branch*-poly(S-*r*-DCNBS$_{30}$). The D siloxane bands in *branch*-poly(S-*r*-DENBS$_x$) polymers were very similar to those in *branch*-poly(S-*r*-DCNBS$_x$), indicating a similar microstructure, such as cycles and linear chains of similar chain length.

In the spectra of *branch*-poly(S-*r*-TENBS$_x$), no peaks assigned to the norbornene C=C double bond (1335, 891, and 706 cm^{-1}) or ethoxy substituents (1164, 1101, 1074, and 953 cm^{-1}) groups of TENBS were found, indicating quantitative conversion of these functional groups during the inverse vulcanization and polycondensation, respectively. Instead, broad T siloxane peaks emerged at 1100, 1077, and 1026 cm^{-1}, which increase from *branch*-poly(S-*r*-TENBS$_{10}$) to *branch*-poly(S-*r*-TENBS$_{20}$), to *branch*-poly(S-*r*-TENBS$_{30}$). For polycondensated poly(S-*r*-TENBS$_{30}$) only the soluble fraction of a mixture of soluble *branch*-poly(S-*r*-TENBS$_{30}$) and insoluble *net*-poly(S-*r*-TENBS$_{30}$) was precipitated and thus examined. In the spectra of *branch*-poly(S-*r*-TCNBS$_x$), no peaks assigned to the norbornene C=C double bond (1335, 890, and 710 cm^{-1}) or chloro substituents (563 cm^{-1}) groups of TCNBS were found, indicating quantitative conversion of these functional groups during the inverse vulcanization and polycondensation, respectively. Instead, broad T siloxane peaks emerged at 1098, 1051, and 1028 cm^{-1}, which increase from *branch*-poly(S-*r*-TCNBS$_{10}$) to *branch*-poly(S-*r*-TCNBS$_{20}$). The absorbance of the T siloxane bands in the spectrum of *branch*-poly(S-*r*-TCNBS$_{30}$) barely increases compared to the spectrum of *branch*-poly(S-*r*-TCNBS$_{20}$). This is because polycondensated poly(S-*r*-TCNBS$_{30}$) is not fully soluble in THF and consists of a mixture of *branch*-poly(S-*r*-TCNBS$_{30}$) and *net*-poly(S-*r*-TCNBS$_{30}$). Thus, only the soluble *branch*-poly(S-*r*-TCNBS$_{30}$) was precipitated, which contains fewer T siloxane bonds. The T siloxane peaks in *branch*-poly(S-*r*-TENBS$_x$) polymers differed from those in *branch*-poly(S-*r*-TCNBS$_x$) in terms of the line shape and peak location, which indicates different microstructures, such as cages or networks. Full spectra can be found in **Appendix 6-11**.

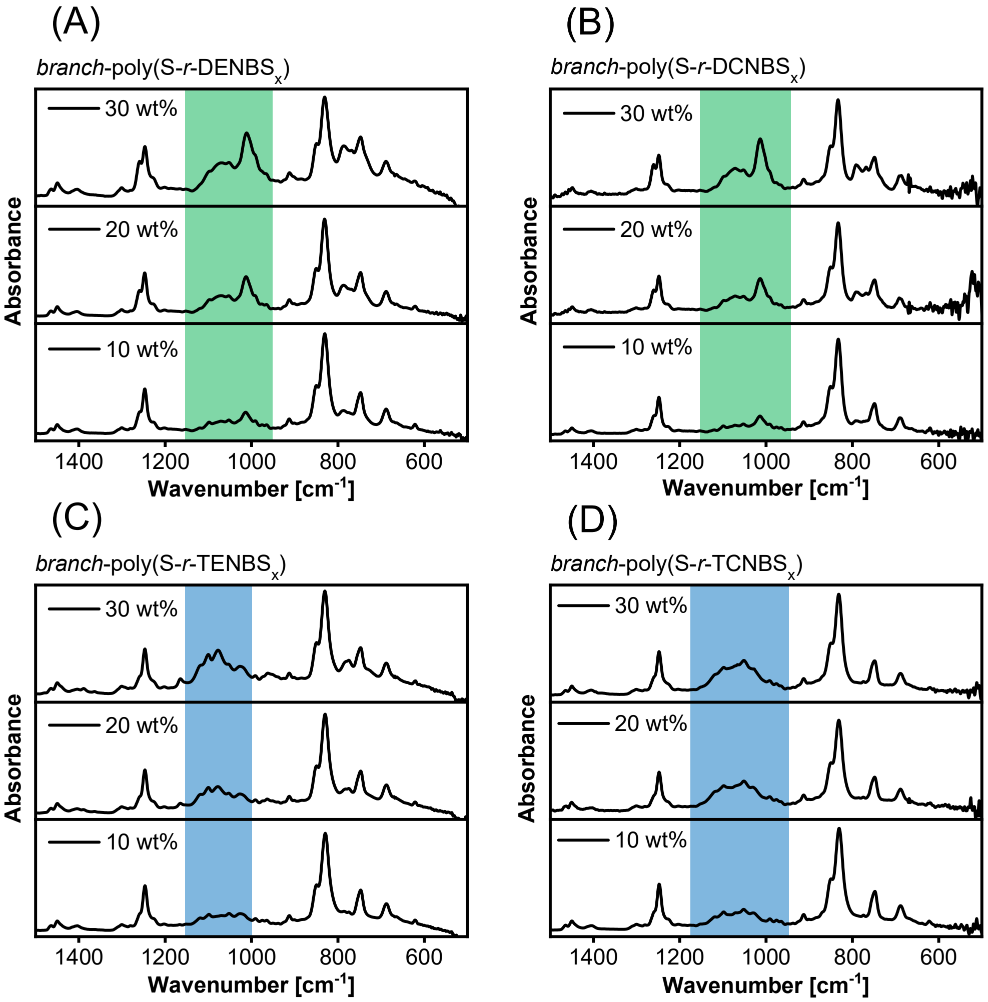

Figure 69. Insets of ATR FT-IR spectra (1500 – 500 cm^{-1}) of (A) *branch*-poly(S-*r*-DENBS$_x$), (B) *branch*-poly(S-*r*-DCNBS$_x$), (C) *branch*-poly(S-*r*-TENBS$_x$), and (D) *branch*-poly(S-*r*-TCNBS$_x$) for *x* being 10, 20, and 30 wt%. Green areas highlight D siloxane vibrations, blue areas highlight T siloxane vibrations.

3.2.12 Molar mass analysis of poly(S$_x$-*r*-DENBS$_{20}$)

To investigate the influence of the sulfur feed ratio on the inverse vulcanization and polycondensation of NBS, *branch*-poly(S$_x$-*r*-DENBS$_{20}$) was chosen as a model system and the feed ratio of sulfur was varied from 30, 40, 50, 60, to 70 wt% of the total mass. The DENBS$_x$ ratio was kept constant at 20 wt% of DENBS and 80 wt% of TMNBS. After the inverse vulcanization, melt polycondensations for all poly(S$_x$-*r*-DENBS$_{20}$) were conducted under identical conditions. The resulting polymers were precipitated in MeOH, and their molar mass was analyzed by GPC. The elemental composition was confirmed using elemental analysis.

The sulfur feed ratio was found to significantly influence the molar mass and the polydispersity of poly(S$_x$-*r*-DENBS$_{20}$). For low sulfur feed ratios, i.e., 30 and 40 wt%, narrow molar mass distributions without low molar mass species were obtained (**Figure 70**). Therefore, the M$_N$ of *branch*-poly(S$_{30}$-*r*-DENBS$_{20}$) and *branch*-poly(S$_{40}$-*r*-DENBS$_{20}$) were higher than for any other *branch*-poly(S-*r*-NBS$_x$) polymer (M$_N$ = 2400, M$_W$ = 6000, Đ = 2.5, and M$_N$ = 2700, M$_W$ = 13900, Đ = 5.2, respectively).

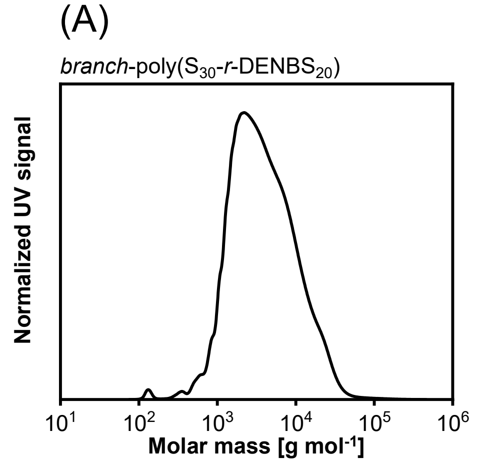

Figure 70. GPC traces of *branch*-poly(S$_x$-*r*-DENBS$_{20}$) with sulfur feed ratios of (A) 30 wt% (M$_N$ = 2400 g mol^{-1}, M$_W$ = 6000 g mol^{-1}, Đ = 2.5) and (B) 40 wt% (M$_N$ = 2700 g mol^{-1}, M$_W$ = 13900 g mol^{-1}, Đ = 5.2).

For high feed ratios of sulfur, i.e., 60 and 70 wt%, a significant amount of low molar mass species was found, which increased with increasing sulfur feed ratio (**Figure 71**). Therefore, the average molar mass of *branch*-poly(S$_{60}$-*r*-DENBS$_{20}$) and *branch*-poly(S$_{70}$-*r*-DENBS$_{20}$) were low (M$_N$ = 700 g mol^{-1}, M$_W$ = 5800 g mol^{-1}, Đ = 8.3 and M$_N$ = 600 g mol^{-1}, M$_W$ = 2900 g mol^{-1}, Đ = 4.8, respectively).

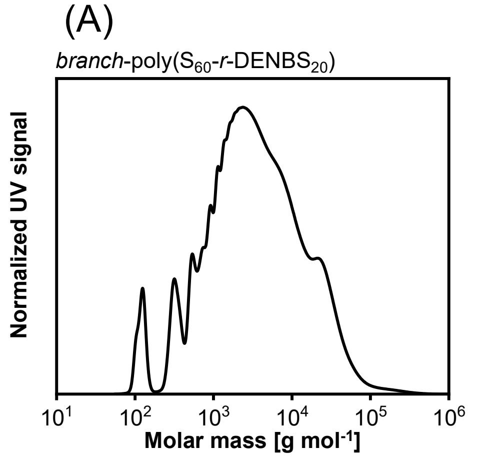

Figure 71. GPC traces of *branch*-poly(S$_x$-*r*-DENBS$_{20}$) with sulfur feed ratios of (A) 60 wt% (M$_N$ = 700 g mol^{-1}, M$_W$ = 5800 g mol^{-1}, Đ = 4.8) and (B) 70 wt% (M$_N$ = 600 g mol^{-1}, M$_W$ = 2900 g mol^{-1}, Đ = 4.8).

M$_N$, M$_W$, and Đ of *branch*-poly(S$_x$-*r*-DENBS$_{20}$) were plotted vs. the sulfur feed ratio to analyize the influence of the sulfur feed ration on the molar mass (**Figure 72**). The lowest polydispersity

Đ of 2.5 was obtained for *branch*-poly(S_{30}-*r*-$DENBS_{20}$), after which it increased from 5.2 of *branch*-poly(S_{40}-*r*-$DENBS_{20}$) to 7.2 for *branch*-poly(S_{50}-*r*-$DENBS_{20}$), to 8.3 for *branch*-poly(S_{60}-*r*-$DENBS_{20}$). *Branch*-poly(S_{70}-*r*-$DENBS_{20}$) had the second lowest dispersity Đ of 4.8, which is due to its low M_W. The maximum of M_N and M_W was 2700 g mol^{-1} and 13900 g mol^{-1} was found for *branch*-poly(S_{40}-*r*-$DENBS_{20}$).

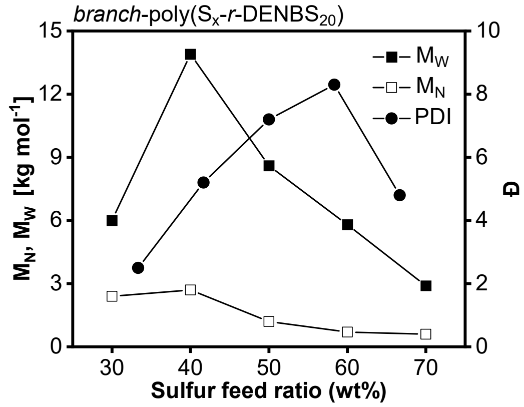

Figure 72. Molar mass M_N, M_W, and polydispersity Đ of *branch*-poly(S_x-*r*-$DENBS_{20}$) in dependence of the sulfur feed ratio for *x* being 30, 40, 50, 60, or 70 wt%.

To determine whether the sulfur feed ratio resembled the sulfur content in the *branch*-poly(S_x-*r*-$DENBS_{20}$), their elemental composition was determined using elemental analysis. The sulfur feed ratio of *branch*-poly(S_{30}-*r*-$DENBS_{20}$), *branch*-poly(S_{40}-*r*-$DENBS_{20}$), *branch*-poly(S_{50}-*r*-$DENBS_{20}$), and *branch*-poly(S_{60}-*r*-$DENBS_{20}$) matched the determined content of sulfur, i.e., 32.7, 41.4, 50.9, and 57.9 wt% S, respectively. However, for *branch*-poly(S_{70}-*r*-$DENBS_{20}$) only 57.8 wt% were obtained, which indicates a maximum sulfur uptake of 58 wt% by a 20:80 wt% mixture of DENBS and TMNBS. This agrees with the visible presence of residual sulfur after the synthesis of poly(S_{70}-*r*-$DENBS_{20}$).

3.2.13 Stability of *branch*-poly(S-*r*-NBS_{20}) against degradation

It is important to confirm that high sulfur content polymers do not degrade back into elemental sulfur since this would lead to drastic changes in the mechanical and chemical properties of a material and could cause fatal material failure. Thus, the presence of crystalline sulfur was tested for *branch*-poly(S-*r*-NBS_{20}), with NBS being MENBS, DENBS, DCNBS, TENBS, and TCNBS. After a storage time of one month, all *branch*-poly(S-*r*-NBS_{20}) were free of elemental sulfur, as indicated by the absence of sulfur melting peaks in DSC curves and the absence of crystalline reflexes in pXRD patterns (**Figure 73**, **Appendix 12**).

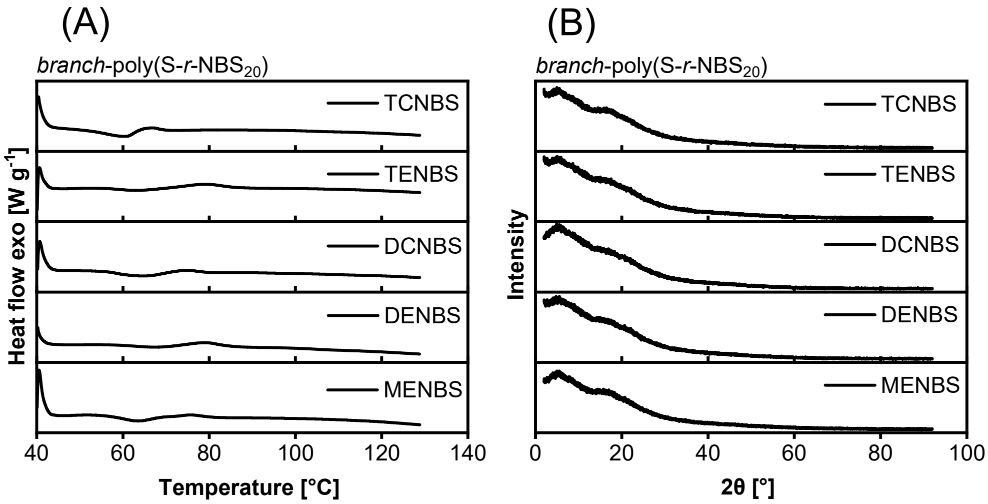

Figure 73. (A) DSC thermograms of the first heat ramp of *branch*-poly(S-*r*-NBS_{20}) from 40 – 130°C and (B) pXRD patterns of *branch*-poly(S-*r*-NBS_{20}) from 2 – 90 ° (2θ) for NBS being MENBS, DENBS, DCNBS, TENBS, and TCNBS.

CIHANER reported the appearance of sulfur crystals on the surface of poly(S-*r*-DIB) with a sulfur content of 80 wt%.[115] It appeared likely, that the presence of micro-sized crystals on the surface of *branch*-poly(S-*r*-NBS_{20}) polymers would remain unnoticed using bulk methods such as DSC and pXRD. Thus, a combination of secondary electron microscopy (SEM) and energy dispersive x-ray spectroscopy (EDX) was used to investigate the surface of *branch*-poly(S-*r*-NBS_{20}) powders for signs of degradation to elemental sulfur. All samples were aged for at least one month prior to the measurements. The surface analysis was conducted in two steps: First, an SEM image of the surface of powdered *branch*-poly(S-*r*-NBS_{20}) was taken. EDX spectra of the bulk *branch*-poly(S-*r*-NBS_{20}) were taken as background, and further spectra of surface inhomogeneities, such as grains, were taken. Because of the high spatial resolution of EDX spectroscopy, the spectrum of a grain of sulfur would only show the characteristic x-ray emission lines of elemental sulfur. As displayed for *branch*-poly(S-*r*-$DENBS_{20}$), the background spectra of the grain and the background were almost identical and showed the presence of silicon and sulfur (**Figure 74**). The same result was obtained for all other EDX spectra of the background and grains of *branch*-poly(S-*r*-NBS_{20}), with NBS being MENBS, DCNBS, TENBS, and TCNBS (**Appendix 13).**

The Kα peaks for C and Si were found at 0.27 and 1.74 keV, respectively, and the peaks corresponding to sulfur were found at 0.15 (Lα), 2.3 (Kα), and 2.47 (Kβ) keV.[208] For each powder, a spectrum of the background and at least two spectra of grains were taken to examine the surface-based polymer degradation into elemental sulfur. Samples were coated with carbon prior to the analysis. Thus, the emission peak of carbon is not diagnostic.

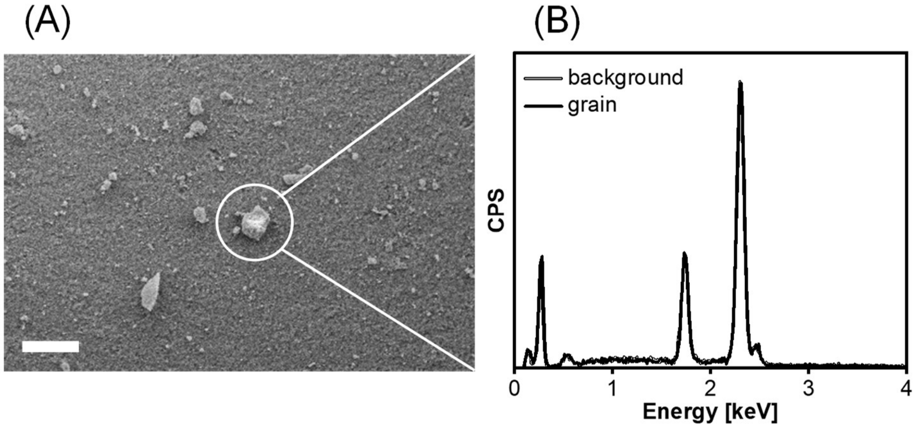

Figure 74. (A) SEM image of the surface of *branch*-poly(S-*r*-NBS$_x$) powder. (B) EDX spectra of the background and the grain highlighted in the SEM image. Scalebar is 20 µm.

3.2.14 Partial polycondensation of poly(S-*r*-MENBS$_x$)

All *branch*-poly(S-*r*-MENBS$_x$) polymers with *x* being 0, 10, 20, 30, and 50 were soluble in tetrahydrofuran, whereas the polycondensation of poly(S-*r*-MENBS$_{100}$) yielded the insoluble *net*-poly(S-*r*-MENBS$_{100}$). The insolubility and brittleness of *net*-poly(S-*r*-MENBS$_{100}$) was attributed to the high degree of M siloxane crosslinking. The degree of crosslinking of *net*-poly(S-*r*-MENBS$_{100}$) can be controlled via partial polycondensation, i.e., by using below stoichiometric amounts of water relative to the hydrolysable ethoxy group (**Figure 75**).

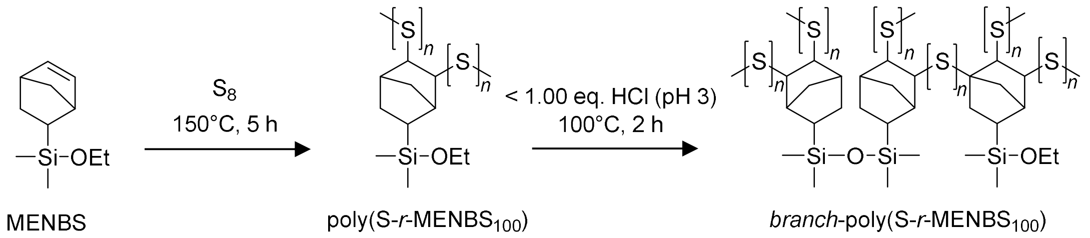

Figure 75. Reaction equation of the inverse vulcanization and partial polycondensation of poly(S-*r*-MENBS$_{100}$) to yield soluble *branch*-poly(S-*r*-MENBS$_{100}$).

Depending on the relative amount of water, partial polycondensation of poly(S-*r*-MENBS$_{100}$) yielded viscous, flexible, and brittle polymers (**Figure 76**).

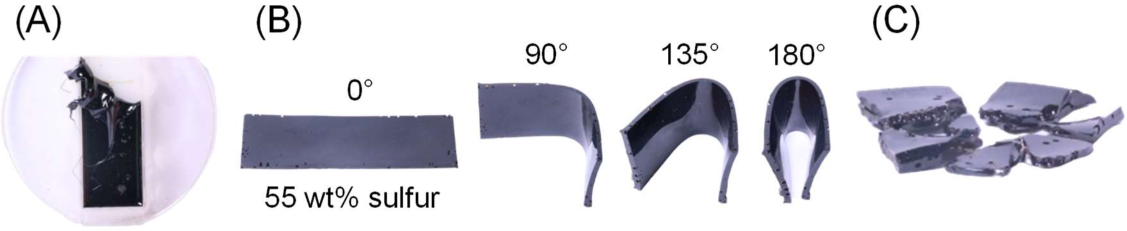

Figure 76. Digital images of a *branch*-poly(S-*r*-MENBS$_{100}$) film prepared using (A) 0.10 eq., (B) 0.20 eq., and 3.00 eq. of HCl (pH 3) for the polycondensation of poly(S-*r*-MENBS$_{100}$). Both (A) and (B) became brittle after several weeks.

Unfortunately, *branch*-poly(S-*r*-MENBS$_{100}$) hardened and became brittle over the course of several weeks. The hardening and increasing brittleness of the partially hydrolyzed *net*-poly(S-*r*-MENBS$_{100}$) is most likely caused by atmospheric moisture, which causes polycondensation of the remaining ethoxy groups and thus increases the crosslinking density (**Figure 77**).

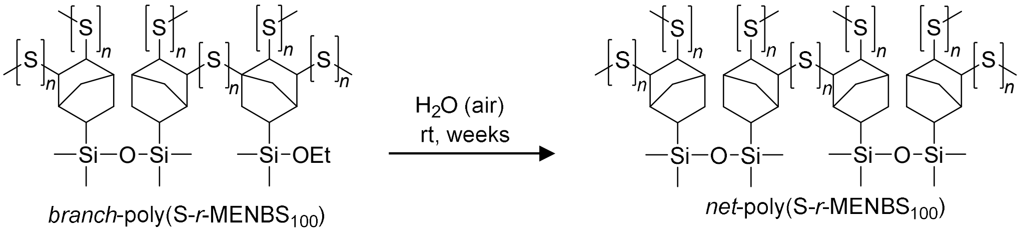

Figure 77. Reaction equation of the polycondensation of soluble *branch*-(S-*r*-MENBS$_{100}$) to form insoluble *net*-poly(S-*r*-MENBS$_{100}$).

Since partially polycondensated *branch*-(S-*r*-MENBS$_{100}$) is soluble in $CDCl_3$, the reaction could be investigated with ^{13}C and ^{29}Si NMR (**Figure 78**). In the ^{13}C NMR spectrum of MENBS, four peaks corresponding to alkene carbon atoms were found at 138.2, 135.6, 134.1, and 133.4 ppm, respectively. No alkene peaks were present in the spectrum of poly(S-*r*-MENBS$_{100}$), indicating quantitative consumption of norbornene C=C double bonds. Peaks assigned to the carbon of ethoxy group ($SiO\mathbf{C}H_2CH_3$) were found at 58.6 and 58.5 ppm in the spectrum of MENBS and at 58.4 and 58.2 in the spectrum of poly(S-*r*-MENBS$_{100}$). After the inverse vulcanization, carbon atoms adjacent to the former alkene carbons experience an upfield shift, whereas peaks emerging between 46.6-41.3 ppm in the spectrum of poly(S-*r*-MENBS$_{100}$) indicate the formation of C-S bonds. Sulfur radicals could add to the norbornene C=C double bonds *syn* or *anti* as well as *exo* or *endo*. Thus, many different isomer combinations are possible, explaining the various C-S bond peaks observed. The shifts from 75.4-67.6 ppm could be explained by partly oxidized sulfide chains or carbons bound to two polysulfide chains. The spectrum of *branch*-poly(S-*r*-MENBS$_{100}$) does not deviate much from the baseline. However, peaks associated with ethoxy group carbons ($SiO\mathbf{C}H_2CH_3$) can still be found at 58.6 and 58.5 ppm, proving the partial hydrolysis of *branch*-poly(S-*r*-MENBS$_{100}$). The decrease of peak intensities from the spectra of MENBS to poly(S-*r*-MENBS$_{100}$) to *branch*-poly(S-*r*-MENBS$_{100}$) is indicative for polymerizations and the increasingly restricted mobility of molecules. In the ^{29}Si NMR spectrum of MENBS two peaks for *exo*-MENBS and *endo*-MENBS were found.

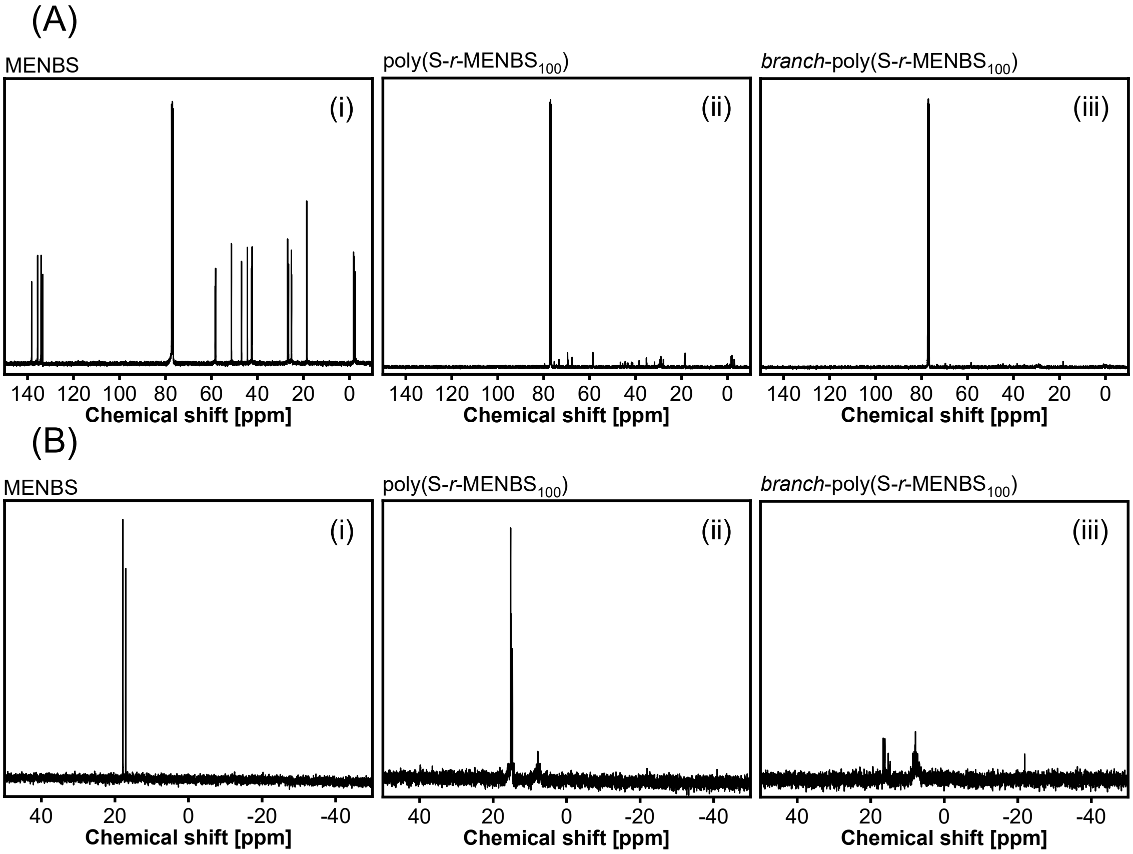

Figure 78. (A) ^{13}C NMR spectra and (B) ^{29} Si NMR spectra of (i) MENBS, (ii) poly(S-*r*-MENBS$_{100}$), and (iii) *branch*-poly(S-*r*-MENBS$_{100}$) in $CDCl_3$. The soluble *branch*-poly(S-*r*-MENBS$_{100}$) was prepared by partial polycondensation of poly(S-*r*-MENBS$_{100}$) with 0.20 eq. of HCl solution (pH 3) relative to the number of ethoxy groups.

In the spectrum of poly(S-*r*-MENBS$_{100}$) the *exo*-MENBS and *endo*-MENBS peaks split up into four peaks and experience a slight upfield shift (15.2, 15.2, 14.9, and 14.7), which is attributed to the *syn*- and *anti*-addition of polysulfide chains to the norbornene C=C double bond. A peak at 7.9 ppm in the spectrum of poly(S-*r*-MENBS$_{100}$) is attributed to the premature formation of M-siloxane bonds due to the hydrolysis and condensation of ethoxy groups. Premature hydrolysis can be caused by water in the NMR solvent ($CDCl_3$) and moisture in the air. In the ^{29}Si spectrum of *branch*-poly(S-*r*-MENBS$_{100}$) the intensity of peaks corresponding to M-siloxanes increased relative to the intensity of peaks corresponding to ethoxy silanes (16.4, 16.4, 16.2, and 15.2). The presence of both M-siloxanes and ethoxy silane moieties is expected, since poly(*S*-*r*-MENBS$_{100}$) was hydrolyzed partially (0.20 eq. of water relative to ethoxy groups). The overall intensity of peaks is reduced because of polymer crosslinking via M-siloxane bonds. In the spectrum of *branch*-poly(S-*r*-MENBS$_{100}$), five M-siloxane moieties rise above the noise level (8.6, 8.4, 8.2, 8.0, and 7.8 ppm) due to the increased amount of M-siloxane bonds in *branch*-

poly(S-*r*-MENBS$_{100}$) compared to poly(*S*-*r*-MENBS$_{100}$), whereas the most intense peak is almost unchanged at 7.8 and 7.9 ppm, respectively.

To elucidate the structure-property relationship of the flexible *branch*-poly(S-*r*-MENBS$_{100}$) and the brittle *net*-poly(S-*r*-MENBS$_{100}$), ATR-FTIR was used (**Figure 79**). *Branch*-poly(S-*r*-MENBS$_{100}$) and *net*-poly(S-*r*-MENBS$_{100}$) were obtained using substoichiometric (0.20 eq.) or overstoichiometric (3.00 eq.) amounts of HCl (pH 3) for the polycondensation of poly(S-*r*-MENBS$_{100}$), respectively. Poly(S-*r*-MENBS$_{100}$) served as a reference, and the characteristic peaks associated with the vibrations of the ethoxy groups in poly(S-*r*-MENBS$_{100}$) were assigned at 1163, 1101, 1076, and 943 cm^{-1}. Upon reaction with 0.20 eq. of H_2O, the intensity of ethoxy peaks at 1163, 1101, and 943 cm^{-1} reduced and the ethoxy peak at 1076 cm^{-1} was covered by the emerging Si-O-Si vibration band centered at 1049 cm^{-1}. For 3.00 eq. of H_2O all peaks related to ethoxy groups disappeared and a siloxane band was observed at 1028 cm^{-1}. Thus, the increase in hardness and brittleness from *branch*-poly(S-*r*-MENBS$_{100}$) to *net*-poly(S-*r*-MENBS$_{100}$) can be attributed to the increase of siloxane bonds.

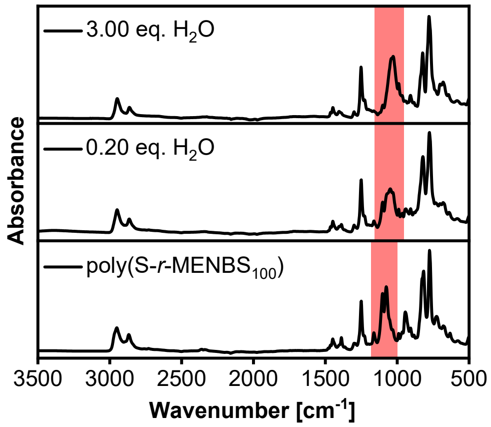

Figure 79. ATR FT-IR spectra of *net*-poly(S-*r*-MENBS$_{100}$) and *branch*-poly(S-*r*-MENBS$_{100}$) prepared using 3.00 eq. and 0.20 eq. of HCl solution (pH 3), respectively. Poly(S-*r*-MENBS$_{100}$) served as a reference. Red areas highlight characteristic vibrations of ethoxy silanes and siloxanes.

3.2.15 Thermomechanical properties of *branch*-poly(S-*r*-NBS$_x$)

The type and amount of siloxane binding in *branch*-poly(S-*r*-NBS$_x$) was expected to influence the thermal properties of the polymers. To investigate the thermal properties of *branch*-poly(S-*r*-NBS$_x$) differential scanning calorimetry (DSC) was employed and the glass transition temperature (T_G) of *branch*-poly(S-*r*-NBS$_x$) was determined for different contents of the M, D, and T precursor (**Figure 80**). With increasing content of siloxane precursor, the T_G increased controllably. The T_G of *branch*-poly(S-*r*-MENBS$_x$) was 10, 14, 18, and 27°C, respectively, for *x* being 10, 20, 30, and 50 wt% of MENBS, respectively, while the T_G of poly(S-*r*-TMNBS), which did not contain siloxane bonds, was 6°C (**Table 8**).

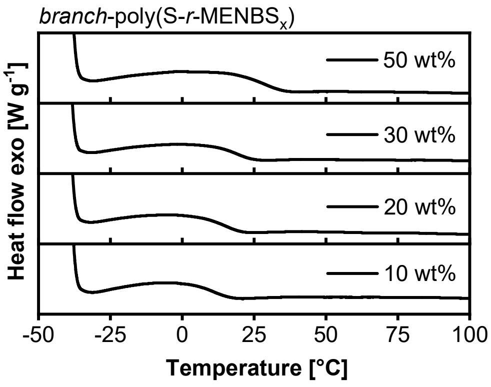

Figure 80. Insets of DSC thermograms of *branch*-poly(S-*r*-MENBS$_x$) with *x* being 10, 20, 30, and 50 wt%.

Table 8. Glass transition temperatures (T$_G$) of *branch*-poly(S-*r*-NBS$_x$) with varying contents of M, D, and T siloxane bonds.

Name	T$_G$ [°C]	Name	T$_G$ [°C]
poly(S-*r*-TMNBS)[a]	6	*branch*-poly(S-*r*-DCNBS$_{10}$)[a]	14
branch-poly(S-*r*-MENBS$_{10}$)	10	*branch*-poly(S-*r*-DCNBS$_{20}$)[a]	23
branch-poly(S-*r*-MENBS$_{20}$)	14	*branch*-poly(S-*r*-DCNBS$_{30}$)[a]	35
branch-poly(S-*r*-MENBS$_{30}$)	18	----------------------------------	
branch-poly(S-*r*-MENBS$_{50}$)	27	*branch*-poly(S-*r*-TENBS$_{10}$)[a]	17
----------------------------------		*branch*-poly(S-*r*-TENBS$_{20}$)[a]	22
branch-poly(S-*r*-DENBS$_{10}$)[a]	15	----------------------------------	
branch-poly(S-*r*-DENBS$_{20}$)[a]	26	*branch*-poly(S-*r*-TCNBS$_{10}$)[a]	11
branch-poly(S-*r*-DENBS$_{30}$)[a]	35	*branch*-poly(S-*r*-TCNBS$_{20}$)[a]	20

[a] DSC thermograms can be found in **Appendix 14**.

For *branch*-poly(S-*r*-DENBS$_x$) the T$_G$ was 15, 26, and 35°C for *x* being 10, 20, and 30 wt%, respectively, while for *branch*-poly(S-*r*-DENBS$_x$) the T$_G$ was 14, 23, and 35°C for *x* being 10, 20, and 30 wt%, respectively. This was expected, since D siloxane bonds cause stronger branching of polymer chains than M siloxane bonds, resulting in a more restricted chain mobility and a higher T$_G$. However, the T$_G$ did not increase further from the D- to the T siloxane bond containing polymers as anticipated. While the T$_G$ of *branch*-poly(S-*r*-TENBS$_{10}$) was the highest amongst the *branch*-poly(S-*r*-NBS$_{10}$) polymers (17°C), the T$_G$s of *branch*-poly(S-*r*-TENBS$_{20}$), *branch*-poly(S-*r*-TCNBS$_{10}$), and *branch*-poly(S-*r*-TCNBS$_{20}$) were comparably low (22, 11, and 20°C, respectively). Presumably, polymers branched by T siloxane bonds do not participate in the chain mobility at the determined T$_G$s. To conclude, the T$_G$ could be increased steadily by the content of M and D siloxane bonds in the polymers. Also, the T$_G$ could be controlled by the type of siloxane bonds, as shown by an increase of the T$_G$ from the M siloxane polymers *branch*-poly(S-*r*-MENBS$_x$) to the D siloxane polymers *branch*-poly(S-*r*-DENBS$_x$) and *branch*-poly(S-*r*-DCNBS$_x$). However, the T$_G$ of T siloxane containing polymers was not indicative for their macroscopic viscous behavior.

To provide a more accurate examination of the thermomechanical properties of *branch*-poly(S-*r*-NBS$_x$) in dependence of the type of siloxane, small amplitude oscillatory shear rheology was conducted using poly(S-*r*-MENBS$_{20}$), *branch*-poly(S-*r*-DCNBS$_{20}$), and *branch*-poly(S-*r*-TCNBS$_{20}$) containing M, D, and T siloxane bonds, respectively. The choice of the type of siloxane in *branch*-poly(S-*r*-NBS$_x$) polymers allowed a controlled increase of the M$_W$, which has significant influence on the viscoelastic properties of polymers. Thus, the storage (G′) and loss moduli (G′′) of poly(S-*r*-MENBS$_{20}$), *branch*-poly(S-*r*-DCNBS$_{20}$), and *branch*-poly(S-*r*-TCNBS$_{20}$) were determined for different temperatures (**Figure 81 A-C**). While *branch*-poly(S-*r*-MENBS$_{20}$) and *branch*-poly(S-*r*-DCNBS$_{20}$) were found to be in the flow regime (G′′ > G′) at 40 and 60°C, *branch*-poly(S-*r*-TCNBS$_{20}$) showed a cross over (G′ = G′′) at 0.17 (60°C), 6.5 (80°C), and 74.5 rad s^{-1} (100°C), before which elastic behavior (G′′ > G′) dominated. At 120°C, *branch*-poly(S-*r*-TCNBS$_{20}$) showed a dominant viscous behavior below 0.22 rad s^{-1}, upon which elastic behavior dominated until 100 rad s^{-1}. After the measurement of *branch*-poly(S-*r*-TCNBS$_{20}$) at 120°C, the polymer had changed chemically. This was indicated by a shift of the cross over at 80°C from 6.51 to 0.99 rad s^{-1}. A decrease of the cross over time relates to a lower relaxation time and presumably indicates the cleavage of sulfur chains due to their dynamic covalent nature at elevated temperatures.[209]

A comparison of the storage and loss moduli of *branch*-poly(S-*r*-NBS$_{20}$) at a temperature of 60°C clearly shows an increase from *branch*-poly(S-*r*-MENBS$_{20}$) to *branch*-poly(S-*r*-DCNBS$_{20}$), and to *branch*-poly(S-*r*-TCNBS$_{20}$) for all frequencies (**Figure 81 B**). For example, the storage and loss moduli at 1 rad s^{-1} were 0.3, 14.0, and 32.5 kPa (G′) and 1.0, 33.0, and 45.0 kPa (G′′) for *branch*-poly(S-*r*-MENBS$_{20}$), *branch*-poly(S-*r*-DCNBS$_{20}$), and *branch*-poly(S-*r*-TCNBS$_{20}$), respectively. The significant difference between the *branch*-poly(S-*r*-NBS$_{20}$) polymers is attributed to the respective M, D, and T siloxane binding.

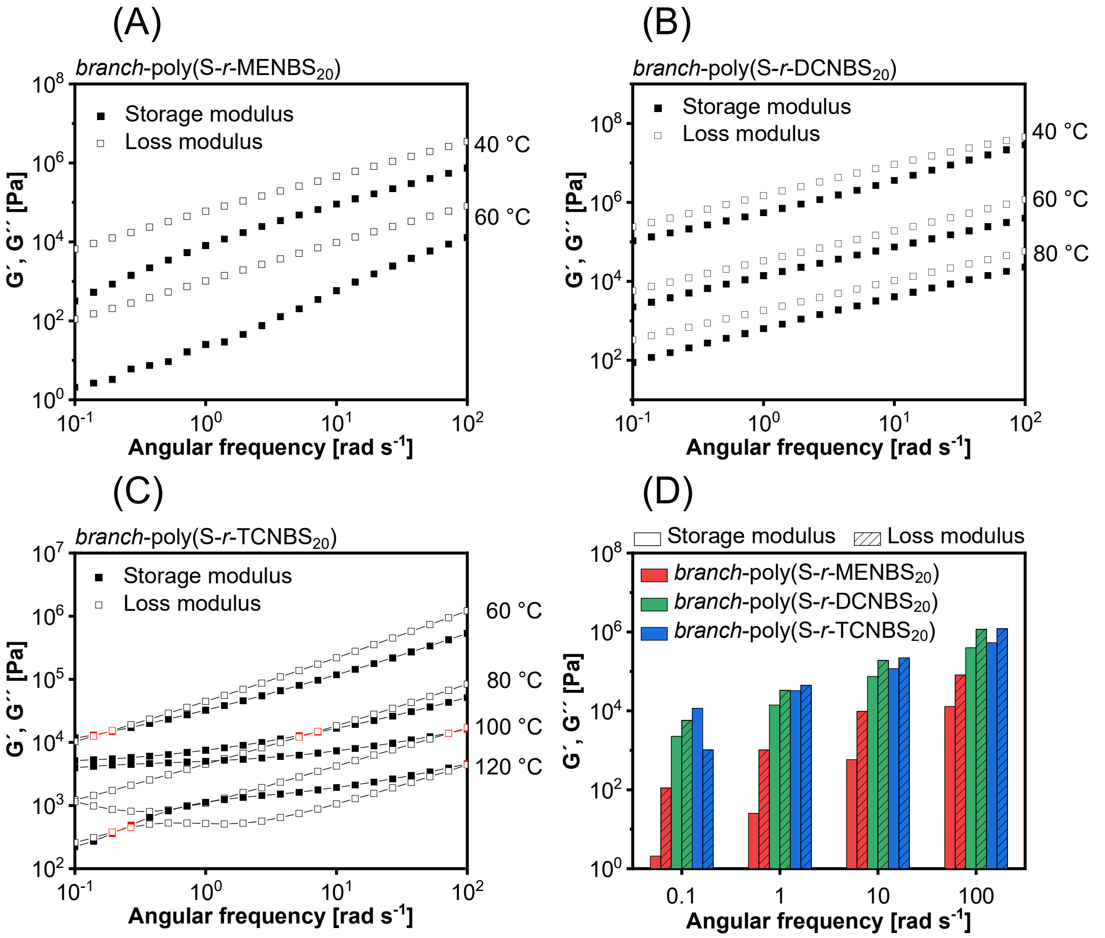

Figure 81. Small amplitude oscillatory shear rheology measurements of the storage (G´) and loss (G´´) modulus of (A) *branch*-poly(S-*r*-MENBS$_{20}$), (B) *branch*-poly(S-*r*-DCCBS$_{20}$), and (C) *branch*-poly(S-*r*-TENBS$_{20}$) at different temperatures. (D) Comparison of G´ and G´´ *branch*-poly(S-*r*-NBS$_{20}$) at 60°C for NBS being MENBS, DCNBS, and TCNBS, respectively. In (C), vicinal data points including cross over points are marked red.

The complex viscosity of *branch*-poly(S-*r*-MENBS$_{20}$) melts was found to be independent of the frequency between 0.1 and 1 rad s^{-1}. Thus, a series of *branch*-poly(S-*r*-MENBS$_x$) with x being 15, 20, and 25 wt% was synthesized to investigate the influence of small compositional differences on the zero-shear viscosity η_0 (**Figure 82**). The zero-shear viscosity η_0 was obtained as the average of the complex viscosity between 0.1 and 1 rad s^{-1} and its standard deviation, i.e., 622 ± 15, 1053 ± 29, 3027 ± 10 Pas at 60°C and 28.500 ± 1100, 63.800 ± 1900, and 149000 ± 12200 Pas at 40°C for *branch*-poly(S-*r*-MENBS$_{15}$), *branch*-poly(S-*r*-MENBS$_{20}$), and *branch*-poly(S-*r*-MENBS$_{25}$), respectively. Thus, the zero-shear viscosity increased as predicted with an increasing content of MENBS. The η_0 of *branch*-poly(S-*r*-MENBS$_x$) were within and above the range of PDMS oils (ca. 0.001 – 2000 Pas).[210,211]

The complex viscosity was further determined for *branch*-poly(S-*r*-DCNBS$_{20}$) and *branch*-poly(S-*r*-TCNBS$_{20}$). When comparing the complex viscosity of *branch*-poly(S-*r*-NBS$_{20}$) the highest values were found for *branch*-poly(S-*r*-TCNBS$_{20}$), whereas the complex viscosity of *branch*-poly(S-*r*-MENBS$_{20}$), was the lowest for all frequencies. Unlike *branch*-poly(S-*r*-MENBS$_{20}$), the complex viscosity of *branch*-poly(S-*r*-NBS$_{20}$) and *branch*-poly(S-*r*-TCNBS$_{20}$) is never independent of the frequency.

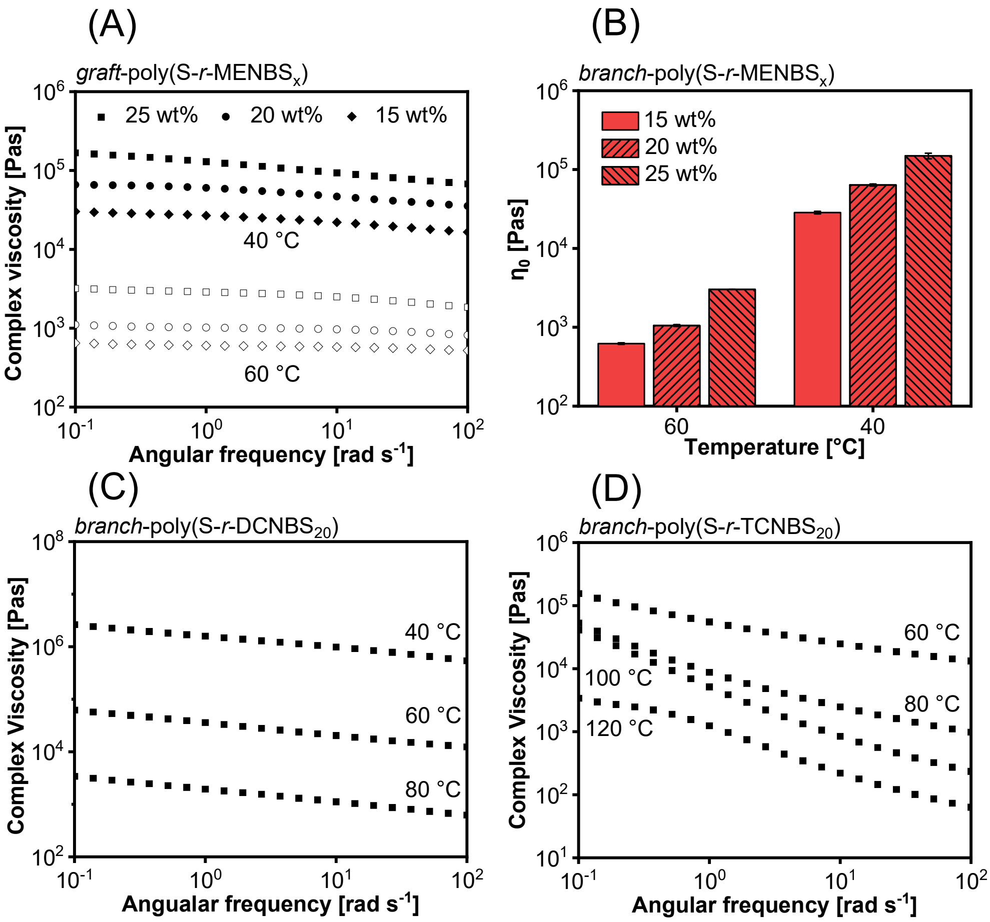

Figure 82. Small amplitude oscillatory shear rheology measurements of the complex viscosity of (A) *branch*-poly(S-*r*-NBS$_{15}$), *branch*-poly(S-*r*-NBS$_{20}$), and *branch*-poly(S-*r*-NBS$_{25}$) at 40 and 60°C (B) Comparison of the zero shear viscosity η_0 of *branch*-poly(S-*r*-NBS$_{15}$), *branch*-poly(S-*r*-NBS$_{20}$), and *branch*-poly(S-*r*-NBS$_{25}$) at 40 and 60°C. Complex viscosity of (C) *branch*-poly(S-*r*-DCNBS$_{20}$) at 40, 60, and 80°C, and (D) *branch*-poly(S-*r*-TCNBS$_{20}$) at 60, 80, 100, and 120°C.

3.2.16 Mechanical properties of *branch*-poly(S-*r*-MENBS$_x$)

To test whether small changes in the MENBS content of *branch*-poly(S-*r*-NBS$_x$) polymers could be used to influence their tensile strength, tensile tests with *branch*-poly(S-*r*-MENBS$_{15}$), *branch*-poly(S-*r*-MENBS$_{20}$), and *branch*-poly(S-*r*-MENBS$_{25}$) polymers were performed (**Figure 83**). All three polymers were able to maintain more than 1000% strain without breaking as expected from the viscoelastic liquid-like behavior observed from rheology. The maximum stress required to deform the polymers was very low but increased with the MENBS content: 122 ± 3 kPa for *branch*-poly(S-*r*-MENBS$_{15}$) 265 ± 84 kPa for *branch*-poly(S-*r*-MENBS$_{20}$), and 418 ± 55 kPa for *branch*-poly(S-*r*-MENBS$_{25}$). The low strength can partly be attributed to the high room temperature (28°C) during the time of the measurements, which was 15°C above the T_G of *branch*-poly(S-*r*-MENBS$_{20}$). The toughness of *branch*-poly(S-*r*-MENBS$_x$) was also enhanced with the MENBS content, which was determined to be 0.40 ± 0.06 MJ m^{-3} for *branch*-poly(S-*r*-MENBS$_{15}$), 1.41 ± 0.48 MJ m^{-3} for *branch*-poly(S-*r*-MENBS$_{20}$), and 1.97 ± 0.37 MJ m^{-3} for *branch*-poly(S-*r*-MENBS$_{25}$).

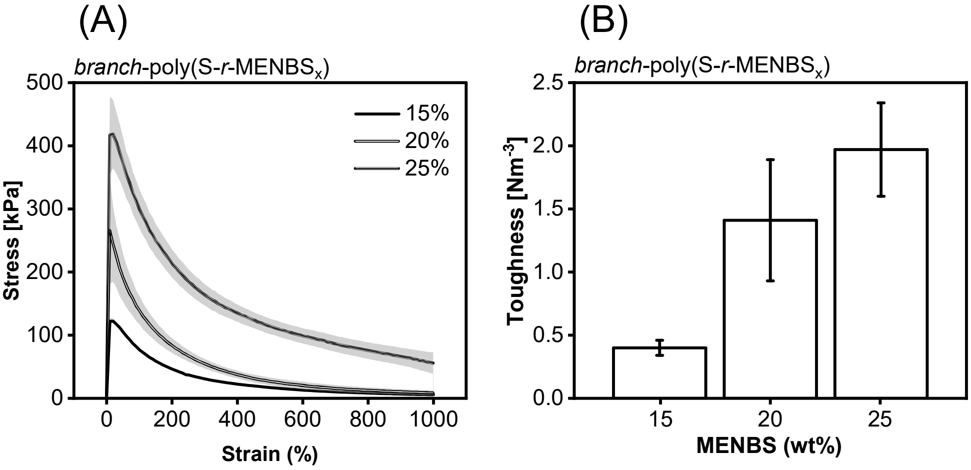

Figure 83. (A) Tensile strength measurements and (B) comparison of the toughness of *branch*-poly(S-*r*-MENBS$_{15}$), *branch*-poly(S-*r*-MENBS$_{20}$), and *branch*-poly(S-*r*-MENBS$_{25}$). Curves and bars are the average of three experiments and error bars are the standard error (N = 3).

3.2.17 Summary

The first ever inverse vulcanizations of ethoxy- and chlorosilanes have been conducted. This strongly hints towards a general compatibility of hydrolysable alkenylsilanes with the inverse vulcanization. Ethoxy- and chlorosilanes used as termonomers were strongly influenced by the properties of inverse vulcanized polymers through M, D, or T siloxane bonds between polymer chains. Both the amount and the type of siloxane bonds could alter the properties of *branch*-poly(S-*r*-NBS$_x$) polymers significantly, while the amount of sulfur could be kept high at ca. 50 wt%. For example, an increase of M-M siloxane bonds in *branch*-poly(S-*r*-MENBS$_x$) caused an increase of the T_G, M_W, η_0 and the tensile strength.

Hydrolysable alkenylsilanes thus appear to be a useful and generally applicable additive for previously described inverse vulcanizations to regulate their molecular and mechanical properties. The siloxane-based approach herein is amongst the first strategies to induce control over inverse vulcanization polymers via post-crosslinking. For the first time, the branching of high sulfur content polymers below the threshold of insolubility and crosslinking has been explored systematically. A near quantitative removal of low molar mass species for *branch*-poly(S$_{30}$-*r*-DENBS$_{20}$) and *branch*-poly(S$_{40}$-*r*-DENBS$_{20}$) was achieved via precipitation to yield a unimodal and a bimodal molar mass distribution, respectively. Such inverse polymers are an important step towards inverse vulcanized model polymers, which are required for standardization and calibration.

3.3 Inverse Vulcanization of Vinyl(cyclo)siloxanes

3.3.1 Introduction

The preparation of flexible and strong polymers with a high content of sulfur has not been achieved in a one-step inverse vulcanization, yet. PYUN and HASELL prepared elastic inverse vulcanized polymers whose strengths were comparable to commercial polymers. However, they relied on post-modification with urethane bonds, which resulted in a reduction of the sulfur content to ca. 20 wt%. Typically, inverse vulcanized polymers prepared from sulfur and monoalkenes such as 10-undecen-1-ol results in viscous oils or creeping, waxy solids composed of low molar mass poly(sulfides).[118,149,212] The rational approach of increasing the amount of C=C double bonds per molecule to facilitate crosslinking, for example by using dialkenes or trialkenes such as 1,3-diisopropylenebenzene or 1,3,5-triisopropenylbenzene leads to glassy, i.e., strong but brittle, materials with little elasticity.[129,213]

There are a few reports about inverse vulcanized polymers showcasing inherent elasticity. FU reported an elastic poly(phenylene tetrasulfide, which requires CS_2 as solvent and 1,3-dithiobenzene as a reagent. Since CS_2 and 1,3-dithiobenzene are toxic and have a limited shelf life, the approach is of limited practical use for the valorization of sulfur on a large scale. Further, the reported molar mass was only 1200 g mol^{-1}, thus, the strength and elasticity of the membrane most likely arose from the carbon nanotube (CNT) paper which was used as a substrate for the polymer.[214] In a similar fashion, researchers started investigating the properties of composites made from sulfur and commercial polymers such as poly(ethylene), Nylon, or poly(styrene).[215,216] A combination of poly(styrene) extrusion with the inverse vulcanization of 1,3-diisopropylenebenzene (DIB) yielded composites with a strength similar to that of poly(styrene) and a far lower brittleness than pure poly(S-*r*-DIB), but the sulfur content is only 10 wt%.[217] Similarly, YAGCI reported on the inverse vulcanization of benzoxazines with poly(butadiene). The flexible polymers obtained from a screening of different compositions contained only 10 – 15 wt% of sulfur.[218] Most crosslinkers used for the inverse vulcanization are vinylaromats or cycloalkenes, e.g., norbornenes, vinylbenzenes, or terpenes, which contain a rigid carbon skeleton, that does not allow free rotational or conformational movement. It was reported that inverse vulcanized polymers prepared from unsaturated fatty acids and for diallyl disulfide flexible materials were obtained.[122,219,220] In fact, the report from ALHASSAN is presumably the only report about a flexible inverse vulcanized polymer with a very high content of sulfur (50 – 90 wt%), which was attributed to flexibility of the S-S bond in diallyl disulfide.[221] Unfortunately, diallyl disulfide is a toxic allergen with a strong smell of garlic, limiting the practical use of the approach.[212] Regardless, these reports demonstrated that the preparation of flexible inverse vulcanized polymers is possible when the comonomer possesses a flexible structure, such as aliphatic chains or disulfide bonds.

The siloxane bond is highly flexible and possesses a very high oxidative and thermal stability.[222] It was thus hypothesized that siloxanes containing vinyl groups could be reacted with sulfur to yield inherently flexible materials. Previous works of inverse vulcanizations using vinylsiloxanes made use of vinylated polyhedral oligomeric silsesquioxanes (POSS). POSS consist of closed-cage structures connected by T siloxane bonds, which are rigid and do not possess the conformational or rotational freedom of linear or cyclic siloxanes.[223,224] Various vinylcyclosiloxanes are commercially available, since they are employed on an industrial scale for the ring opening polymerization of poly(organosiloxane)s. Cyclosiloxane rings are less rigid than those of vinylaromats or cycloalkenes, which might lead to flexible inverse vulcanized polymers. The size of vinylcyclosiloxane rings was expected to have an impact on the mechanical properties of the inverse vulcanized polymer, which could ultimately be useful to synthesize polymers with targeted mechanical properties. Further, it was hypothesized that inverse vulcanized polymers containing cyclosiloxanes could undergo cationic ring opening polymerization to reinforce their network structure or to generate high molar mass polymers.

3.3.2 Nomenclature

3.3.2.1 Monomers

The complex names of vinyl(cyclo)siloxanes were not used in full to improve the readability of the text. The IUPAC names of the respective chemicals were simplified, and acronyms were formed. The simplified names were derived from the amount of vinyl groups (i.e., di, tri, tetra, penta) and the common nomenclature for organosiloxane rings and chains (i.e., MM, D_3, D_4, D_5) respectively. Methyl substituents were excluded from the simplified names (**Table 9**).

Table 9. Nomenclature of vinyl(cyclo)siloxanes in this thesis.

IUPAC name	Simplified name	Acronym
1,1,3,3-tetramethyl-1,3-divinyldisiloxane	Divinylsiloxane-MM	DVS-MM
1,3,5-trimethyl-1,3,5-trivinyltricyclosiloxane	Trivinylcyclosiloxane-D_3	TVS-D_3
1,3,5,7-tetramethyl-1,3,5,7-tetravinyltetracyclosiloxane	Tetravinylcyclosiloxane-D_4	TVS-D_4
1,3,5,7,9-pentamethyl-1,3,5,7,9-pentavinylpentacyclosiloxane	Pentavinylcyclosiloxane-D_5	TVS-D_5

3.3.2.2 Polymers

The products of the inverse vulcanization were termed poly(S_n-*r*-acronym) and poly(S_x-*r*-acronym) in accordance with previous reports on the inverse vulcanization. The index *n* refers to the factual weight percentage of sulfur in the polymer, whereas the index *x* refers to the feed ratio of sulfur.

3.3.3 Inverse vulcanization of TVS-D_4

3.3.3.1 Synthesis and characterization of poly(S_x-*r*-TVS-D_4)

In 2019 HASELL reported zinc bis(diethyldithiocarbamate) to catalyze a broad range of inverse vulcanization reactions. In their work, HASELL firstly reported the inverse vulcanization of TVS-D_4 to demonstrate that the vinylsiloxanes C=C double bond does not react with sulfur at 160°C unless 1 wt% of the zinc bis(diethyldithiocarbamate) catalyst is added (**Figure 84**).[108] The product, poly(S_{50}-*r*-TVS-D_4), was described as insoluble, glassy solid. This result could be reproduced using the same conditions as reported, however, only ca. 120 min instead of 3.5 h were required for the solidification of the reaction mixture. Only traces of poly(S$_{50}$-*r*-TVS-D$_4$) were soluble in dichloromethane, tetrahydrofuran, or toluene. Thus, the feed ratio of sulfur was reduced to 40, 30, and 20 wt% to decrease the degree of crosslinking. For all feed ratios of sulfur, the reaction mixture solidified after 120 min and poly(S$_{40}$-*r*-TVS-D$_4$) was obtained as a brittle solid, whereas poly(S$_{30}$-*r*-TVS-D$_4$) and poly(S$_{20}$-*r*-TVS-D$_4$) yielded a mainly a soft and ductile product, as well as a hard product sticking to the glass.

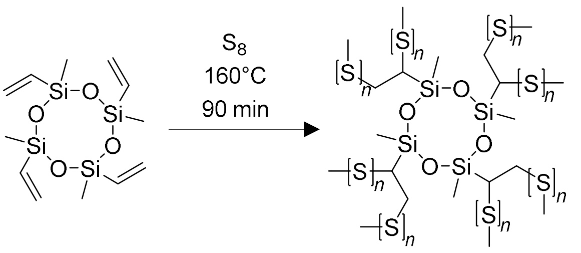

Figure 84. Reaction equation of the inverse vulcanization of TVS-D$_4$ and sulfur to form poly(S$_n$-*r*-TVS-D$_4$).

An investigation of poly(S$_{30}$-*r*-TVS-D$_4$) and poly(S$_{20}$-*r*-TVS-D$_4$) with ATR FT-IR spectroscopy revealed that the consumption of vinyl bonds was incomplete (**Figure 85**). This was concluded from the presence of peaks in the spectra of poly(S$_{30}$-*r*-TVS-D$_4$) and poly(S$_{20}$-*r*-TVS-D$_4$) assigned to different vinyl bond vibrations, e.g., at 3056 cm^{-1} and 3016 cm^{-1} (C-H$_{\text{stretch}}$ in C=C-H), 1598 cm^{-1} (C=C$_{\text{stretch}}$), 1006 cm^{-1} (C-H$_{\text{twist}}$ in C=C-H), and 959 cm^{-1} (C-H$_{\text{wag}}$ in C=C-H).[225] The partial consumption of vinyl groups is evidenced by the decrease of the vinyl peak at 3056 cm^{-1} and the increase of the peaks at 2960 and 2903 cm^{-1} (C-H$_{\text{stretch}}$). The spectra of poly(S$_{30}$-*r*-TVS-D$_4$) and poly(S$_{20}$-*r*-TVS-D$_4$) showed no difference in terms of vinyl group consumption, which might be explained with the presence of the hard and non-retractable side products, which are believed to be poly(S$_n$-*r*-TVS-D$_4$) with a high consumption of vinyl groups. The retractable soft and ductile products thus represent a weakly crosslinked fraction of poly(S$_{30}$-*r*-TVS-D$_4$). Elemental analysis of poly(S$_{30}$-*r*-TVS-D$_4$) confirmed that the soft and ductile fraction must contain less sulfur than the hard, non-retractable fraction of the product, since it contained a less weight percentage of sulfur than the feed ratio, which were 19.3 and 30 wt%, respectively (0.1 wt% N, 34.2 wt% C, 5.6 wt% H).

It appeared possible that the presence of Lewis acidic zinc (II) catalyst at 160°C could initiate a ring opening polymerization of TVS-D$_4$. However, the peak maximum of the broad Si-O-Si absorption shifted insignificantly from 1055 cm^{-1} in the spectrum of TVS-D$_4$ to 1051 cm^{-1} in the spectra of poly(S$_{30}$-*r*-TVS-D$_4$) and poly(S$_{20}$-*r*-TVS-D$_4$). Since the resolution of the spectroscope was set to 4 cm^{-1}, a retention of the cyclosiloxane rings can be assumed.

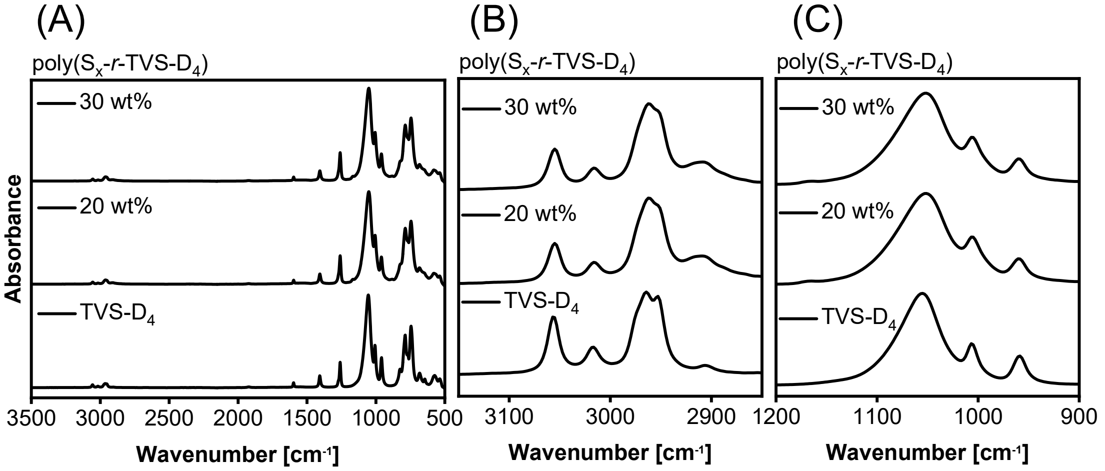

Figure 85. ATR FT-IR spectra of (A) TVS-D_4, poly(S_{20}-*r*-TVS-D_4), and poly(S_{30}-*r*-TVS-D_4). Inset into (B) the C-H stretching region and (C) the Si-O-Si absorbance. The index *x* in S_x refers to the feed ratio of sulfur and not to the factual weight percentage of sulfur.

To confirm the presence of intact cyclosiloxanes instead of linear chains in poly(S_{30}-*r*-TVS-D_4), a cationic polymerization of TVS-D_4 was conducted using 1 wt% of concentrated sulfuric acid (H_2SO_4) as an initiator at 75°C for 1 h to prepare poly(methylvinylsiloxane) as a reference material. The successful ring opening polymerization was indicated by an increase of the viscosity. M_N and M_W of poly(methylvinylsiloxane) after one hour of reaction time were determined to be 140.000 g mol^{-1} and 347.000 g mol^{-1}, respectively (**Figure 86 A**). If the reaction is allowed to proceed for 24 h, an M_N and M_W of 33.500 and 62.000 were obtained, respectively. The decrease of the molar mass accompanied by a decrease of the dispersity Đ from 2.48 to 1.85 observed for longer reaction times is a common phenomenon for ring opening polymerizations of siloxanes, which can be explained by the initial formation of a kinetically favored high molar mass polymer and the equilibration of the chains via transfer reactions into a thermodynamic equilibrium. The refractive indices n of poly(alkylsiloxanes) are around 1.40 at 589 nm and thus similar to that of the GPC eluent tetrahydrofuran (1.4072 at 589 nm). Consequently, the GPC traces as detected by a differential refractive index detector appear noisy.[226,227] UV detectors cannot be used for the detection of poly(alkylsiloxanes), since their UV absorbance above 200 nm is low.[228]

The chemical structure of poly(methylvinylsiloxane) was confirmed with ATR FT-IR (**Figure 86 B**). In the spectrum of poly(methylvinylsiloxane), a splitting of the Si-O-Si peak into two peaks of similar intensity at 1067 cm^{-1} and 1017 cm^{-1} was observed, which is typical for long polyorganosiloxane chains. This can be confirmed by a comparison with the spectrum of commercial poly(dimethylsiloxane) oil (PDMS, 350 cSt), which shows two peaks at 1080 cm^{-1} and 1010 cm^{-1}. Cyclosiloxanes D_3 – D_5 typically show only one Si-O-Si absorption around 1000 cm^{-1}, as observed for the Si-O-Si peak in the spectrum of TVS-D_4 at 997 cm^{-1}. There is a strong absorption in the spectrum of poly(methylvinylsiloxane) at 1002 cm^{-1}, indicating the presence of residual monomer. Diagnostic peaks for the vinyl groups at 3056 cm^{-1} and 3016 cm^{-1} (C-$H_{stretch}$ in C=C-H), 1598 cm^{-1} (C=$C_{stretch}$), 1006 cm^{-1} (C-H_{twist} in C=C-H), and 959 cm^{-1} (C-H_{wag} in C=C-H) were retained in the spectrum of poly(methylvinylsiloxane). From a comparison of the spectra of poly(S_{30}-*r*-TVS-D_4), poly(S_{20}-*r*-TVS-D_4), poly(methylvinylsiloxane), and TVS-D_4 it can be concluded that the inverse vulcanization of TVS-D_4 does not cause ring opening of TVS-D_4 despite the high temperatures of 160°C and the presence of a Lewis acid (Zn^{2+}).

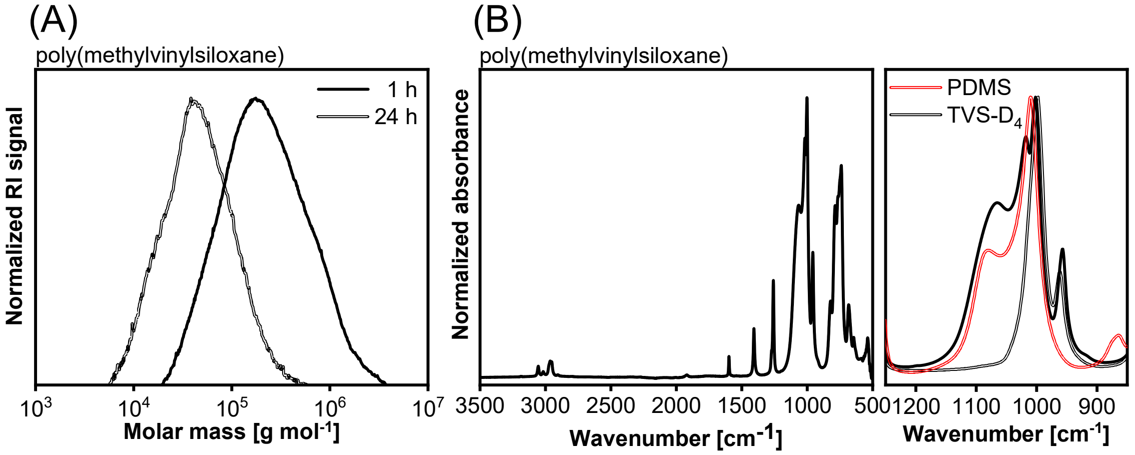

Figure 86. (A) GPC traces and (B) ATR FT-IR spectrum of poly(methylvinylsiloxane). Right: Inset (1300 – 800 cm^{-1}) highlighting the siloxane vibration of poly(methylvinylsiloxane). PDMS (10 cSt) and TVS-D_4 were used as references.

Motivated by these results, the synthesis of poly(S_{30}-*r*-TVS-D_4) was upscaled to the 10 g scale to enable an investigation of its mechanical properties. TVS-D_4 and sulfur were reacted in a vial until a homogeneous liquid phase formed, which was poured into a silicone mold. The mold was kept in an oven for 2 h at 160°C to yield a flexible sheet of poly(S_{30}-*r*-TVS-D_4), which could be bent and twisted gently without breaking (**Figure 87**). Specimens for rheological and mechanical analysis were stamped out of the poly(S_{30}-*r*-TVS-D_4) sheet to obtain circles and dumbbell shapes. Stamping showed to be a better manufacturing method than the direct molding of circle or dumbbell shapes. This is because molded samples were not perfectly flat. Instead, they adopted a slightly paraboloid surface structure, which generated inherent weaknesses towards the thin edges of the material when tensile stress was applied.

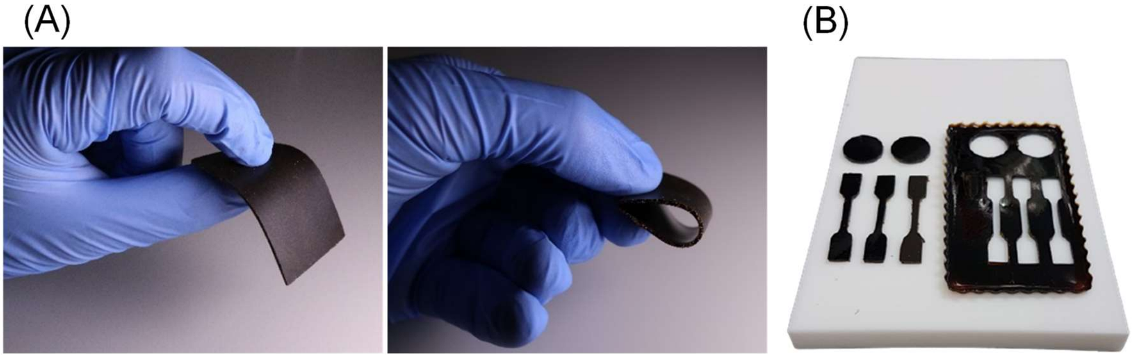

Figure 87. Digital images of (A) a sheet and (B) stamped out specimens of poly(S_{30}-*r*-TVS-D_4). The dimensions of the sheet are 40 × 80 × 1 mm.

To prove the elastic behavior of poly(S$_{30}$-*r*-TVS-D$_4$), small amplitude oscillatory shear rheology was performed at a constant temperature of 30°C (**Figure 88**). From the frequency sweep it could be observed that the storage modulus was higher than the loss modulus (G´<G´´) for all frequencies tested, indicating that the elastic properties of poly(S$_{30}$-*r*-TVS-D$_4$) dominated over its viscous properties. From 0.1 – 3.73 rad s^{-1} the moduli are approximately independent of the frequency, which is typical for rubbery behavior. The complex viscosity decreases monotonously from 1.99 MPas to 5.44 kPas between 0.1 and 100 rad s^{-1} due to shear shinning.

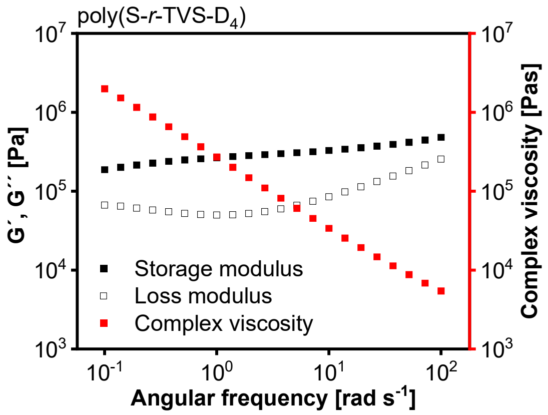

Figure 88. Small amplitude oscillatory shear rheology measurements of poly(S$_{30}$-*r*-TVS-D$_4$).

Poly(organosiloxane)s such as crosslinked PDMS are inherently hydrophobic materials.[229] I was imagined that the incorporation of sulfur would increase the hydrophobicity further. Thus, the static water contact angle (SCA) of a poly(S$_{30}$-*r*-TVS-D$_4$) sheet was determined using a contact angle goniometer (**Figure 89**). A SCA of 123.5 ± 2.0° (N=7) was obtained, which is more hydrophobic than regular PDMS (ca. 100°).[229] Thus, the incorporation of sulfur can make PDMS even more hydrophobic. It would be interesting to further investigate whether the inherently poor resistance of poly(organosiloxane)s against organic solvents can be improved by the introduction of sulfur.

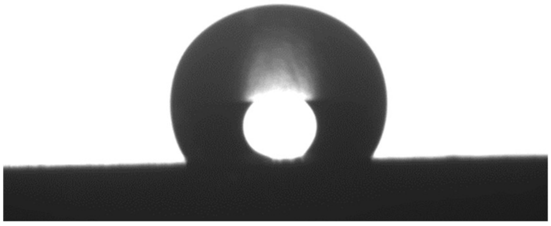

Figure 89. Digital image of a water droplet with a volume of 5 µL on the surface of poly(S$_{30}$-*r*-TVS-D$_4$).

3.3.3.2 Cationic ring opening polymerization of poly(S$_{30}$-*r*-TVS-D$_4$)

The ring opening polymerization (ROP) of cyclosiloxanes is industrially relevant to produce high molar mass poly(organosiloxane)s with a narrow molar mass distribution. It was thus interesting to investigate the potential of ring opening polymerization as a novel post-modification for inverse vulcanized polymers to potentially obtain high molar mass thermoplastics. Since poly(S_{30}-*r*-TVS-D_4) cured for 120 – 150 min is an insoluble solid, the reaction can only be conducted as an interfacial reaction or with partially cured poly(S_{30}-*r*-TVS-D_4) in solution. In a proof of principle experiment, 10 mg L^{-1} triflic acid (TfOH) in dichloromethane (DCM) was brushed onto the surfaces of two poly(S_{30}-*r*-TVS-D_4) discs. The discs were then pressed tightly onto each other for 12 at room temperature. After this time, the two discs were noticeably stuck together, which might be due to interfacial ROP.

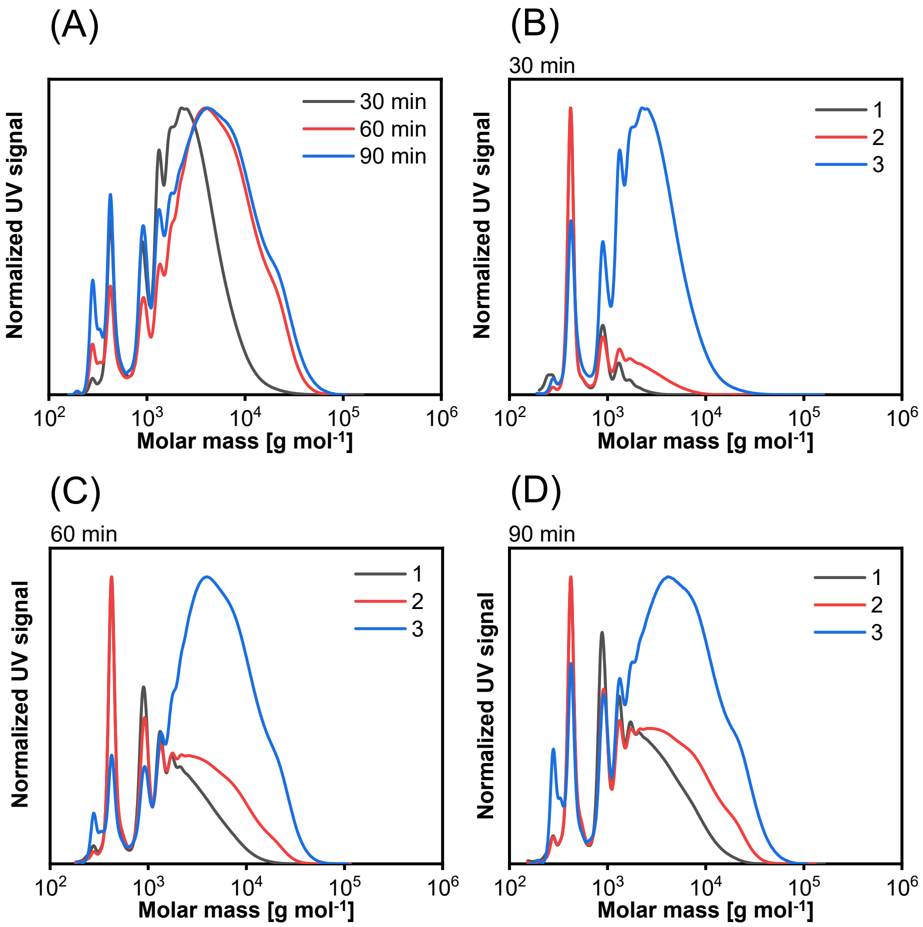

Figure 90. GPC traces of (A) precipitated poly(S_{30}-*r*-TVS-D_n) for different reaction times and (B-D) GPC traces after the reaction steps (1) inverse vulcanization, (2) ROP, and (3) precipitation.

To investigate the ring opening polymerization in solution, partially crosslinked poly(S_{30}-*r*-TVS-D_4) was prepared by reacting TVS-D_4 with sulfur at 160°C for 30, 60, and 90 min in a 70:30 weight ratio using 1 wt% of zinc bis(dithioethylcarbamate) as catalyst. After 30, 60, and 90 min, poly(S_{30}-*r*-TVS-D_4) did not solidify, apart from a black solid forming at the glass of the vials. The liquid fractions of poly(S_{30}-*r*-TVS-D_4) were decanted and dissolved in DCM and 1 wt% of TfOH relative to the mass of poly(S_{30}-*r*-TVS-D_4) was added. The reaction was stirred for 10 min and quenched with DI water. The phases were separated, and the solution of poly(S_{30}-*r*-TVS-D_n) was precipitated in methanol. GPC measurements in THF were conducted for each sample after each step, i.e., after the inverse vulcanization, the ROP, and the precipitation (**Figure 90**).

The molar mass increased with increasing reaction time of the inverse vulcanization of TVS-D_4. For all samples, i.e., 30, 60, and 90 min, an increase of the molar mass after each step was observed. From the increase of the molar mass after the addition of TfOH it can be concluded that a ROP takes place, however, no high molar mass polymers were obtained. This could be due to the short reaction time (10 min) of the ROP or a decreased entropic driving force of chain formation due to sulfur-sulfur crosslinking, which decreases the potential rotational degrees of freedom of the poly(organosiloxane) chain. The precipitation of the poly(S_{30}-*r*-TVS-D_n) proved to be efficient in removing low molar mass species and thus had more impact on the determinable molar mass than the ROP (**Table 10**).

Table 10. Molar masses (M_N, M_W) and dispersity (Đ) of poly(S_{30}-*r*-TVS-D_4) and poly(S_{30}-*r*-TVS-D_n)

Curing Time	Step	M_N [g mol^{-1}]	M_W [g mol^{-1}]	Đ
30 min	(1) Inverse Vulcanization	500	700	1.4
	(2) ROP	600	1300	2.2
	(3) Precipitation	1600	3100	1.9
60 min	(1) Inverse Vulcanization	900	2100	2.3
	(2) ROP	1200	3900	3.3
	(3) Precipitation	2300	6800	3.0
90 min	(1) Inverse Vulcanization	1000	2700	2.7
	(2) ROP	1200	4600	3.8
	(3) Precipitation	1800	7000	3.9

3.3.4 Inverse vulcanization of DVS-MM, TVS-D_3, and PVS-D_5

Inverse vulcanizations of DVS-MM, TVS-D_3, and PVS-D_5 were conducted analogue to the upscaled protocol of inverse vulcanization of TVS-D_4, using a 30 wt% feed ratio of sulfur and 1 wt% of zinc bis(diethyldithiocarbamate) as catalyst (**Figure 91**).

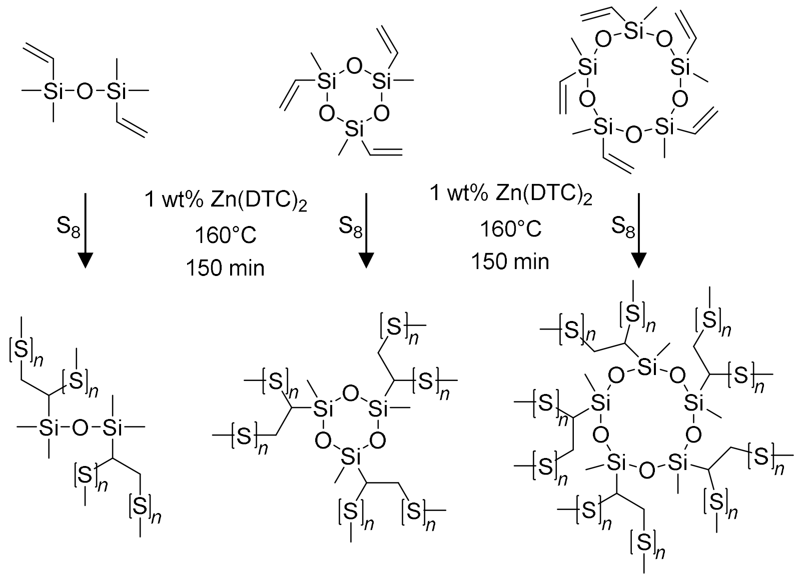

Figure 91. Reaction equation of the inverse vulcanization of poly(S_{30}-*r*-DVS-MM), poly(S_{30}-*r*-TVS-D_3), and poly(S_{30}-*r*-PVS-D_5).

The reactions were started in a vial at 160°C for 30 min until a homogeneous liquid formed, followed by 120 min of curing in an oven at 160°C. Poly(S_{30}-*r*-DVS-MM) was obtained as a flexible but delicate solid, poly(S_{30}-*r*-TVS-D_3) was obtained as a tough but brittle solid, and poly(S_{30}-*r*-PVS-D_5) was obtained as flexible and bendable solid, like poly(S_{30}-*r*-TVS-D_4). The formation of a solid attached to the glass walls was observed for the reactions including poly(S_{30}-*r*-TVS-D_3) and poly(S_{30}-*r*-PVS-D_5).

The polymers were analyzed with ATR FT-IR spectroscopy and elemental analysis (**Table 11**, **Figure 91**). Elemental analysis revealed a counterintuitive trend regarding the sulfur content of the inverse vulcanized polymers. Although DVS-MM contained the least amount of vinyl groups per molecule amongst the monomers tested, poly(S_{30}-*r*-DVS-MM) contained the highest amount of sulfur (40.8 wt%), which even exceeded the feed ratio of sulfur (30 wt%). This can be explained with the boiling point of DVS-MM at 139°C being below the reaction temperature of 160°C. The amount of sulfur further decreased from 24.8 wt% for poly(S_{30}-*r*-TVS-D_3) and 19.3 wt% for poly(S_{30}-*r*-TVS-D_4) to 15.2 wt% for poly(S_{30}-*r*-PVS-D_5). This is attributed to a larger fixation of sulfur as a highly crosslinked inverse vulcanized polymer in the order PVS-D_5 > TVS-D_4 > TVS-D_3.

Table 11. Elemental composition of poly(S-*r*-XVS-XX).

Name[a]	N (wt%)	C (wt%)	H (wt%)	S (wt%)
poly(S_{30}-*r*-DVS-MM)	0.0	30.8	5.7	40.6
poly(S_{30}-*r*-TVS-D_3)	0.1	31.8	5.2	24.8
poly(S_{30}-*r*-TVS-D_4)	0.1	34.2	5.6	19.3
poly(S_{30}-*r*-PVS-D_5)	0.1	36.3	5.9	15.2

[a] The index at sulfur refers to the feed ratio of sulfur.

ATR-FTIR spectra of poly(S_{30}-*r*-DVS-MM) revealed a quantitative conversion of C=C double bonds, as seen by the disappearance of peaks associated with vinyl groups at 3052 cm^{-1} and 3014 cm^{-1} (C-H$_{\text{stretch}}$ in C=C-H), 1596 cm^{-1} (C=C$_{\text{stretch}}$), 1008 cm^{-1} (C-H$_{\text{twist}}$ in C=C-H), 955 cm^{-1} (C-H$_{\text{wag}}$ in C=C-H). The maximum of the siloxane (Si-O-Si) vibration in the spectrum of poly(S_{30}-*r*-DVS-MM) shifted from 1047 cm^{-1} to 1034 cm^{-1} and was strongly broadened in comparison to the spectrum of DVS-MM, which is presumably a consequence of polymerization and solidification. Similar conclusions could be drawn from the ATR FT-IR spectrum of poly(S_{30}-*r*-TVS-D_3), in which no signals corresponding to vinyl groups could be observed, which were identified in the spectrum of TVS-D_3 at 3057 cm^{-1} and 3017 cm^{-1} (C-H$_{\text{stretch}}$ in C=C-H), 1596 cm^{-1} (C=C$_{\text{stretch}}$), and 961 cm^{-1} (C-H$_{\text{wag}}$ in C=C-H). The maximum of the siloxane (Si-O-Si) vibration in the spectrum of poly(S_{30}-*r*-TVS-D_3) shifted from 998 cm^{-1} to 1037 cm^{-1} and was broadened in comparison to the spectrum of TVS-D_3. Residual peaks of vinyl groups were found in the spectrum of poly(S_{30}-*r*-PVS-D_5) at 3054 cm^{-1} and 3016 cm^{-1} (C-H$_{\text{stretch}}$ in C=C-H), 1597 cm^{-1} (C=C$_{\text{stretch}}$), 1009 cm^{-1} (C-H$_{\text{twist}}$ in C=C-H), and 960 cm^{-1} (C-H$_{\text{wag}}$ in C=C-H). The maximum of the siloxane (Si-O-Si) vibration in the spectrum of poly(S_{30}-*r*-PVS-D_5) shifted from 1057 cm^{-1} to 1051 cm^{-1} and was broadened in comparison to the spectrum of TVS-D_3. Further, the intensity of the siloxane (Si-O-Si) peak reduced. Because of peak broadening, the peak maxima of siloxane vibrations in the spectra of the polymers are reduced relative to the spectra of their respective siloxane monomers. No splitting of the Si-O-Si signal was observed for any of the cyclosiloxanes, which would indicate the formation of chains of poly(organosiloxane)s. Thus, it is assumed that the siloxane bonds remained unchanged during the inverse vulcanization and the cyclosiloxane ring structures were retained. Further ^{29}Si NMR experiments will be necessary to verify this assumption.

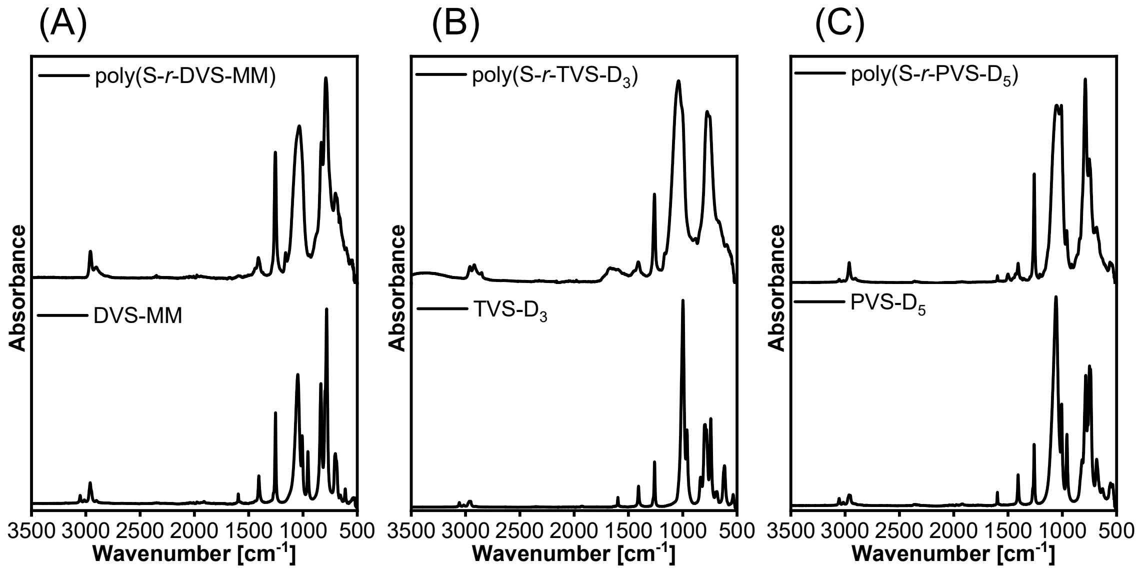

Figure 92. ATR FT-IR spectra of (A) DVS-MM and poly(S_{30}-*r*-DVS-MM),(B) TVS-D_3 and poly(S_{30}-*r*-TVS-D_3), and (C) PVS-D_5 and poly(S_{30}-*r*-PVS-D_5).

3.3.5 DSC, tensile-, and compression tests

To confirm that the poly(S_{30}-*r*-DVS-MM), poly(S_{30}-*r*-TVS-D_3), poly(S_{30}-*r*-TVS-D_4) and poly(S_{30}-*r*-PVS-D_5) did not contain residual crystalline sulfur and to investigate their thermo-mechanical properties DSC was employed (**Figure 93**).

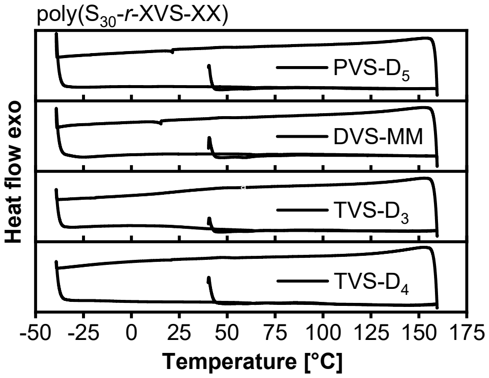

Figure 93. DSC thermograms of poly(S_{30}-*r*-DVS-MM), poly(S_{30}-*r*-TVS-D_3), poly(S_{30}-*r*-TVS-D_4) and poly(S_{30}-*r*-PVS-D_5) from -40 – 160°C with 10 K s^{-1}.

In the first heat ramp from 40 – 160°C no melting peak can be observed and thus the absence of crystalline sulfur was concluded. No signs of degradation were found in the DSC thermograms of poly(S_{30}-*r*-DVS-MM), poly(S_{30}-*r*-TVS-D_3), poly(S_{30}-*r*-TVS-D_4) and poly(S_{30}-*r*-PVS-D_5), which confirms their thermal stability at least up to 160°C. Further, no thermal transitions (e.g., T_M or T_G) could be identified in the DSC thermograms for any of the inverse vulcanized polymers, which is presumably due to their crosslinked structure.

Since poly(S_{30}-*r*-TVS-D_4) and poly(S_{30}-*r*-PVS-D_5) were the seemingly the most flexible polymers regarding reversible deformations such as bending, pulling, or pressing, they were selected for tensile tests (**Figure 94**). In the stress-strain diagrams, both polymers show an elastic deformation until they rupture at a strain of 38.3 ± 3.7 % (N=3) and 32.5 ± 8.1 % (N=3) at a tensile stress of 1.63 ± 0.26 MPa (N=3) and 95.0 ± 25.1 kPa (N=3) for poly(S_{30}-*r*-TVS-D_4) and poly(S_{30}-*r*-PVS-D_5), respectively. The much lesser tensile strength of poly(S_{30}-*r*-PVS-D_5) can presumably be attributed to the lower content compared to poly(S_{30}-*r*-TVS-D_4), i.e., 19.3 vs. 15.2 wt%. This discrepancy is more pronounced when comparing the normalized sulfur content per vinyl group, i.e., 4.8 wt% and 3.04 wt% of sulfur per vinyl group in poly(S_{30}-*r*-TVS-D_4) and poly(S_{30}-*r*-PVS-D_5), respectively. It appears reasonable, that networks consisting of cyclosiloxanes interconnected by polysulfide chains rupture after the cyclosiloxanes conformational flexibility has been exhausted. The network should break via the sulfur-sulfur bonds since they are significantly weaker than Si-O bonds. The energy required to rupture the polymer should be governed by the amount of vinyl groups connected by sulfur. This hypothesis is strengthened by the similar strain at break. However, a larger number of specimens is necessary due to the large standard deviations in between measurements.

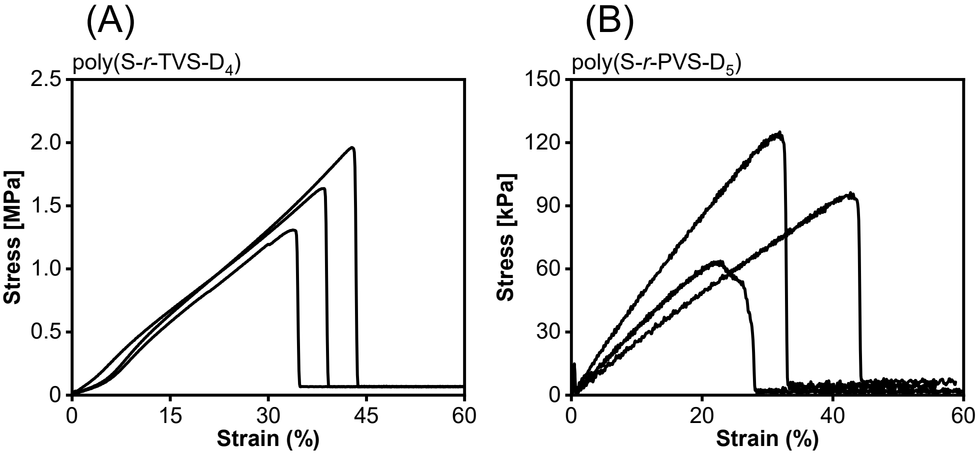

Figure 94. Stress-strain diagrams for poly(S_{30}-*r*-TVS-D_4) and poly(S_{30}-*r*-PVS-D_5). Three specimens were measured for each polymer.

With a tensile strength of 1.63 ± 0.26 MPa, poly(S_{30}-*r*-TVS-D_4) is stronger than any other flexible inverse vulcanized polymers, at least when only inverse vulcanized polymers without additional crosslinking were considered. For example, the tensile strengths of inverse vulcanized polymers prepared by the reaction of sulfur with either diallyl disulfide or cottonseed oil were below 1 MPa.[220,221] However, the maximum elongations of diallyl disulfide based inverse vulcanized polymers were slightly higher (30 – 70 % strain) than for poly(S_{30}-*r*-TVS-D_4) (38.3 ± 3.7 %).

To compare the mechanical properties of poly(S_{30}-*r*-DVS-MM), poly(S_{30}-*r*-TVS-D_3), poly(S_{30}-*r*-TVS-D_4) and poly(S_{30}-*r*-PVS-D_5), compression tests were performed (**Figure 95**). All samples could be compressed to 90% after which no cracks were visible, indicating high ductility. The stress at 90 % strain of poly(S_{30}-*r*-TVS-D_3) and poly(S_{30}-*r*-TVS-D_4) is 46.5 ± 3.9 MPa (N=3) and 42.9 ± 4.7 MPa (N=2), respectively, which is much higher than the stress 11.1 ± 2.4 MPa (N=3) and 3.6 ± 0.98 MPa (N=3) determined for poly(S_{30}-*r*-PVS-D_5) and poly(S_{30}-*r*-DVS-MM), respectively. It appears reasonable, that less energy is required to compress linear siloxane bonds as in poly(S_{30}-*r*-DVS-MM), or a large cyclosiloxane ring as in poly(S_{30}-*r*-PVS-D_5), rather than small or strained cyclosiloxane rings with less conformational freedom as in poly(S_{30}-*r*-TVS-D_4), poly(S_{30}-*r*-TVS-D_3). However, In the comparison of poly(S_{30}-*r*-TVS-D_3), poly(S_{30}-*r*-TVS-D_4) and poly(S_{30}-*r*-PVS-D_5) the sulfur content presumably has a large impact on the compressional stress, too, since the connections between rings restrict their compressibility.

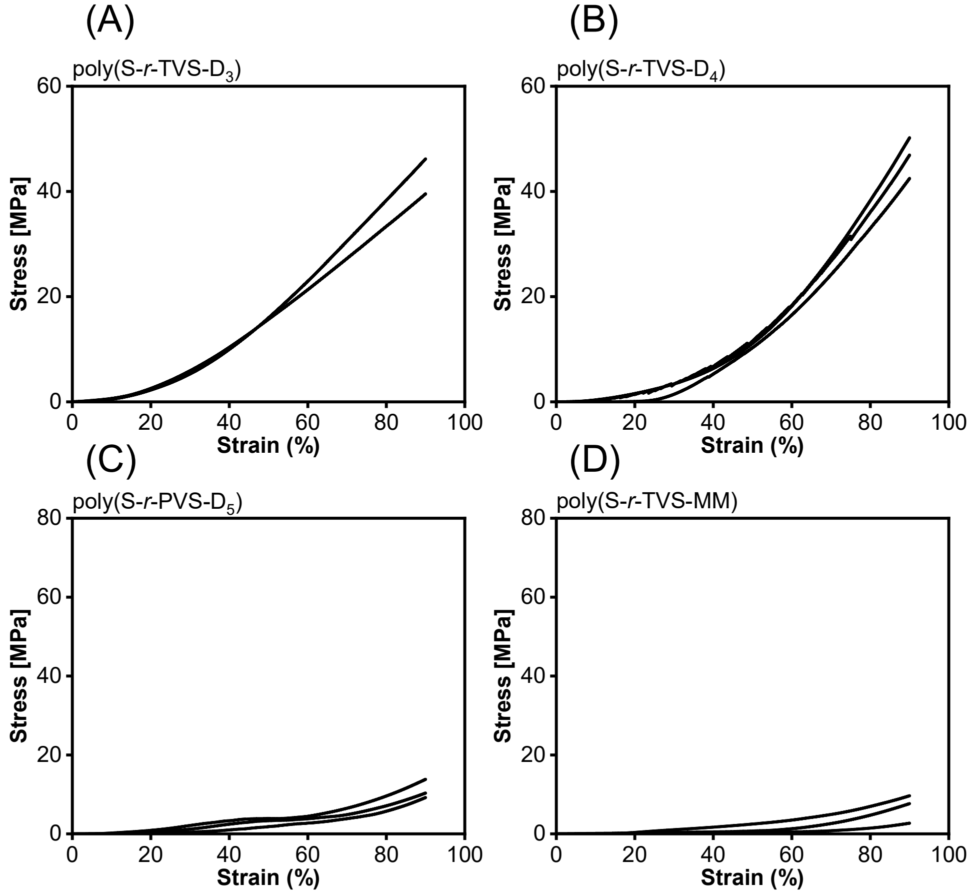

Figure 95. Stress-strain diagrams of compression tests for (A) poly(S_{30}-*r*-TVS-D_3), (B) poly(S_{30}-*r*-TVS-D_4), (C) poly(S_{30}-*r*-PVS-D_5), and (D) poly(S_{30}-*r*-DVS-MM). Three specimens were measured for each polymer.

3.3.6 Summary

A systematic investigation of the inverse vulcanization of vinyl(cyclo)siloxanes has been conducted for the first time, using linear DVS-MM, and the cyclic tri-, tetra-, and pentavinylcyclosiloxanes TVS-D_3, TVS-D_4, and PVS-D_5, respectively. Due to the industrial relevance of cyclosiloxanes for the preparation of poly(organosiloxane)s all chemicals used in this chapter are affordable. This allowed for the generous upscaling of the reactions, which led to a rapid transfer from chemical synthesis to the mechanical analysis of polymers. All polymers except for poly(S_{30}-*r*-TVS-D_3) were non-sticky, bendable and elastic, which is different from most inverse vulcanized polymers reported. These desirable properties are believed to be a result of the flexible silicon-oxygen bond as well as the non-strained nature of cyclosiloxanes ($D_{>3}$). Future synthesis goals aim at the synthesis of inverse vulcanized polymers with identical sulfur contents to allow an improved understanding of the structure-property relationships of these materials. A promising strategy is the sequential addition of sulfur into the monomer at 160°C to avoid the precipitation of highly crosslinked polymers.

4 Experimental

4.1 Analysis

This chapter contains information about the devices and software used to analyze the samples described in this thesis in alphabetical order.

4.1.1 AFM

Atomic force microscopy was conducted using a Dimension Icon with ScanAsyst from Bruker (Billerica, USA). Cantilevers with a resonance frequency of 325 kHz from Olympus (Shinjuku, Japan) were used. The data was curated using the software Gwyddion (General Public License) and NanoScope Analysis from Bruker (Billerica, USA).

4.1.2 ATR FT-IR

Attenuated total reflection Fourier transform infrared spectroscopy was conducted with a Bruker Tensor 27 ATR FT-IR spectrometer from Bruker Optik (Ettlingen, Germany) in a 45° geometry on a diamond crystal (single reflection). Additionally, ATR FT-IR spectra were recorded using a Vertex 80 spectrometer from Bruker Optik (Ettlingen, Germany) in 45° a geometry (single reflection) on a diamond/ZnSe crystal and a MIRacle ATR setup from PIKE Technologies (Madison, USA). Peaks are assigned by their wavenumber and their relative intensity indicated with *vs* (very strong), *s* (strong), *m* (medium), *w* (weak), or *vw* (very weak). Broad signals are indicated with "br.". Diagnostic signals are assigned in brackets. Indexes of assigned vibrations are abbreviated with "stretch" (stretching), "bend" (bending), and "wag" (wagging). For aid the assignment of peaks in experimental ATR FT-IR spectra, suitable references from the literature were consulted.[230-233]

4.1.3 Digital microscopy and light microscopy

Digital microscopy and light microscopy were conducted using a VHX-7000 and a BZ-9000 microscope from Keyence Deutschland (Lichtenfeld, Germany).

4.1.4 DLS

Dynamic light scattering was measured using a Zetasizer Nano ZS from Malvern Instruments (Malvern, United Kingdom) equipped with a 633 nm laser. Dispersions were measured in Suprasil quartz cuvettes with a thickness of 1 cm.

4.1.5 DSC

Differential scanning calorimetry was measured on a Discovery DSC from TA Instruments (Newcastle, USA). Additionally, DSC was measured on a DSC 2500 from TA Instruments (Newcastle, USA). Samples were measured a heat rate of 10 K min^{-1} between -40 and 160°C in Tzero sample holders from TA Instruments (Newcastle, USA). The glass transition temperature (T_G) was determined in the second heat run to eliminate possible interference from the polymer's processing history. The presence of residual sulfur was examined for the first heat ramp.

4.1.6 EDX and SEM

Energy dispersive x-ray spectroscopy and secondary electrom microscopy was conducted with a LEO 1530 scanning electron microscope from Leica (Hillsboro, USA) with an accelerating voltage of 5 – 10 kV. Specimens were sputtered with a thin layer of gold or carbon. For EDX a NORAN System SIX from Thermo Scientific (Waltham, USA) was used.

4.1.7 Elemental analysis

Elemental analysis was carried out using a vario MICRO cube from elementar (Langenselbold, Germany). Samples were measured in the CHNS mode. The amount of sulfur was quantified with an IR detector. Each sample was measured twice to form an average, if they did not differ more than 1 % for any element.

4.1.8 Ellipsometry

Spectroscopic ellipsometry measurements were performed on a M2000 from Woollam (Lincoln, USA). Samples were prepared via spin-coating on silicon wafers (ca. 2 × 2 cm^2). Measurements were taken at an angle of incidence of 45°, 55° and 65° in the spectral range of 300-1000 nm. To evaluate the experimental data, an optical box model was applied using the instrument software CompleteEase (V6.51). Silicon substrates were fitted with database values for Si and SiO_2.[234] To determine the thickness and optical constants of the layer, all spectra of samples with varying thickness were fit together in a multi-sample analysis. For this, the Cauchy function with Urbach extension terms was used to consider the absorption band of the polymer in the UV range. Common fit parameters were A_n, B_n, as well as A_k and B_k. The thickness was allowed to vary freely between samples. As the band edge, 400 nm was assumed.

4.1.9 GPC

Gel permeation chromatography was conducted using a Tosoh EcoSEC GPC system from Tosoh (Tokio, Japan). Samples were dissolved in THF (2 mg mL^{-1}), filtered through 0.43 µm PTFE filters and injected in the Tosoh EcoSEC GPC system from Tosoh (Tokio, Japan) equipped with a SDV 5 µm bead size guard column (50 × 8 mm) followed by three SDV 5 µm columns (300 × 7.5 mm) from PSS (Mainz, Germany) with a pore size of 100, 1000, and 105 , respectively, a differential refractive index (DRI) detector, and a UV-Vis detector (254 nm).

THF was used as the eluent at 35°C with a flow rate of 1.0 mL $\mathrm{min^{-1}}$. The SEC system was calibrated by using linear poly(styrene) or poly(methyl methacrylate) standards ranging from 800 to 1.82×10^6 g $\mathrm{mol^{-1}}$.

4.1.10 Raman spectroscopy

Raman spectra were recorded on a MultiRAM from Bruker Optik (Ettlingen, Germany) equipped with a Nd:YAG (1064 nm) laser.

4.1.11 Rheometry

Small oscillatory shear rheology measurements were performed using an ARES G2 rheometer from TA instruments (New Castle, USA) at different temperatures using strains from 0.5% to 5% in a frequency range from 0.1 to 100 rad $\mathrm{s^{-1}}$ using a 13 mm parallel plate geometry. The samples were punched out resulting in round disks with a diameter of 13 mm and a thickness of 1 mm.

4.1.12 PXRD

Powder X-ray diffraction was measured using a PANanlytical X´Pert PRO diffractometer from Malvern Panalytical (Malvern, United Kingdom) operating in transmission geometry. All data were measured over the range 5 – 50° 2θ or 2 – 90°C 2θ.

4.1.13 Universal Tester

Tensile tests were performed using an AGS-X Universal tester from Shimadzu Inc. (Kyōto, Japan). Three samples were prepared for each tensile experiment. The tested samples were in a dumbbell shape with 1-2 mm thickness, 7.5 mm width and 5 mm length. The tensile speed was set at 50 mm $\mathrm{min^{-1}}$.

4.1.14 TGA coupled MS

Thermogravimetric analysis coupled with mass spectrometry was measured on a STA 449 C Jupiter from Netzsch-Gerätebau GmbH (Selb, Germany) equipped with a quadrupole mass spectrometer 403 C Aëolos from InProcess Instruments (Bremen, Germany). The measurement conditions applied were as follows: heating rate 10 K $\mathrm{min^{-1}}$, temperature range 50 – 400°C, streaming synthetic air (SynA: 79 wt% N_2, 21 wt% O_2 at 50 mL $\mathrm{min^{-1}}$) as purge gas and 20 mL $\mathrm{min^{-1}}$ N_2 as protective gas. An empty Pt/Rh crucible (diameter 5 mm, height 5 mm) with a punched lid was used as an inert reference sample. The gas released was detected by mass spectrometry. The following mass fragment numbers m/z were investigated: 18, 44, 64, corresponding to H_2O, CO_2, and SO_2, respectively.

4.1.15 ToF-SIMS

Time-of-flight secondary ion mass spectrometry was performed on a TOF.SIMS5 from ION-TOF GmbH (Münster, Germany), equipped with a Bi cluster liquid metal primary ion source and a non-linear time-of-flight analyzer. A surface area of 0.025 mm² (500 × 500 µm) was investigated. The Bi source was operated in bunched mode providing 0.7 ns Bi^{1+} ion pulses at 25 keV energy and a lateral resolution of approx. 4 µm. The short pulse length allowed for high mass resolution to analyze the complex mass spectra of the immobilized organic layers.

4.1.16 UV-vis

UV-visible spectra were recorded using a PerkinElmer Lambda 35 UV/VIS spectrometer from PerkinElmer Ink. (Waltham, USA). Solutions were measured in quartz cuvettes against a background of HPLC grade water.

4.1.17 WCA

Water contact angle measurements were performed using a DSA 25 contact angle goniometer from Krüss (Hamburg, Germany) using the sessile drop technique. The droplet volume was 5 µL.

4.1.18 XPS

X-ray photoelectron spectroscopy was conducted on an Axis Ultra DLD from Shimadzu (Kyoto, Japan) using monochromatized Al Kα radiation. The survey scan and the high-resolution scans were operated at an analyzer pass energy of 160.0 eV and 40.0 eV, respectively. Recorded spectra were calibrated on the S $2p_{3/2}$ peak at a binding energy of 164.0 eV.

4.1.19 ^{1}H and ^{13}C NMR

^{1}H and ^{13}C nuclear magnetic resonance spectra were recorded on a Bruker Avance III 400 MHz spectrometer from Bruker (Rheinstetten, Germany) using $CDCl_3$ (99.8 atom% D, 1 v/v% TMS) or THF-d^8 (99.5 atom% D) from Merck (Darmstadt, Germany) as a solvent. For ^{1}H spectra between 32 and 128 scans were collected and for ^{13}C spectra between 512 and 1024 scans were collected. Data were analyzed using MestReNova 14.1.0 from Mestrelab Research S.L. (Santiago de Compostela, Spain).

4.1.20 ^{29}Si NMR

^{29}Si magnetic resonance spectra were recorded on a Bruker Avance Neo 400 NB spectrometer equipped with a 5 mm BBO probe from Bruker (Rheinstetten, Germany) at a read-out temperature of 298 K. The spectra of styrylethyltrimethoxysilane and poly(S_n-*r*-StyTMS) were recorded with 512 and 2560 scans, respectively. The spectra of TMNBS and MENBS were recorded with 512 scans. For the spectra of poly(S-*r*-$MENBS_{100}$) and *branch*-poly(S-*r*-$MENBS_{100}$) 1024 and

4096 scans were accumulated, respectively. A recycle delay of 60 s was used. Samples were dissolved in $CDCl_3$ (99.8% D, 0.03 v/v% TMS) from ARMAR AG (Döttingen, Switzerland). The optimized ^{29}Si 90° pulse length was 10.5 µs. WALTZ-16 heteronuclear decoupling was used during the acquisition.[235] ^{29}Si chemical shifts were externally referenced to the ^{29}Si signal of TMS at 0 ppm. Processed data were further analyzed using MestReNova 14.1.0 from Mestrelab Research S.L. (Santiago de Compostela, Spain).

4.1.21 ^{29}Si CP/MAS and HPDEC NMR

^{29}Si high-power decoupled (HPDEC) and cross-polarization (CP) magic-angle spinning (MAS) NMR spectra were recorded using a Bruker Avance III 400 WB spectrometer from Bruker (Rheinstetten, Germany) equipped with a 4-mm double resonance MAS probe at a read-out temperature of 300 K. The spectra were acquired at a spinning speed of 12 kHz using TMS at 0 ppm as external reference. Optimized ^{1}H and ^{29}Si 90° pulse lengths were 2.5 and 5.97 µs, respectively. The ^{29}Si CP spectrum was acquired with 1024 scans and a recycle delay of 5 s. ^{1}H to ^{29}Si magnetization transfer was achieved by using linear 70–100% ^{1}H ramped CP with a contact time of 8 ms to fulfill the Hartmann–Hahn condition.[236] Heteronuclear decoupling during acquisition was achieved with swept-frequency two-pulse phase modulation (SWf-TPPM).[237,238] For HPDEC experiments, 664 and 736 scans were collected for powdered *net*-poly(S_n-*r*-StyTMS) and the background, respectively, with a recycle delay of 90 s. SWf-TPPM 7 heteronuclear decoupling was used during the acquisition. Processed data were analyzed using MestReNova 14.1.0 from *Mestrelab Research S.L.* (Santiago de Compostela, Spain).

4.2 Methods

This chapter contains information about the preparation of materials and the experimental or theoretical background of their examination.

4.2.1 AFM scratch analysis

The height of coatings was determined via a scratch analysis. A needle was used to generate a thin scratch on a coated surface. AFM scans were then conducted perpendicular to the extension of the scratch. For each substrate, three scratches were analyzed to obtain an average and a standard deviation. For each scratch a width of at least 3 µm was used to calculate the height difference. The height difference was analysed using the software Nanoscope Analysis from Bruker (Billerica, USA).

4.2.2 Spin-coating

Different substrates, such as glass, gold, and silicon were spin-coated using a SPIN 150i-NPP spin-coater from SPS-Europe (Putten, Netherlands). To prepare samples for AFM scratch test analysis, silicon wafers were cut in square shapes (ca. 2 × 2 cm), covered with 250 µL hydrolyzed poly(S_n-r-StyTMS)) solution in THF, and spun at 1500 rpm for 15 s. The same volume was then added on the substrate within 10 s, and it was spun at 1500 rpm for 15 s again. For gold coated glass slides and glass slides (2.5 × 7.5 cm) 800 µL of hydrolyzed poly(S_n-*r*-styrylsilane) were used for both pipetting steps. When multipile spin-coating cycles were applied, the same procedure was repeated after air drying the specimens at least 20 min before the next spinning cycle. Glass slides were activated by immersion into concentrated HCl and MeOH in a 1:1 volumentric ratio for at least one day. The static water contact angles of glass slides before and after activation were 49.4° ± 0.2° and 31.3° ± 0.3°, respectively. For ellipsometry measurements, silicon wafers were cut in square shapes (ca. 2 × 2 cm), covered with 250 µL hydrolyzed poly(S_n-*r*-StyTMS) solution in THF, and spun at 6000 rpm for 35 s.

4.2.3 Dip-coating

Glass slides were dip-coated using an RCD 15 dip-coater from Bungard (Windeck, Germany). Activated glass slides were immersed into a hydrolyzed poly(S_n-*r*-StyTMS) THF solution with a concentration of 40 mg mL^{-1} for 5 min. The speed of substrate removal was set to 40, 45, 125, and 760 mm min^{-1}, respectively.

4.2.4 Preparation of *net*-poly(S_{35}-*r*-StyTMS) coated silica particles

3.00 g of sulfur powder and 3.00 g of styrylethyltrimethoxysilane were weighed into a 25 mL round bottom flask with a stir bar and sealed with a stopper. The vial was heated to 130 °C for 8 h under stirring at 400 rpm. The vial was extracted with ca. 40 mL THF and poured into a beaker. The solution was then decanted to remove residual sulfur and filled up to a total of 300 mL THF. 50.13 g silica particles (40 – 63 µm) were charged into a 1 L round bottom flask and the poly(S_n-*r*-StyTMS) solution was poured in. 1.5 mL of HCl solution (pH 4) were added and the dispersion was stirred vigorously for 24 h. The mixure was then filtered through a buchner filter. The filter cake was briefly dried in an oven at 80 °C. The modified particles were washed with 80, 50, and 3 × 20 mL of THF and then with 3 × 20 mL of CS_2, until the washings were colorless. They were dried for 20 min at 110 °C. 51.86 g coated particles were obtained.

4.2.5 Mercury(II) ion removal

Silica particles coated with *net*-poly(S_{35}-*r*-StyTMS) (200 mg) were stirred in 10 mL of aqueous $HgCl_2$ solution (15 mg L^{-1}) for 1 h. The dispersion was then centrifuged, and ca. 3 mL of the solution were decanted and filtered. The filtrate was diluted with 1:30 v/v% water (HPLC grade) and 300 µL of concentrated was added. The Hg^{2+} concentration was determined with Hydride-AAS (atom absorbance spectroscopy). Pristine silica particles (40 – 63 µm) were used as a reference. The pH of the filtrate after the remediation experiment was neutral.

4.2.6 Solution casting of *net*-poly(S_{35}-*r*-StyTMS)

Hydrolyzed poly(S_n-*r*-StyTMS) with a mass concentration of 40 mg mL^{-1} (referring to the mass of styrylethyltrimethoxysilane used for the inverse vulcanization) was casted into a PTFE mold and THF was allowed to evaporate at room temperature to 50 % of the initial volume. This was repeated two more times. After evaporation of THF a film of *net*-poly(S_{35}-*r*-StyTMS) was obtained.

4.2.7 Molding of *branch*-poly(*S*-*r*-NBS$_x$)

Polymers were molded using silicone or PTFE molds. Polymers were cured at 80°C in an oven overnight or at 160°C for 2 h. Silicone molds were purchased from household appliances stores. PTFE molds were designed using the software Rhinoceros 3D and were mill-cut into PTFE plates with a thickness of 1 cm.

4.2.8 Thin film interference color calculation

To calculate the thin film interference in dependence of the viewing angle and the thickness of the polymer layer, a script created by Dr. Jens Raacke was used. Based on the Cauchy parameters n_0, n_1 and n_2 and the absorption coefficients k_0, k_1 and k_2 as input parameters, the functions n(λ) and k(λ) are calculated in increments of 5 nm from 380 nm to 780 nm. Then, n and k are combined as complex refractive index N according to the Kramers-Kronig relation (I) for further calculations

$$\text{(I)} \qquad N = n + ik$$

The steps 1 and 2 are then executed for every data point, i.e., for all linear combinations of the viewing angle and the thickness from 20 - 40° and 0 - 300 nm, respectively.

1) Calculation of the reflection and transmission coefficients of the transverse electric (TE) and transverse magnetic (TM) polarizations based on the Fresnel law. $E_{0,i}$, $E_{0,t}$ and $E_{0,r}$ are the electric field strength of the incoming, transmitted and reflected beam, respectively.

$$t_{TE} = \left(\frac{E_{0,t}}{E_{0,i}}\right)_{TE} \qquad t_{TM} = \left(\frac{E_{0,t}}{E_{0,i}}\right)_{TM}$$

$$r_{TE} = \left(\frac{E_{0,r}}{E_{0,i}}\right)_{TE} \qquad r_{TM} = \left(\frac{E_{0,r}}{E_{0,i}}\right)_{TM}$$

2) The refracted beams are a superposition of multiple beams. To calculate the total reflectivity, the sum of all refracted beams is formed based on series development.

The reflectivity spectrum is multiplied with the sensitivity spectra of all three human color receptors to obtain a XYZ color scheme and the obtained XYZ colors are converted into RGB colors. A light source correction is then applied from Illuminant E (constant emission intensity for all wavelengths of the visible light spectrum) to the selected light source (5300 K) and averaging over TE and TM polarization yields the thin film interference color in dependence of the viewing angle and thickness. The script is openly available under the following link: http://www.raacke.de/index.html?airy.html (last access: 30.09.2021).

4.3 Synthesis

This chapter contains information about the synthesis of monomers and polymers. Spectra confirming the chemical structures are discussed in the results and discussion part or can be found in the appendix.

4.3.1 General procedures

Chemicals were obtained from abcr (Karlsruhe, Deutschland), Acros Organics (Geel, Belgium), Alfa Aesar (Haverhill, USA), Gelest (Morrisville, USA), Merck (Darmstadt, Germany), or TCI (Tokio, Japan) and used as received.

Inverse vulcanization reactions were conducted in an aluminum heat block with nine drilled holes with a diameter of 20 mm. For temperature control, a thermostat was fitted in a drill-hole filled with silicon oil. Crimping vials (10 mL) sealed with crimping caps were used for most experiments. When the combined mass of reactants exceeded 2 g, the inverse vulcanizations were conducted in round bottom flasks using a silicon oil bath.

4.3.2 Synthesis of monomers, polymers, and polymer networks

4.3.2.1 *net*-poly(S$_{35}$-*r*-StyTMS)

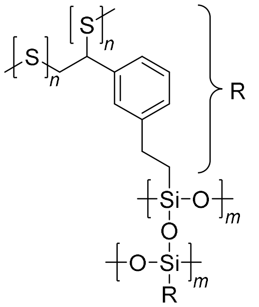

500 mg of sulfur powder and 500 mg of styrylethyltrimethoxysilane were weighed into a crimp vial with a stir bar and sealed with a crimp cap. The vial was heated to 130°C for 8 h under stirring at 400 rpm. The vial was extracted stepwise with 4, 2 and 2 mL of THF, respectively. The THF solution was cooled to -20°C for 20 min to precipitate excess sulfur. The phases were separated by centrifugation at 2500 rpm for 5 min. Evaporation of volatiles yielded poly(S$_n$-*r*-StyTMS) as brown, viscous oil. ^{1}H NMR (400 MHz, CDCl$_3$) δ = 7.38-7.01 (4H, m, Ar-H), 4.66 (1H, m, Ar-C**H**(S$_n$)-CH$_2$(S$_n$)), 4.38 (1H, m, Ar-C**H**(S$_n$)-CH$_2$(S$_n$)), 3.89 (1H, m, Ar-C**H**(S$_n$)-CH$_3$), 3.57 (9H, s, Si-OCH$_3$), 3.48 (1H, m, Ar-CH(S$_n$)-C**H**$^a_2$(S$_n$)), 3.04 (1H, m, Ar-CH(S$_n$)-C**H**$^b_2$(S$_n$)), 2.82-2.68 (2H, m, Ar-C**H**$_2$-CH$_2$-Si), 2.65-2.58 (1H, m, Ar-C**H**-(CH$_3$)Si), 2.41-2.30 (1H, m, Ar-C**H**-(CH$_3$)Si), 1.76 (3H, m, Ar-CH(S$_n$)-C**H$_3$**) 1.43-1.40 (3H, m, Ar-CH(Si)-C**H**$_3$), 1.08-0.98 (2H, m, Ar-CH$_2$-C**H**$_2$-Si). ^{29}Si NMR (CDCl$_3$, 400 MHz): δ [ppm] = -42.7, -42.8, -42.9, -43.0. Usually, poly(S$_n$-*r*-StyTMS) was not isolated but directly processed in solution instead. A solution of poly(S$_n$-*r*-StyTMS) in 12 mL THF was hydrolyzed with 5 vol% (600 µL) of dilute HCl (pH 4) for 60 min by stirring at room temperature. The solution could then be coated onto glass, gold, or silicon surfaces, cellulose or glass fiber filters, and silica micro- and nanoparticles. To obtain films or powders of *net*-poly(S$_{35}$-*r*-StyTMS), hydrolyzed poly(S$_n$-*r*-StyTMS) was charged in a Teflon mold or round bottom flask, respectively. Volatiles were removed at room temperature, in an oven at 80°C, or in a rotary evaporator. The obtained orange-red solid was washed thoroughly with THF and CS$_2$ to obtain *net*-poly(S$_{35}$-*r*-StyTMS) in a yield of 73%. For DSC, TGA, solid state NMR and PXRD measurements, the orange-red solid was milled into a powder and was allowed to age for two months prior to the

measurements. ATR-FT-IR: ν [cm^{-1}] = 3500 – 3050 *w*, br. (SiOH), 3055 *vw* and 3018 *vw* (C_{ar}-$H_{stretch}$), 2957 *m*, 2923 *m*, and 2867 *m* (C-$H_{stretch}$), 1602 *s* and 1587 *m*, and 1512 *m* (C-$C_{stretch}$), 1442 *m* (C-C_{bend}), 1188 *s* ($SiOCH_3$), 1031 *vs* (Si-O-Si), br., 876 *vs*, br., 778 *vs*, br., 698 *vs*, br. ^{29}Si CP/MAS NMR ($CDCl_3$, 400 MHz): δ [ppm] = -49.5 (T_1), -58.2 (T_2), -68.0 (T_3).

4.3.2.2 Synthesis of bicyclo[2.2.1]hept-5-en-2-yltrimethylsilane (TMNBS)

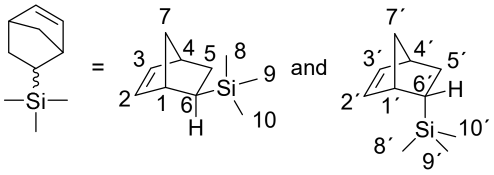

TMNBS was synthesized from the reaction of methyl lithium (MeLi) with monoethoxynorbornenylsilane (MENBS). A 50 mL Schlenck flask was charged with 7.14 g (0.036 mol, 1.00 eq.) of MENBS and 20 mL of dry THF and fitted with an addition funnel. The air in the apparatus was replaced with a nitrogen atmosphere by three cycles of evacuation and purging with nitrogen. The addition funnel was charged with 25 mL of MeLi solution (1.6 mol L^{-1}, 0.04 mol, 1.10 eq.) in diethylether (DET) and the Schlenck flask was cooled down to 0°C using an ice bath. The MeLi solution was added dropwise under stirring over the course of roughly 5 min. A slight yellow color can be observed upon addition of MeLi, presumably due to the reduction of the inhibitor MEHQ in MENBS. After the addition was completed, the reaction was stirred for 4 h at 0°C. The reaction mixture was given onto 20 mL of ice water to quench excess MeLi. The phases were separated in a separation funnel and the organic phase was washed at least three times with 20 mL of deionized water and until the aqueous phase was pH neutral. The organic phase was dried over anhydrous magnesium sulfate and filtered. The volatiles of the filtrate were removed under reduced pressure. A slightly yellow, clear liquid was obtained in a yield of 77 % (4.61 g, 0.028 mol). ATR FT-IR: ν [cm^{-1}] = 3059 *vw* (C-$H_{stretch}$ in C=C-H), 2953 *m*, 2864 *w* (C-$H_{stretch}$), 1568 *vw* (C=$C_{stretch}$), 1406 br. *vw* (Si-$CH_{3,\text{ anti. deform}}$), 1388 *w*, 1333 *w* (C-H_{bend} in C=C-H), 1246 *s* (Si-$CH_{3,\text{ sym. deform}}$), 945 *w*, 912 *w*, 891 *s* (C=C_{bend}), 827 *vs* (Si-CH_3), 802 *s*, 785 *s*, 746 *w*, 714 *vs* (C-H_{wag}), 689 *s*, 631 *w*. ^{1}H NMR ($CDCl_3$, 400 MHz): δ [ppm] = 6.15 and 5.94 (m, 2H, HC=CH), 2.87 (m, 2H, CH_{tert}), 1.86 (m), 1.52 (m), 1.37 (m), 1.13 (m), 1.04 (m), 0.92 (m), 0.31 (m), 0.00 and -0.09 (s, 9H, $SiCH_3$). ^{13}C NMR ($CDCl_3$, 400 MHz): δ [ppm] = 138.5, 135.4, 134.0, and 133.2 (C2, C3, C2′, C3′), 51.5 and 46.8 (C7, C7′), 44.8, 42.9, 42.5, and 42.4 (C1, C1′, C4, C4′), 27.1 and 27.0 (C6, C6′), 25.3 and 25.2 (C5, C5′), -1.4, -2.0 (C8, C9, C10, C8′, C9′, C10′). ^{29}Si NMR ($CDCl_3$, 400 MHz): δ [ppm] = 3.2, 2.7 (*exo*- and *endo*-TMNBS).

Note: MeLi solution was purchased in small bottles containing 25 mL of MeLi solution. To ensure that MeLi could not hydrolyze prior to the reaction and to avoid storing bottles of MeLi with a punctured septum, a full bottle was used for each reaction. The use of THF as a cosolvent is necessary to obtain a full conversion yield, presumably due to the kinetic inhibition of MeLi aggregates in pure DET.

4.3.2.3 poly(*S*-*r*-TMNBS)

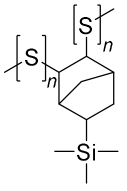

500 mg of sulfur powder and 500 mg of TMNBS were weighed into a crimp vial with a stir bar and sealed with a crimp cap. The vial was heated to 150°C for 5 h. Sulfur was allowed to melt for 5 min before stirring at 400 rpm. After the reaction, the vial was cooled to room temperature and was extracted with 40 mL of THF. The resulting solution containing 25 mg mL^{-1} of crude poly(S-*r*-TMNBS) in THF was

added dropwise to a beaker containing 300 mL of methanol stirring at 1000 rpm. After the addition of the crude poly(S-*r*-TMNBS) was completed, the resulting suspension was continuously stirred for 5 more minutes to facilitate coagulation and was allowed to sediment for 5 min. The phases were separated by vacuum filtration using a Buchner funnel and the filter cake was rinsed with methanol and ethanol until the washings were colorless. The precipitate was dried in a vacuum oven at 40°C overnight. Poly(S-*r*-TMNBS) was obtained as a grey granule with a yield of 32 %. ATR FT-IR: ν [cm^{-1}] = 2948 *s*, 2864 *m* (C-H$_{\text{stretch}}$), 1449 *m*, 1404 *w* (Si-CH$_{3,\ \text{anti. deform}}$), 1246 *s* (Si-CH$_{3,\ \text{sym. deform}}$), 1100 *w*, 1052 *w*, 1030 *w*, 990 *w*, 962 *w*, 906 *m*, 827 *vs* (Si-CH$_3$), 746 *s*, 688 *s*, 620 *m*.

4.3.2.4 poly(S-*r*-MENBS$_{100}$)

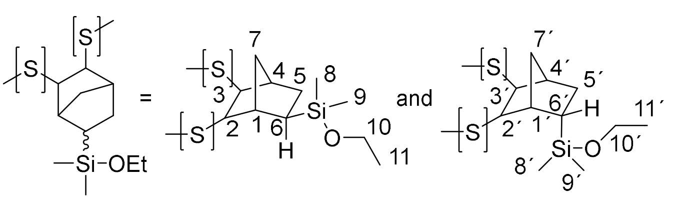

500 mg of sulfur powder and 500 mg of MENBS were weighed into a crimp vial with a stir bar and sealed with a crimp cap. The vial was heated to 150°C for 5 h. Sulfur was allowed to melt for 5 min before stirring at 400 rpm. After the reaction, the vial was cooled to room temperature and poly(S-*r*-DENBS$_{100}$) was obtained in quantitative yield. ATR FT-IR: ν [cm^{-1}] = 2951 *m* and 2866 *m* (C-H$_{\text{stretch}}$), 1449 *w*, 1389 *m*, 1250 *s* (Si-CH$_{3,\ \text{sym. stretch}}$), 1163 *m*, 1103 *s*, 1072 *s*, and 943 *s* (Si-OEt), 907 *m*, 816 *vs*, 775 *vs*, 725 *s*, 677 *m*, 632 *m*. ^{13}C NMR (CDCl$_3$, 400 MHz): δ [ppm] = 75.4, 73.3, 69.6, 69.3, 67.9, and 67.6 (S$_n$-(S=O)-C, (S$_n$)$_2$C), 58.6 and 58.5 (C10, C10′), 46.6, 45.6, 44.5. 43.6, 43.3, 41.7, and 41.3 (C2, C2′, C3, C3′), 38.4, 35.3, and 35.1 (C4, C4′, C7, C7′) 31.7, 29.3, 29.0, 28.9, 27.9, and 27.8 (C1, C1′, C5, C5′, C6, C6′) 18.7, 18.6 and 18.4 (C11, C11′), 0.0, -1.6, 1-8. -1.9, -2.8, -3.0 (C8, C8′, C9, C9′). ^{29}Si NMR (CDCl$_3$, 400 MHz): δ [ppm] = 15.2, 15.2, 14.9, 14.7, 7.9.

4.3.2.5 poly(S-*r*-DENBS$_{100}$)

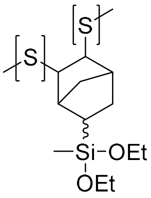

500 mg of sulfur powder and 500 mg of DENBS were weighed into a crimp vial with a stir bar and sealed with a crimp cap. The vial was heated to 150°C for 5 h. Sulfur was allowed to melt for 5 min before stirring at 400 rpm. After the reaction, the vial was cooled to room temperature and poly(S-*r*-DENBS$_{100}$) was obtained in quantitative yield. ATR FT-IR: ν [cm^{-1}] = 2966 *m* and 2872 *m* (C-H$_{\text{stretch}}$), 1448 *w*, 1389 *m*, 1256 *m* (Si-CH$_{3,\ \text{sym. stretch}}$), 1163 *m*, 1101 *vs*, 1072 *vs*, and 945 *s* (Si-OEt), 905 *s*, 795 *vs*, 756 *vs*.

4.3.2.6 *branch*-poly(S-*r*-MENBS$_{10}$)

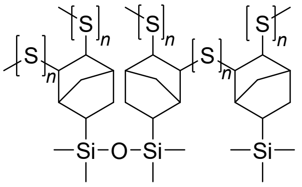

500 mg of sulfur powder, 450 mg of TMNBS, and 50 mg of MENBS (0.255 mmol, 1.00 eq.) were weighed into a crimp vial with a stir bar and sealed with a crimp cap. The vial was heated to 150°C for 5 h. Sulfur was allowed to melt for 5 min before stirring at 400 rpm. After the reaction was completed, the temperature was reduced to 100 °C. To hydrolyze poly(S-*r*-MENBS$_{10}$), 92 mg (5.09 mmol, 20.0 eq.) of diluted HCl (pH 3) were added to the melt. After the addition of HCl, the crimping vial was sealed with a cap and the reaction was stirred with 100 rpm at 100°C for 18 h. The vial was cooled to room tem-

perature and rinsed with methanol to remove excess HCl. The crude *branch*-poly(S-*r*-MENBS$_{10}$) was first dried in an oven at 80°C for five days and then dried in a vacuum oven at 40°C overnight to remove residual HCl and to drive the equilibrium towards formation of siloxane bonds. The crude *branch*-poly(S-*r*-MENBS$_{10}$) was extracted from the vial with 40 mL of THF. The resulting solution containing 25 mg mL^{-1} of crude *branch*-poly(S-*r*-MENBS$_{10}$) in THF was added dropwise to a beaker containing 300 mL of methanol stirring at 1000 rpm. After the addition of the crude *branch*-poly(S-*r*-MENBS$_{10}$) was completed, the resulting suspension was stirred for 5 more minutes to facilitate coagulation and was allowed to sediment for 5 min. The phases were separated by vacuum filtration using a Buchner funnel and the filter cake was rinsed with methanol and ethanol until the washings were colorless. The precipitate was dried in a vacuum oven at 40°C overnight. *Branch*-poly(S-*r*-MENBS$_{10}$) was obtained as a grey granule with a yield of 40 %. ATR FT-IR: ν [cm^{-1}] = 2949 *m*, 2862 *w* (C-H$_{\text{stretch}}$), 1449 *w*, 1403 *w* (Si-CH$_{3,\text{ anti. deform}}$), 1300 *w*, 1247 *s* (Si-CH$_{3,\text{ sym. deform}}$), 1044 *w*, br. (Si-O-Si), 990 *w*, 913 *w*, 850 *s*, 829 *vs* (Si-CH$_3$), 783 *s*, 746 *s*, 688 *m*.

4.3.2.7 *branch*-poly(S-*r*-MENBS$_{20}$)

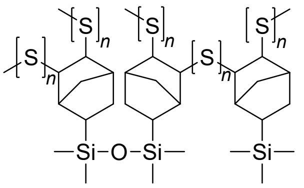

500 mg of sulfur powder, 400 mg of TMNBS, and 100 mg of MENBS (0.510 mmol, 1.00 eq.) were weighed into a crimp vial with a stir bar and sealed with a crimp cap. The vial was heated to 150°C for 5 h. Sulfur was allowed to melt for 5 min before stirring at 400 rpm. After the reaction was completed, the temperature was reduced to 100 °C. To hydrolyze poly(S-*r*-MENBS$_{20}$), 184 mg (10.2 mmol, 20.0 eq.) of diluted HCl (pH 3) were added to the melt. After the addition of HCl, the crimping vial was sealed with a cap and the reaction was stirred with 100 rpm at 100°C for 18 h. The vial was cooled to room temperature and rinsed with methanol to remove excess HCl. The crude *branch*-poly(S-*r*-MENBS$_{20}$) was first dried in an oven at 80°C for five days and then dried in a vacuum oven at 40°C overnight to remove residual HCl and to drive the equilibrium towards formation of siloxane bonds. The crude *branch*-poly(S-*r*-MENBS$_{20}$) was extracted from the vial with 40 mL of THF. The resulting solution containing 25 mg mL^{-1} of crude *branch*-poly(S-*r*-MENBS$_{20}$) in THF was added dropwise to a beaker containing 300 mL of methanol stirring at 1000 rpm. After the addition of the crude *branch*-poly(S-*r*-MENBS$_{20}$) was completed, the resulting suspension was stirred for 5 more minutes to facilitate coagulation and was allowed to sediment for 5 min. The phases were separated by vacuum filtration using a Buchner funnel and the filter cake was rinsed with methanol and ethanol until the washings were colorless. The precipitate was dried in a vacuum oven at 40°C overnight. *Branch*-poly(S-*r*-MENBS$_{20}$) was obtained as a grey granule with a yield of 41 %: ν [cm^{-1}] = 2949 *m*, 2862 *w* (C-H$_{\text{stretch}}$), 1449 *w*, 1402 *w* (Si-CH$_{3,\text{ anti. deform}}$), 1300 *w*, 1247 *s* (Si-CH$_{3,\text{ sym. deform}}$), 1046 *m*, br. (Si-O-Si), 989 *w*, 912 *w*, 850 *s*, 829 *vs* (Si-CH$_3$), 783 *s*, 746 *s*, 688 *m*.

4.3.2.8 *branch*-poly(S-*r*-MENBS$_{30}$)

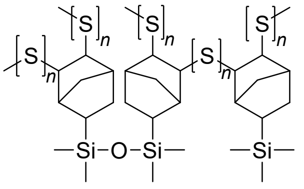

500 mg of sulfur powder, 350 mg of TMNBS, and 150 mg of MENBS (0.765 mmol, 1.00 eq.) were weighed into a crimp vial with a stir bar and sealed with a crimp cap. The vial was heated to 150°C for 5 h. Sulfur was allowed to melt for 5 min before stirring at 400

rpm. After the reaction was completed, the temperature was reduced to 100 °C. To hydrolyze poly(S-*r*-MENBS$_{30}$), 276 mg (15.3 mmol, 20.0 eq.) of diluted HCl (pH 3) were added to the melt. After the addition of HCl, the crimping vial was sealed with a cap and the reaction was stirred with 100 rpm at 100°C for 18 h. The vial was cooled to room temperature and rinsed with methanol to remove excess HCl. The crude *branch*-poly(S-*r*-MENBS$_{30}$) was first dried in an oven at 80°C for five days and then dried in a vacuum oven at 40°C overnight to remove residual HCl and to drive the equilibrium towards formation of siloxane bonds. The crude *branch*-poly(S-*r*-MENBS$_{30}$) was extracted from the vial with 40 mL of THF. The resulting solution containing 25 mg mL^{-1} of crude *branch*-poly(S-*r*-MENBS$_{30}$) in THF was added dropwise to a beaker containing 300 mL of methanol stirring at 1000 rpm. After the addition of the crude *branch*-poly(S-*r*-MENBS$_{30}$) was completed, the resulting suspension was stirred for 5 more minutes to facilitate coagulation and was allowed to sediment for 5 min. The phases were separated by vacuum filtration using a Buchner funnel and the filter cake was rinsed with methanol and ethanol until the washings were colorless. The precipitate was dried in a vacuum oven at 40°C overnight. *Branch*-poly(S-*r*-MENBS$_{30}$) was obtained as a grey granule with a yield of 41 %. ATR FT-IR: ν [cm^{-1}] = 2949 *m*, 2862 *w* (C-H$_{\text{stretch}}$), 1449 *w*, 1405 *w* (Si-CH$_{3,\text{ anti. deform}}$), 1300 *w*, 1248 *s* (Si-CH$_{3,\text{ sym. deform}}$), 1044 *s*, br. (Si-O-Si), 990 *w*, 912 *w*, 850 *s*, 829 *vs* (Si-CH$_3$), 783 *s*, 748 *s*, 688 *m*.

4.3.2.9 *branch*-poly(S-*r*-MENBS$_{50}$)

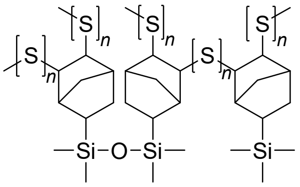

500 mg of sulfur powder, 250 mg of TMNBS, and 250 mg of MENBS (1.28 mmol, 1.00 eq.) were weighed into a crimp vial with a stir bar and sealed with a crimp cap. The vial was heated to 150°C for 5 h. Sulfur was allowed to melt for 5 min before stirring at 400 rpm. After the reaction was completed, the temperature was reduced to 100 °C. To hydrolyze poly(S-*r*-MENBS$_{50}$), 459 mg (25.5 mmol, 20.0 eq.) of diluted HCl (pH 3) were added to the melt. After the addition of HCl, the crimping vial was sealed with a cap and the reaction was stirred with 100 rpm at 100°C for 18 h. The vial was cooled to room temperature and rinsed with methanol to remove excess HCl. The crude *branch*-poly(S-*r*-MENBS$_{50}$) was first dried in an oven at 80°C for five days and then dried in a vacuum oven at 40°C overnight to remove residual HCl and to drive the equilibrium towards formation of siloxane bonds. The crude *branch*-poly(S-*r*-MENBS$_{50}$) was extracted from the vial with 40 mL of THF. The resulting solution containing 25 mg mL^{-1} of crude *branch*-poly(S-*r*-MENBS$_{50}$) in THF was added dropwise to a beaker containing 300 mL of methanol stirring at 1000 rpm. After the addition of the crude *branch*-poly(S-*r*-MENBS$_{50}$) was completed, the resulting suspension was stirred for 5 more minutes to facilitate coagulation and was allowed to sediment for 5 min. The phases were separated by vacuum filtration using a Buchner funnel and the filter cake was rinsed with methanol and ethanol until the washings were colorless. The precipitate was dried in a vacuum oven at 40°C overnight. *Branch*-poly(S-*r*-MENBS$_{50}$) was obtained as a grey granule with a yield of 27 %. ATR FT-IR: ν [cm^{-1}] = 2950 *m*, 2864 *w* (C-H$_{\text{stretch}}$), 1449 *w*, 1405 *w* (Si-CH$_{3,\text{ anti. deform}}$), 1300 *w*, 1251 *s* (Si-CH$_{3,\text{ sym. deform}}$), 1046 *s*, br. (Si-O-Si), 990 *w*, 912 *w*, 831 *vs* (Si-CH$_3$), 783 *s*, 748 *s*, 687 *m*.

4.3.2.10 *branch*-poly(S-*r*-DENBS$_{10}$)

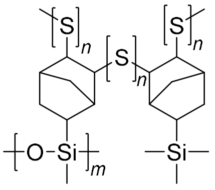

500 mg of sulfur powder, 450 mg of TMNBS, and 50 mg of DENBS (0.220 mmol, 0.50 eq.) were weighed into a crimp vial with a stir bar and sealed with a crimp cap. The vial was heated to 150°C for 5 h. Sulfur was allowed to melt for 5 min before stirring at 400 rpm. After the reaction was completed, the temperature was reduced to 100 °C. To hydrolyze poly(S-*r*-DENBS$_{10}$), 79 mg (4.40 mmol, 20.0 eq.) of diluted HCl (pH 3) were added to the melt. After the addition of HCl, the crimping vial was sealed with a cap and the reaction was stirred with 100 rpm at 100°C for 18 h. The vial was cooled to room temperature and rinsed with methanol to remove excess HCl. The crude *branch*-poly(S-*r*-DENBS$_{10}$) was first dried in an oven at 80°C for five days and then dried in a vacuum oven at 40°C overnight to remove residual HCl and to drive the equilibrium towards formation of siloxane bonds. The crude *branch*-poly(S-*r*-DENBS$_{10}$) was extracted from the vial with 40 mL of THF. The resulting solution containing 25 mg mL^{-1} of crude *branch*-poly(S-*r*-DENBS$_{10}$) in THF was added dropwise to a beaker containing 300 mL of methanol stirring at 1000 rpm. After the addition of the crude *branch*-poly(S-*r*-DENBS$_{10}$) was completed, the resulting suspension was stirred for 5 more minutes to facilitate coagulation and was allowed to sediment for 5 min. The phases were separated by vacuum filtration using a Buchner funnel and the filter cake was rinsed with methanol and ethanol until the washings were colorless. The precipitate was dried in a vacuum oven at 40°C overnight. *Branch*-poly(S-*r*-DENBS$_{10}$) was obtained as a grey granule with a yield of 40 %. ATR FT-IR: ν [cm^{-1}] = 2950 *m*, 2864 *w* (C-H$_{\text{stretch}}$), 1449 *w*, 1403 *w* (Si-CH$_{3,\text{ anti. deform}}$), 1301 *w*, 1246 *s* (Si-CH$_{3,\text{ sym. deform}}$), 1069 *s*, br., 1052 *s*, 1012 *m* (Si-O-Si), 912 *w*, 849 *s*, 829 *vs* (Si-CH$_3$), 786 *s*, 747 *s*, 688 *m*.

4.3.2.11 *branch*-poly(S-*r*-DENBS$_{20}$)

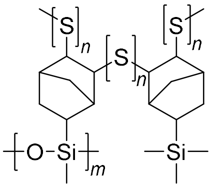

500 mg of sulfur powder, 400 mg of TMNBS, and 100 mg of DENBS (0.440 mmol, 0.50 eq.) were weighed into a crimp vial with a stir bar and sealed with a crimp cap. The vial was heated to 150°C for 5 h. Sulfur was allowed to melt for 5 min before stirring at 400 rpm. After the reaction was completed, the temperature was reduced to 100 °C. To hydrolyze poly(S-*r*-DENBS$_{20}$), 158 mg (8.80 mmol, 20.0 eq.) of diluted HCl (pH 3) were added to the melt. After the addition of HCl, the crimping vial was sealed with a cap and the reaction was stirred with 100 rpm at 100°C for 18 h. The vial was cooled to room temperature and rinsed with methanol to remove excess HCl. The crude *branch*-poly(S-*r*-DENBS$_{20}$) was first dried in an oven at 80°C for five days and then dried in a vacuum oven at 40°C overnight to remove residual HCl and to drive the equilibrium towards formation of siloxane bonds. The crude *branch*-poly(S-*r*-DENBS$_{20}$) was extracted from the vial with 40 mL of THF. The resulting solution containing 25 mg mL^{-1} of crude *branch*-poly(S-*r*-DENBS$_{20}$) in THF was added dropwise to a beaker containing 300 mL of methanol stirring at 1000 rpm. After the addition of the crude *branch*-poly(S-*r*-DENBS$_{20}$) was completed, the resulting suspension was stirred for 5 more minutes to facilitate coagulation and was allowed to sediment for 5 min. The phases were separated by vacuum filtration using a Buchner funnel and the filter cake was rinsed with methanol and ethanol until the washings were colorless. The precipitate was dried in a vacuum oven at 40°C overnight. *Branch*-poly(S-*r*-DENBS$_{20}$) was obtained as a grey granule with a yield of 44 %. ATR FT-IR: ν

[cm^{-1}] = 2950 *m*, 2864 *w* (C-H$_{\text{stretch}}$), 1449 *w*, 1403 *w* (Si-CH$_{3,\text{ anti. deform}}$), 1301 *w*, 1246 *s* (Si-CH$_{3,\text{ sym. deform}}$), 1069 *s*, br., 1052 *s*, 1012 *s* (Si-O-Si), 912 *w*, 849 *s*, 829 *vs* (Si-CH$_3$), 786 *s*, 747 *s*, 688 *m*.

4.3.2.12 *branch*-poly(S-*r*-DENBS$_{30}$)

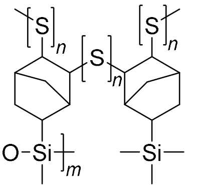

500 mg of sulfur powder, 350 mg of TMNBS, and 150 mg of DENBS (0.660 mmol, 0.50 eq.) were weighed into a crimp vial with a stir bar and sealed with a crimp cap. The vial was heated to 150°C for 5 h. Sulfur was allowed to melt for 5 min before stirring at 400 rpm. After the reaction was completed, the temperature was reduced to 100 °C. To hydrolyze poly(S-*r*-DENBS$_{30}$), 237 mg (13.2 mmol, 20.0 eq.) of diluted HCl (pH 3) were added to the melt. After the addition of HCl, the crimping vial was sealed with a cap and the reaction was stirred with 100 rpm at 100°C for 18 h. The vial was cooled to room temperature and rinsed with methanol to remove excess HCl. The crude *branch*-poly(S-*r*-DENBS$_{30}$) was first dried in an oven at 80°C for five days and then dried in a vacuum oven at 40°C overnight to remove residual HCl and to drive the equilibrium towards formation of siloxane bonds. The crude *branch*-poly(S-*r*-DENBS$_{30}$) was extracted from the vial with 40 mL of THF. The resulting solution containing 25 mg mL^{-1} of crude *branch*-poly(S-*r*-DENBS$_{30}$) in THF was added dropwise to a beaker containing 300 mL of methanol stirring at 1000 rpm. After the addition of the crude *branch*-poly(S-*r*-DENBS$_{30}$) was completed, the resulting suspension was stirred for 5 more minutes to facilitate coagulation and was allowed to sediment for 5 min. The phases were separated by vacuum filtration using a Buchner funnel and the filter cake was rinsed with methanol and ethanol until the washings were colorless. The precipitate was dried in a vacuum oven at 40°C overnight. *Branch*-poly(S-*r*-DENBS$_{30}$) was obtained as a grey granule with a yield of 37 %. ATR FT-IR: ν [cm^{-1}] = 2950 *m*, 2864 *w* (C-H$_{\text{stretch}}$), 1449 *w*, 1403 *w* (Si-CH$_{3,\text{ anti. deform}}$), 1301 *w*, 1246 *s* (Si-CH$_{3,\text{ sym. deform}}$), 1069 *s*, br., 1052 *s*, 1012 *vs* (Si-O-Si), 912 *w*, 849 *s*, 829 *vs* (Si-CH$_3$), 786 *s*, 747 *s*, 688 *m*.

4.3.2.13 *branch*-poly(S-*r*-TENBS$_{10}$)

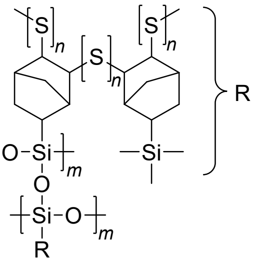

500 mg of sulfur powder, 450 mg of TMNBS, and 50 mg of TENBS (0.195 mmol, 0.33 eq.) were weighed into a crimp vial with a stir bar and sealed with a crimp cap. The vial was heated to 150°C for 5 h. Sulfur was allowed to melt for 5 min before stirring at 400 rpm. After the reaction was completed, the temperature was reduced to 100 °C. To hydrolyze poly(S-*r*-TENBS$_{10}$), 70 mg (3.90 mmol, 20.0 eq.) of diluted HCl (pH 3) were added to the melt. After the addition of HCl, the crimping vial was sealed with a cap and the reaction was stirred with 100 rpm at 100°C for 18 h. The vial was cooled to room temperature and rinsed with methanol to remove excess HCl. The crude *branch*-poly(S-*r*-TENBS$_{10}$) was first dried in an oven at 80°C for five days and then dried in a vacuum oven at 40°C overnight to remove residual HCl and to drive the equilibrium towards formation of siloxane bonds. The crude *branch*-poly(S-*r*-TENBS$_{10}$) was extracted from the vial with 40 mL of THF. The resulting solution containing 25 mg mL^{-1} of crude *branch*-poly(S-*r*-TENBS$_{10}$) in THF was added dropwise to a beaker containing 300 mL of methanol stirring at 1000 rpm. After the addition of the crude *branch*-poly(S-*r*-TENBS$_{10}$) was completed, the resulting suspension was stirred for 5 more minutes to facilitate coagulation and was al-

lowed to sediment for 5 min. The phases were separated by vacuum filtration using a Buchner funnel and the filter cake was rinsed with methanol and ethanol until the washings were colorless. The precipitate was dried in a vacuum oven at 40°C overnight. *Branch*-poly(S-*r*-TENBS$_{10}$) was obtained as a grey granule with a yield of 39 %. ATR FT-IR: ν [cm^{-1}] = 2950 *m*, 2866 *w* (C-H$_{\text{stretch}}$), 1449 *w*, 1403 br. *vw* (Si-CH$_{3,\text{ anti. deform}}$), 1389 *w*, 1301 *w*, 1247 *s* (Si-CH$_{3,\text{ sym. deform}}$), 1164 *w*, 1100 *s*, 1077 *s*, 1026 *w* (Si-O-Si), 962 *m*, 912 *m*, 850 *s*, 830 *vs* (Si-CH$_3$), 774 *s*, 689 *s*, 620 *m*.

4.3.2.14 *branch*-poly(S-*r*-TENBS$_{20}$)

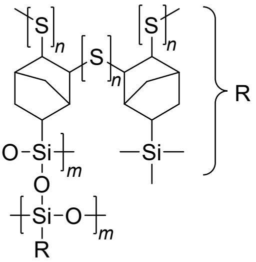

500 mg of sulfur powder, 400 mg of TMNBS, and 100 mg of TENBS (0.390 mmol, 0.33 eq.) were weighed into a crimp vial with a stir bar and sealed with a crimp cap. The vial was heated to 150°C for 5 h. Sulfur was allowed to melt for 5 min before stirring at 400 rpm. After the reaction was completed, the temperature was reduced to 100 °C. To hydrolyze poly(S-*r*-TENBS$_{20}$), 140 mg (7.80 mmol, 20.0 eq.) of diluted HCl (pH 3) were added to the melt. After the addition of HCl, the crimping vial was sealed with a cap and the reaction was stirred with 100 rpm at 100°C for 18 h. The vial was cooled to room temperature and rinsed with methanol to remove excess HCl. The crude *branch*-poly(S-*r*-TENBS$_{20}$) was first dried in an oven at 80°C for five days and then dried in a vacuum oven at 40°C overnight to remove residual HCl and to drive the equilibrium towards formation of siloxane bonds. The crude *branch*-poly(S-*r*-TENBS$_{20}$) was extracted from the vial with 40 mL of THF. The resulting solution containing 25 mg mL^{-1} of crude *branch*-poly(S-*r*-TENBS$_{20}$) in THF was added dropwise to a beaker containing 300 mL of methanol stirring at 1000 rpm. After the addition of the crude *branch*-poly(S-*r*-TENBS$_{20}$) was completed, the resulting suspension was stirred for 5 more minutes to facilitate coagulation and was allowed to sediment for 5 min. The phases were separated by vacuum filtration using a Buchner funnel and the filter cake was rinsed with methanol and ethanol until the washings were colorless. The precipitate was dried in a vacuum oven at 40°C overnight. *Branch*-poly(S-*r*-TENBS$_{20}$) was obtained as a grey granule with a yield of 40 %. ATR FT-IR: ν [cm^{-1}] = 2950 *m*, 2866 *w* (C-H$_{\text{stretch}}$), 1449 *w*, 1403 br. *vw* (Si-CH$_{3,\text{ anti. deform}}$), 1389 *w*, 1301 *w*, 1247 *s* (Si-CH$_{3,\text{ sym. deform}}$), 1164 *w*, 1100 *s*, 1077 *s*, 1026 *m* (Si-O-Si), 962 *m*, 912 *m*, 850 *s*, 830 *vs* (Si-CH$_3$), 774 *s*, 689 *s*, 620 *m*.

4.3.2.15 *branch*-poly(S-*r*-DCNBS$_{10}$)

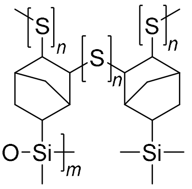

500 mg of sulfur powder, 450 mg of TMNBS, and 50 mg of DCNBS (0.241 mmol, 0.50 eq.) were weighed into a crimp vial with a stir bar and sealed with a crimp cap. The vial was heated to 150°C for 5 h. Sulfur was allowed to melt for 5 min before stirring at 400 rpm. After the reaction was completed, the temperature was reduced to 100 °C. To hydrolyze poly(S-*r*-DCNBS$_{10}$), 87 mg (4.83 mmol, 20.0 eq.) of deionized water were added to the melt. After the addition of deionized water, the crimping vial was sealed with a cap and the reaction was stirred with 100 rpm at 100°C for 18 h. The vial was cooled to room temperature and rinsed with methanol to remove excess HCl. The crude *branch*-poly(S-*r*-DCNBS$_{10}$) was first dried in an oven at 80°C for five days and then dried in a vacuum oven at 40°C overnight to remove residual HCl and to drive the equilibrium towards formation of siloxane bonds. The crude *branch*-poly(S-*r*-DCNBS$_{10}$) was extracted from the vial with 40 mL of THF. The resulting solution containing 25 mg mL^{-1} of crude *branch*-poly(S-*r*-DCNBS$_{10}$) in THF was added dropwise to a

beaker containing 300 mL of methanol stirring at 1000 rpm. After the addition of the crude *branch*-poly(S-*r*-DCNBS$_{10}$) was completed, the resulting suspension was stirred for 5 more minutes to facilitate coagulation and was allowed to sediment for 5 min. The phases were separated by vacuum filtration using a Buchner funnel and the filter cake was rinsed with methanol and ethanol until the washings were colorless. The precipitate was dried in a vacuum oven at 40°C overnight. *Branch*-poly(S-*r*-DCNBS$_{10}$) was obtained as a grey granule with a yield of 41 %. ATR FT-IR: ν [cm^{-1}] = 2951 *m*, 2866 *w* (C-H$_{\text{stretch}}$), 1449 *w*, 1405 *w* (Si-CH$_{3,\text{ anti. deform}}$), 1301 *w*, 1249 *s* (Si-CH$_{3,\text{ sym. deform}}$), 1071 *m* br., 1052 *m*, 1014 *m* (Si-O-Si), 791 *m*, 748 *s*, 688 *m*.

4.3.2.16 ***branch*-poly(S-*r*-DCNBS$_{20}$)**

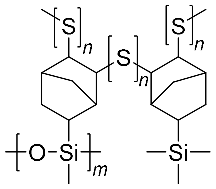

500 mg of sulfur powder, 400 mg of TMNBS, and 100 mg of DCNBS (0.482 mmol, 0.50 eq.) were weighed into a crimp vial with a stir bar and sealed with a crimp cap. The vial was heated to 150°C for 5 h. Sulfur was allowed to melt for 5 min before stirring at 400 rpm. After the reaction was completed, the temperature was reduced to 100 °C. To hydrolyze poly(S-*r*-DCNBS$_{20}$), 174 mg (9.66 mmol, 20.0 eq.) of deionized water were added to the melt. After the addition of deionized water, the crimping vial was sealed with a cap and the reaction was stirred with 100 rpm at 100°C for 18 h. The vial was cooled to room temperature and rinsed with methanol to remove excess HCl. The crude *branch*-poly(S-*r*-DCNBS$_{20}$) was first dried in an oven at 80°C for five days and then dried in a vacuum oven at 40°C overnight to remove residual HCl and to drive the equilibrium towards formation of siloxane bonds. The crude *branch*-poly(S-*r*-DCNBS$_{20}$) was extracted from the vial with 40 mL of THF. The resulting solution containing 25 mg mL^{-1} of crude *branch*-poly(S-*r*-DCNBS$_{20}$) in THF was added dropwise to a beaker containing 300 mL of methanol stirring at 1000 rpm. After the addition of the crude *branch*-poly(S-*r*-DCNBS$_{20}$) was completed, the resulting suspension was stirred for 5 more minutes to facilitate coagulation and was allowed to sediment for 5 min. The phases were separated by vacuum filtration using a Buchner funnel and the filter cake was rinsed with methanol and ethanol until the washings were colorless. The precipitate was dried in a vacuum oven at 40°C overnight. *Branch*-poly(S-*r*-DCNBS$_{20}$) was obtained as a grey granule with a yield of 43 %. ATR FT-IR: ν [cm^{-1}] = 2951 *m*, 2866 *w* (C-H$_{\text{stretch}}$), 1449 *w*, 1405 *w* (Si-CH$_{3,\text{ anti. deform}}$), 1301 *w*, 1249 *s* (Si-CH$_{3,\text{ sym. deform}}$), 1071 *m* br., 1052 *m*, 1014 *s* (Si-O-Si), 791 *m*, 748 *s*, 688 *m*.

4.3.2.17 ***branch*-poly(S-*r*-DCNBS$_{30}$)**

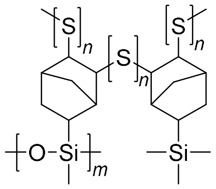

500 mg of sulfur powder, 350 mg of TMNBS, and 150 mg of DCNBS (0.723 mmol, 0.50 eq.) were weighed into a crimp vial with a stir bar and sealed with a crimp cap. The vial was heated to 150°C for 5 h. Sulfur was allowed to melt for 5 min before stirring at 400 rpm. After the reaction was completed, the temperature was reduced to 100 °C. To hydrolyze poly(S-*r*-DCNBS$_{30}$), 261 mg (14.5 mmol, 20.0 eq.) of deionized water were added to the melt. After the addition of deionized water, the crimping vial was sealed with a cap and the reaction was stirred with 100 rpm at 100°C for 18 h. The vial was cooled to room temperature and rinsed with methanol to remove excess HCl. The crude *branch*-poly(S-*r*-DCNBS$_{30}$) was first dried in an oven at 80°C for five days and then dried in a vacuum oven at 40°C overnight to remove residual HCl and to drive the equilibrium towards formation of siloxane bonds. The crude *branch*-poly(S-*r*-DCNBS$_{30}$) was extracted from the vial with 40 mL of THF. The resulting solution

containing 25 mg mL^{-1} of crude *branch*-poly(S-*r*-DCNBS$_{30}$) in THF was added dropwise to a beaker containing 300 mL of methanol stirring at 1000 rpm. After the addition of the crude *branch*-poly(S-*r*-DCNBS$_{30}$) was completed, the resulting suspension was stirred for 5 more minutes to facilitate coagulation and was allowed to sediment for 5 min. The phases were separated by vacuum filtration using a Buchner funnel and the filter cake was rinsed with methanol and ethanol until the washings were colorless. The precipitate was dried in a vacuum oven at 40°C overnight. *Branch*-poly(S-*r*-DCNBS$_{30}$) was obtained as a grey granule with a yield of 47 %. ATR FT-IR: ν [cm^{-1}] = 2951 *m*, 2866 *w* (C-H$_{\text{stretch}}$), 1449 *w*, 1405 *w* (Si-CH$_{3,\text{ anti. deform}}$), 1301 *w*, 1249 *s* (Si-CH$_{3,\text{ sym. deform}}$), 1071 *m* br., 1052 *m*, 1014 *vs* (Si-O-Si), 791 *m*, 748 *s*, 688 *m*.

4.3.2.18 *branch*-poly(S-*r*-TCNBS$_{10}$)

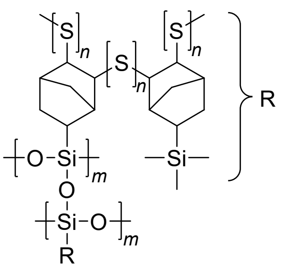

500 mg of sulfur powder, 450 mg of TMNBS, and 50 mg of TCNBS (0.220 mmol, 0.33 eq.) were weighed into a crimp vial with a stir bar and sealed with a crimp cap. The vial was heated to 150°C for 5 h. Sulfur was allowed to melt for 5 min before stirring at 400 rpm. After the reaction was completed, the temperature was reduced to 100 °C. To hydrolyze poly(S-*r*-TCNBS$_{10}$), 79 mg (4.39 mmol, 20.0 eq.) of deionized water were added to the melt. After the addition of deionized water, the crimping vial was sealed with a cap and the reaction was stirred with 100 rpm at 100°C for 18 h. The vial was cooled to room temperature and rinsed with methanol to remove excess HCl. The crude *branch*-poly(S-*r*-TCNBS$_{10}$) was first dried in an oven at 80°C for five days and then dried in a vacuum oven at 40°C overnight to remove residual HCl and to drive the equilibrium towards formation of siloxane bonds. The crude *branch*-poly(S-*r*-TCNBS$_{10}$) was extracted from the vial with 40 mL of THF. The resulting solution containing 25 mg mL^{-1} of crude *branch*-poly(S-*r*-TCNBS$_{10}$) in THF was added dropwise to a beaker containing 300 mL of methanol stirring at 1000 rpm. After the addition of the crude *branch*-poly(S-*r*-TCNBS$_{10}$) was completed, the resulting suspension was stirred for 5 more minutes to facilitate coagulation and was allowed to sediment for 5 min. The phases were separated by vacuum filtration using a Buchner funnel and the filter cake was rinsed with methanol and ethanol until the washings were colorless. The precipitate was dried in a vacuum oven at 40°C overnight. *Branch*-poly(S-*r*-TCNBS$_{10}$) was obtained as a grey granule with a yield of 32 %. ATR FT-IR: ν [cm^{-1}] = 2950 *m*, 2866 *w* (C-H$_{\text{stretch}}$), 1449 *w*, 1404 *w* (Si-CH$_{3,\text{ anti. deform}}$), 1301 *w*, 1248 *s* (Si-CH$_3$), 1098 *s*, 1051 *s*, 1028 *m* (Si-O-Si), 991 *s*, 913 *m*, 850 *s*, 831 *vs* (Si-CH$_{3,\text{ sym. deform}}$), 748 *s*, 689 *m*.

4.3.2.19 *branch*-poly(S-*r*-TCNBS$_{20}$)

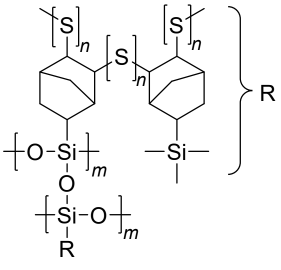

500 mg of sulfur powder, 400 mg of TMNBS, and 100 mg of TCNBS (0.440 mmol, 0.33 eq.) were weighed into a crimp vial with a stir bar and sealed with a crimp cap. The vial was heated to 150°C for 5 h. Sulfur was allowed to melt for 5 min before stirring at 400 rpm. After the reaction was completed, the temperature was reduced to 100 °C. To hydrolyze poly(S-*r*-TCNBS$_{10}$), 158 mg (8.78 mmol, 20.0 eq.) of deionized water were added to the melt. After the addition of deionized water, the crimping vial was sealed with a cap and the reaction was stirred with 100 rpm at 100°C for 18 h. The vial was cooled to room temperature and rinsed with methanol to remove excess HCl. The crude *branch*-poly(S-*r*-TCNBS$_{20}$) was first dried in an oven at 80°C for five

days and then dried in a vacuum oven at 40°C overnight to remove residual HCl and to drive the equilibrium towards formation of siloxane bonds. The crude *branch*-poly(S-*r*-TCNBS$_{20}$) was extracted from the vial with 40 mL of THF. The resulting solution containing 25 mg mL^{-1} of crude *branch*-poly(S-*r*-TCNBS$_{20}$) in THF was added dropwise to a beaker containing 300 mL of methanol stirring at 1000 rpm. After the addition of the crude *branch*-poly(S-*r*-TCNBS$_{20}$) was completed, the resulting suspension was stirred for 5 more minutes to facilitate coagulation and was allowed to sediment for 5 min. The phases were separated by vacuum filtration using a Buchner funnel and the filter cake was rinsed with methanol and ethanol until the washings were colorless. The precipitate was dried in a vacuum oven at 40°C overnight. *Branch*-poly(S-*r*-TCNBS$_{20}$) was obtained as a grey granule with a yield of 33 %. ATR FT-IR: ν [cm^{-1}] = 2950 *m*, 2866 *w* (C-H$_{\text{stretch}}$), 1449 *w*, 1404 *w* (Si-CH$_{3,\text{ anti. deform}}$), 1301 *w*, 1248 *s* (Si-CH$_3$), 1098 *s*, 1051 *s*, 1028 *s* (Si-O-Si), 991 *s*, 913 *m*, 850 *s*, 831 *vs* (Si-CH$_{3,\text{ sym. deform}}$), 748 *s*, 689 *m*.

4.3.2.20 poly(S_{41}-*r*-DVS-MM)

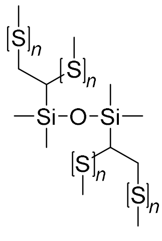

3.00 g of sulfur powder, 100 mg of zinc bis(diethyldithiocarbamate) and 7.00 g of DVS-MM were weighed into a crimp vial with a stir bar and sealed with a crimp cap. The vial was heated to 160°C for 30 min and was stirred 200 rpm until the liquid reaction mixture was homogeneous. The reaction mixture was poured into a PDMS mold and cured in an oven at 160°C for 120 min. Poly(S$_n$-*r*-DVS-MM) was obtained as a sheet with a yield of 94%. For mechanical analysis, the sheet was cut into circle and dumbbell shapes using cut-out stamps. ATR FT-IR v = 2957 *w*, 2901 *vw*, br. (C-H$_{\text{stretch}}$), 1410 *w* (Si-CH$_{3,\text{ anti. stretch}}$), br., 1255 *s* (Si-CH$_{3,\text{ sym. stretch}}$), 1160 *w*, 1034 *s*, br. (Si-O-Si), 831 *s* (Si-CH$_3$), 790 *s*, 701 *m*.

4.3.2.21 *net*-poly(S_{25}-*r*-TVS-D_3)

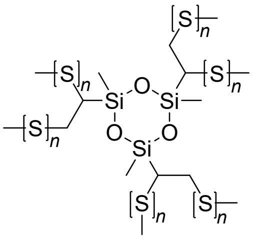

3.00 g of sulfur powder, 100 mg of zinc bis(diethyldithiocarbamate) and 7.00 g of TVS-D$_3$ were weighed into a crimp vial with a stir bar and sealed with a crimp cap. The vial was heated to 160°C for 30 min and was stirred 200 rpm until the liquid reaction mixture was homogeneous. The reaction mixture was poured into a PDMS mold and cured in an oven at 160°C for 120 min. Poly(S$_n$-*r*-TVS-D$_3$) was obtained as a sheet with a yield of 87%. For mechanical analysis, the sheet was cut into circle and dumbbell shapes using cut-out stamps. ATR FT-IR v = 2959 *w*, 2920 *w*, br., 2851 *vw* (C-H$_{\text{stretch}}$), 1408 *m* (Si-CH$_{3,\text{ anti. stretch}}$), br., 1260 *s* (Si-CH$_{3,\text{ sym. stretch}}$), 1165*w*, 1037 *vs*, br. (Si-O-Si), 775 *vs*, 750 *vs*.

4.3.2.22 *net*-poly(S_{19}-*r*-TVS-D_4)

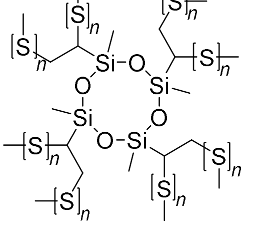

3.00 g of sulfur powder, 100 mg of zinc bis(diethyldithiocarbamate) and 7.00 g of TVS-D$_4$ were weighed into a crimp vial with a stir bar and sealed with a crimp cap. The vial was heated to 160°C for 30 min and was stirred 200 rpm until the liquid reaction mixture was homogeneous. The reaction mixture was poured into a PDMS mold and cured in an oven at 160°C for 120 min. Poly(S$_n$-*r*-TVS-D$_4$) was obtained as a sheet with a yield of 75%. For mechanical analysis, the sheet was cut into

circle and dumbbell shapes using cut-out stamps. ATR FT-IR v = 3056 *w,* 3015 *vw*, 2960 *w*, 2909 *vw*, br. (C-H$_{\text{stretch}}$), 1598 *w* (C=C$_{\text{stretch}}$), 1407 *m* (Si-CH$_{3,\text{ anti. stretch}}$), br., 1250 *s* (Si-CH$_{3,\text{ sym. stretch}}$), 1166 *w*, 1034 *vs*, br. (Si-O-Si), 1006 *s* (C-H$_{\text{twist}}$ in C=C-H), 959 *s* (C-H$_{\text{wag}}$ in C=C-H), 823 *m* (Si-CH$_3$), 786 *vs*, 745 *vs*, 683 *m*.

4.3.2.23 ***net*-poly(S$_{15}$-*r*-PVS-D$_5$)**

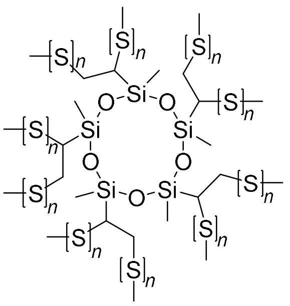

3.00 g of sulfur powder, 100 mg of zinc bis(diethyldithiocarbamate) and 7.00 g of TVS-D$_5$ were weighed into a crimp vial with a stir bar and sealed with a crimp cap. The vial was heated to 160°C for 30 min and was stirred 200 rpm until the liquid reaction mixture was homogeneous. The reaction mixture was poured into a PDMS mold and cured in an oven at 160°C for 120 min. Poly(S$_n$-*r*-TVS-D$_5$) was obtained as a sheet with a yield of 68%. For mechanical analysis, the sheet was cut into circle and dumbbell shapes using cut-out stamps. ATR FT-IR v = 3054 *w,* 3016 *vw* (C-H$_{\text{stretch}}$ in C=C-H), 2962 *w*, 2905 *vw*, br. (C-H$_{\text{stretch}}$), 1597 *w* (C=C$_{\text{stretch}}$), 1501 *w*, br., 1407 *m* (Si-CH$_{3,\text{ anti. stretch}}$), br., 1258 *s* (Si-CH$_{3,\text{ sym. stretch}}$), 1166 *w*, 1051 *vs*, br. (Si-O-Si), 1009 *s* (C-H$_{\text{twist}}$ in C=C-H), 960 *s* (C-H$_{\text{wag}}$ in C=C-H), 823 *m* (Si-CH$_3$), 788 *vs*, 752 *vs*, 699 *m,* 683 *m*.

5 Conclusion and Outlook

The realization that various resources on Earth are finite and are used up at alarming rates has led to research fields such as green chemistry. In this context, keywords such as atom economy or resource efficiency have become increasingly important. Millions of tons of sulfur are landfilled as a side product of natural oil and gas refining. Producing polymers from waste sulfur is an important contribution towards resource efficient polymers with a more diverse feedstock. Chemical strategies to improve existing upconversion reactions of elemental sulfur, such as the inverse vulcanization, are required to achieve this goal.

The inverse vulcanization and organosilicon chemistry were successfully combined to produce stable polymers with controllable properties and a high sulfur content between 15 – 50 wt%. The formed polymers represent a novel class of polymers that consists mainly of sulfur, carbon, silicon, and oxygen. Since S, Si, and O are elements primarily found in inorganic chemistry, the obtained polymers can be considered inorganic-organic hybrid polymers. It was demonstrated, for the first time, that methoxysilanes, ethoxysilanes, and chlorosilanes tolerate the harsh reaction conditions of the inverse vulcanization, i.e., high temperatures and the presence of thiyl radicals. Thus, the follow-up chemistry of alkoxysilanes and chlorosilanes, i.e., hydrolysis and (poly-) condensation, was unlocked as a post-modification toolbox for inverse vulcanized polymers. Hydrolysable silanes are industrially relevant and available with numerous functional groups. Thus, the range of design options for inverse vulcanized polymers extends far beyond the scope of this thesis.

The incorporation of T siloxane bonds into inverse vulcanized polymers allowed for the control over the polymer solubility at room temperature, as demonstrated for the soluble poly(S-*r*-StyTMS) prepared from the reaction of styrylethyltrimethoxysilane (StyTMS) and elemental sulfur. Polycondensation of poly(S-*r*-StyTMS) solutions converted the polymer into the insoluble *net*-poly(S-*r*-StyTMS) upon evaporation of the volatiles. This mechanism enabled the covalent coating of an inverse vulcanized polymer to a variety of surfaces and substrates for the first time. Important surface-based applications of inverse vulcanized polymers, such as pollutant remediation or anti-bacterial surfaces, can apply this strategy for the advanced design of filter materials. Further, thin-film interference allowed an inverse vulcanized polymer to appear in various colors such as blue or pink for the first time, which was enabled by precise control of the polymers thickness on reflective Si surfaces.

Control over the molecular and macroscopic properties of inverse vulcanized polymers was demonstrated without the need to alter their elemental composition. This was achieved by installing defined amounts of M, D, or T siloxane bonds into inverse vulcanized polymers via the inverse vulcanization and polycondensation of various chloro- and ethoxynorbornenylsilanes. Chloro- and alkoxysilanes react with oxygen-based nucleophiles, such as water or alcohols, but do not react with the comonomers frequently used for the inverse vulcanization, e.g., styrenes, norbornenes, terpenes, and more. Thus, the polycondensation of hydrolysable silanes could be used to reinforce various reported inverse vulcanized polymers with a controlled amount and type of siloxane bonds. The post-modification using siloxane bonds described in the present thesis is only the second reported strategy to induce control over inverse vulcanization polymers via post-crosslinking. However, it is the first strategy to comprehensively explore the branching of high sulfur content polymers systematically below the threshold of insolubility. Functional groups that cannot endure the reaction conditions of the inverse vulcanization could be incorporated into inverse vulcanized polymers using silanol condensation. Purification by precipitation resulted in near quantitative removal of low molar mass species for inverse vulcanized polymers with a sulfur content of 30 wt%. The resulting unimodal molar mass distribution is the narrowest obtained so far for an inverse vulcanized polymer, which is an important milestone towards inverse vulcanized model polymers. Such model polymers are urgently required as references for the gel permeation chromatography of inverse vulcanized polymers, since the molar mass data reported for inverse vulcanized polymer with equal compositions differs significantly depending on the reports.

The combination of organosilicon chemistry and the inverse vulcanization bears the potential to drive high sulfur content polymers closer to real life applications by offering a broadly applicable post-modification chemistry for crosslinking and branching of inverse vulcanized polymers. To trigger the post-modification of inverse vulcanized polymers via silane hydrolysis and polycondensation, water or a dilute aqueous acid are required, which are both ecologic and economic reagents. Further, the polycondensation of inverse vulcanized polymers carrying hydrolysable silane groups can be conducted as a heterogeneous reaction in the melt. The unecological and expensive use of a potentially hazardous solvent can thus be avoided.

Lastly, it was shown that the inverse vulcanization of linear and cyclic vinylsiloxanes readily gives access to shape persistent, ductile, and elastic polymers. This is attributed to the unique properties of the siloxane bond, i.e., the low energy barriers of rotation and bond linearization. However, more synthetic effort is necessary to keep parameters such as the sulfur content per vinyl group constant, which would allow a detailed comparison of the ring size and strain on the strength and elasticity.

Future challenges in the field of inverse vulcanization will revolve around fundamental problems such as the high yield of low molar mass products that are frequently obtained by researchers. Precipitations are useful to remove low molar mass products of inverse vulcanized polymers, as demonstrated in this thesis and earlier by PYUN. However, precipitation leads to a decrease of the yield and is not a feasible solution for upscaled procedures. Further scalable design principles are required to inherently reduce the amount of side products with a low molar mass. Soon, the most promising inverse vulcanized polymers could enter the domains of polymer engineering and polymer processing to evaluate their performance on a larger scale and to test the influence of composites and additives in prototype materials. In parallel, end of life aspects need to be investigated to ensure that no detrimental environmental problems arise from inverse vulcanized polymer waste. Ideally, inverse vulcanized polymers in the future will not only compete with carbon polymers based on their price, but rather excel in certain applications.

Literature

[1] G. M. Whitesides, *Adv. Mater.* **2004**, *16*, 1375.

[2] H. Nielsen in *Lectures in Isotope Geology* (Eds.: E. Jäger, J. C. Hunziker), Springer Berlin Heidelberg, Berlin, Heidelberg, **1979**, pp. 283–312.

[3] E. Jäger, J. C. Hunziker (Eds.) *Lectures in Isotope Geology*, Springer Berlin Heidelberg, Berlin, Heidelberg, **1979**.

[4] I. Krossing, Y. Steudel, R. Steudel, *Chemistry of Non-metals*, Walter de Gruyter, Berlin, New York, **2008**.

[5] J. T. Brosnan, M. E. Brosnan, *J.nutr.* **2006**, *136*, 1636S-1640S.

[6] E. Block, *Angew. Chem. Int. Ed.* **1992**, *31*, 1135.

[7] E. Lellouch, D. F. Strobel, M. J. S. Belton, M. E. Summers, G. Paubert, R. Moreno, *Astrophys. J.* **1996**, *459*.

[8] A. F. Holleman, N. Wiberg, E. Wiberg, *Lehrbuch der Anorganischen Chemie*, Walter de Gruyter, **2007**.

[9] R. Steudel, H.-J. Mäusle, *Angew. Chem. Int. Ed.* **1979**, *18*, 152.

[10] L. Crapanzano, W. A. Crichton, G. Monaco, R. Bellissent, M. Mezouar, *Nat. mater.* **2005**, *4*, 550.

[11] *Mineral commodity summaries 2021*, Reston, VA, **2021**.

[12] C. W. Tullock, F. S. Fawcett, W. C. Smith, D. D. Coffman, *J. Am. Chem. Soc.* **1960**, *82*, 539.

[13] A. G. Evans, G. W. Meadows, *Trans. Faraday Soc.* **1947**, *43*, 667.

[14] T. B. Nguyen, *Adv. Synth. Catal.* **2017**, *359*, 1066.

[15] R. Steudel, *Angew. Chem. Int. Ed.* **1975**, *14*, 655.

[16] K.-P. Wanczek, C. Bliefert, R. Budenz, *Z. Naturforsch. A* **1975**, *30*, 1156.

[17] B. Beagley, G. H. Eckersley, D. P. Brown, D. Tomlinson, *Trans. Faraday Soc.* **1969**, *65*, 2300.

[18] E. Hirota, *BCSJ* **1958**, *31*, 130.

[19] L.-F. Zou, Y. Fu, K. Shen, Q.-X. Guo, *J. Mol. Struct.* **2007**, *807*, 87.

[20] D. M. Gardner, G. K. Fraenkel, *J. Am. Chem. Soc.* **1956**, *78*, 3279.

[21] R. Steudel, *Z. Naturforsch. B* **1975**, *30*, 281.

[22] A. Kausar, S. Zulfiqar, M. I. Sarwar, *Polym. Rev.* **2014**, *54*, 185.

[23] R. Steudel, *Chem. rev.* **2002**, *102*, 3905.

[24] K. J. Saunders in *Organic Polymer Chemistry* (Ed.: K. J. Saunders), Springer Netherlands, Dordrecht, **1973**, pp. 394–405.

[25] E. M. Fettes, J. S. Jorczak, *Ind. Eng. Chem.* **1950**, *42*, 2217.

[26] A. Pirayesh, M. Salami-Kalajahi, H. Roghani-Mamaqani, F. Najafi, *Polym. Rev.* **2019**, *59*, 124.

[27] M. Sheydaei, S. Talebi, M. Salami-Kalajahi, *J. Sulfur Chem.* **2021**, *42*, 67.

[28] E. R. Bertozzi, *Rubber Chem. Technol.* **1968**, *41*, 114.

[29] H. Iimori, Y. Shibasaki, S. Ando, M. Ueda, *Macromol. Symp.* **2003**, *199*, 23.

[30] S. Watanabe, O. Shishido, M. Murata, Y. Masuda, *Macromol. Rapid Commun.* **1998**, *19*, 75.

[31] O. Daglar, B. Gungor, G. Guric, U. S. Gunay, G. Hizal, U. Tunca, H. Durmaz, *J. Polym. Sci.* **2020**, *58*, 824.

[32] D. P. Nair, M. Podgórski, S. Chatani, T. Gong, W. Xi, C. R. Fenoli, C. N. Bowman, *Chem. Mater.* **2014**, *26*, 724.

[33] P. Wadhwa, A. Kharbanda, A. Sharma, *Asian J. Org. Chem.* **2018**, *7*, 634.

[34] X.-H. Cao, C.-J. Zhang, J.-L. Yang, L.-F. Hu, X.-H. Zhang, *Polym. Chem.* **2020**, *11*, 309.

[35] C.-J. Zhang, T.-C. Zhu, X.-H. Cao, X. Hong, X.-H. Zhang, *J. Am. Chem. Soc.* **2019**, *141*, 5490.

[36] O. Daglar, U. S. Gunay, G. Hizal, U. Tunca, H. Durmaz, *Macromolecules* **2019**, *52*, 3558.

[37] O. Daglar, E. Cakmakci, U. S. Gunay, G. Hizal, U. Tunca, H. Durmaz, *Macromolecules* **2020**, *53*, 2965.

[38] G. Ruiyi, Z. Jianzheng, W. Songhua, *Proc. Eng.* **2015**, *99*, 1234.

[39] S. Matsumura, N. Kihara, T. Takata, *Macromolecules* **2001**, *34*, 2848.

[40] S. Matsumura, N. Kihara, T. Takata, *High Perform. Polym.* **2001**, *13*, S293-S304.

[41] M. Ueda, T. Abe, M. Oda, *J. Polym. Sci. A* **1992**, *30*, 1993.

[42] T. Fujisawa, M. Kakutani, N. Kobayashi, *J. Polym. Sci. B* **1971**, *9*, 91.

[43] L. Infante Teixeira, K. Landfester, H. Thérien-Aubin, *Macromolecules* **2021**, *54*, 3659.

[44] V. A. Nikonov, G. V. Leplyanin, *Sulfur rep.* **1989**, *9*, 1.

[45] S. C. Mamah, P. S. Goh, A. F. Ismail, N. D. Suzaimi, L. T. Yogarathinam, Y. O. Raji, T. H. El-badawy, *J. Water Proc. Eng.* **2021**, *40*, 101835.

[46] J. Xu, W. Zhang, Q. Jiang, J. Mu, Z. Jiang, *Polymer* **2015**, *62*, 77.

[47] Q. Zhang, S. Li, S. Zhang, *Chem. commun.* **2010**, *46*, 7495.

[48] K. Matsumoto, H. Komuro, T. Kai, M. Jikei, *Polym. J.* **2013**, *45*, 909.

[49] C. Yuan, Y. Wang, *Colloid Polym. Sci.* **2021**, *299*, 93.

[50] E. K. Macdonald, M. P. Shaver, *Polym. Int.* **2015**, *64*, 6.

[51] J. Liu, M. Ueda, *J. Mater. Chem.* **2009**, *19*, 8907.

[52] T. Higashihara, M. Ueda, *Macromolecules* **2015**, *48*, 1915.

[53] J. M. Scheiger, P. Theato in *Sulfur-Containing Polymers* (Eds.: X.-H. Zhang, P. Theato), Wiley, **2021**, pp. 305–338.

[54] T. P. Kaloni, P. K. Giesbrecht, G. Schreckenbach, M. S. Freund, *Chem. Mater.* **2017**, *29*, 10248.

[55] R. Cugola, U. Giovanella, P. Di Gianvincenzo, F. Bertini, M. Catellani, S. Luzzati, *Thin Solid Films* **2006**, *511-512*, 489.

[56] M. Mellah, E. Labbé, J.-Y. Nédélec, J. Périchon, *New J. Chem.* **2002**, *26*, 207.

[57] F. Louwet, L. Groenendaal, J. Dhaen, J. Manca, J. van Luppen, E. Verdonck, L. Leenders, *Synth. Met.* **2003**, *135-136*, 115.

[58] S. Kirchmeyer, *Pedot. Principles and Applications of an Intrinsically Conductive Polymer*, Taylor & Francis Group, Baton Rouge, **2010**.

[59] Y. Xia, S. Dai, *J. Mater. Sci.: Mater. Electron.* **2021**, *32*, 12746.

[60] T. Minami, W. Tang, K. Asano, *Polym. J.* **2021**.

[61] V. Singh, T. L. Bougher, A. Weathers, Y. Cai, K. Bi, M. T. Pettes, S. A. McMenamin, W. Lv, D. P. Resler, T. R. Gattuso et al., *Nat. nanotechnol.* **2014**, *9*, 384.

[62] H. R. Kricheldorf, G. Schwarz, *J. Macromol. Sci. A* **2007**, *44*, 625.

[63] L.-Y. Wang, G.-G. Gu, T.-J. Yue, W.-M. Ren, X.-B. Lu, *Macromolecules* **2019**, *52*, 2439.

[64] T.-J. Yue, M.-C. Zhang, G.-G. Gu, L.-Y. Wang, W.-M. Ren, X.-B. Lu, *Angew. Chem. Int. Ed.* **2019**, *58*, 618.

[65] T. J. Bannin, M. K. Kiesewetter, *Macromolecules* **2015**, *48*, 5481.

[66] T. Lütke-Eversloh, A. Fischer, U. Remminghorst, J. Kawada, R. H. Marchessault, A. Bögershausen, M. Kalwei, H. Eckert, R. Reichelt, S.-J. Liu et al., *Nat. mater.* **2002**, *1*, 236.

[67] T. Lütke-Eversloh, K. Bergander, H. Luftmann, A. Steinbüchel, *Biomacromolecules* **2001**, *2*, 1061.

[68] Y. Kamei, A. Nagai, H. Nishida, H. Kimura, T. Endo, *Macromol. biosci.* **2007**, *7*, 364.

[69] H. Mutlu, E. B. Ceper, X. Li, J. Yang, W. Dong, M. M. Ozmen, P. Theato, *Macromol. Rapid Commun.* **2019**, *40*, e1800650.

[70] N.-H. You, T. Higashihara, S. Yasuo, S. Ando, M. Ueda, *Polym. Chem.* **2010**, *1*, 480.

[71] T.-J. Yue, W.-M. Ren, Y. Liu, Z.-Q. Wan, X.-B. Lu, *Macromolecules* **2016**, *49*, 2971.

[72] T. M. McGuire, A. Buchard, *Polym. Chem.* **2021**, *12*, 4253.

[73] L. H. Tagle, F. R. Diaz, P. E. Riveros, *Polym. J.* **1986**, *18*, 501.

[74] C. Berti, A. Celli, E. Marianucci, *Eur. Polym. J.* **2002**, *38*, 1281.

[75] B. OCHIAI, T. ENDO, *Progr. Polym. Sci.* **2005**, *30*, 183.

[76] K. Soga, M. Sato, H. Imamura, S. Ikeda, *J. Polym. Sci. B.* **1975**, *13*, 167.

[77] K. Soga, H. Imamura, M. Sato, S. Ikeda, *J. Polym. Sci. B.* **1976**, *14*, 677.

[78] G. A. Bhat, D. J. Darensbourg in *Sulfur-Containing Polymers* (Eds.: X.-H. Zhang, P. Theato), Wiley, **2021**, pp. 39–79.

[79] K. Nakano, G. Tatsumi, K. Nozaki, *J. Am. Chem. Soc.* **2007**, *129*, 15116.

[80] K. Shimokawa, M. Kato, S. Matsumura, *Macromol. Chem. Phys.* **2011**, *212*, 150.

[81] W. J. Chung, J. J. Griebel, E. T. Kim, H. Yoon, A. G. Simmonds, H. J. Ji, P. T. Dirlam, R. S. Glass, J. J. Wie, N. A. Nguyen et al., *Nat. chem.* **2013**, *5*, 518.

[82] G. B. Kauffman, *Chem. Educator* **2001**, *6*, 50.

[83] M. Akiba, *Prog. in Polym. Sci.* **1997**, *22*, 475.

[84] J. Emsley, D. W. Griffiths, G. J. J. Jayne, *J. Chem. Soc., Perkin Trans. 1* **1979**, 228.

[85] J. Emsley, D. W. Griffiths, *Phosphorus Sulfur Relat. Elem.* **1980**, *9*, 227.

[86] A. Ahmed, L.-P. Blanchard, *J. Appl. Polym. Sci.* **1984**, *29*, 1225.

[87] L. Blight, B. R. Currell, B. J. Nash, R. A. M. Scott, C. Stillo, *Advances in Chemistry* (Eds.: D. J. Miller, T. K. Wiewiorowski, American Chemical Society, Washington, D. C., **1972**, pp. 13–30.

[88] B. K. Bordoloi, E. M. Pearce, L. Blight, B. R. Currell, R. Merrall, R. A. M. Scott, C. Stillo, *J. Polym. Sci. Polym. Chem. Ed.* **1980**, *18*, 383.

[89] E. H. Farmer, F. W. Shipley, *J. Chem. Soc.* **1947**, *0*, 1519.

[90] H. Fritz, C. D. Weis, *Tetrahedron. Lett.* **1974**, *15*, 1659.

[91] A. L. Klebanskii, N. Ja. Zukerman, L. P. Fomina, *J. Polym. Sci.* **1958**, *30*, 363.

[92] C. G. Krespan, W. R. Brasen, H. N. Cripps in *Advances in Chemistry* (Eds.: D. J. Miller, T. K. Wiewiorowski), American Chemical Society, Washington, D. C., **1972**, pp. 179–189.

[93] C. G. Krespan, W. R. Brasen, *J. Org. Chem.* **1962**, *27*, 3995.

[94] D. J. Miller, T. K. Wiewiorowski (Eds.) *Advances in Chemistry*, American Chemical Society, Washington, D. C., **1972**.

[95] Y. MIYATA, M. SAWADA, *Polymer* **1988**, *29*, 1683.

[96] Y. Miyata, M. Sawada, *Polymer* **1988**, *29*, 1495.

[97] W. E. Mochel, *J. Polym. Sci.* **1952**, *8*, 583.

[98] T. C. Shields, A. N. Kurtz, *J. Am. Chem. Soc.* **1969**, *91*, 5415.

[99] D. Todorova, St. Todorov, *Spectrosc. Lett.* **1999**, *32*, 321.

[100] J. L. Kice, *J. Polym. Sci.* **1956**, *19*, 123.

[101] P. D. Bartlett, H. Kwart, *J. Am. Chem. Soc.* **1952**, *74*, 3969.

[102] M. M. Collinson, *Trends Analyt.Chem.* **2002**, *21*, 31.

[103] L. J. Dodd, Ö. Omar, X. Wu, T. Hasell, *ACS Catal.* **2021**, *11*, 4441.

[104] Y. Zhang, K. M. Konopka, R. S. Glass, K. Char, J. Pyun, *Polym. Chem.* **2017**, *8*, 5167.

[105] D. A. Boyd, C. C. Baker, J. D. Myers, V. Q. Nguyen, G. A. Drake, C. C. McClain, F. H. Kung, S. R. Bowman, W. Kim, J. S. Sanghera, *Chem. commun.* **2016**, *53*, 259.

[106] Y. Zhang, N. G. Pavlopoulos, T. S. Kleine, M. Karayilan, R. S. Glass, K. Char, J. Pyun, *J. Polym. Sci. A* **2019**, *57*, 7.

[107] Y. Zhang, T. S. Kleine, K. J. Carothers, D. D. Phan, R. S. Glass, M. E. Mackay, K. Char, J. Pyun, *Polym. Chem.* **2018**, *9*, 2290.

[108] X. Wu, J. A. Smith, S. Petcher, B. Zhang, D. J. Parker, J. M. Griffin, T. Hasell, *Nat. commun.* **2019**, *10*, 647.

[109] C. R. Westerman, C. L. Jenkins, *Macromolecules* **2018**, *51*, 7233.

[110] J. A. Smith, X. Wu, N. G. Berry, T. Hasell, *J. Polym. Sci. Part A* **2018**, *56*, 1777.

[111] A. Abbasi, M. M. Nasef, W. Z. N. Yahya, *Green Mater.* **2020**, 1.

[112] J. J. Griebel, R. S. Glass, K. Char, J. Pyun, *Progr. Polym. Sci.* **2016**, *58*, 90.

[113] J. M. Chalker, M. J. H. Worthington, N. A. Lundquist, L. J. Esdaile, *Top. curr. Chem.* **2019**, *377*, 16.

[114] J. Lim, J. Pyun, K. Char, *Angew. Chem.* **2015**, *54*, 3249.

[115] M. K. Salman, B. Karabay, L. C. Karabay, A. Cihaner, *J. Appl. Polym. Sci.* **2016**, *133*, 329.

[116] Y. Zhang, R. S. Glass, K. Char, J. Pyun, *Polym. Chem.* **2019**, *10*, 4078.

[117] M. J. H. Worthington, R. L. Kucera, I. S. Albuquerque, C. T. Gibson, A. Sibley, A. D. Slattery, J. A. Campbell, S. F. K. Alboaiji, K. A. Muller, J. Young et al., *Chemistry* **2017**, *23*, 16219.

[118] M. P. Crockett, A. M. Evans, M. J. H. Worthington, I. S. Albuquerque, A. D. Slattery, C. T. Gibson, J. A. Campbell, D. A. Lewis, G. J. L. Bernardes, J. M. Chalker, *Angew. Chem.* **2016**, *55*, 1714.

[119] M. Thielke, L. Bultema, D. Brauer, B. Richter, M. Fischer, P. Theato, *Polymers* **2016**, *8*, 266.

[120] N. A. Lundquist, M. J. Sweetman, K. R. Scroggie, M. J. H. Worthington, L. J. Esdaile, S. F. K. Alboaiji, S. E. Plush, J. D. Hayball, J. M. Chalker, *ACS Sust. Chem. Eng.* **2019**, *7*, 11044.

[121] D. J. Parker, H. A. Jones, S. Petcher, L. Cervini, J. M. Griffin, R. Akhtar, T. Hasell, *J. Mater. Chem. A* **2017**, *5*, 11682.

[122] M. J. H. Worthington, C. J. Shearer, L. J. Esdaile, J. A. Campbell, C. T. Gibson, S. K. Legg, Y. Yin, N. A. Lundquist, J. R. Gascooke, I. S. Albuquerque et al., *Adv. Sust. Syst.* **2018**, *2*, 1800024.

[123] L.-A. Ko, Y.-S. Huang, Y. A. Lin, *ACS Appl. Polym. Mater.* **2021**, *3*, 3363.

[124] Z. Deng, A. Hoefling, P. Théato, K. Lienkamp, *Macromol. Chem. Phys.* **2018**, *219*, 1700497.

[125] J. A. Smith, R. Mulhall, S. Goodman, G. Fleming, H. Allison, R. Raval, T. Hasell, *ACS Omega* **2020**, *5*, 5229.

[126] C. Herrera, K. J. Ysinga, C. L. Jenkins, *ACS appl. Mater. int.* **2019**, *11*, 35312.

[127] Y. Xin, H. Peng, J. Xu, J. Zhang, *Adv. Funct. Mater.* **2019**, *29*, 1808989.

[128] T. R. Martin, K. A. Mazzio, H. W. Hillhouse, C. K. Luscombe, *Chem. commun.* **2015**, *51*, 11244.

[129] T. S. Kleine, N. A. Nguyen, L. E. Anderson, S. Namnabat, E. A. LaVilla, S. A. Showghi, P. T. Dirlam, C. B. Arrington, M. S. Manchester, J. Schwiegerling et al., *ACS Macro Lett.* **2016**, *5*, 1152.

[130] L. E. Anderson, T. S. Kleine, Y. Zhang, D. D. Phan, S. Namnabat, E. A. LaVilla, K. M. Konopka, L. Ruiz Diaz, M. S. Manchester, J. Schwiegerling et al., *ACS Macro Lett.* **2017**, *6*, 500.

[131] J. J. Griebel, S. Namnabat, E. T. Kim, R. Himmelhuber, D. H. Moronta, W. J. Chung, A. G. Simmonds, K.-J. Kim, J. van der Laan, N. A. Nguyen et al., *Advanced mater.* **2014**, *26*, 3014.

[132] A. J. Berndt, J. Hwang, M. D. Islam, A. Sihn, A. M. Urbas, Z. Ku, S. J. Lee, D. A. Czaplewski, M. Dong, Q. Shao et al., *Polymer* **2019**, *176*, 118.

[133] M. Babaeian, L. R. Diaz, S. Namnabat, T. S. Kleine, A. Azarm, J. Pyun, N. Peyghambarian, R. A. Norwood, *Opt. Mater. Expr.* **2018**, *8*, 2510.

[134] J. J. Griebel, N. A. Nguyen, S. Namnabat, L. E. Anderson, R. S. Glass, R. A. Norwood, M. E. Mackay, K. Char, J. Pyun, *ACS Macro Lett.* **2015**, *4*, 862.

[135] T. S. Kleine, L. R. Diaz, K. M. Konopka, L. E. Anderson, N. G. Pavlopolous, N. P. Lyons, E. T. Kim, Y. Kim, R. S. Glass, K. Char et al., *ACS Macro Lett.* **2018**, *7*, 875.

[136] T. S. Kleine, T. Lee, K. J. Carothers, M. O. Hamilton, L. E. Anderson, L. Ruiz Diaz, N. P. Lyons, K. R. Coasey, W. O. Parker, L. Borghi et al., *Angew. Chem.* **2019**.

[137] D. A. Boyd, V. Q. Nguyen, C. C. McClain, F. H. Kung, C. C. Baker, J. D. Myers, M. P. Hunt, W. Kim, J. S. Sanghera, *ACS Macro Lett.* **2019**, *8*, 113.

[138] S. Zhuo, Y. Huang, C. Liu, H. Wang, B. Zhang, *Chem. commun.* **2014**, *50*, 11208.

[139] O. Bayram, B. Kiskan, E. Demir, R. Demir-Cakan, Y. Yagci, *ACS Sust. Chem. Eng.* **2020**, *8*, 9145.

[140] I. Gomez, O. Leonet, J. A. Blazquez, D. Mecerreyes, *Chem. Sus. Chem* **2016**, *9*, 3419.

[141] Y. Zhang, J. J. Griebel, P. T. Dirlam, N. A. Nguyen, R. S. Glass, M. E. Mackay, K. Char, J. Pyun, *J. Polym. Sci. Part A* **2017**, *55*, 107.

[142] H. Kang, M. J. Park, *Nano Energy* **2021**, *89*, 106459.

[143] L. Zhang, L. Ge, G. He, Z. Tian, J. Huang, J. Wang, D. J. Brett, J. Hofkens, F. Lai, T. Liu, *J. Phys. Chem. C* **2021**, *125*, 18604.

[144] T. Zhang, F. Hu, W. Shao, S. Liu, H. Peng, Z. Song, C. Song, N. Li, X. Jian, *ACS Nano* **2021**.

[145] N. A. Lundquist, A. D. Tikoalu, M. J. H. Worthington, R. Shapter, S. J. Tonkin, F. Stojcevski, M. Mann, C. T. Gibson, J. R. Gascooke, A. Karton et al., *Chem. Eur. J.* **2020**, *26*, 10035.

[146] S. J. Tonkin, C. T. Gibson, J. A. Campbell, D. A. Lewis, A. Karton, T. Hasell, J. M. Chalker, *Chem. Sci.* **2020**.

[147] A. M. Abraham, S. V. Kumar, S. M. Alhassan, *Chem. Eng. J.* **2018**, *332*, 1.

[148] M. S. Karunarathna, M. K. Lauer, T. Thiounn, R. C. Smith, A. G. Tennyson, *J. Mater. Chem. A* **2019**, *7*, 15683.

[149] K.-S. Kang, A. Phan, C. Olikagu, T. Lee, D. A. Loy, M. Kwon, H.-J. Paik, S. J. Hong, J. Bang, W. O. Parker et al., *Angew. Chem. Int. Ed.* **2021**.

[150] I. Bu Najmah, N. A. Lundquist, M. K. Stanfield, F. Stojcevski, J. A. Campbell, L. J. Esdaile, C. T. Gibson, D. A. Lewis, L. C. Henderson, T. Hasell et al., *Chem. Sus. Chem.* **2021**, *14*, 2352.

[151] M. Mann, J. E. Kruger, F. Andari, J. McErlean, J. R. Gascooke, J. A. Smith, M. J. H. Worthington, C. C. C. McKinley, J. A. Campbell, D. A. Lewis et al., *Org. biomol. Chem.* **2019**, *17*, 1929.

[152] S. F. Valle, A. S. Giroto, R. Klaic, G. G. Guimarães, C. Ribeiro, *Polym. Degrad. Stab.* **2019**, *162*, 102.

[153] K. Orme, A. H. Fistrovich, C. L. Jenkins, *Macromolecules* **2020**, *53*, 9353.

[154] J. A. Smith, S. J. Green, S. Petcher, D. J. Parker, B. Zhang, M. J. H. Worthington, X. Wu, C. A. Kelly, T. Baker, C. T. Gibson et al., *Chemistry* **2019**, *25*, 10433.

[155] B. Zhang, S. Petcher, T. Hasell, *Chem. Commun.* **2019**, *55*, 10681.

[156] P. Yan, W. Zhao, B. Zhang, L. Jiang, S. Petcher, J. A. Smith, D. J. Parker, A. I. Cooper, J. Lei, T. Hasell, *Angew. Chem.* **2020**, *59*, 13371.

[157] S. F. Thames, K. G. Panjnani, *J. Inorg. Organomet. Polym.* **1996**, *6*, 59.

[158] J. Czochralski, *Z. Phys. Chem.* **1918**, *92U*, 219.

[159] W. P. Weber, *Silicon Reagents for Organic Synthesis*, Springer Berlin, Heidelberg, **1983**.

[160] Z. Rappoport, Y. Apeloig, *The Chemistry of Organic Silicon Compounds*, John Wiley & Sons, Ltd, Chichester, UK, **1998**.

[161] G. Ren, H. Su, S. Wang, *J. Sol-Gel Sci. Technol.* **2020**, *96*, 108.

[162] Tamon, Kitamura, Okazaki, *J. coll. Interf. Sci.* **1998**, *197*, 353.

[163] Z. Pan, M. Liu, C. Zheng, D. Gao, W. Huang, *Chin. J. Chem.* **2017**, *35*, 1227.

[164] J. L. Speier, J. A. Webster, G. H. Barnes, *J. Am. Chem. Soc.* **1957**, *79*, 974.

[165] A. S. Manoso, C. Ahn, A. Soheili, C. J. Handy, R. Correia, W. M. Seganish, P. Deshong, *J. Org. Chem.* **2004**, *69*, 8305.

[166] R. Wakabayashi, Y. Sugiura, T. Shibue, K. Kuroda, *Angew. Chem. Int. Ed.* **2011**, *50*, 10708.

[167] P. Elsner, *Dominghaus - Kunststoffe. Eigenschaften und Anwendungen*, Springer, Dordrecht, **2011**.

[168] M. Bols, C. M. Pedersen, *Beilstein J. Org. Chem.* **2017**, *13*, 93.

[169] T. Köhler, A. Gutacker, E. Mejía, *Org. Chem. Front.* **2020**, *7*, 4108.

[170] J. Chojnowski, M. Cypryk in *Silicon-Containing Polymers* (Eds.: R. G. Jones, W. Ando, J. Chojnowski), Springer Netherlands, Dordrecht, **2000**, pp. 3–41.

[171] L. Wang, U. S. Schubert, S. Hoeppener, *Chem. Soc. Rev.* **2021**, *50*, 6507.

[172] E. Ayandele, B. Sarkar, P. Alexandridis, *Nanomater.* **2012**, *2*, 445.

[173] K. D. Kim, H. T. Kim, *J. Sol-Gel Sci. Technol.* **2002**, *25*, 183.

[174] C.-H. Cheng, D. F. Shantz, *J. Phys. Chem. B* **2005**, *109*, 7266.

[175] A. A. Issa, A. S. Luyt, *Polymers* **2019**, *11*.

[176] S. J. Clarson, Z. Wang, J. E. Mark, *Eur. Polym. J.* **1990**, *26*, 621.

[177] F. Normand, X. W. He, J. M. Widmaier, G. C. Meyer, J. E. Herz, *Eur. Polym. J.* **1989**, *25*, 371.

[178] C. M. Kuo, S. J. Clarson, *J. Inorg. Organomet. Polym.* **2012**, *22*, 577.

[179] R. M. Pasternack, S. Rivillon Amy, Y. J. Chabal, *Langmuir* **2008**, *24*, 12963.

[180] B. Arkles, J. R. Steinmetz, J. Zazyczny, P. Mehta, *J. Adh. Sci. Technol.* **1992**, *6*, 193.

[181] G. Qing, C. Cui, *Dalton Trans.* **2017**, *46*, 8746.

[182] E. Perju, E. Cuervo-Reyes, S. Shova, D. M. Opris, *RSC Adv.* **2018**, *8*, 7569.

[183] B. Yactine, A. Ratsimihety, F. Ganachaud, *Polym. Adv. Technol.* **2010**, *21*, 139.

[184] B. Yactine, B. Boutevin, F. Ganachaud, *Polym. Adv. Technol.* **2009**, *20*, 66.

[185] C. J. Teng, W. P. Weber, G. Cai, *Macromolecules* **2003**, *36*, 5126.

[186] P. Dubois, O. Coulembier, J. M. Raquez (Eds.) *Handbook of ring-opening polymerization*, Wiley-VCH, Weinheim, **2008**.

[187] L. Pauling, *The nature of the chemical bond and the structure of molecules and crystals. An introduction to modern structural chemistry*, Cornell Univ. Press, Ithaca, New York, **2000**.

[188] L. Pauling, *Am. Mineral.* **1980**, *65*, 321.

[189] L. Pauling, *J. Phys. Chem.* **1952**, *56*, 361.

[190] L. Pauling, *General chemistry*, Dover Publ, New York, **1988**.

[191] S. Shambayati, S. L. Schreiber, J. F. Blake, S. G. Wierschke, W. L. Jorgensen, *J. Am. Chem. Soc.* **1990**, *112*, 697.

[192] F. Weinhold, R. West, *Organomet.* **2011**, *30*, 5815.

[193] V. Chandrasekhar, *Inorganic and Organometallic Polymers*, Springer-Verlag Berlin Heidelberg, Berlin, Heidelberg, **2005**.

[194] K. Kimura, M. Kubo, *J. Chem. Phys.* **1959**, *30*, 151.

[195] J. Passmore, J. M. Rautiainen, *Eur. J. Inorg. Chem.* **2012**, *2012*, 6002.

[196] F. Cataldo, *Angew. Makromol. Chem.* **1997**, *249*, 137.

[197] J. M. Scheiger, C. Direksilp, P. Falkenstein, A. Welle, M. König-Edel, S. Heissler, J. Matysik, P. Levkin, P. Theato, *Angew. Chem. Int. Ed.* **2020**.

[198] M. K. Denk, *Eur. J. Inorg. Chem.* **2009**, *2009*, 1358.

[199] B. A. Trofimov, L. M. Sinegovskaya, N. K. Gusarova, *J. Sulfur Chem.* **2009**, *30*, 518.

[200] S. Wilhelm, N. Bloom, *Fuel Proc. Technol.* **2000**, *63*, 1.

[201] M. Mann, B. Zhang, S. Tonkin, C. Gibson, Z. Jia, T. Hasell, J. Chalker, *Process for coating surfaces with a copolymer made from sulfur and dicyclopentadiene*, **2021 (preprint)**.

[202] H. Ramadan, A. Ghanem, H. El-Rassy, *Chem. Eng. J.* **2010**, *159*, 107.

[203] M. Dishon, O. Zohar, U. Sivan, *Langmuir* **2011**, *27*, 12977.

[204] C. Sun, F. Ma, G. Zhang, R. Qu, Y. Zhang, *J. Chem. Eng. Data* **2011**, *56*, 4407.

[205] J. Sanchez, S. E. Rankin, A. V. McCormick, *Ind. Eng. Chem. Res.* **1996**, *35*, 117.

[206] Y. Sugahara, S. Okada, S. Sato, K. Kuroda, C. Kato, *J. Non-Crys. Sol.* **1994**, *167*, 21.

[207] Y. Sugahara, S. Okada, K. Kuroda, C. Kato, *J. Non-Crys. Sol.* **1992**, *139*, 25.

[208] L. Hudson, *X-ray Transition Energies, NIST Standard Reference Database 128*, National Institute of Standards and Technology, **2003**.

[209] J. J. Griebel, N. A. Nguyen, A. V. Astashkin, R. S. Glass, M. E. Mackay, K. Char, J. Pyun, *ACS Macro Lett.* **2014**, *3*, 1258.

[210] M. Venczel, G. Bognár, Á. Veress, *Processes* **2021**, *9*, 331.

[211] Z. Kőkuti, K. van Gruijthuijsen, M. Jenei, G. Tóth-Molnár, A. Czirják, J. Kokavecz, P. Ailer, L. Palkovics, A. C. Völker und G. Szabó, *Appl. Rheol.* **2014**, *24*, 6.

[212] M. S. Alvarez, S. Jacobs, S. B. Jiang, R. R. Brancaccio, N. A. Soter, D. E. Cohen, *Am. J. Cont. Derm.* **2003**, *14*, 161.

[213] S. Diez, A. Hoefling, P. Theato, W. Pauer, *Polymers* **2017**, *9*.

[214] A. Bhargav, M. E. Bell, Y. Cui, Y. Fu, *ACS Appl. Energy Mater.* **2018**, *1*, 5859.

[215] V. S. Wadi, K. K. Jena, K. Halique, S. M. Alhassan, *ACS Appl. Polym. Mater.* **2020**, *2*, 198.

[216] K. K. Jena, S. M. Alhassan, *J. Appl. Polym. Sci.* **2016**, *133*, 14924.

[217] V. S. Wadi, K. K. Jena, K. Halique, R. Brigita, L. Cmok, V. Tzitzios, S. M. Alhassan, *Sci. Rep.* **2020**, *10*, 14924.

[218] B. Akkus, B. Kiskan, Y. Yagci, *Polym. Chem.* **2019**, *10*, 5743.

[219] P. Yan, W. Zhao, B. Zhang, L. Jiang, S. Petcher, J. A. Smith, D. J. Parker, A. I. Cooper, J. Lei, T. Hasell, *Angew. Chem. Int. Ed.* **2020**, *132*, 13473.

[220] Y. Chen, Y. Liu, Y. Chen, Y. Zhang, X. Zan, *Polymers* **2020**, *12*.

[221] S. Z. Khawaja, S. Vijay Kumar, K. K. Jena, S. M. Alhassan, *Mater. Lett.* **2017**, *203*, 58.

[222] M. Preißinger, D. Brüggemann, *Energies* **2016**, *9*, 183.

[223] H.-K. Lin, Y.-L. Liu, *Macromol. Rapid Commun.* **2017**, *38*.

[224] R. Anyszka, M. Kozanecki, A. Czaderna, M. Olejniczak, J. Sielski, M. Siciński, M. Imiela, J. Wręczycki, D. Pietrzak, T. Gozdek, *J. Sulfur Chem.* **2019**, *40*, 587.

[225] J. R. Durig, W. J. Natter, M. Johnson-Streusand, *Appl. Spectrosc.* **1980**, *34*, 60.

[226] X. Zhang, J. Qiu, X. Li, J. Zhao, L. Liu, *Appl. Opt.* **2020**, *59*, 2337.

[227] B.G. Belenkii, L.Z. Vilenchik in *Modern Liquid Chromatography*, Elsevier, **1983**, pp. 149–269.

[228] N. E. Stankova, P. A. Atanasov, R. Nikov, R. G. Nikov, N. N. Nedyalkov, T. R. Stoyanchov, N. Fukata, K. N. Kolev, E. I. Valova, J. S. Georgieva et al., *Appl. Surf. Sci.* **2016**, *374*, 96.

[229] T. Trantidou, Y. Elani, E. Parsons, O. Ces, *Microsyst. Nanoeng.***2017**, *3*, 16091.

[230] A. Groza, A. Surmeian, *J. Nanomater.* **2015**, *2015*, 1.

[231] L. M. Johnson, L. Gao, C. W. Shields IV, M. Smith, K. Efimenko, K. Cushing, J. Genzer, G. P. López, *J. nanobiotechnol.* **2013**, *11*, 22.

[232] I. W. Levin, W. C. Harris, *Spectrochim. Acta A Mol. Spectrosc.* **1973**, *29*, 1815.

[233] V. K. Tomazett, W. G. Santos, B. S. Lima-Neto, *Reac. Kinet. Mech. Cat.* **2017**, *120*, 663.

[234] C. M. Herzinger, B. Johs, W. A. McGahan, J. A. Woollam, W. Paulson, *J. Appl. Phys.* **1998**, *83*, 3323.

[235] A. Shaka, J. Keeler, R. Freeman, *J. Magn. Res.* **1983**, *53*, 313.

[236] G. Metz, X. L. Wu, S. O. Smith, *J. Magn. Res. A* **1994**, *110*, 219.

[237] R. S. Thakur, N. D. Kurur, P. K. Madhu, *Chem. Phys. Lett.* **2006**, *426*, 459.

[238] C. Vinod Chandran, P. K. Madhu, N. D. Kurur, T. Bräuniger, *Magn. Reson. Chem.* **2008**, *46*, 943.

Appendix

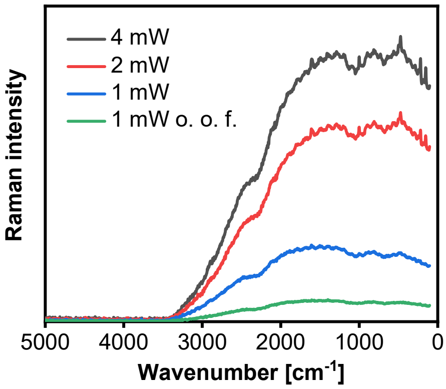

Appendix 1. Raman spectra of powdered *net*-poly(S_{35}-*r*-StyTMS). No peaks could be identified due to fluorescence or black body irradiation. A reduction of the laser intensity from 4 to 1 mW decreased the background noise, however, no spectrum could be obtained. A further reduction of the laser intensity by moving the sample out of the focus of the laser failed to improve the spectrums quality.

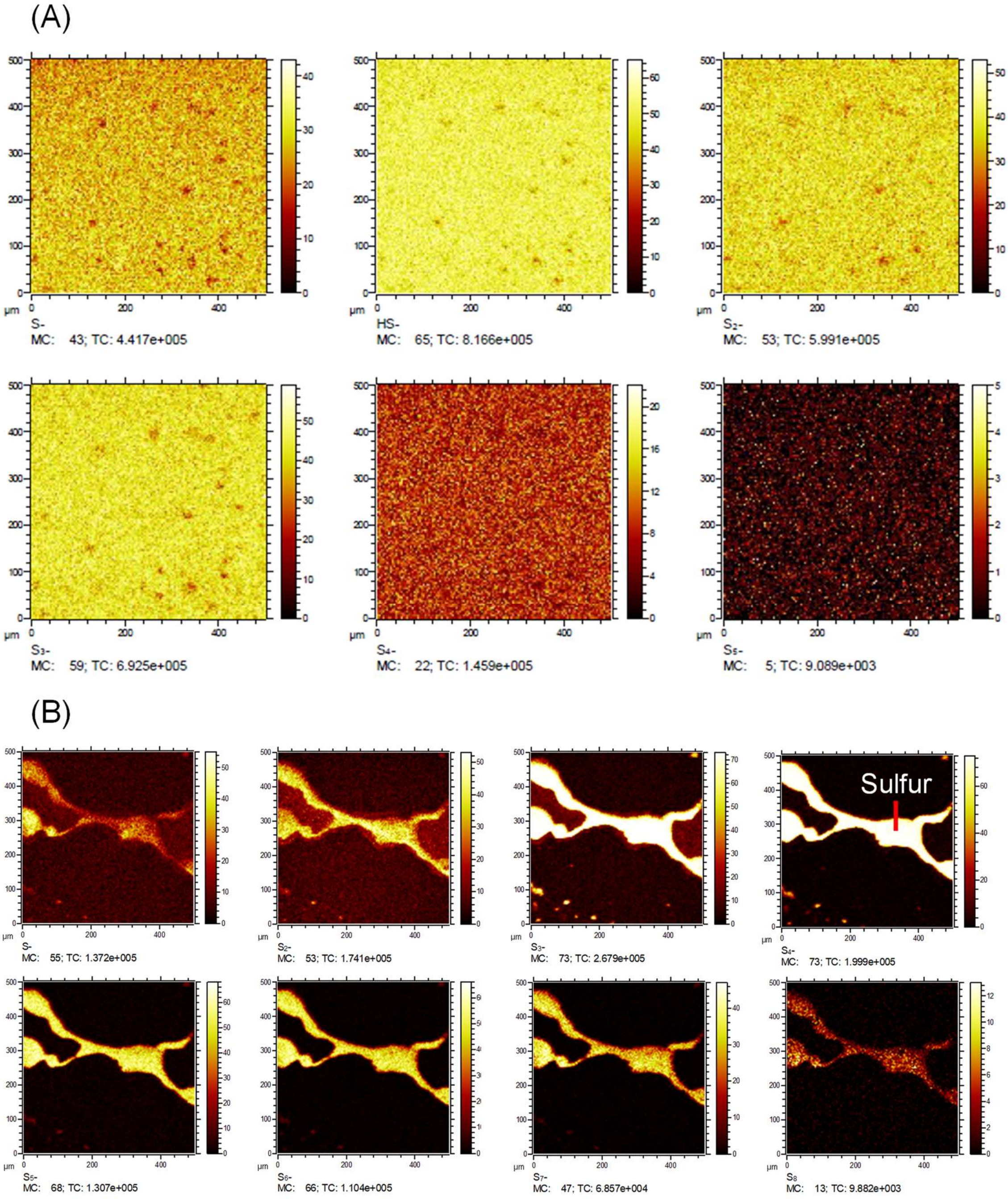

Appendix 2. Color-coded ion count obtained from ToF-SIMS examination of (A) *net*-poly(S-*r*-StyTMS) and (B) elemental sulfur. Unlike *net*-poly(S-*r*-StyTMS), elemental sulfur was not distributed homogeneously on the surface. The examined surface area was 500 × 500 µm (0.025 mm²).

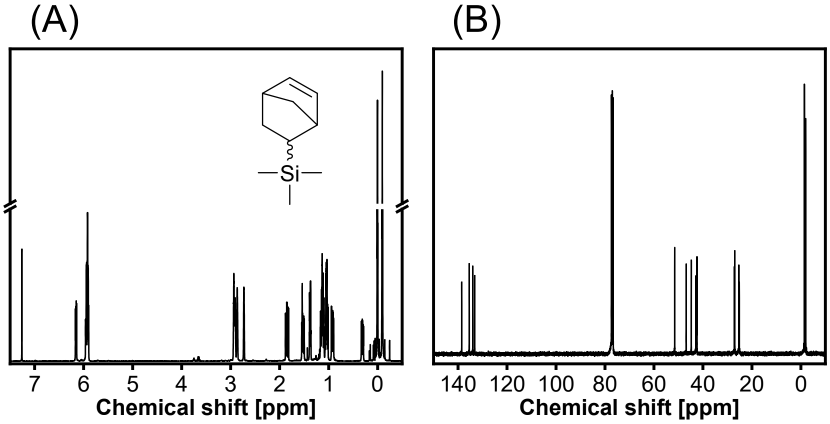

Appendix 3. (A) ^{1}H NMR and (B) ^{13}C spectra of TMNBS in $CDCl_3$ referenced to the solvent peak at 7.26 and 77.0 ppm, respectively.

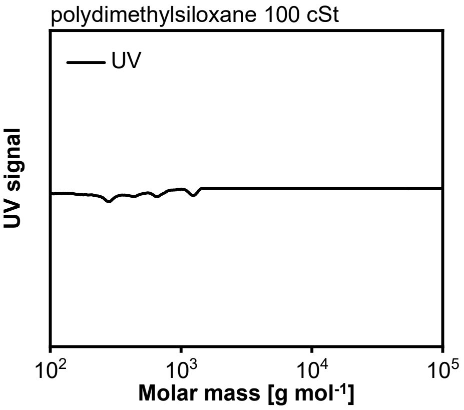

Appendix 4. GPC traces of PDMS with a viscosity of 100 cSt. Aliphatic poly(siloxane)s do not absorb UV light rendering the polymer invisible for the UV detector.

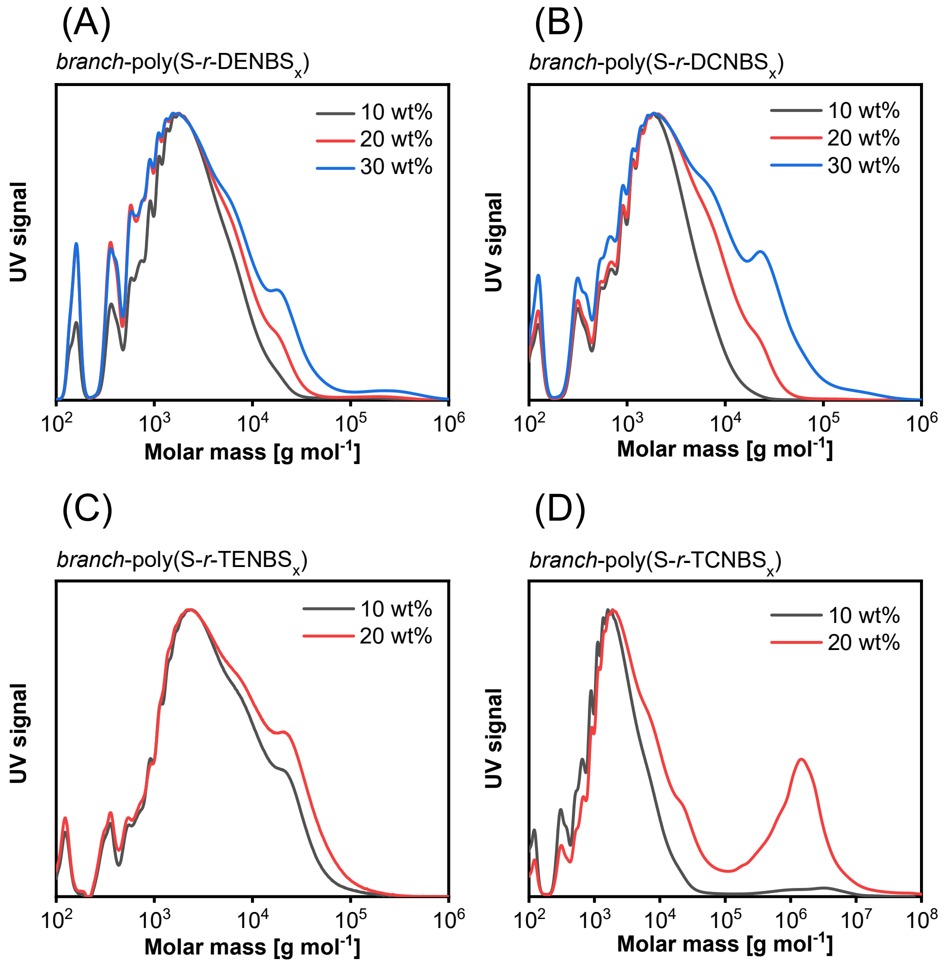

Appendix 5. GPC traces of (A) *branch*-poly(S-*r*-DENBS$_x$), (B) *branch*-poly(S-*r*-DCNBS$_x$), (C) *branch*-poly(S-*r*-TENBS$_x$), and (D) *branch*-poly(S-*r*-TCNBS$_x$).

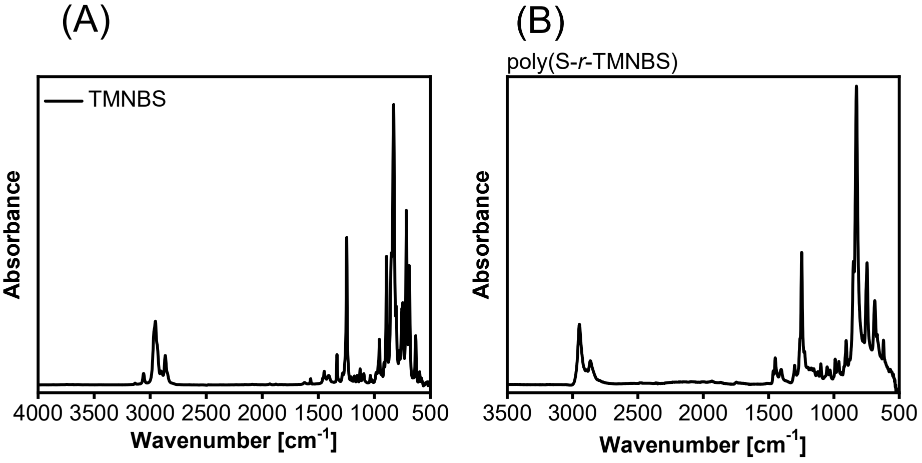

Appendix 6. ATR FTIR spectra of (A) TMNBS and (B) poly(S-*r*-TMNBS).

ATR FT-IR TMNBS: ν [cm^{-1}] = 3059 *vw* (C-H$_{\text{stretch}}$ in C=C-H), 2953 *m*, 2864 *w* (C-H$_{\text{stretch}}$), 1568 *vw* (C=C$_{\text{stretch}}$), 1406 br. *vw* (Si-CH$_{3,\text{ anti. deform}}$), 1388 *w*, 1333 *w* (C-H$_{\text{bend}}$ in C=C-H), 1246 *s* (Si-CH$_{3,\text{ sym. deform}}$), 945 *w*, 912 *w*, 891 *s* (C=C$_{\text{bend}}$), 827 *vs* (Si-CH$_3$), 802 *s*, 785 *s*, 746 *w*, 714 *vs* (C-H$_{\text{wag}}$), 689 *s*, 631 *w*.

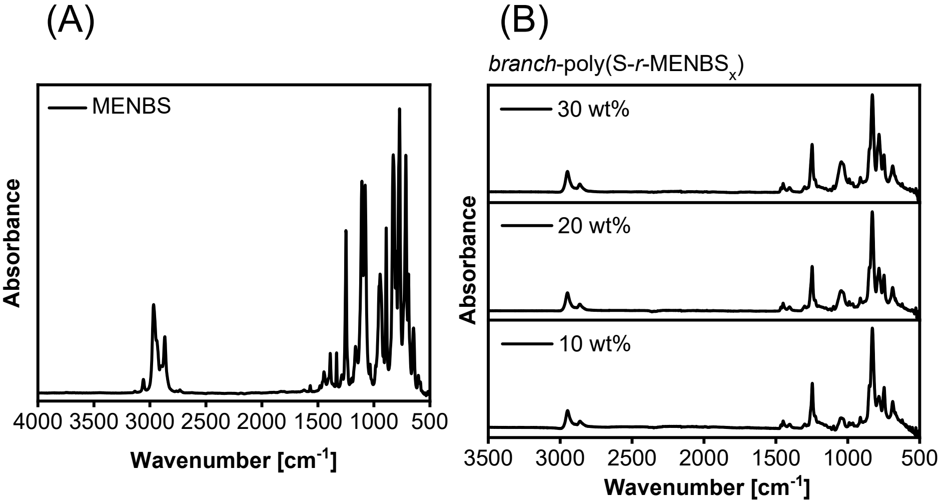

Appendix 7. ATR FTIR spectra of (A) MENBS and (B) *branch*-poly(S-*r*-MENBS$_x$).

ATR FT-IR MENBS: ν [cm^{-1}] = 3059 *vw* (C-H$_{\text{stretch}}$ in C=C-H), 2966 *m*, 2866 *m* (C-H$_{\text{stretch}}$), 1568 *vw* (C=C$_{\text{stretch}}$), 1447 *vw*, 1391 *w*, 1333 *w* (C-H$_{\text{bend}}$ in C=C-H), 1250 *s* (Si-CH$_{3,\text{ sym. deform}}$), 1164 *w*, 1107 *vs*, 1078 *vs*, and 945 *s* (Si-OEt), 889 *s* (C=C$_{\text{bend}}$), 827 *vs* (Si-CH$_3$), 802 *s*, 771 *vs*, 716 *vs* (C-H$_{\text{wag}}$), 691 *s*, 646 *m*.

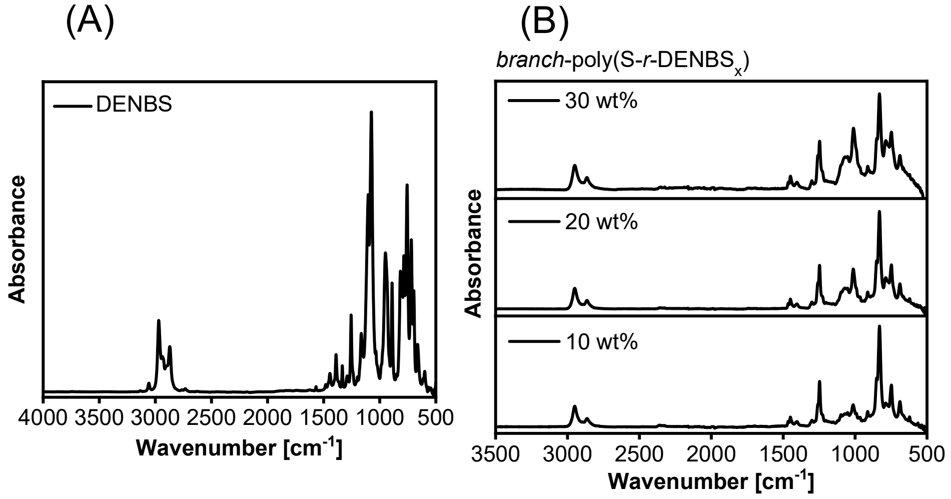

Appendix 8. ATR FTIR spectra of (A) DENBS and (B) *branch*-poly(S-*r*-DENBS$_x$).

ATR FT-IR DENBS: ν [cm^{-1}] = 3057 *vw* (C-H$_{\text{stretch}}$ in C=C-H), 2970 *m* and 2871 *m* (C-H$_{\text{stretch}}$), 1568 *vw* (C=C$_{\text{stretch}}$), 1445 *vw*, 1388 *w*, 1333 *w* (C=CH$_{\text{bend}}$), 1256 *s* (Si-CH$_{3,\text{ sym. deform}}$), 1164 *m*, 1103 *vs*, 1074 *vs*, and 948 *s* (Si-OEt), 891 *s* (C=C$_{\text{bend}}$), 816 *s*, 802 *m*, 785 *s*, 756 *vs*, 717 *s* (C-H$_{\text{wag}}$), 696 *s*, 662 *m*.

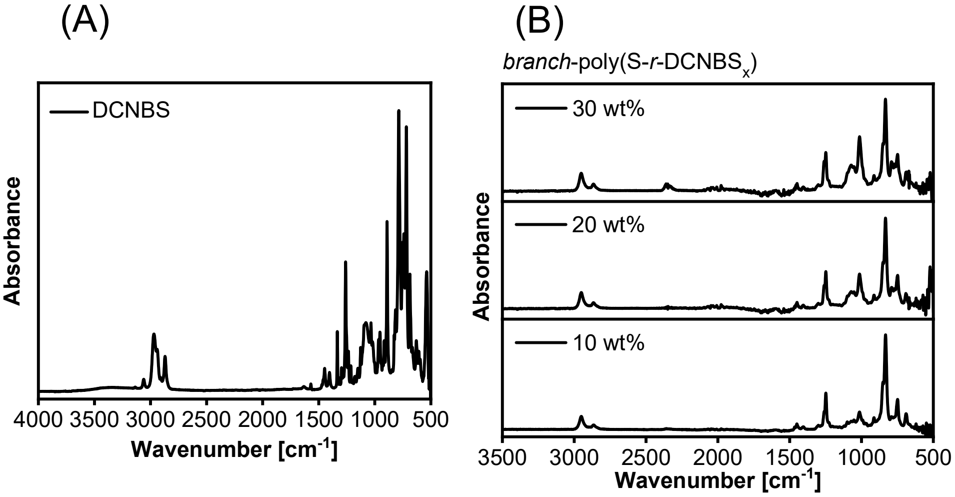

Appendix 9. ATR FTIR spectra of (A) DCNBS and (B) *branch*-poly(S-*r*-DCNBS$_x$).

ATR FT-IR DCNBS: ν [cm^{-1}] = 3600-3100 *vw* br. (O-H), 3060 *vw* (C-H$_{\text{stretch}}$ in C=C-H), 2970 *m*, 2869 *m* (C-H$_{\text{stretch}}$), 1570 *vw* (C=C$_{\text{stretch}}$), 1447 *vw*, 1404 *w* (Si-CH$_{3,\text{ anti. deform}}$), 1335 *w* (C-H$_{\text{bend}}$ in C=C-H), 1260 *s* (Si-CH$_{3,\text{ sym. deform}}$), 1226 *m*, 1079 *m*, br., 1034 *m*, 965 *m*, 954 *m*, 891 *s* (C=C$_{\text{bend}}$), 815 *m*, 786 *vs*, 741 *s*, 718 v*s* (C-H$_{\text{wag}}$), 687 *s*, 623 *m*, 537 s, br. (Si-Cl).

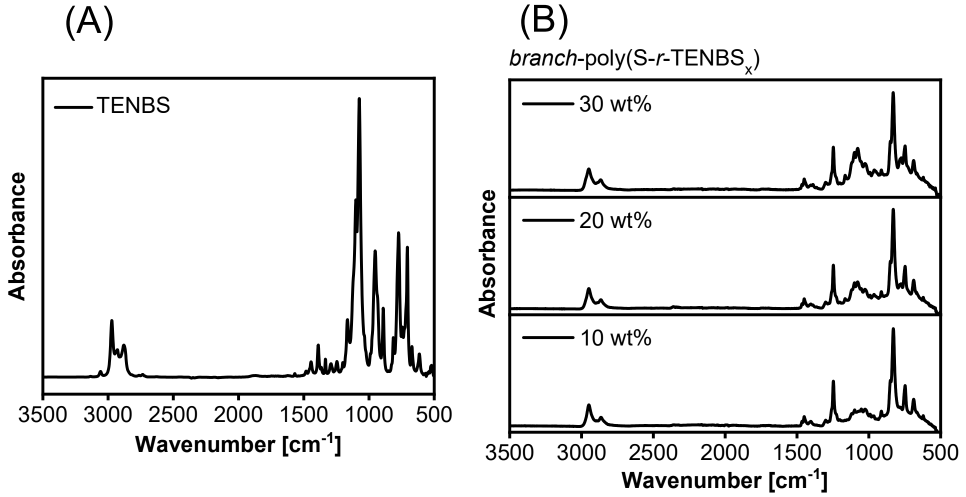

Appendix 10. ATR FTIR spectra of (A) TENBS and (B) *branch*-poly(S-*r*-TENBS$_x$).

ATR FT-IR TENBS: ν [cm^{-1}] = 3059 *vw* (C-H$_{\text{stretch}}$ in C=C-H), 2972 *m* and 2880 *w* (C-H$_{\text{stretch}}$), 1568 *vw* (C=C$_{\text{stretch}}$), 1445 *w*, 1389 *w*, 1335 *w* (C-H$_{\text{bend}}$ in C=C-H), 1292 *w*, 1246 w, 1164 *m*, 1101 *vs*, 1074 *vs*, and 953 *s* (Si-OEt), 891 *m* (C=C$_{\text{bend}}$), 813 w, 802 *m*, 773 *s*, 744 *m*, 706 *s* (C-H$_{\text{wag}}$), 671 *w*, 613 *m*.

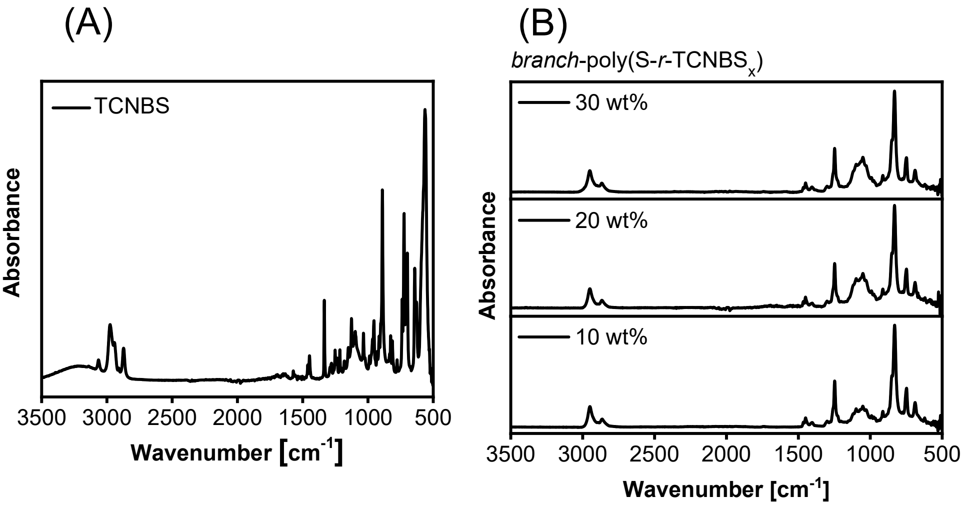

Appendix 11. ATR FTIR spectra of (A) TCNBS and (B) *branch*-poly(S-*r*-TCNBS$_x$).

ATR FT-IR TCNBS: ν [cm^{-1}] = 3500-3000 *vw* br. (O-H), 3065 *vw* (C-H$_{\text{stretch}}$ in C=C-H), 2975 *m*, 2870 *w* (C-H$_{\text{stretch}}$), 1572 *vw* (C=C$_{\text{stretch}}$), 1447 *w*, 1335 *w* (C-H$_{\text{bend}}$ in C=C-H), 1252 *w*, 1126 *m*, 1097 *m*, 1034 *m*, 955 *m*, 890 *vs* (C=C$_{\text{bend}}$), 826 *m*, 813 *m*, 777 *vw*, 738 *m*, 723 *s*, 710 *s* (C-H$_{\text{wag}}$), 698 *s*, 641 *s*, 627 *m*, 563 br. (Si-Cl).

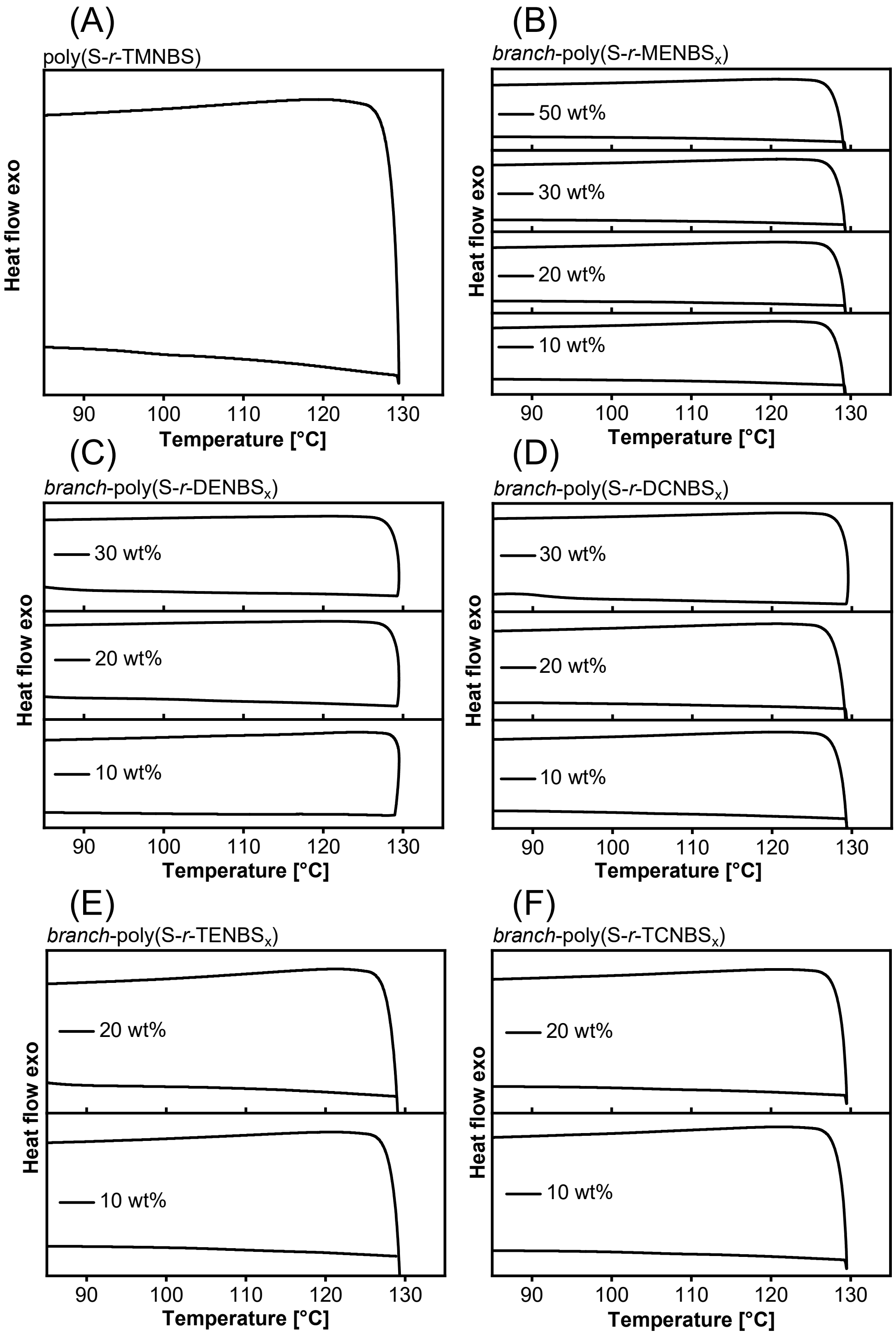

Appendix 12. DSC thermograms showing the first heat ramp from 85 – 130°C of (A) poly(S-*r*-TMNBS), (B) *branch*-poly(S-*r*-MENBS$_x$), (C) *branch*-poly(S-*r*-DENBS$_x$), (D) *branch*-poly(S-*r*-DCNBS$_x$), (E) *branch*-poly(S-*r*-TENBS$_x$), and (F) *branch*-poly(S-*r*-TCNBS$_x$).

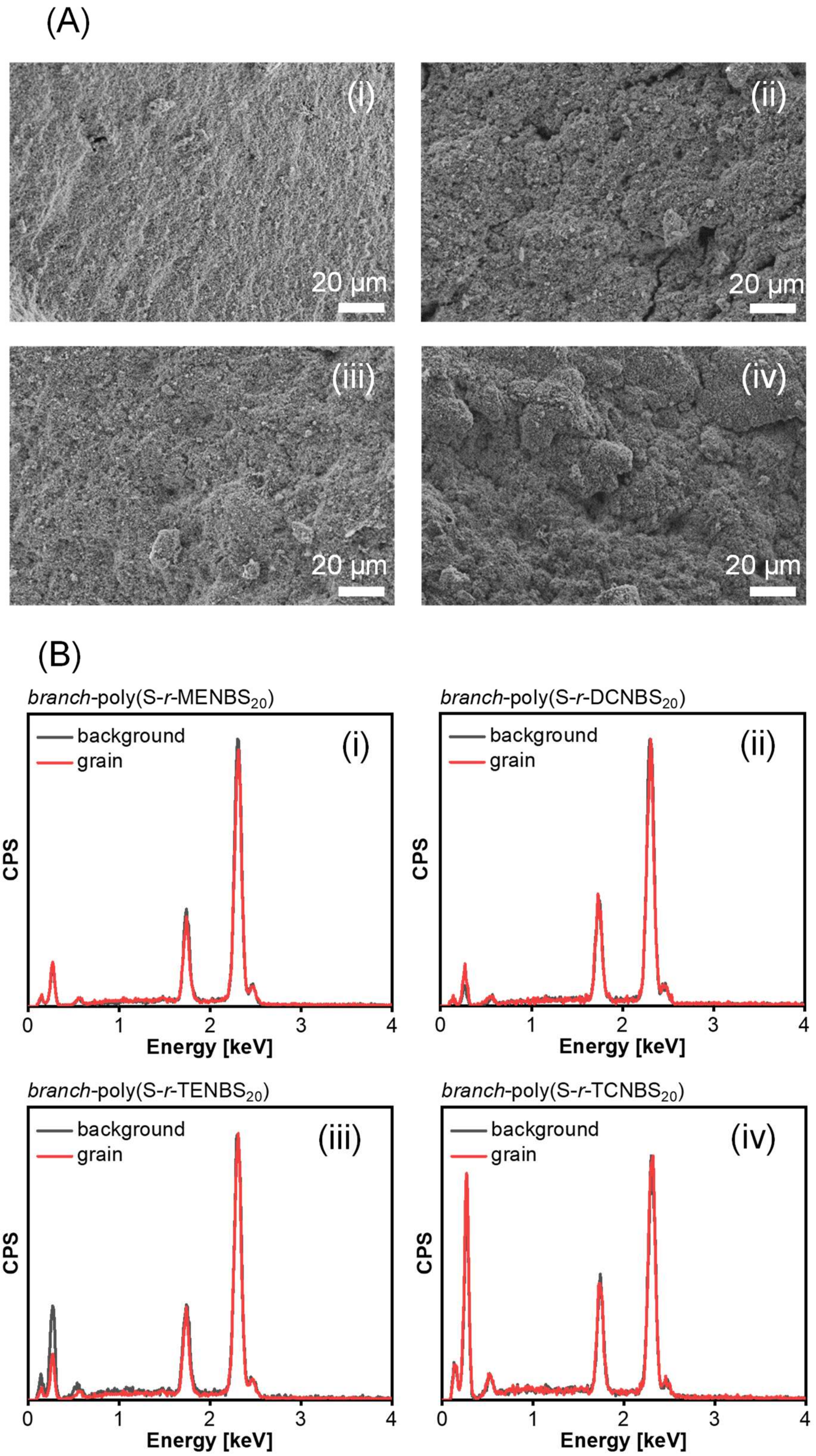

Appendix 13. (A) SEM images and (B) EDX spectra of granulated (i) poly(S-*r*-MENBS$_{20}$), (ii) *branch*-poly(S-*r*-DCNBS$_{20}$), (iii) *branch*-poly(S-*r*-TENBS$_{20}$), and (iv) *branch*-poly(S-*r*-TCNBS$_{20}$).

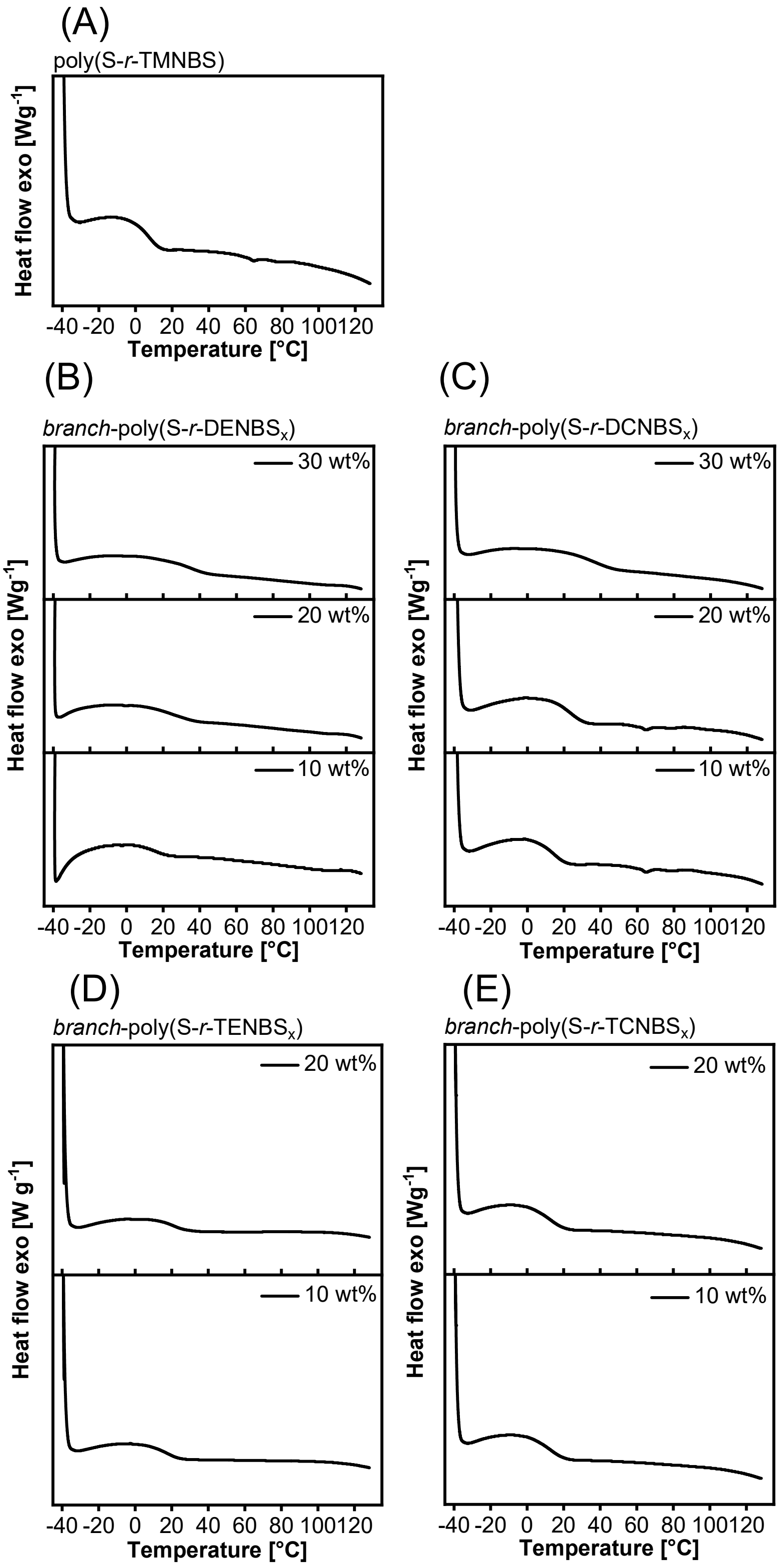

Appendix 14. DSC thermograms showing the second heat ramp from -40 – 130°C of (A) poly(S-*r*-TMNBS), (B) *branch*-poly(S-*r*-DENBS$_x$), (C) *branch*-poly(S-*r*-DCNBS$_x$), (D) *branch*-poly(S-*r*-TENBS$_x$), and (E) *branch*-poly(S-*r*-TCNBS$_x$).